Brick-mortar interaction in masonry under compression

bouwstenen

Ad Vermeltfoort

Brick-mortar interaction in masonry under compression

/ faculteit bouwkunde

85

Bouwstenen 85
ISBN 90-6814-582-7

Cover by A. van Gennip / A.T. Vermeltfoort
Printed by University Press Facilities, Eindhoven University of Technology,
Eindhoven, The Netherlands

Brick-mortar interaction in masonry under compression

Proefschrift

ter verkrijging van de graad van doctor aan de
Technische Universiteit Eindhoven op gezag van
de Rector Magnificus, prof.dr.ir. C.J. van Duijn,
voor een commissie aangewezen door het
College voor Promoties in het openbaar
te verdedigen op
donderdag 28 april 2005 om 16.00 uur

door

Arduïnus Theodorus Vermeltfoort

geboren te Sint-Oedenrode

Dit proefschrift is goedgekeurd door de promotoren:

prof.ir-arch. D.R.W. Martens
en
prof.ir. C.S. Kleinman

Copromotor:
prof.dr.ir. G.P.A.G. van Zijl

Brick-mortar interaction in masonry under compression

A.T. Vermeltfoort

Constitution of the doctoral committee.

prof.ir. J. Westra (chair)
Department of Architecture, Building and Planning,
Technische Universiteit Eindhoven

prof. ir-arch. D.R.W. Martens
Department of Architecture, Building and Planning,
Technische Universiteit Eindhoven

prof.ir. C.S. Kleinman
Department of Architecture, Building and Planning,
Technische Universiteit Eindhoven

prof.dr.ir. G.P.A.G. van Zijl,
Division for structural Engineering and Civil Engineering Informatics
Stellenbosch University, Stellenbosch, South Africa

prof.dr.ir. J.G.M. Kerstens,
Department of Architecture, Building and Planning,
Technische Universiteit Eindhoven

prof.dr.ir. B. de Vries
Department of Architecture, Building and Planning,
Technische Universiteit Eindhoven

prof.dr.ir. J.G. Rots
Departement of Archtecture, Urbanism and Building Sciences,
Technische Universiteit, Delft

prof.dr.ir. K. van Balen,
Departement Burgerlijke Bouwkunde en
R. Lemaire International Center for Conservation
Katholieke Universiteit Leuven, Belgium

dr,ir. C.J.W.P. Groot,
Departement Building Materials and Building Technology
Technische Universiteit Delft

dr.ir. R. van der Pluijm,
Wienerberger BV, Zaltbommel

Dankwoord

Promoveren doe je niet alleen. Het is dan ook niet meer dan logisch dat dit proefschrift begint met een dankwoord aan allen die mij op een of andere wijze hebben geholpen.

Het onderzoek waarover in dit proefschrift wordt gerapporteerd is uitgevoerd bij de groep Constructief Ontwerpen van de faculteit bouwkunde van de TU/e. Mijn collega's wil ik bedanken voor hun collegialiteit, voor hun geduld en dat ze me de ruimte gaven om aan dit proefschrift te werken. Bij het secretariaat kon ik altijd voor ondersteuning terecht.

Het vertrouwen dat ik kreeg van prof. Martens, prof. Kleinman en prof. Kerstens heeft mij gemotiveerd de rode draad van mijn promotie op te pakken en vast te houden.
Prof. Van Zijl kwam op een cruciaal moment de commissie versterken. Doordat hij als "vragende numerieke partij" optrad kreeg het proefschrift meer richting.

Erg vereerd en verheugd was ik door de spontane toezegging tot deelname aan de promotiecommissie van de overige leden. Bij prof. J. Rots (TU Delft) en zijn team mocht ik enige tijd 'stage' lopen. Van prof. K. van Balen (Katholieke Universiteit Leuven) en prof. B. de Vries kreeg ik nuttige tips en opmerkingen. Dr. C. Groot, heeft mij diverse malen geattendeerd op de positieve kanten van het promoveren en op de waarde van mijn onderzoek.

De leden van CUR commissie B50 bedank ik voor hun reacties en commentaren op de tekstbijdragen aan de CUR rapporten 171 en 193 die voor een deel de basis vormen van dit proefschrift.

De collega's uit het Pieter van Musschenbroeklaboratorium wil ik allen hartelijk danken voor het uitvoeren van de proeven maar ook voor hun gastvrijheid en het beschikbaar stellen van kranten en koffie. Altijd was er wel iemand die even naar mijn verhaal wilde luisteren. C. Naninck wil ik hartelijk danken voor het uitvoeren van de proeven op stukken metselwerk en het bijhouden van een logboek. Hij maakte ook vele dia’s en foto’s. E. Wijen heeft de proeven met de ESPI apparatuur uitgevoerd, hem bedank ik daarvoor en ook voor zijn Excell macro'tjes. Samen met J. van den Oever hield hij mijn computer draaiend. H. Donders, R. Canters en C. Baselmans wil ik bedanken voor het zorgvuldig vervaardigen en prepareren van de proefstukken. Bij T. van de Loo, en daarvoor P. van Hoof, kon ik altijd terecht voor wat fijnmechanisch werk, S. Neggers zorgde dat de olie op druk bleef.

Last but not least in dit rijtje noem ik Sip Overdijk, het hoofd van het lab. Hij was vaak mijn rots in de branding. Zijn rustige aard had vaak een kalmerende werking. Samen met prof. C. Kleinman heeft hij er voor gezorgd dat de ESPI apparatuur er kwam.
De 'drukschommel' werd gemaakt door E. Dekkers en zijn team van de CTD.

Ik wil alle studenten bedanken voor hun bijdragen, hetzij via projectwerk, afstudeerwerk, promotie werk, als studentassistent of hoe dan ook.

De participanten van de Stichting Stapelbouw hebben vele jaren bijgedragen aan het werk van de leerstoel Steenconstructies en daarmee indirect aan de totstandkoming van dit proefschrift.

Rob van der Pluijm wil ik bijzonder bedanken voor de vele keren dat hij teksten van commentaar heeft voorzien en mij attendeerde op de kronkels in het betoog. Vaak hebben we onze zorgen gedeeld, en samen gemetseld aan onze vriendschap, die, zoals het goed metselwerk betaamt, duurzaam is en tegen een stootje kan.

Zaken gaan voor het meisje. Margriet, te vaak was dat bij ons het geval. Ik dank je voor je liefde, je begrip en je zorg voor mijn overleven. Dit proefschrift draag ik dan ook op aan jou, aan onze drie dochters en aan mijn moeder, ter nagedachtenis aan mijn vader.

Appendix

1. Introduction

Developments in building with masonry units and in brick laying activities inspired this study. These developments concern for instance the use of thin layer mortar for clay-brick work and the use of industrially made masonry mortars. The need to characterise the mechanical properties, for a scope of contemporary masonry types, under carefully controlled and detailed experimental conditions is addressed.
Because masonry is a layered structure, made of two materials, it is self evident that the interaction of these layers is important for the behaviour, especially when subjected to compression, which is the main loading situation for masonry structures.
Recent developments on the ESPI measuring technique enabled detailed measurements of the brick-mortar interaction.

1.1 Scope of the work

Masonry is a composite material made from units, jointed by mortar. When loaded, the materials interact. Important for the final interaction is the way the masonry has been made and what happened when the materials were brought in contact with each other. The interaction between units and (fresh) mortar causes variation of mortar properties and this variation is amplified by the way the mortar is applied. Mortar has to cure, which has an effect on the final form and properties of the mortar joint as well.
To predict failure of masonry, various equations and models, based on ideas about brick-mortar interaction have been proposed. However, these equations and models are not universally applicable since they assume that the contact between the materials is perfect and that the materials are homogeneous. They also neglect fissures.
Therefore, the brick-mortar interaction in (contemporary) masonry is studied in detail to establish the effects of these parameters in compressive loading conditions. These effects include eccentricities due to imperfections and joint filling practice and delamination due to drying shrinkage.

Figure 1 The joint is formed during building of masonry

1.2 Objectives of the work

The objectives of the work are to:

a) establish the deformation behaviour of mortar in a joint as part of masonry loaded in compression,

b) acquire more insight into the role of the brick-mortar contact surface in the mechanical behaviour of masonry and

c) acquire a database that can be used in numerical simulations.

a) Joint deformation is difficult, if not impossible, to be measured accurately with traditional instruments. One technique to measure deformations accurately is ESPI, a laser speckle technique. With this method, the specimen is illuminated with laser light and the reflected light is captured with a digital camera. By successive photographs during load evolution, the deformation can be monitored accurately.

b) The main objective of the research program is to acquire more insight into the role of the brick-mortar contact surface in the mechanical behaviour of masonry under compression.

c) The main practical aim of the study was to acquire a database of mechanical properties of brick, mortar and masonry to be used in numerical simulations. The properties of brick and mortar separately were established in real masonry. In addition, ideas about the shape of the contact layer - required to model it correctly - were obtained.

1.3 Method

Masonry wallettes and stack bonded specimens, made of various contemporary brick mortar combinations were loaded in uni-axial compression and deformations were measured with gauge-lengths varying between 100 and 450 mm.

Three joint-thicknesses were used, i.e. traditional 12-15 mm thick, medium 8-10 mm thick and 3 mm thick, thin layer mortar joints.

Specimens cut from similar two-brick-one-joint couplets, were used for detailed measurements under compressive loading, using ESPI. The displacements of the points of a 100 mm square surface, in a 2mm square grid, were measured.

To support the experiments, numerical simulations with assumed linear elastic material behaviour were made, using DIANA [DIA 96].

1.4 Preview

After this introductory chapter, Chapters 2 and 3 treat, as a state-of-the-art, the features of the compressive response of masonry and its components.
Chapter 2, discusses the materials that can be used for contemporary masonry and the way the contact between clay-brick and mortar is made. Some models developed to explain fracture are discussed in Chapter 3. The literature research shows a clear development from simple analytical formulations, to a high level of complexity.

Chapters 4, 5 and 6, treat the experimental characterisation of brick, mortar and masonry under compression. The strength and the values for Young's modules and Poison’s ratios of these materials were established experimentally. Several types of brick and mortar were tested separately. The results are discussed in Chapter 4 and 5 respectively.
Chapter 6 deals with experiments on masonry specimens and wallettes. Two important phenomena were encountered: a) A delayed unit reaction, due to closing of fissures during loading of the specimen and b) An unequal strain distribution due to material variation and un-intended load eccentricity.

In Chapters 7 through 10, the detailed investigation of the brick-mortar interaction is reported. The behaviour of 25 mm thick specimens, studied by laser speckle technique (ESPI), is discussed.
In Chapter 7, the functioning of ESPI and the consequences of its use, like the necessity of building a new test-rig, are explained. Items like: ‘the effects of joint type and thickness', (Chapter 8), ‘the effects of load eccentricities', (Chapter 9) and ‘the effect of pointing', (Chapter 10) are discussed. The effects of these phenomena on fracture when brick and mortar interact became clear from these experiments.

In Chapter 11, the results and findings are synthesized and discussed. Both in traditional masonry and in contemporary thin layer mortar masonry, large strain variations occur at the edge of the bed joint. These large strains may introduce spalling of masonry, as were observed in the tests on stack bonded specimens and wallettes discussed in Chapter 6. Improvement of the contact between clay-brick and mortar improves the load bearing capacity of masonry.
Concluding remarks, proposals for further research and recommendations are presented in Chapter 12.

2 The structure of the clay-brick mortar contact area

Abstract

The main types of clay-brick production - extrusion versus soft mud moulded - are clearly recognisable in the material structure. Mortar, usually factory made in the Netherlands, has similarities with concrete as it also consists of sand grains and a binder. Weak spots (pores) and stronger spots (grains of sand) initiate fracture, as can be explained by the stress distribution around these inclusions. In the brick-mortar contact area irregularities occur. The interaction between brick and fresh mortar is of importance for the quality of the connection. The shape of the brick-mortar contact area depends on the how the mortar is put on the wall and on the surface and the suction properties of the units used. Fissure-tips in the brick mortar contact area experience higher levels of stress.

2.1 Introduction

When a specimen fails, the material structure often becomes visible. Therefore, it is important to know the structure of a material. The structure of clay-brick is a result of the production process, the mortar structure develops during the brick-laying process. Because mortar is a mixture of grains of sand and a binder its behaviour has similarities with concrete.

Some features of brick-laying, during which process the structure of the mortar-joint is formed, are discussed. The mason can manipulate the interaction process between fresh mortar and brick. The condition of the brick mortar contact area is important for load transfer.

2.2 Making masonry

2.2.1 Unit types

Units used to build structures can be made of natural or artificial stone. Artificial masonry units can be made of fired clay, (light weight) concrete, calcium silicate, autoclaved aerated concrete (AAC) or gypsum. In this thesis, solid clay brick units were used with a size of approximately 50 x 100 x 210 mm^3. The specific mass is between 1800-2000 kg/m^3. Clay-units are produced with a 'soft mud moulding process' or with an 'extrusion process'. The structure and the mechanical properties of the clay-bricks used are presented in Chapter 4.

2.2.2 Mortar types

Originally, mortar was a mixture of sand and lime, applied as a dough or paste. Later, it became a sand-cement mixture. Nowadays, masonry mortar is a mixture of one or

more inorganic binders, aggregates and water, and sometimes additions and/or admixtures.

In most cases, the mix design of the constituents will be chosen in relation to the application. Designs are available for a) sand / cement mortar, b) cement sand lime mortar (= special purpose mortar) and c) lime mortar. The binder in thin layer mortar is usually cement with fine (ground) sand as the main constituent. According to the mixing method used, the following distinction can be made for masonry mortars:

made on site: hand mixed (occurs seldom nowadays in the Netherlands),
machine mixed on site,

factory made, further divided into:

dry delivery on site; sand, cement, lime and additives are dried and delivered in bags or containers, water is added on site

delivery of wet sand and dry binder; (wet)sand is delivered separately from cement, lime and additives, but in the desired ratio, and

wet delivery on site, (= retarded ready to use mortar)

2.2.3 Brick-laying

Brick-laying is the piling of bricks on top of each other. Mortar serves as a tolerance aid, allowing for size variation of the bricks. In The Netherlands, the mason puts the quantity of mortar needed for one brick on the wall and then presses a brick on top of it, Figure 2a, b and c. The brick being placed is used to move some of the mortar in order to fill the head joint.

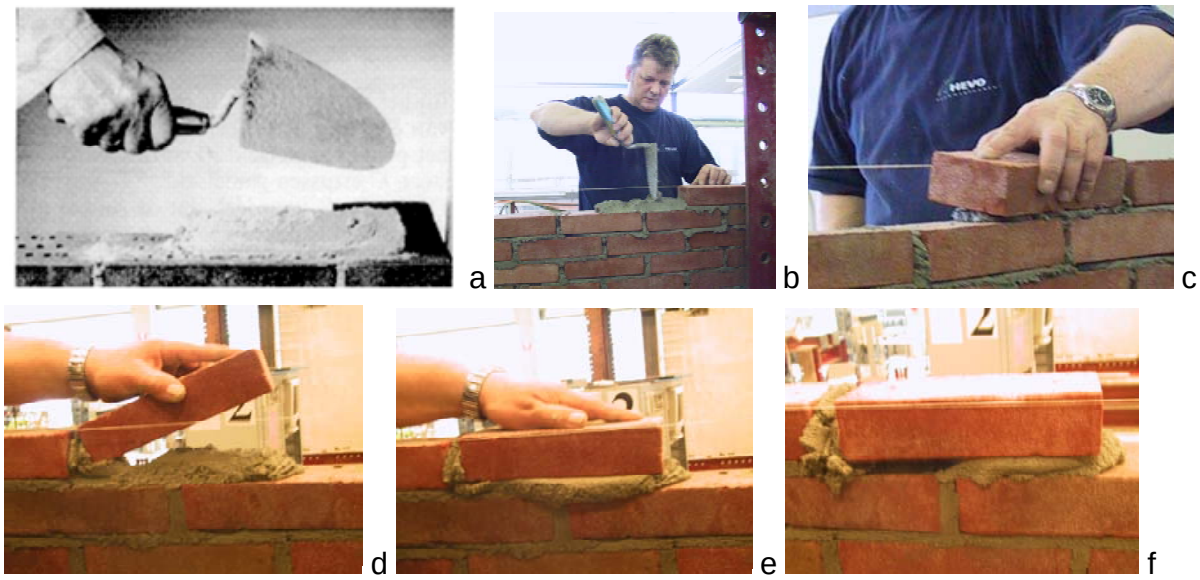

Figure 2 a) Putting mortar on the wall. b) The mortar is distributed over the joint. c) The brick is pushed into the mortar and rotated length wise. d) Some mortar is moved to fill the head joint, e) the brick is squeezed into the fresh mortar, f) poorly filled bed joint due to the false way of scraping with the brick to fill the head joint.

The workability of the mortar has to allow for positioning of the bricks and, on the other hand, the mortar has to stiffen quickly enough to be able to erect a wall of sufficient height per working day. In the case of slow setting mortar, the freshly built wall may become unstable and eventually topple over. An experienced brick layer has a feeling for the brick and mortar (moisture) conditions needed to obtain optimal masonry.

Figure 2 shows the steps in the brick laying process. The brick is first pushed into the fresh mortar and then the surplus of mortar is scraped of, Figure 2e. The fresh mortar in the centre of the joint is compressed to the appropriate joint thickness, and the mortar moves from the centre to the edges. At the edges, the mortar is hardly compressed vertically. After scraping off, the fresh mortar is not supported at the outside, (Figure 3), it needs the adhesion of the water to remain stuck in the joint. However, due to gravity, the top surface will drop a little. Depending on the moisture content and the sand used, the edge material runs off under a certain slope (approximately 30 - 45°).

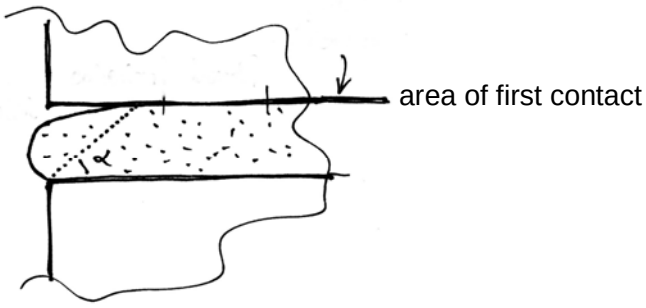

Figure 3 Unsupported mortar at the edge of a joint.

Too much mortar is used for the explanation of the brick-laying process in Figure 2. Usually, an experienced mason ‘feels’ how much mortar is needed for one unit and he will not use more than necessary. There is a critical balance between the mortar quantity used and the amount of joint filling. Joints should be filled completely but then more mortar is applied and scraped off. As complete joint filling needs more effort of the mason, it is temping to use as little mortar as possible.

2.2.4 The role of mortar

Mortar acts as a bonding agent. However, it fulfils an important role in accommodating irregularities, allowing dimensional differences of the bricks. The mortar thickness is, apart from strength considerations, determined by matching the units and mortar. During bricklaying, the mortar assists in getting bricks to rest firmly upon each other. For this, it must remain soft enough for each brick to be pressed down into position before suction by the dry clay brick of moisture from the mortar causes it to stiffen.

Throughout the structural life, the mortar transmits forces and plays a governing role in the deformation of the structure. The mechanical properties of mortar, in relation with curing conditions, are presented in Chapter 5.
Joints are important for the appearance of brickwork and it is essential that, in the course of time, the mortar should not become filthy, or lose its coherence due to ageing.
The mortar has to be sufficiently workable and should stiffen rapidly enough during the construction of the wall. In order to obtain these properties, a skeleton has to be formed by the grains of sand. Consequently, the grain size determines the possible joint thickness. If the ‘paste’ or ‘dough’ is sufficiently fine, thin joints can be made.

2.2.5 The shape of the bed- joints

The shape of the mortar joint is affected by the following actions.
a. The mortar is compressed when the unit is positioned, (Figure 2 and Figure 6b) and so the grains in the centre of the mortar joint are more closely packed than at the edges. The grain-packing is also less dense near a hard surface due to the so called wall effect, Figure 4. Figure 5 shows a section over mortar poured against a tile. Near the tile-surface more fine material is present.
Anson [ANS 64] stated the following about the behaviour of the contact area between a concrete specimen and the load platen, referring to Figure 4b, which represents a concrete cross-section. Close to the platen the soft mortar pockets at level C will carry less load than the adjacent stones, which will bear down on the stones in the next layer, and an uneven stress distribution is to be expected at the specimen end. It seems that the load concentrations are added internally by the stones, although the latter effect will be much reduced at levels higher than the pockets at level A [ANS 64].

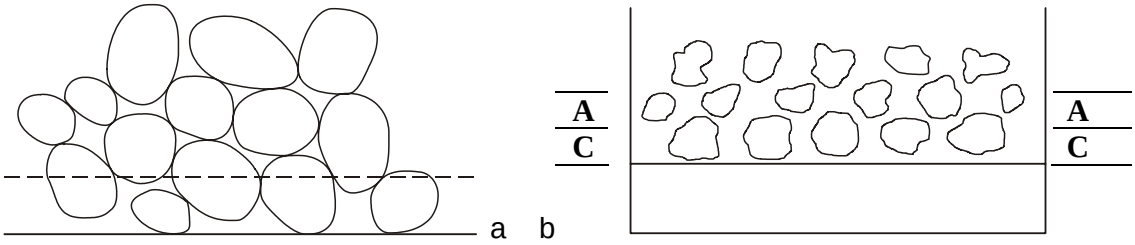

Figure 4 Wall-effect: a) Near a wall the grain-packing is less dense. Compare the configuration near the edge-line representing the wall and in the centre. The wall effect acts in a layer with a thickness of approximately the averaged grain radius. b) soft mortar pockets, close to the contact surface.

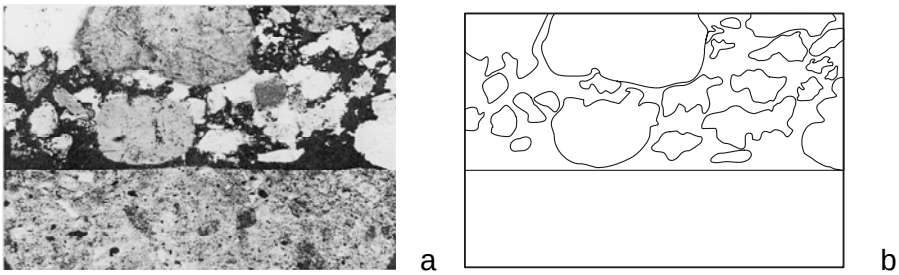

Figure 5 a) Section of an interface between mortar (above) and a tile (below), magnification x60 [WAT 59]. b) a schematic representation.

b. The fresh mortar is not supported at the face of the wall. Mortar would fall off if this was not somewhat prevented by the consistency of the moisturized grains and adhesion between fresh mortar and brick, (Figure 3). Therefore, brick suction properties are important.

c. During building, the wall is moved slightly towards the thickness direction and bricks are rotated length wise, (Figure 6a).

d. The surface of a wall dries faster than its centre, so shrinkage may cause the fissure to open wider.

e. Bleeding may occur in some parts between the centre and the edge of the joint.

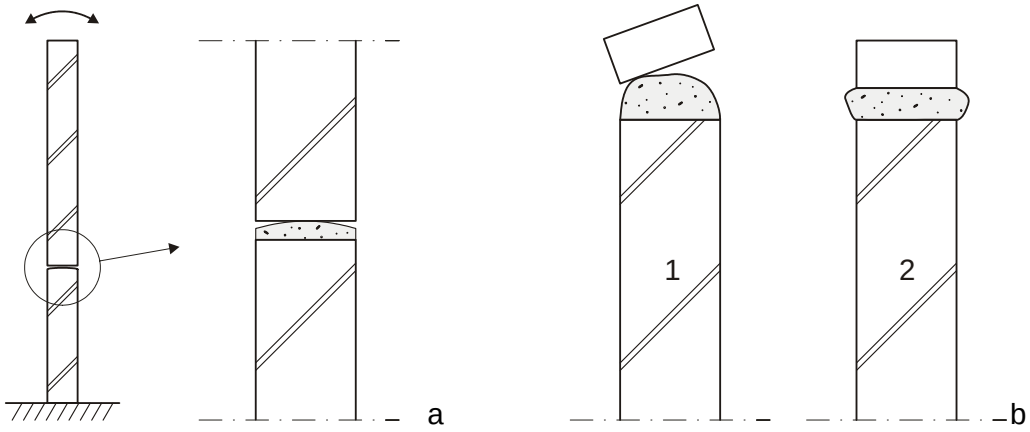

Figure 6 a) In the bricklaying process a wall is moved slightly towards the thickness direction and 'pillow shaped' bed joints are formed. b) When the unit is positioned, the brick is rotated length wise and the mortar compressed, see also Figure 2c.

Pointing

Some time after brick laying, when the brickwork has some initial strength, the joints can be finished by a process called jointing, or they can be scraped out for later completion, a process called (re)pointing. The latter finishing is sometimes performed several months after building of the wall. The pointer gives the joints a special finish with esthetical qualities, Figure 7. Usually, special sand is used, a little finer than masonry sand, in combination with grey or white cement and, in modern mortars, special additions.

Jointing is not done quite often in the Netherlands, where masonry facades are usually pointed. In restoration works, the old pointing material is removed and replaced by new material ('repointed'). This (re)pointing is a potential source of stress concentration due to the combination of different materials, [VIN 01].

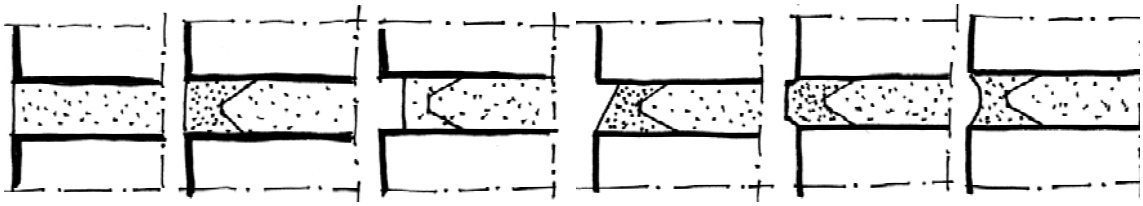

'jointed' flush with face recessed tapered V-shaped hollow shaped

Some of these Dutch joint profiles are similar to the English profiles given in [HOD 93].

Figure 7 Section over several types of pointing.

2.2.6 Thin layer masonry

In the last few decades, the availability of skilled masons has dramatically decreased. The clay-brick industry has recognized this threat to the future of masonry and developed new building techniques using thin layer mortar in combination with brick sized units, [NIE 95].

A system has been developed, using a pump to apply the mortar quickly and conveniently, thus saving the mason's back from repetitive stress. Mortar may be applied to the headers of the unit before they are placed, for which process a special stand was developed. Then, the units are positioned, using cord guiding to obtain a level and plumb wall, comparable with normal brick laying, see Figure 8.

Figure 8 a) Brick laying using thin layer mortar. b) Vertical section over a thin layer mortar joint, recessed at the right hand side.

In this way a wall can be built faster than with the traditional brick laying technique. The size tolerances of the units are critical for the joint thickness and the quantity of mortar that is needed. The relatively small size of the units makes it possible to compensate errors. For aesthetical reasons, thin layer joints are recessed, (Figure 8).

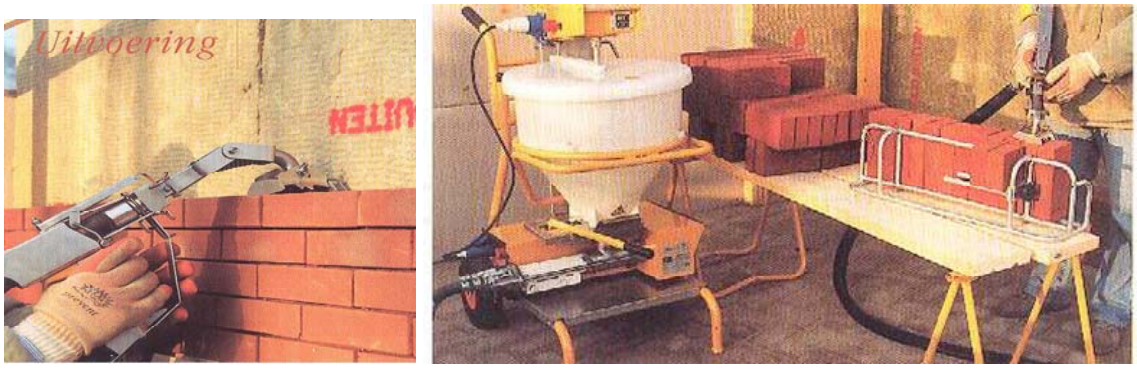

Figure 9 Execution of thin layer masonry using a stand to mortar the unit headers.

2.3 Mortar - a porous material with grains

2.3.1 The role of water in mortar

Pores form when water evaporates. Water is important to obtain an acceptable workability. Wet sand has a certain consistency while sand and water attract each other by nature. This is because the surface of a grain of sand is charged positively and attracts the negative ion of a water molecule. This forms a shell of water around the grain, which in its turn forms so called hydrogen bridges to other water molecules. A certain stratification develops, giving some coherence to the whole. If there is too much water the sand grains will float.

2.3.2 Pores and shrinkage

Besides water, the fresh mortar consists of cement and/or another binder and sand, if necessary supplemented with additives. The cement will react (hydrate) with a part of the water and the moisture content in the mortar will change. The mortar will contain rests of unreacted cement, as well as pores, which may be filled with water. Pores may be enclosed spaces or channels connected with each other. In capillary pores, water is stored that is not used for the reaction process.

Due to loss of moisture, shrinkage cracks may develop. By keeping the masonry moist this shrinkage may be prevented or minimized. An important benefit of mortar containing lime is that the curing process evolves slower [BAL 91], thereby significantly reducing shrinkage. The carbonation process of lime progresses by diffusion, at a rate proportional to the square root of time.

Sufficient water is a condition to obtain optimal strength and durability. When water disappears from a capillary pore, a contractive force develops and the material shrinks, i.e. the volume decreases. Plastic shrinkage occurs when water evaporates during the plastic stage of the mortar, resulting in a web-like crack pattern.

This type of shrinkage depends on the amount of water available for evaporation and the pore structure. The more water available in the fresh mortar, the more shrinkage occurs. So a water cement ratio as low as possible is of importance. Note that the dehydrated mortar will absorb water when it is moisturized and it will swell again, however, the original volume will not be reached. Plastic shrinkage may cause severe cracking when curing is neglected, especially during hot summer weather.
Internal shrinkage occurs during the hydration of cement. The volume of cement plus water is larger than the volume of the cement-paste, but the effects of this type of shrinkage may be neglected.

The structures of the units and the mortar play an important role in the hygroscopic behaviour of masonry. During execution, it should be ensured that clay-bricks have the appropriate moisture condition. Clay-bricks that are too dry will absorb water too much from the fresh mortar, whereby the hardening of the mortar will be disturbed. When the clay-bricks are too wet, plastic or drying shrinkage will occur. For practical reasons, the bricks should absorb some water.

The study of the effect of water absorption on mortar-brick bond by Groot [GRO 93] showed that the highest moisture variation occurs at the clay-brick-mortar interface. This is elaborated further in section 2.4.1.
Another non-mechanical source of cracking lies in the fact that clay-brick and mortar, in the hardened state, are two different materials that react differently to temperature and moisture variations. At the brick-mortar interface stresses will develop which, in the long run, may break bond [WIJF 04].

2.3.3 Pores, Porosity and strength

Models for the pore structure and the stress distribution around pores are presented in [DafSt 232]. From this study it became clear that peak stresses develop near pores, which may induce fracture, (Figure 10).
This is in agreement with the observation that a lower porosity is associated with higher strength of a material, or rather the higher resistance of the material.
A close logarithmic relationship exists between strength and porosity of cement-paste [MAS 96].

A similar relationship between compressive strength and porosity was observed for concrete. The compressive strength of concrete decreases 5-6% for every 1% increase of the porosity. The compressive strength of concrete is smaller than that of its constituents, because the bond between the aggregate and the cement-paste is weaker than the cohesion in the constituents. This bond is weaker because the porosity in the sand grain-cement interface is larger than in the paste, and porosity and strength are related as stated earlier.

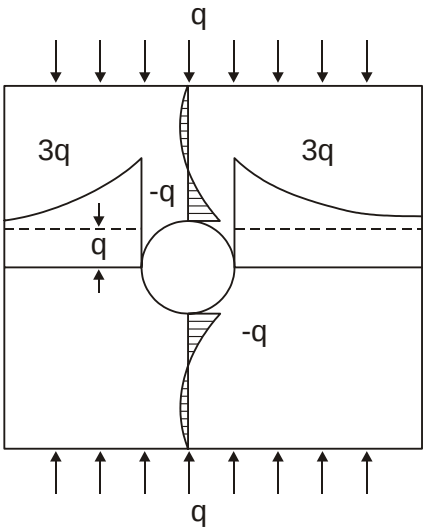

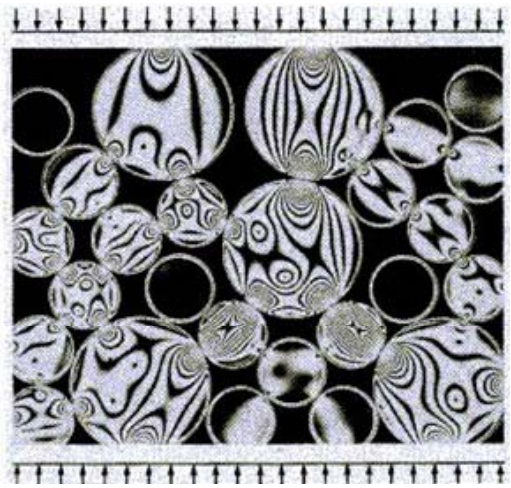

Figure 10 Stress distribution around a pore [DafSt 232] + = compression, - = tension

Figure 11 Photo elastic recording with lines of equal principal stresses (isochromates) in modelled concrete. Lines close to each other indicate high stresses [REI 85].

2.3.4 Sand grains

Mortar may be represented as a pile of grains, bedded in a paste- a mixture of cement and/or lime and fine materials. The grains, being stiffer than the paste, attract force, therefore the stress distribution inside the mortar is irregular, even when the specimen is loaded evenly. Figure 11 shows a photo-elastic picture with isochromates (lines representing the same principle stress differences). From this figure stress concentrations can be deducted from the distances between isochromates. It is apparent from Figure 11 that the (compressive) stresses concentrate near stronger contact points

The load is mainly transmitted via the sand grains, causing lateral tractions to develop, Figure 12, [REI 85]. Thereby, tensile tractions arise in the orthogonal direction to compressive loading. Equilibrium is only possible if the material has a tensile strength and/or when lateral compression is applied.
The tensile strength, or adhesion, exists between the cement hydrate paste and grains. Tension acts in the transition between paste and grain, so there, cracking may occur.
Loaded further, an inclined crack-surface will develop, and shear will occur along this surface. The debris of concrete after destructive testing contains grains with conical toppings of the matrix material [STR 73], Figure 12b.

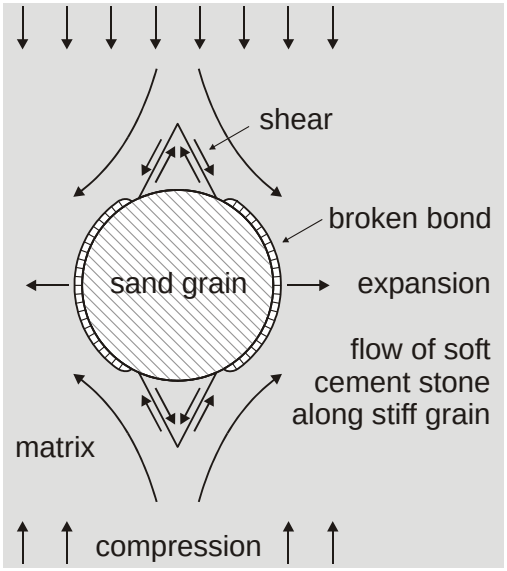

a

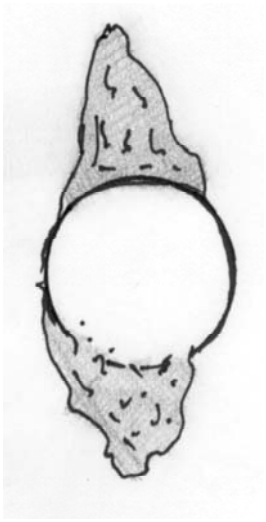

b

Figure 12 a) Illustration of the "flow of material" around a grain of sand [REI 85]. b) Sketch of debris of concrete after destructive testing, showing grains with conical toppings and broken bond at the sides, [STR 73], [MIE 84] and [MIE 97].

According to [REI 85] strength and deformation of concrete may be affected by:

- the ratio between E-values of sand grains and paste,
- the bond between paste and grain,
- the tensile strength of the paste depending on the water cement ratio,
- the existence of cracks as a consequence of cooling and drying,
- the grain texture, affecting shear between grain and paste,
- the amount of paste material, i.e. the distance between the grains.

The model only treats one grain of sand, in reality grains with varying dimensions and shapes are present. Therefore, the load distribution may be more irregular.
However, the model demonstrates the behaviour of sand grains in a loaded volume.

2.3.5 Interfaces in mortar

An interface can be recognized between the paste - a mixture of cement and fine materials- and the grains of sand, as shown in a Rilem publication [MAS 96] and by Larbi, [LAR 91] and Vervuurt [VER 97]. An effect of the distance to the brick mortar interface is recognized by Brocken [BRO 00]. In concrete, the transition zone between grain and cement-paste is the most porous component that can be considered as a 'weak link', Figure 12.

Generally, the transition zone has a thickness of approximately 50 μm and it constitutes approximately 30 to 50% of the total cement volume, [LAR 91]. Micro-segregation occurs, because the water concentration around the sand grains is relatively high and the packing of cement particles, with an averaged diameter 10-30 μm, is inefficient comparable with the 'wall-effect' when pouring concrete, [LAR 91].

2.4 The brick-mortar contact area

2.4.1 Moisture exchange

The moment the brick contacts the fresh mortar, the brick absorbs water from the fresh mortar and the moisture transmission process starts. This process is described by Pel [PEL 95] for porous building materials, like brick and mortar is. If the bricks are (too) wet, a water film will form. Also, porous, high absorption bricks that are too dry make brick laying almost impossible. If the water content in the fresh mortar is not optimal, the hardening process will be disturbed.

Müller en Meyer [MUL 94] concluded that the compressive strength of general purpose mortar can be strongly affected in the joint by the capillary absorption of the units. The water absorption speed during the first minutes after making contact is ruled by the capillary absorption properties of the unit (IRA). This effect of suction by the unit is also recognised in the water distribution profiles established by Groot [GRO 93], who measured moisture migration in masonry specimens of two bricks joined together with one joint. An example is shown in Figure 13.

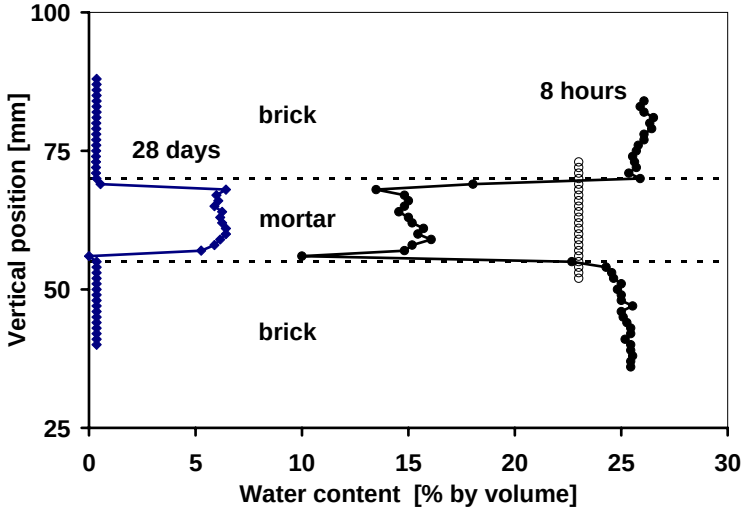

Neutron transmission measurement result

Waterdistribution profile determined by neutron radiography and a lift facility to change the scan position.

MB15 PCS1 [GRO 93]

The vertical axis represents the scan position in mm and the horizontal axis the related water content as a percentage by volume. Each graph shows a profile scanned 8 hours after preparation of the test specimen stored under RH 95%, 20 °C and a profile of a specimen dried at 105 °C after 28 days of hardening. The brick-mortar interfaces are indicated by horizontal dotted lines, the initial water content (23 %) of the mortar by a vertical dotted line. MB15 was a pre-wetted machine moulded brick (~15 mas %).

Figure 13 Water distribution profiles over brick-mortar-brick cross-sections [GRO 93].

The practice of sanding bricks has another negative effect on bond. Loose sand hanging on the brick surface is hardly connected. Even when this sand is well bonded by the mortar, the brick bond is poor. When masonry is demolished, quite often the mortar loosens in slices. In bending, fracture occurs almost always at the brick-mortar interface, e.g. [PLU 96a]. This interface is evidently the weakest link.

2.4.2 Surfaces after fracture

Because bed joints are shaped as discussed in section 2.2.5 and because of the moisture exchange mentioned above, the bond between the unit and the mortar can be disturbed and it may not be as complete across the surface of the brick as assumed. Variation in bonding was found by Vermeltfoort and Van der Pluijm [VMF 91], [PLU 92]. The inspection of fracture surfaces after bond wrench testing showed that three areas could be recognized. A well bonded central area, a middle area and an outer area with no bond at all. Figure 14 shows a vertical section through the brick/mortar area in a wall.

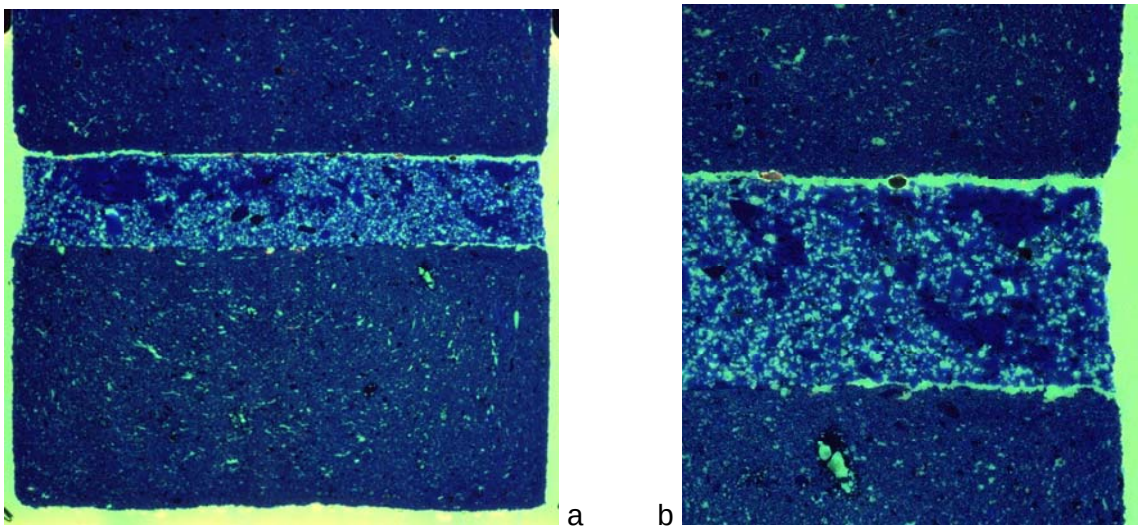

Figure 14 a) Vertical section over a full general purpose mortar bed-joint. b) Detail showing the edge of the mortar bed. Fissures from the outside run into the masonry. Photographs taken after impregnation [VMF 98].

The variation of mortar properties over the joint was studied by Hobs with pulse velocity measurements. As pulse velocity is an indication of stiffness (and indirectly of strength) it may be clear that there is variation of the properties over the joint. Figure 15 shows an example of the pulse velocity contours [HOB 91]. For comparison, the fractured surface after bond wrench testing is added. In both figures a similar pattern may be recognized.

The borders between these areas are not always so clear to recognise as in Figure 15. Three areas with different types of bonding are recognised, (Figure 16): a fissure at the edge, less bond due to bleeding, and best bond in the area where the first contact was made. Variation in water distribution causes higher stresses in the brick mortar contact area, highest at the surface of the masonry.

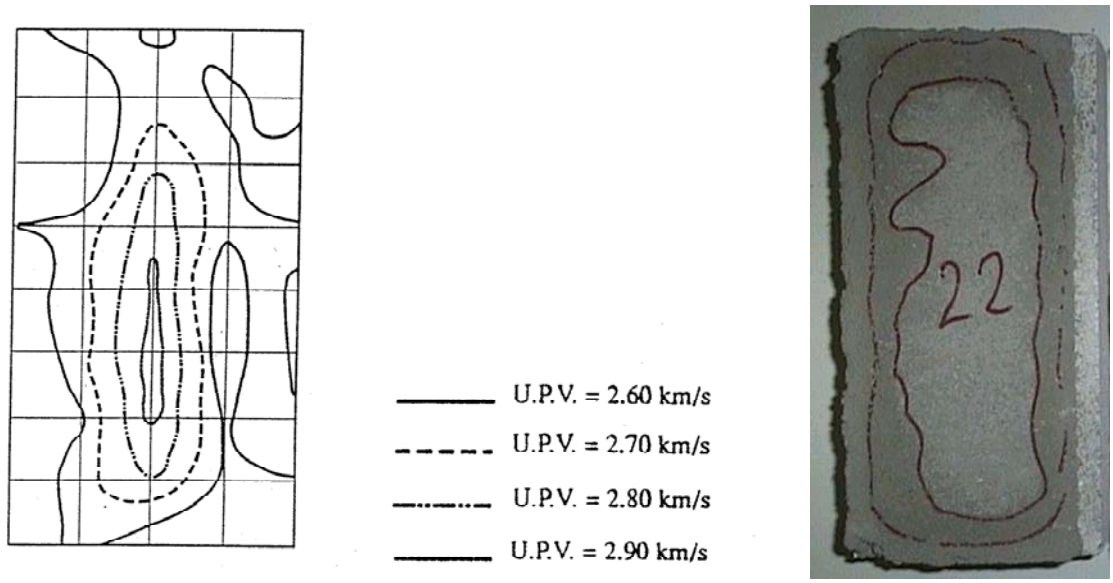

Figure 15 Ultra pulse velocity (UPV) contours [HOB 91] and a fracture surface after a bond wrench test. The lines indicate the boundaries of the three areas with different types of bonding.

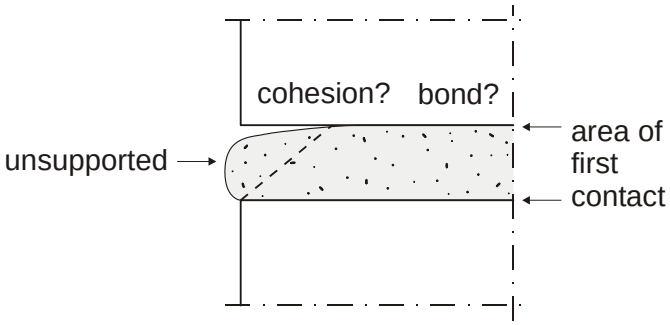

Three areas in the brick-mortar contact zone with possible different kinds of bonding.
A fissure, less bond due to bleeding and best bond in the area where the first contact was made.

Figure 16 Three types of bonding in the brick mortar contact area.

2.4.3 Modelling fissures

At the end of the fissure, the higher stresses due to differential shrinkage driven by variation in the moisture content can initiate cracking. For concrete, cracking processes are studied intensively, e.g. [MIE 97]. Because the similarities between concrete and (cement-based) mortar, these models can contribute to understand the behaviour of the brick mortar fissure.

Models for crack formation in concrete all show high normal stresses at the tip of the crack. Two examples will be discussed.

The first example shows the stress distribution near a sharp ended crack with a length 2a in a concrete plate, Figure 17.

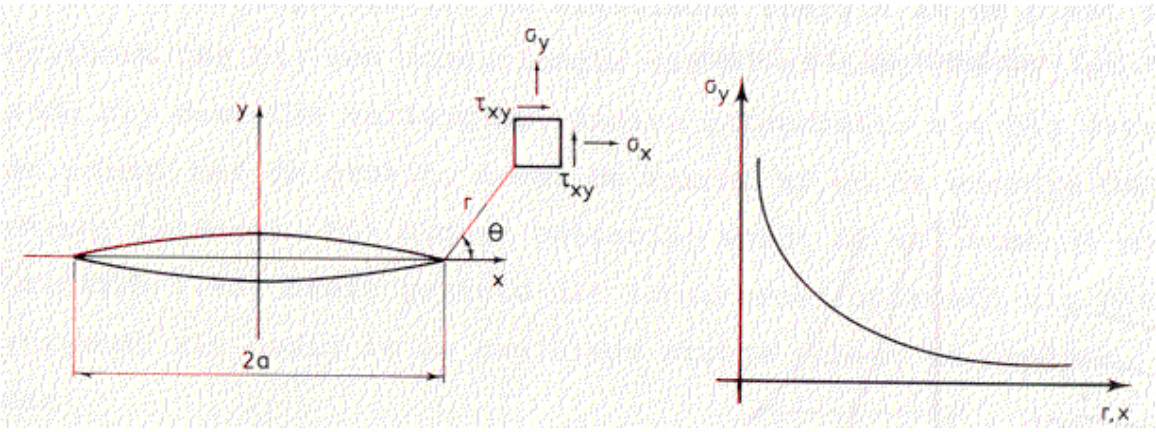

Figure 17 Definitions and axial stress distribution near a crack in a plate, [REI 85]

The stress distribution is drawn schematically in Figure 17 and is represented by the following Equations:

$$\sigma_x = \sigma\sqrt{\frac{a}{2r}}\cdot\left(\cos\frac{\theta}{2}\left(1-\sin\frac{\theta}{2}\sin\frac{3\theta}{2}\right)\right) \quad (1)$$

$$\sigma_y = \sigma\sqrt{\frac{a}{2r}}\cdot\left(\cos\frac{\theta}{2}\left(1+\sin\frac{\theta}{2}\sin\frac{3\theta}{2}\right)\right) \quad (2)$$

$$\tau_{xy} = \sigma\sqrt{\frac{a}{2r}}\cdot\left(\sin\frac{\theta}{2}\cos\frac{\theta}{2}\cos\frac{3\theta}{2}\right) \quad (3)$$

Near the crack tip, r~0, σ_y is infinite.

The second example is the fictitious crack model of Hillerborg [HIL 76]), where (elastic) calculations show that the stresses around a crack tip go to infinity as well, (Figure 18). This means that non linear effects will be present [VON 92].

In Figure 19, the fictitious crack model is shown, which is applicable for brittle materials like concrete, masonry and both its constituents. Over a certain length at the end of the 'fictitious crack' cohesive stresses are present. The model predicts microcrack formation when the tensile strength f_t is reached.

In the two examples mentioned above, the crack is opening. When masonry is loaded in compression, the fissure will close. Initially, the stress distribution will be similar, however, in the reverse direction. Also, non linear behaviour in the crack tip area is reasonable.

Closing of cracks will increase the effective section and decrease the averaged normal stress. However, the lateral (tensile) stresses present may cause cracking perpendicular to the fissure surface, i.e. in the axial direction.

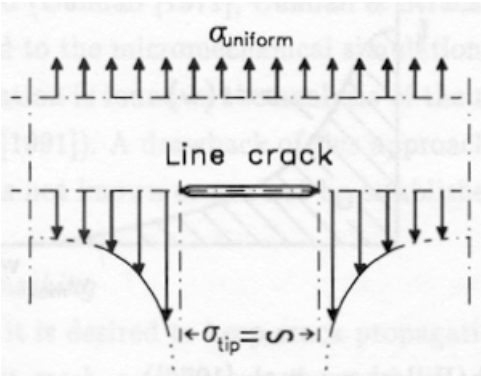

Figure 18 Stresses around a crack tip.

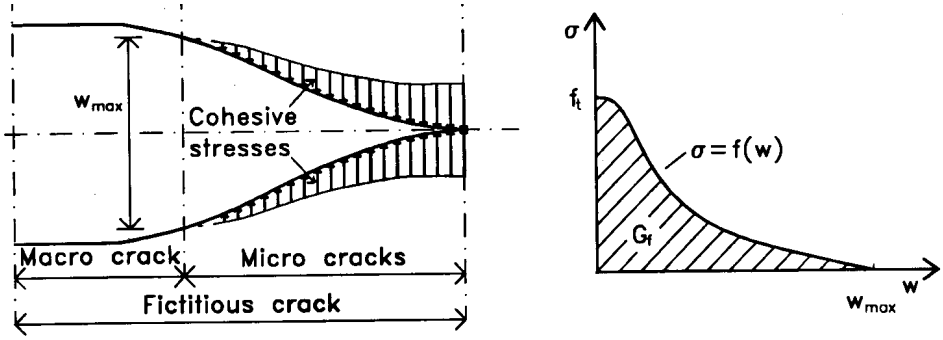

Figure 19 Fictitious crack model (Hillerborg et. al. [HIL 76]), and a (post peak) stress-crack width relationship.

2.5 Conclusions

• Nowadays masonry is an industrial product.

The fabrication of bricks is a highly automated process, the mortars used are factory made. General purpose mortars are used to build masonry with joints of 10 to 15 mm in thickness.

A development (for clay brick work) is the use of special made mortars to obtain joints with a thickness of 3 to 4 mm, called thin layer masonry.

• The final properties of a mortar-joint depend on the way the mortar is applied in combination with the interaction between clay-brick and fresh mortar.

• Important for the brick-mortar contact area are: a) the surface of the brick (possibly sanded) b) the absorption of the brick (moisture exchange) and c) the way the brick is positioned.

- Mortar constituents and mix designs must be adapted to the properties of the brick used.

- Mortar joints are formed during building of masonry. The execution of the brick laying has an effect on the brick-mortar contact area. The lateral movement of a brick during laying affects the shape of the joint.

- Thin layer mortar joints usually are recessed at the visual side of the wall. Through these mechanisms the joint geometry is determined, which may considerably influence the stress distribution.
- Against the surface of larger elements (brick, sand-grain) a layer develops with a different, less dense packing of grains. Moisture exchange causes a variation of the moisture content over a few mm and so mortar-brick bond is affected.
- Fissures develop in joints due to shrinkage and gravity.
- Pores, stronger parts, inclusions, dislocations and fissures cause stress concentrations and eventually failure around these inclusions.

- A peak stress situation occurs at the end of a fissure which is under pressure.

3 Modelling brick-mortar interaction in masonry under compression

Abstract

Empirical equations use brick and mortar compressive strengths to predict the compressive strength of masonry. Because only some execution parameters are prescribed, the result of the prediction should be relatively low to stay on the safe side.

When masonry, which is a piling of alternating layers of brick and mortar, is compressed, the softer material will be squeezed out, causing tension in the stiffer material. Haller was the first to use this 'sandwich' model to estimate the lateral stresses in mortar and units in the centre of a piece of masonry.

The model also assists in comprehending that the mortar and units are in a three dimensional stress state even for uni-axial external loading. The discussed models assume perfect contact between mortar and unit.

At the edges, the mortar is not supported, which causes larger lateral deformations and larger stresses, as illustrated by numerical models. An extreme situation is the mortar joint between two prefabricated concrete columns. If the full bed joint is taken into consideration, the found stresses give an explanation for the spalling observed in experiments.

3.1 Introduction

To 'predict' the compressive strength, empirical and analytical equations were developed.

Empirical equations that use brick and mortar compressive strength to predict the compressive strength of masonry date back to the mid eighteen hundreds, [CAR 66]. Since then, many new formulations were proposed. They all only use brick and mortar strength as parameters. Each code, that means each country, has its own formulation, in which much (local) knowledge and customs are incorporated. Equations are also tuned to (local) habits and circumstances, like a) the method of brick laying, b) the brick properties that vary per country (type of clay) and the production method and c) the mortar mix designs e.g. the amount of lime used and the type of sand available.

For most equations only some execution parameters are prescribed, e.g. the joint thickness should be between certain limits, while many of the execution effects are not accounted for. Besides that, brick and mortar compressive strengths are established according to codes in a situation that differs from the situation in real masonry. All these influences are reason for conservatism in strength prediction.

Usually, the long time effects are not incorporated in the formulations mentioned above. According to [EC6 96] this effect is accounted for with the material resistance factor, as applied in structural design.

3.2 Analytical modelling of brick-mortar interaction, a sandwich model

Analytical models use the fact that masonry consists of alternating layers of brick and mortar like bread and ham in a sandwich. When such a pile of layers is compressed, the softer material will be squeezed out, causing tension in the stiffer material.
A number of investigators have attempted to derive failure theories based on the brick-mortar interaction. The earliest of these is by Haller [HAL 58]. Their analytical models enable the prediction of the lateral stresses in the units and in the mortar.

3.2.1 Model based on elastic analysis

The basic idea is that when a combination of layers of alternating soft material (mortar) and stiffer material (clay-brick) is compressed, the materials will deform both in the loading direction and in the lateral direction. However, the soft material deforms more than the stiffer material. A common hypothesis is that the mortar and the units are connected at their interfaces and no sliding occurs when the brickwork is under compression.
As a consequence, the stiff material prevents the movement in lateral direction of the soft material. This causes lateral tension in the stiff material and compression in the soft material. The lateral stresses induced in the central brick and adjacent mortar layers are indicated in Figure 20.

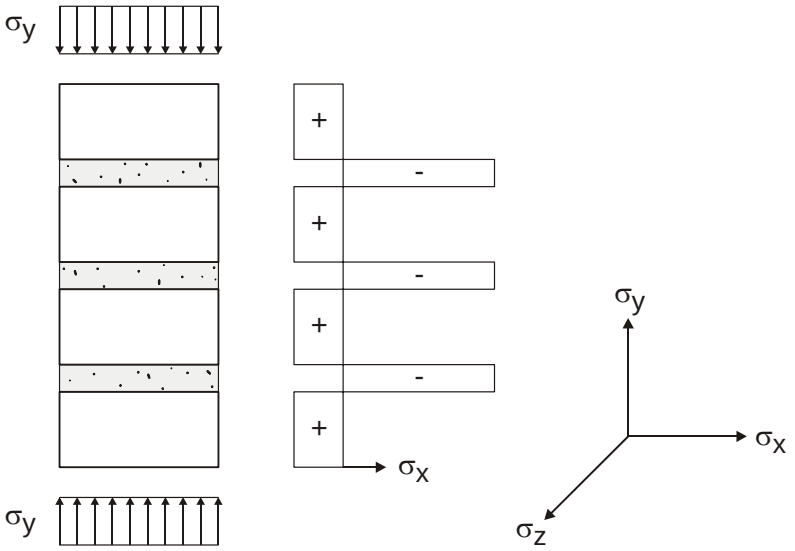

Figure 20 Stresses in unit and mortar, Haller model from [HIL 69].

Using the theory of linear elasticity the following relationship is derived:

$$\sigma_{x,bri} = \sigma_y \cdot \frac{\upsilon_{bri} \cdot \frac{E_{bri} \cdot \nu_{mor}}{E_{mor} \cdot \nu_{bri}} - 1}{\frac{E_{bri}}{E_{mor}} * \frac{h_{bri}}{h_{mor}}(1-\nu_{mor}) + (1-\nu_{bri})} \quad (4)$$

When deriving Equation (4), it was assumed that the (stronger) bricks were in tension and the (weaker) mortar in compression, due to the large difference in properties. In contemporary masonry, brick and mortar are adapted to each other and consequently their mechanical properties are more equal. In Appendix A.3 the effects of differences between brick and mortar properties on the lateral stress are discussed.

Further, it was assumed that the stresses in the units and the mortar are equally distributed over the height, and that mortar-unit bond is perfect. Implicitly it was also assumed that a) Unit and mortar behave linear elastically, b) Unit and mortar are homogeneous and isotropic, and c) there is no variation of dimensions, i.e bricks have a rectangular section.

The lateral tensile stresses in the units, $\sigma_{x,bri}$, were considered to be the main cause of failure, because they induce vertical cracks.

Equation (4) only gives an impression of the stresses that may occur in the unit and the mortar, (see also Appendix A.3.). A weakness of Equation (4) is the assumed uniform stress distribution, with brick in tension and mortar in compression as shown in Figure 20. Due to the shape of the joints this is not true.

In the model only the mechanical aspects due to an external compression load are discussed. Shrinkage and creep may however have effects on the behaviour as well.

3.2.2 Prediction of masonry failure

Various researchers tried to improve the 'sandwich' model. Equation (4) was used to predict the lateral tensile stresses in the unit ($\sigma_{x,bri}$). The result was checked against the uni-axial tensile strength of the unit ($f_{t,bri}$) to estimate masonry compressive strength, with:

$$\sigma_{x,bri} \leq f_{t,bri} \quad (5)$$

As the unit is both in compression in one direction and tension in the other direction(s) masonry strength can be overestimated. Therefore, failure envelopes for brick and mortar were developed by Hilsdorf, Khoo [KHO 72], Atkinson [ATK 83], Francis et.al. [FRA 71] and others.

The brick failure envelope described by Hilsdorf [HIL 69] has an assumed linear relationship between compressive ($f_{c,1}$) and lateral tensile strength ($f_{t,1}$).

Failure occurs when:

$$\frac{\sigma_c}{f_{c,1}} + \frac{\sigma_t}{f_{t,1}} > 1 \quad (6)$$

(see Figure 21, original Coulomb's). Equation (3) shows that the brick 'compressive' strength is severely reduced by the presence of an orthogonal tensile stress.
Khoo and Hendry [KHO 72] investigated the behaviour of brick material under a state of biaxial compression-tension and established experimentally that the compression strength envelope for brick can be represented by the relationship:

$$\frac{\sigma_c}{f_{c,1}} + \left(\frac{\sigma_t}{f_{t,1}}\right)^n = 1 \qquad (7)$$

where the exponent n equalled the value 0.546. The results of biaxial tests performed by McNary and Abrams gave a factor for n = 0.58 [McN 85]. Equation (4) was based on the results of tests on a large number of brick specimens, (Figure 21).

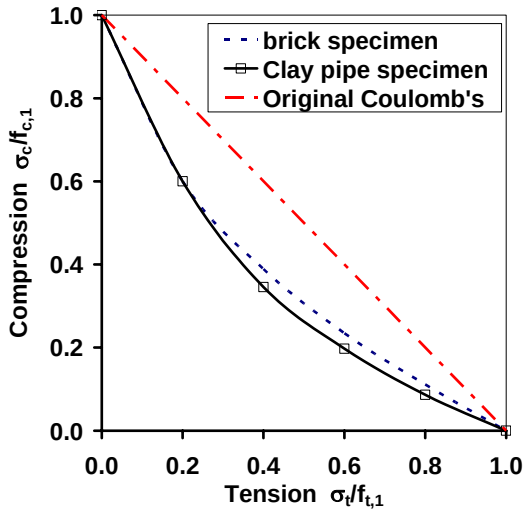

Figure 21 Brick failure envelopes

Besides brick strength, mortar compressive strength is a criterion for masonry failure as well. Therefore, the mortar properties were taken into account in other models.
As discussed in section 3.2.1, bricks are in lateral tension, which limits strength, while mortar, with a usually smaller compressive strength, is in lateral compression. Note however, that mortar compressive strength increases with lateral pressure, or confinement.

Atkinson et al. [ATK 85] also gave a linear relationship. However, they postulated that the inclination of the mortar failure envelope, m_{mor} depends on the uni-axial compressive strength of the mortar: for $f_{c,mor}$ = 30 N/mm^2, m_{mor} = 5 and for $f_{c,mor}$ = 6 N/mm^2, m_{mor} = 2.

Hilsdorf [HIL 69] assumed that the tri-axial strength of mortar could be represented by the equation (obtained originally for concrete):

$$\frac{\sigma_c}{f_{c,1}} = 1 + m_{mor}\frac{\sigma_{c,2}}{f_{c,1}} \qquad (8)$$

where:

$f_{c,1}$ = uniaxial compressive strength, in this case of a cylinder,

σ_c = compressive stress in axial direction

$\sigma_{c,2}$ = lateral confinement stress, in this case applied on a cylinder

m_{mor} = parameter for mortar failure envelope, in this case $m_{mor} = 4.1$

Khoo and Hendry [KHO 72] investigated the effect of confinement on the mortar compressive strength using a tri-axial cell. The increase in strength was less than for concrete. They found a stress criterion that may be defined by the expression:

$$\frac{\sigma_c}{f_{c,1}} + 2.91\cdot\left(\frac{\sigma_2}{f_{c,1}}\right)^{0.805} = 1 \qquad (9)$$

Bierwirdt et al [BIE 91] performed tests on tri-axially loaded mortar specimens.
The uni-axial compressive strength ranged between 6 and 15 N/mm^2; the strength increased with a factor between 1 and 2 due to tri-axial loading, which would mean that $1 < m_{mor} < 2$.

It is clear that the researchers mentioned above recognized the positive effect of confinement on mortar strength. Other researchers, like Probst, [PRO 81], Schubert, [SCHb82], Ohler, [OHL 86] and Betzler, [BET 95], also gave their interpretation and established experimental relationships. Often these relationships are related to specific brick-mortar combinations.

3.2.3 Failure process as described with the Haller model

When a masonry prism is loaded in compression, both mortar and brick are in a bi-axial or even tri-axial stress state. For both brick and mortar a failure envelope can be drawn in one diagram. In Figure 22 line A represents the failure envelope for brick (similar to Figure 21) and line C defines the tri-axial strength of the mortar. If external compression is applied to the prism, the internal stresses induced follow some line, for instance as suggested by line B1. For a certain load the line B1 will intersect line A and the brick will crack locally. Stresses will redistribute and internal stresses will follow line B2 until line B2 intersects line A, and so on untill failure.
Generally, failure occurs when the brick can no longer provide the bi-axial restraint necessary to prevent mortar failure. This will occur when the tri-axial mortar failure line C intersects line A. The intersection between mortar and unit failure envelope gives an upper boundary for the masonry compressive strength.

Hilsdorf [HIL 69] established the magnitude of the local stress at failure, that is the intersection of the lines A and C in Figure 22 as:

$$\sigma_y = f_{c,bri} \frac{f_{t,bri} + \frac{h_{mor} \bullet f_{c,mor}}{4.1 \bullet h_{bri}}}{f_{t,bri} + \frac{h_{mor}}{4.1 \bullet h_{bri}} f_{c,bri}} \qquad (10)$$

using Equations (3) and (5). The equilibrium of forces in the brick-mortar composite is taken into account by incorporating the height of brick and mortar joint.

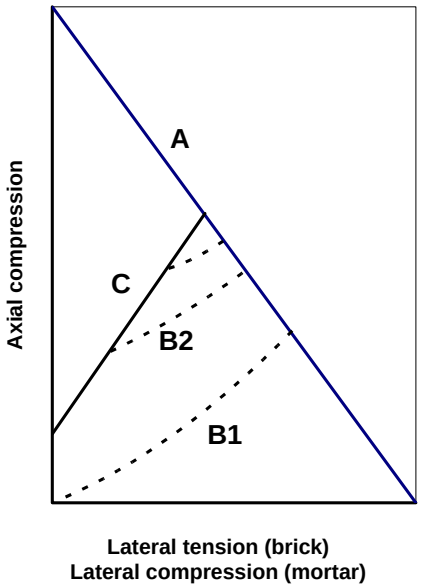

Figure 22 Brick and mortar failure combined in one figure [HEN 87]. Lateral tension for brick is plotted in the same direction as lateral confinement pressure for the mortar.

The assumed linear relationship, for both brick and mortar, in Figure 22 was improved by e.g. Ohler [OHL 86], who used a tri-linear representation of the bi-axial failure curve for the brick material.

In 1985, McNary and Abrams [MCN 85] developed a theory that characterizes the strength and deformational properties of stack-bonded prisms loaded in compression and recognized that mortar behaviour was non linear i.e. E_{mor} and ν_{mor} changed in the process. Using these assumptions, they created a computer program which made it possible to describe the lateral stress relationship in the mortar (line B in Figure 23) for increasing external compressive load. The theory is simplified by considering nominal average stresses over the thickness of the brick and mortar. The properties of the brick are assumed to be constant under all stress states. These models differ from previous failure theories because the effects of the non linear behaviour of mortar are included.

For small loads the brick and mortar stresses increase linearly. At higher loads, the lateral stresses increase faster than the applied vertical stress, i.e. non linear behaviour. Failure of the system is defined as a stress curve intersecting a failure envelope, points D and E in Figure 23. Although failure of a prism occurs as a result of lateral tensile splitting of a masonry unit, it is the mortar that induces tensile stresses. At failure, the mortar is in a tri-axial stress state. The mortar does not reach the failure envelope; line B is more or less parallel to the mortar failure envelope, while the line that describes the development of lateral brick stresses intersects the brick failure envelope in point E.

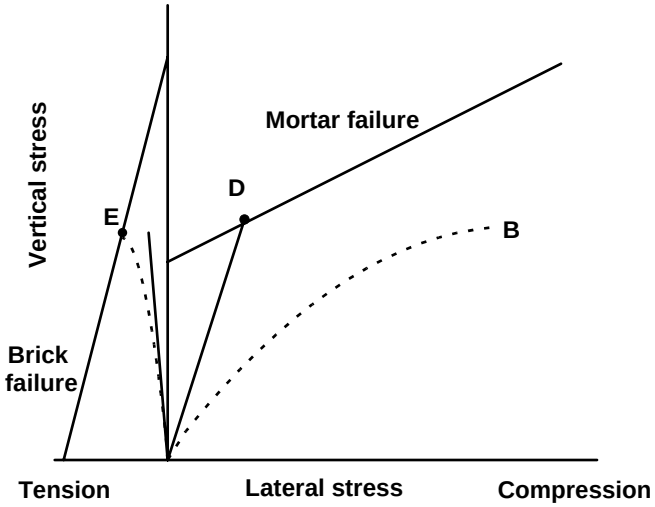

Figure 23 Schematic representation of stress paths for brick and mortar considering linear and nonlinear mortar properties, [MCN 85].

3.3 The tri-axial stress state of mortar in brickwork

3.3.1 Numerical simulation of joint behaviour

In the previous section it is recognized that the bricks confine the lateral expansion of the mortar in the centre of a wall. However, numerical simulations show that the mortar is squeezed out at the edges of the wall [ROT 92]. Tension acts more at the outside than expected from earlier modelling. This could explain the spalling of specimens often observed in compression tests of masonry prisms. When the brick-mortar contact area has fissures, the effect may become even worse.

3.3.2 Mortar joint in a concrete column connection

A soft layer between stiffer and stronger elements will be squeezed out when the elements move closer to each other. An extreme case to explain this phenomenon is a mortar joint between two concrete columns, placed vertically on top of each other as studied by Van der Plas [PLA 86]. The ‘units’ are extremely high and the strength of the mortar in the joint is smaller than the strength of the concrete. Therefore, it is expected

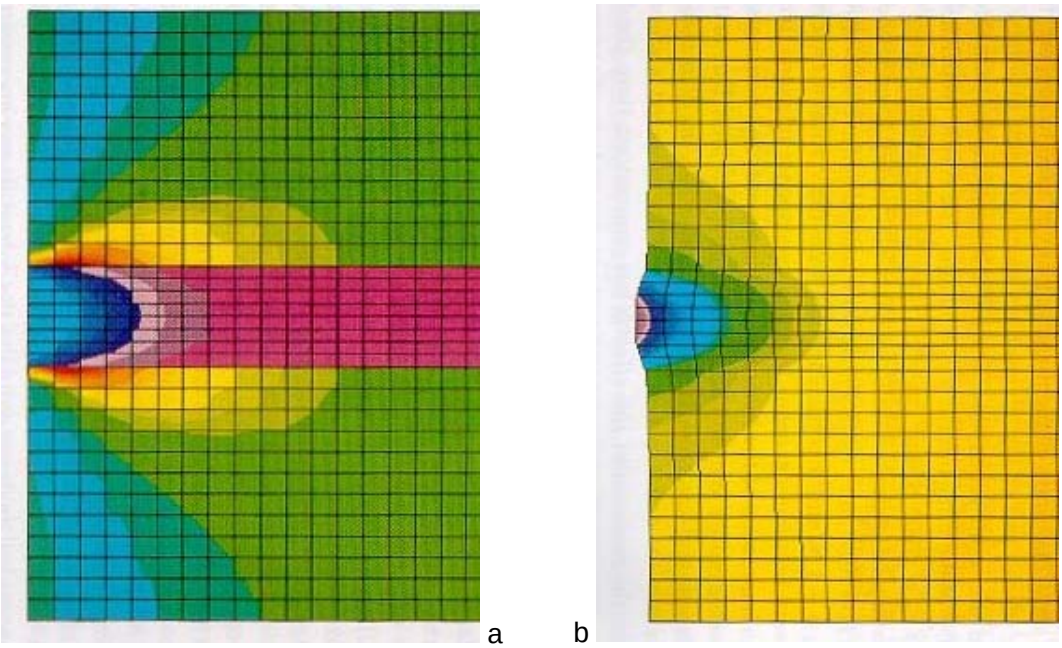

Figure 24 a) Stresses in horizontal direction and b) displacements found with numerical DIANA simulations [ROT 92]. E_{mor}/E_{bri} = 1300/18000.

that the joint is the weakest link. However, tests show a much more complicated behaviour. The load capacity is limited by splitting stresses in the end of the columns. These splitting stresses have two causes:

a) The difference in Poisson's ratios of mortar and concrete. The mortar is squeezed out, causing lateral horizontal stresses at the head of the column, similar as in masonry as discussed earlier in section 3.2.1
b) The differences in material properties. Due to local crushing of the joint material the compressive stresses are unevenly distributed and cause splitting stresses in the centre of the column.

The squeezing of the mortar is seen as a possible cause for the development of cracks, however this mechanism is much less obvious than it seems. Squeezing out will happen at first at the outside of a joint, see Figure 24. Then, after crumbling of the mortar at the outside, the effective joint area becomes smaller. As a consequence, the vertical force transmission will concentrate more in the centre.

The stress concentration in the centre of the column causes lateral tensile stresses in the column. At first, when loads are small, some squeezing out will occur. After that, the 'stress concentration' mechanism develops. This latter mechanism will control the behaviour when loads become higher.

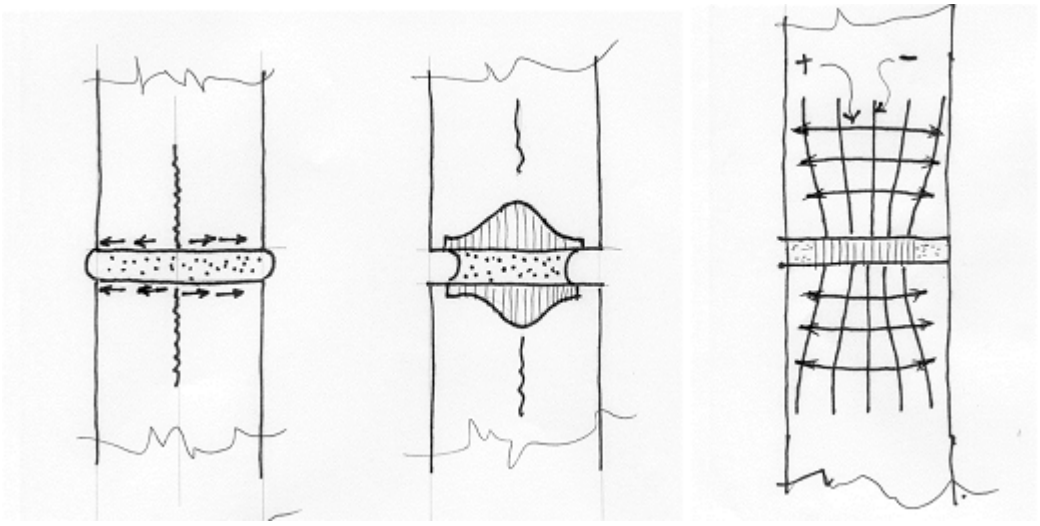

Figure 25 Model of the behaviour of a joint between pre-cast concrete columns Cracking due to lateral stresses, unequal axial stresses due to the squeezing out of the mortar, stress trajectories + = tension [PLA 86]

3.3.3 Soft joints in historic masonry

The behaviour of historic masonry built of natural stone and relatively soft mortar was studied by Sabha and Söhne [SAB 94], Sabha [SAB 98] and Berndt and Schöne [BERs91]. Their failure model is based on the observation that the joints bulge out (squeeze) before the ultimate load is reached. As a consequence, splitting tensile stresses develop in the units, which have their maximum half way up the unit height, while tensile stresses due to lateral confinement are largest near the joints. In [SAB 94] a stress distribution as shown in Figure 26, is proposed.

From numerical simulations, Sabha et.al. [SAB 94] found that the compressive stress peaks at the edge of the brick decrease due to mortar plasticity and fracture of the edges of the wall. The friction between mortar and brick prevents the squeezing of the mortar, a tri-axial stress state develops and the load bearing capacity of the mortar is increased.

A hydrostatic stress condition is assumed for the mortar in the centre, i.e. the mortar does not fail and break out. The joint height is limited to 1/5 of specimen thickness to allow for a tri-axial stress condition to develop.

From FEM analysis the critical bulge-out dept for the joints was established. For this situation the relationship between vertical compressive strength in masonry and the lateral tensile stress in the unit can be represented by:

$$\sigma_X = \left[-3.22 \cdot \left(2.5 \frac{h_{mor}}{h_{bri}} \right)^{2.5} + 1.524 \cdot \left(2.5 \frac{h_{mor}}{h_{bri}} \right) \right] \cdot \sigma_y \qquad (11)$$

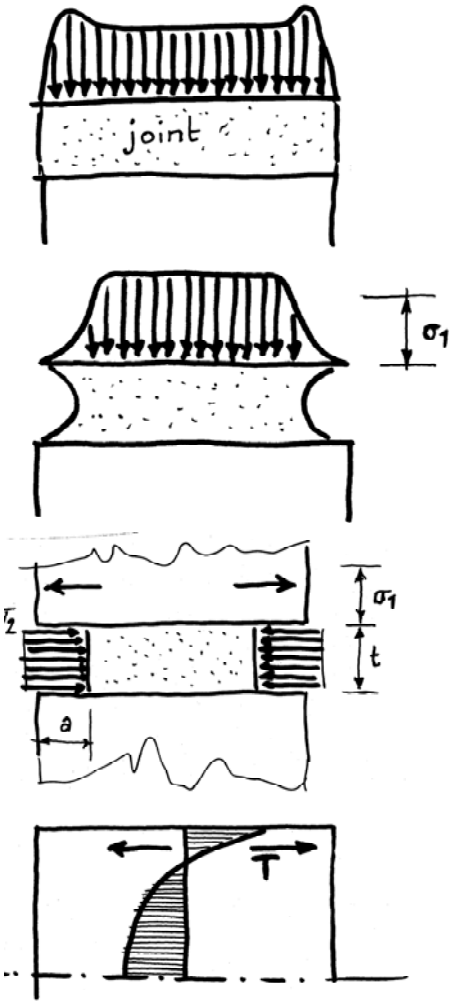

Before crumbling. Some stress increase near the edges.

After crumbling. Stresses concentrate in the centre of the wall.

Lateral stresses in the mortar ($\sigma 2$ in the centre) causing tension in the brick.

Lateral stress distribution over the height of the brick.

Figure 26 Stress distribution in a mortar joint, [SAB 94]. Compressive stress peaks at the edges. Results of a numerical simulation with assumed elastic behaviour. Proposed stress distribution after crumbling of the mortar, redrawn from [SAB 94].

The tensile splitting stress in the unit only develops as the mortar changes from its elastic to its plastic phase and squeezes (bulges) out near the surface. In their model, Sabha et.al. [SAB 94] assume that tensile splitting (i.e. the squeezing out of the mortar) starts at a vertical compressive stress of twice the uni-axial mortar compressive strength.

It is stated again that large values for E_{stone}, and low values of E_{mortar}, (smaller than 1 kN/mm^2) were used in [SAB 94]. The E_{stone} ranged between 20 and 30 kN/mm^2.

3.4 Fracture of prismatic concrete specimens

The behaviour of masonry is governed by the fact that it is a layered two material composite. However, when the two materials are well adjusted to each other, a specimen may behave more or less as a homogeneous material. Therefore a comparison with concrete may by useful.

Bazant [BAZ 94] and [BAZ 97] discusses the fracture processes under compression of concrete. In Figure 27 the microscopic mechanisms of compression fracture are presented. Bazant recognises: a) pores with micro cracks, b) inclusions with micro cracks and c) wing tip micro cracks. The crack initiators for masonry are similar.

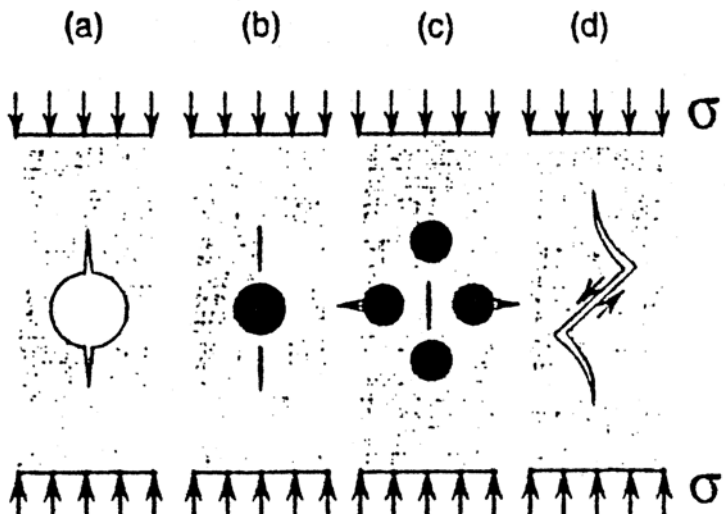

Microscopic mechanisms of compression fracture,
(a) pore,
(b) one inclusion, and
(c) a group of two inclusions pressed between two others
(d) wing tip.

Figure 27 Crack formation around discontinuities in concrete, [BAZ 94].

Often it is assumed that the bottom end is fixed, while the top end can rotate, and only translates in axial, i.e. the loading, direction. When, the rotation of the top end is negligible as well, both the bottom and top end are fixed. Then, diagonal shear failure will occur as found by e.g. Vonk [VON 92] and Torrentini et al, [TOR 89], (Figure 28). Because one side is stronger than the other, the non-symmetry initiates a predominant shear surface.

Torrentini studied strain localization in compression using stereo-photogrammetry. Figure 28 shows how a shear band develops and how the relatively intact parts of the specimen interact. The stereo-photogrammetry technique requires specimens to be loaded in plane stress. Consequently, thin specimens are used. The specimens used to obtain the images in Figure 28 were 120 x 60 x 20 mm.

The Stereo-photogrammetry technique can only be used for large deformation measurements, e.g. in the post-peak phase. The method is similar to ESPI. However, with ESPI only small deformations can be measured, preferably before cracking.

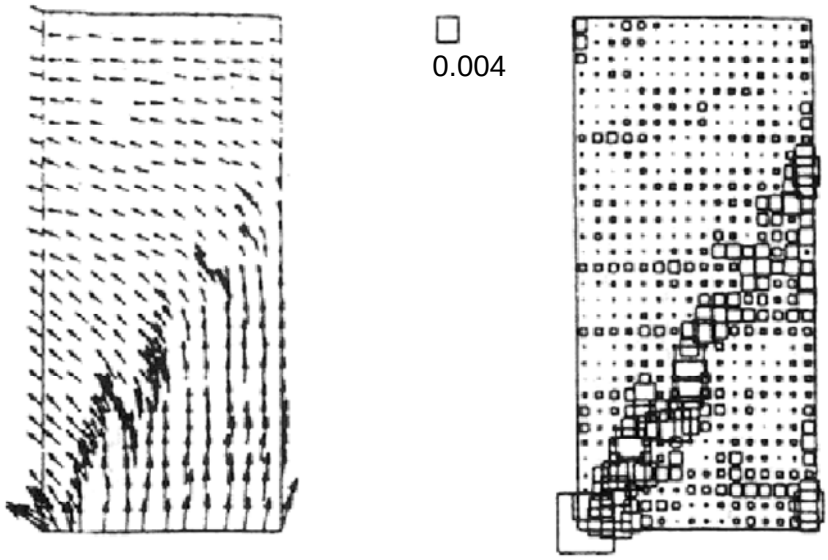

Figure 28 Development of a shear band in a prism subjected to uni-axial compression between non-rotating end-platens and aluminium sheets as friction reducing measure: block displacements (left) and distortion images obtained with stereo-photogrammetry [MIE 97].

Usually, tests are assumed to produce concentric loading, but due to irregularities (variation of material properties over the volume of a specimen), the force will act with some eccentricity. This means that, besides an axial force, an unintended bending moment is applied in a compressed specimen.

3.5 Fracture of stack bonded masonry specimens

In testing, it is assumed that platens do not rotate (after perhaps some initial rotation during settling of the specimen) and that lateral movement of the whole specimen is (more or less) prevented by friction between load platen and specimen. The loading direction is the only direction of free movement.

Loaded in this way, specimens made of uniform/homogeneous materials, like concrete or glass, exhibit an hourglass failure pattern (h/t <3). Depending on the height-thickness ratio and the friction between load platen and specimen, the fracture surfaces develop. Low friction causes splitting, high friction causes diagonal shear with shear planes under a slope of 70°.

Masonry is not homogeneous as a whole: it has layers made of two different materials. The differences in mechanical properties of unit and mortar cause lateral stresses as shown by the ‘sandwich model’. However, numerical simulation of the whole joint shows that deformation of mortar at the wall surface is largest. Sabha et al [SAB 94]

confirm this image of stress concentration in the central part of the wall experimentally for natural stone masonry.

In Chapter 2 it has been argued that the positioning of the units affects the shape of joint and variation of the mortar properties over the joint. Fissures are found as well. Besides that, the unit absorbs water from the mortar, causing a weaker interface.
In masonry made with general purpose mortar, the bulging of the mortar causes the highest stresses at the masonry surface. Fissures in the brick-mortar contact area affect this process and change this stress situation.

In thin layer masonry with recessed joints notch effects will occur at the end of the recessing. These effects can cause cracking in the surface area before diagonal shear failure occurs.

If the surface area fails, the load bearing section decreases, reducing the load bearing capacity. This effect will have a preference for one side of a specimen above the other. Consequently, there may be less symmetry than assumed, due to the shape of the fissures (or notches) in the brick-mortar interface.

Thus, two possibilities are recognized: a) the lateral deformations of mortar and brick are more or less equal and the specimen acts as a homogeneous material, or b) the lateral deformations of mortar and brick are different. Then, one large splitting crack in the centre can occur or the surface area can fail. The occurrence of splitting cracks is enhanced by the presence of head joints.

3.6 Conclusions

- The discussed theories relate to solid units.
  In empirical equations masonry strength is the result of brick and mortar strength. Execution effects are often underestimated.
- Traditionally, it is assumed that the brick is the strongest and stiffest of the two masonry materials.
  Consequently, the brick element is subjected to bilateral tension, as envisaged in most of the mentioned theories. However, the properties of modern factory made mortars are equal to brick properties, while mortars are adapted to brick. Therefore, traditional models are no longer applicable.
- Models based on uniform stress distributions are not completely realistic.
  Material properties are not uniformly distributed over the volume of the wall which causes stress variations. Another cause of stress variation is bulging of the mortar. The behaviour of the interface (fissures) as a cause of failure, or at least as a cause

of reduced stiffness, is not mentioned in the literature. This brick-mortar interaction can cause spalling before the peak load is reached.

- Uneven stress distributions act around head joints.

  The way of making head joints causes that they act as weak spots. Stresses will 'flow' around these weak spots and may cause lateral tension resulting in vertical splitting cracks. Furthermore, bricks can bend due to irregularities of the mortar bed, (Hilsdorf [HIL 69] and Berndt [BERs 91]).

- Variation of material properties in the specimen affects fracture and failure behaviour.

  In general, the more homogeneous the specimen, the more brittle the fracture process will be. In less homogeneous specimens, material strength may be reached locally, where the specimen will crack. However, the load can still be carried but via a different path, indicated by e.g. Hilsdorf [HIL 69], Figure 22, and McNary and Abrams [MCN 85], Figure 23. The cracked part has a reduced stiffness and, consequently, the stiffness of the whole specimen is reduced. Thereby, the global load deformation relationship will become less linear.

- The modulus of elasticity and Poisson's ratios of brick and mortar are crucial in all models. However, how can the modulus of elasticity and the Poisson's ratio of the mortar be measured while the gauge length is too short to be accurate?

4 Brick properties

Abstract

The physical properties of the bricks used for building masonry test wallettes are presented. The bricks were intensively tested under various loading conditions, and in different directions. Absorption, splitting, tension and compression tests were performed. In a few cases specimens were first loaded to failure in tension and then to failure in compression as well. This showed a smooth transition from tension to compression in the σ-ε-diagram. The C.o.V. of compressive strength was approximately 10%, while the C.o.V. equalled 25 % for tensile strength.

4.1 Introduction

To characterize the materials, tests according to current masonry codes were performed. When parameters are established according to a certain code, it should be kept in mind that each code gives specific rules for performing the test. Table 1 presents an overview of some of these properties. More details are given in Appendix A.5.1.

Table 1 Overview of the bricks used for tests on masonry specimens (Chapter 6) and their properties tested according to codes.

producer /		dimensions	free water Absorption	specific dry mass	strength $f_{c,bri}$*)
supplier	code	mm^3	Mass%	kg/m^3	N/mm^2
extrusion wire-cut brick, Brand Joosten (JO)					
Yellow	JG	204 x 98 x 50	7.3	1994	66
	G1	204 x 98 x 50	--	1897	60
	G2	204 x 98 x 50	--	1900	60
White	JW	206 x 98 x 50	--	2040	81
Blue	JB	210 x 97 x 50	--	2053	120
soft-mud machine-moulded brick, three factories.					
van Erp	ER	212 x 99 x 51	13.6	1750	27
Hapert	HA	210 x 99 x 50	--	1750	19
Vijf Eiken	VE	208 x 98 x 50	17.4	1880	33
Rijswaard	RW	206 x 96 x 50	15.5	1630	27
light weight clay brick made by adding sawdust to the fresh clay					
Poriso	PO	cut to size	18.4	1356	12

*) according to code for clay-brick: NEN 2489:1976.

More detailed measurements are required when the interaction of two materials and their deformation behaviour are studied. Therefore, dedicated experiments were performed to establish both physical and mechanical properties for the typical Dutch soft-mud machine-moulded and extrusion wire-cut clay-bricks used. Test principles were partly based on ideas given by Huizer [HUI 66] and Kasten [KAS 90] and [KAS 94].

Tests on single, whole bricks, on parts of brick and on specimens made of bricks, glued together to a prism with a two component material (brand Bolidt), were performed. An overview of the mechanical tests is given in Table 2.

Table 2 Key to method of loading for testing bricks

Code*)	Compression	Alternated **)	Bending
C1 C7 Cs CL Cf	1 brick 7 brick high On Side face On Header face On Bed face		
AL A6		1 brick 6 brick prism	
Bs Bsn Bf			On Side face On Side face notched On Bed face, across thickness

*) Code: see Figure 29
**) compression and tension alternated

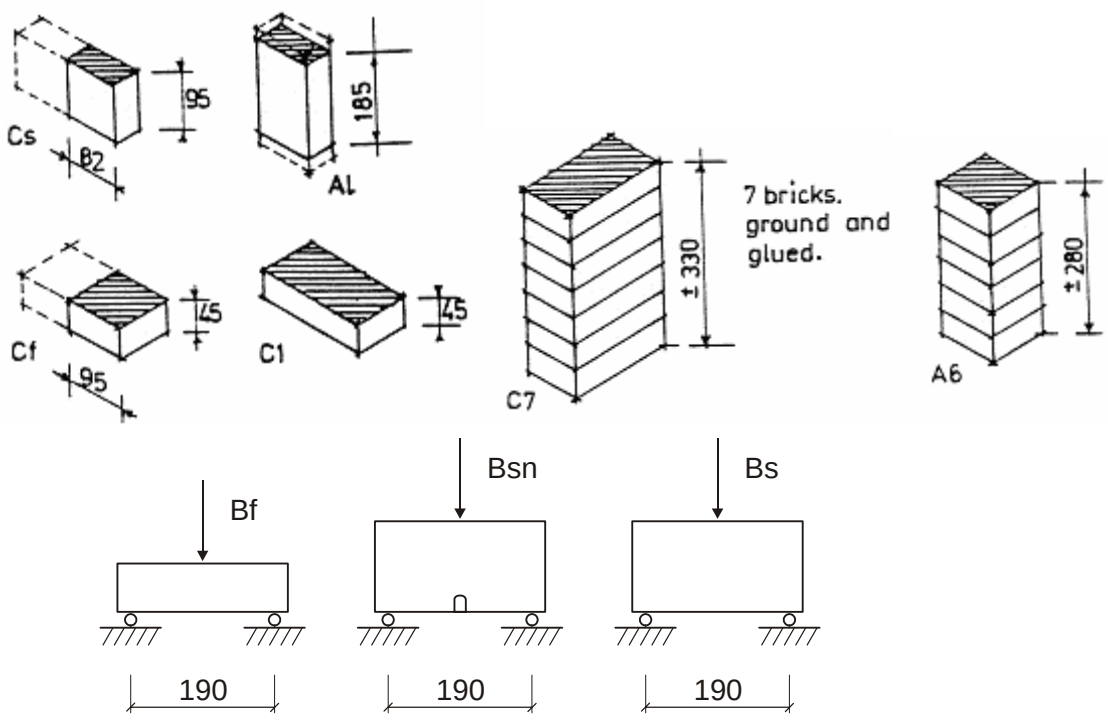

Figure 29 Specimen sizes used for testing brick under various conditions

4.2 Clay-brick as a porous material

Clay is a mixture of fine sand, lime, iron and other chemical compounds called the clay minerals. The latter have a flat very fine chip-like shape, on average smaller than 10 μm. Iron and lime compounds give colour to the bricks. Much iron gives a red colour; more lime gives a yellow colour. Clay minerals are responsible for the behaviour of the clay during forming of the brick, during drying and in the firing process.

The general properties of clay may be explained by the assumption that the chip-shaped clay minerals have negative electrical loading. This silicate structure is able to adhere / bond positive ions (like Ca- or Na-ions). Due to their difference in electric charge, Ca++ ions are stronger bonded than Na+ ions. When clay is in a plastic phase, the water parts (H_20 dipoles) will have a negative loading at their oxygen side and a positive load at their H-side. Then, they form a flexible bridge between the electrically loaded metal ions of the clay minerals. Consequently, plastic clay can easily be shaped. When an extrusion process is used to form the clay-bricks, the chips will have a direction parallel to the extrusion direction and this causes anisotropy. For soft mud bricks, formed by throwing clay in a mould, the direction of the chips is more at random, and consequently their behaviour is more isotropic.

When the formed bricks are dried, some initial strength develops and the volume will shrink (6% or more). The outside shrinks faster than the inside and, if the evaporation of water is too fast, shrinkage cracks may develop while the strength of the material is too small. The pore volume can be up to 25%, [WIN 89], [PEL 95]. Drying and firing of brick are described in detail in [BOR 01].
During the brick-firing process, the final free water parts will disappear and very fine pores (voids) (0.5 – 50 μm) will develop. At a temperature of around 1050 °C some of the minerals will melt. The clay-brick's final strength depends on the final temperature. A higher temperature gives a higher strength, as more minerals melt. The volume decreases while the weight of the brick remains constant. Consequently, the volumetric mass increases and so the denser the brick, the stronger it is.

4.3 Physical brick properties

All bricks used were of the Dutch 'Waal' format, i.e. of size nominally 210 x 100 x 50 mm^3. The deviation between the dimensions of bricks from one batch did not exceed 0.5% of the average dimension measured according [NEN 2489]. Usually this deviation is in the order of 1 % [SYM 90].
Suction properties are important for mortar workability and bonding. Therefore, the Initial Rate of Absorption (IRA) was established for each brick type and they are presented in Table 3.

Also, long-term suction properties were established by recording the water quantity (W) absorbed over a given period of time (t). Figure 30 shows, as an example, W versus √t relationships for two types of bricks and a scheme of the test set-up. The absorption rates are given in Table 3. The IRA gives an indication of the inclination in the first phase of moisture absorption, as expressed by the W-√t relationship. The second phase in the W-√t relationship was reached when the specimen with a thickness of 50 mm was almost saturated. In this phase W only increased a few percent, resulting in the absorption quantities obtained after minimal 24 hours given in Table 3. These absorption quantities give an indication of the pore volume of the brick.

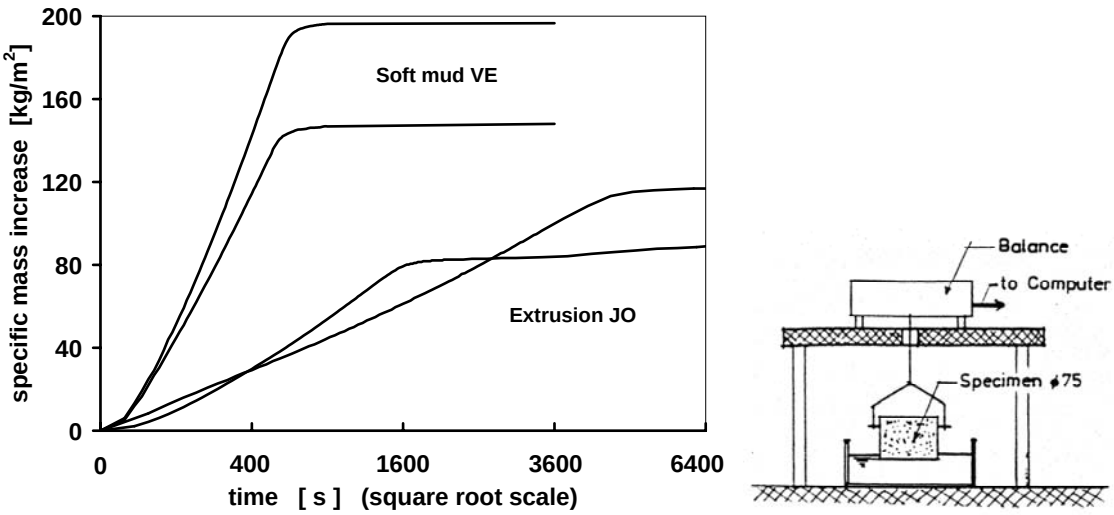

Figure 30 Brick absorption properties and scheme of test set-up, [GRO 93].

Table 3 Waterabsorption properties of bricks.

Type	1 min[1]) IRA	> 24 h kg/m³	%	Type	1 min[1]) IRA	> 24 h kg/m³	%
JG	--	--	--	ER	--	238	13.6
G1 [2])	0.9	83	4.4	HA	4.5	174	10.8
G2 [2])	0.9	91	4.8	VE	4.2	238	14.5
JW	--	--	--	RW	4.4	220	13.5
JB	0.3	77	3.7	PO	--	250	18.4

[1]) IRA: Initial rate of absorption (kg/m²/min).

[2]) G1 and G2 were two batches from the same JO works

4.4 Compressive properties of clay-brick

4.4.1 Separate brick specimens

Different manufacturing methods produce different brick material structures. The influence on the compressive strength was studied by performing tests on bricks fabricated by the two processes described earlier. Samples of such a unit were compressed in both the bedding as well as the brick face direction. Specimens were prepared by grinding to obtain a smooth and level surface. The NEN 2871 and NEN 2489 code prescriptions were followed, but dry bricks were tested.
The results are shown in Table 4 and Table 5 for C1 and C7 specimen.

Table 4 Compressive strength of bricks

Type	C1 [1]) N/mm^2	C7 [1]) N/mm^2	Type N/mm^2	C1 [1]) N/mm^2	C7 [1]) N/mm^2
JG	66	35.8	ER	30	12.0
G1 [2])	60	33.0	HA	19	10.6
G2 [2])	60	26.7	VE	25	14.2
JW	81	68.9	RW	27	17.0
JB	120	64.8	PO	12	10.5

[1]) see Figure 29

[2]) G1 and G2 were two batches from the same JO works

4.4.2 Bolidt tests

Besides tests according to codes, tests were also performed to establish the modulus of elasticity of the units. Therefore, specimens with a height over thickness (h/t) ratio between 4 and 5 were constructed by gluing whole or half units on top of each other using Bolidt, after removal of loose sand from the brick's production process. Bolidt is a high strength, two component jointing material allowing for thin joints and well filled pores [VMF 96]. Consequently, forces were transmitted optimally from one unit to the next. Were necessary, surfaces were ground smooth and level.

It is assumed that the confining effects of the load platens did not disturb the stress distribution in the middle of these larger specimens. In addition, the deformation can be measured over a larger length instead of only a part of the thickness of the unit, which improves accuracy. Therefore, LVDTs on each side of the specimen with a gauge length of 110 mm were used. Clip-on gauges were used for measurements over 40 mm gauge length, Figure 31.

In a number of cases the lateral deformations of these Bolidt specimens were measured as well, to establish Poisson's ratios. In Table 5 the mean compressive strength ($f_{c,Bo}$), modulus of elasticity (E_{Bo}) and Poisson's ratios resulting from the Bolidt tests are presented. Appendix A1 explains the method of establishing of the modulus of elasticity.

Table 5 Compressive properties of bricks established with specimens made of seven ground bricks with smoothed surfaces and bonded together into a prism with a height of 330 mm.

unit type	type of test	# of tests	$f_{c,Bo}$ N/mm^2	E_{Bo} N/mm^2	ν (-) a*)	ν (-) b*)
Extruded wire-cut bricks						
JG	C7	2	35.8	16700	0.28	0.28
G1[3])	C7	5	33.0	15400	--	0.28
G2[3])	C7	3	26.7	13900	--	--
JW	C7	2	68.9	19900	--	--
JB	C7	2	64.8	15400	--	0.19
Soft mud machine mould bricks						
ER	C7	2	12.0	4500	--	--
HA	C7	2	10.6	3200	--	--
VE	C7	2	14.2	6050	--	0.14
VE[1])	C7	4	12.9	5330	--	
RW[1])	C7	2	17.0	4000	--	0.13
RW[2])	A1	3	23.6	6240	--	--
PO	C7	1	10.5	7110	--	--

a*) in masonry with a 1:2:9 mortar (cement:lime:sand ratio; by weight).

b*) in Bolidt specimens

1) prism made of half bricks, ± 95x95 mm².
The other prisms were nominally ± 210 x 100 mm².

2) brick tested in the stretcher direction. Height 180 mm.

3) G1 and G2 were two batches from the same JO factory.

From the results of deformation measurements on the Bolidt specimens over various gauge lengths, some including and others excluding Bolidt joints, (Figure 31), it could be concluded that the effect of the Bolidt layer on the overall deformation was negligible.
All E-values and Poisson ratios were established using a linear best fit relationship of a part of the σ-ε diagram as explained in appendix A.1. In Figure 32 the E-moduli versus brick strength are plotted for all tests.

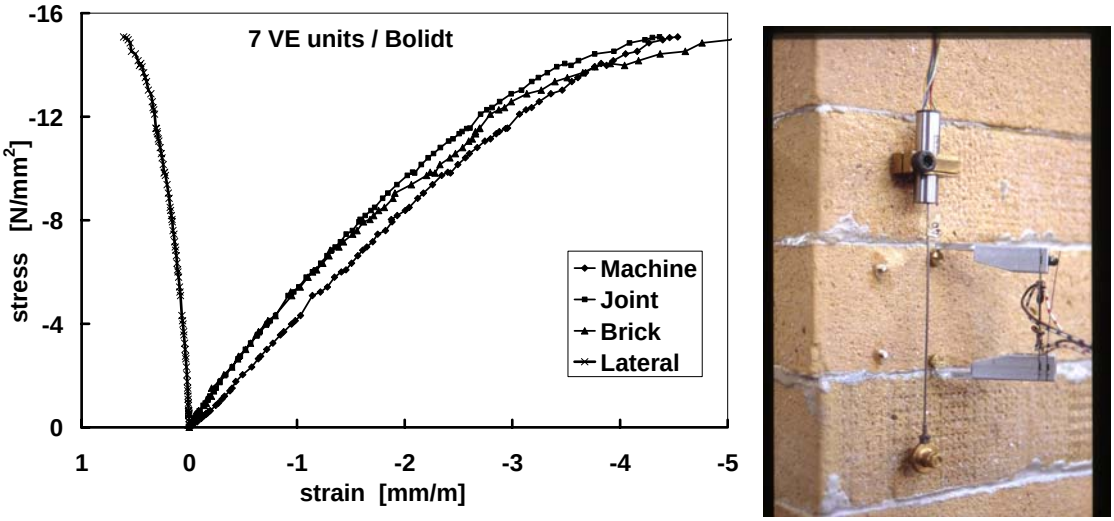

Figure 31 a) Stress strain diagram for a VE-Bolidt specimen illustrating the resemblance of deformation measurements over various gauge lengths. b) Clip on 40 mm gauge with strain gauges and an LVDT on a Bolidt specimen.

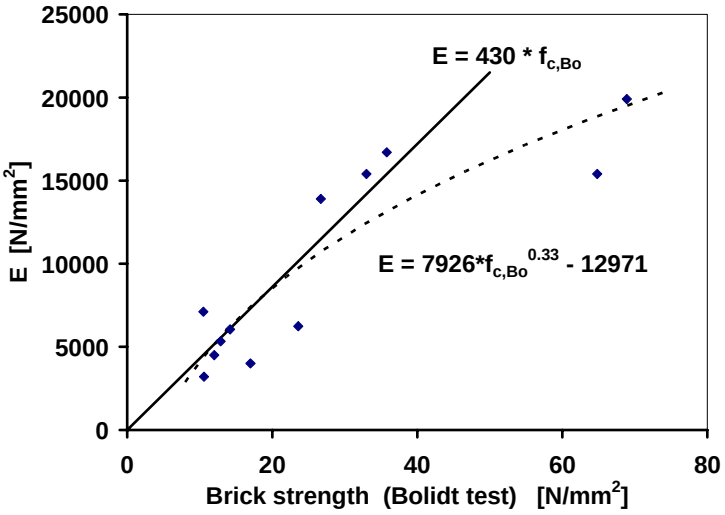

Figure 32 Modulus of elasticity versus brick compressive strength.

The strongest extruded bricks had a relatively low E-modulus. Excluding these two values, the following relationship between E-value (E_{Bo}) and strength ($f_{c,Bo}$) with a correlation $R^2 = 0.81$ was found:

$$E_{Bo} = 430 * f_{c,Bo} \quad (12)$$

These two results were less extreme in the following relationship (all results):

$$E_{Bo} = 7926 * f_{c,Bo}^{0.33} - 12971 \quad (13)$$

The number of tests is relatively small to make such estimations.

Lateral deformations were measured in the middle of the specimens and Poisson's ratios were established. The experimental results indicate that the Poisson's ratio (ν)

varies with the stress level. The ν-values in Table 5 were calculated at the commonly accepted stress level of one third of the ultimate load, e.g. NEN-EN 1052-1:98.

Table 6 presents the results of tests to establish the effect of loading direction. Specimens taken from the same batch were loaded either sideways, or on their flat faces, or in the length direction.

After correction for the size of the brick-specimens with the Dutron equation [DUT 80] the compressive strength was approximately 40% higher when loaded on the brick face than loaded on the bedding surface. The difference in strength is believed to be due to anisotropy in the material.

Table 6 Compressive strength (average of 12 tests) of RW bricks, loaded in different directions. See Figure 29 for sizes and shapes.

		position, loaded area and test-code			
	mm^2	side ways 50 x 82 **Cs**	longitudinal 50 x 95 **CL**	flat 95 x95 **Cf**	flat 95 x 205 [1]) **C1**
height	mm	92	185	45	45
average	N/mm^2	24.2	16.6	22.1	27.0
corrected [a])	N/mm^2	24.5	20.4	12.7	12.2
corrected [b])	N/mm^2	26.6	23.3	16.0	19.4
C.o.V.	%	10	18	12	8

[1]) whole bricks, with smoothed surface tested according to NEN 2871

[a]) Corrected with Dutron 200 mm cube [NBN 80] or [DUT 80]

[b]) Corrected according to EC6 [EC6 96], 10 cm cube

4.5 Tensile properties of clay-brick

4.5.1 Tensile tests

Detailed tensile experiments were carried out on single bricks. For tensile testing, the specimens were glued to steel platens. This method provides lateral confinement at the ends of the specimen, therefore the specimens were made as long as possible. Making a (central) notch in the specimen created a weak spot where fracture should occur, but often a crack was found near the loading platen.

To make the notch, the top skin, which is assumed to have other properties than the internal brick material, was removed to a depth of approximately 5mm.

Stress concentrations around a notch influence the results. Not only the strength is affected, but also the modulus of elasticity. Furthermore, it can be expected that the possibility of the occurrence of weak spots is greater in longer specimens, resulting in lower strength, than in shorter specimens.

Other effects on apparent strength are: a) test specimens are not homogeneous, e.g. there may be cracks, b) the centre of gravity of the cross section of a specimen does not coincide with the line of action of the applied load and, c) in addition to normal stresses,

bending will occur. In brick-like materials, eccentric loading is usually the case if tensile tests are performed with hinged loading platens. Thus, bending influences the results of tests. For this test series however, steel loading platens were connected to the end of a hydraulic jack. From LVDT measurements at opposite sides, it could be derived that rotation of the platens was relatively small.

The tensile test results are presented in Table 7. The tensile strength of the RW soft mud specimens loaded with these parallel moving platens was 1.04 N/mm² which is about 1.6 times the value of 0.67 N/mm^2 for specimens loaded with hinged platens, see Table 8.

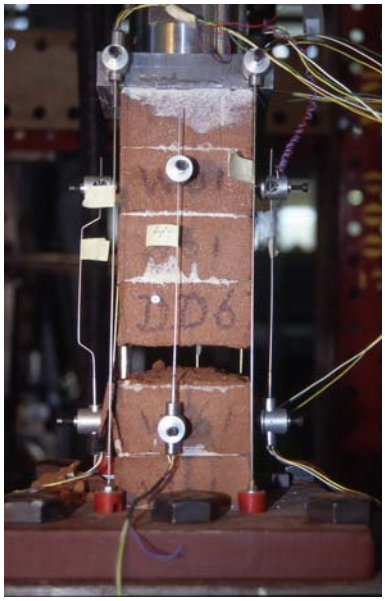

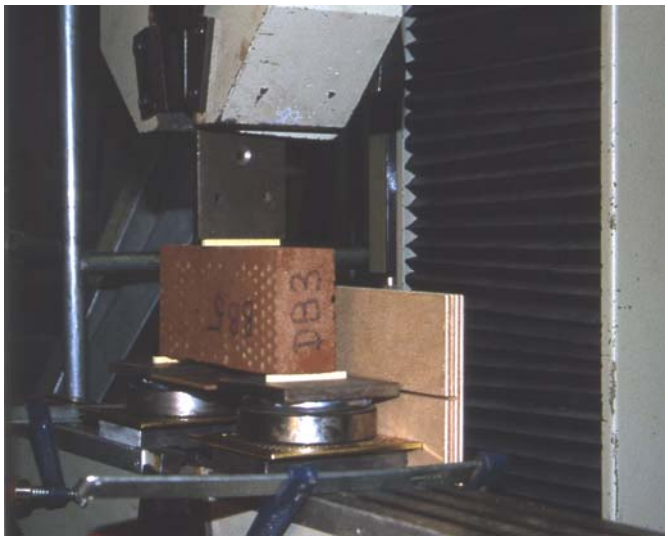

Figure 33 Uni-axial tensile test and bending test.

Table 7 Tensile strength of bricks.

Brick type	Specimen type	loading direction	strength N/mm^2		type test
VE	cylinder	thickness	1.50		
	prism	length	2.47		
RW	prism	length	1.09	24*)	CL
	prism	thickness	1.04	5 *)	A6
G1[2])	cylinder	thickness	3.51		
	prism	length	2.36		
	prism	length	1.13 [1])		AL
G2[2])	prism	length	1.82 [1])		AL

[1]) Hinged loading platens.

[2]) G1 and G2 were two different batches from the same factory

*) C.o.V. of 12 tests, the other results are from 3 tests per type.

4.5.2 Modulus of rupture

To establish the modulus of rupture, brick specimens were loaded in a three point bending test. The stress distribution over the height is not linear [PLU 97], [PLU 99b]. When, however, a linear distribution is assumed, the modulus of rupture equals:

$$f_r = 1.5\ Fl / (bh^2) \qquad (14)$$

The span of the specimen (l) has an influence on the result. The direction of the stress trajectories run steeper in short beams. Therefore, it is assumed that arch action is smaller in longer bending specimens. The specimens were made as long as possible and supported by roller-plates to minimise horizontal reaction forces, preventing this arch action in the specimen. The roller plates reduced friction, resulting in the horizontal reaction to be about 3% of the vertical load.

A notch was also made in the flexural specimens, similar to the one used in the tensile tests.

Therefore, the modulus of rupture shown in Table 8 did not completely agree with the real tensile strength but it may be seen as an indication.

The specimens for this test series had no visible cracks. Only in one or two specimens discontinuities were observed around lumps of clay. These lumps had a diameter of approximately 6 mm.

A large difference in strength was found for bricks loaded on their sides, with or without a notch. The strength of the side loaded, notched bricks was the same as the strength of the bricks loaded in a flat position, height 50 mm.

Table 8 Mean results from tensile and bending tests on RW bricks, 12 tests per parameter.

Test type		direction of loading	*)	N/mm^2	C.o.V.
uniaxial		longitudinal	AL	0.67	57
tensile	alternating	longitudinal	AL	1.03	29
test	loading	across thickness	A6	1.04	5
bending test		on side, plain	Bs	2.93	33
modulus of rupture		on side, plain, notched	Bsn	1.89	27
		across thickness	Bf	1.88	32

*) see Table 2 and Figure 29.

4.5.3 Stiffness under alternating tension and compression

Loading a brick in tension could open small cracks and reduce the cross-section area, but under compression, the initial cracks are closed. Therefore, single RW-brick specimens and specimens comprising six half RW-bricks with smoothed surfaces and bonded together with a two component adhesive (Bolidt), were loaded alternately in tension and in compression, in order to study this phenomenon.

First the specimens were loaded in tension to 0.5 N/mm². Then the displacement direction of the machine cross head was reversed and the specimen loaded in compression to 7.5 N/mm² (50% of the estimated strength). Again the direction was reversed and thus the specimen was loaded in tension until fracture occurred. Reversing the direction, first the 'crack'-opening had to be closed and then the specimen was loaded in compression to fracture.

The stress/strain diagram for one of the specimens, given in Figure 31, shows a smooth relationship even for small stresses. No discontinuity near the origin was observed, as sometimes assumed. This can be seen in detail in Figure 31, right. After tensile cracking, the strain grows fast, causing a shift from A to B. When reloading in compression, initially a curve with increasing stiffness develops due to the closing of the mentioned tensile crack. Later, the slope of the line (modulus of elasticity) of the first loading cycle was resumed.

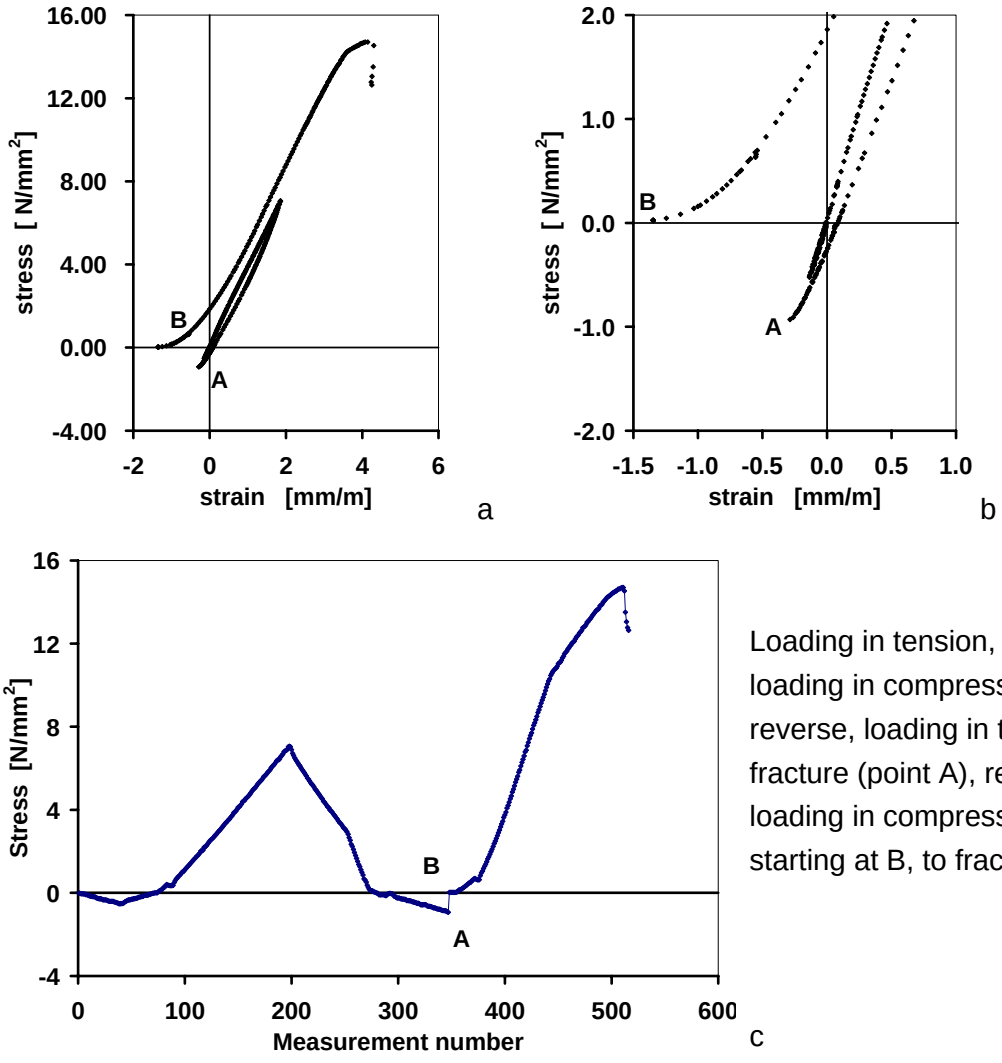

Loading in tension, reverse, loading in compression, reverse, loading in tension to fracture (point A), reverse, loading in compression starting at B, to fracture.

Figure 34 a) Stress-strain diagram for tensile and compressive loading of one brick, b) detail, c) load history.

For the extruded G1 and G2 bricks the E-values were 9700 and 9100 N/mm² respectively in tension and 15400 and 13900 N/mm² respectively in compression. Also for the bricks described in [GRO 88], the E-modulus in tension was considerably smaller than in compression. Those values were obtained from different specimens.
This indicated that, even when the stress/strain relationship was a smooth curve, as found for RW-bricks, the deformation under tension grew quicker than under compression. This difference may be attributed to the fact that, in compression, cracks or openings close and more material transfers load. In tension, on the other hand, cracks open and less material transfers the load.

4.6 Conclusions

- Brick properties differ per batch (see the results given for G1 and G2 in this chapter).
  When producing bricks, more attention is paid to their uniformity of colour, shape and dimensions than uniformity of strength. It is therefore advisable that each batch should be tested to indicate and eventually improve uniformity in mechanical properties, to make masonry a more predictable material.
- The differences between the dimensions of bricks taken from one batch did not exceed 0.5 % of the average dimension.
- Specimens loaded in a way in which compressive stresses prevail, show a C.o.V. of about 10%; while, when tensile stresses prevail, the C.o.V. is about 25%
- As a tendency, the modulus of elasticity (E_{tan}) of most of the bricks used may be estimated to be about 430 times its compressive strength.
- The way clay particles are oriented in a brick (both soft-mud and extruded) influences the strength, stiffness and failure pattern of a specimen.

5 Mortar properties

An overview of the properties of the mortars used for building masonry test wallettes is presented. Mortar properties were determined from standard tests on 40x40x160 mm^3 prisms made in steel moulds. The results were used to evaluate the 'potency' of the mortar, i.e. for product control purposes and characterization. Curing conditions and suction from bricks may result in completely different properties for mortar in a wall. Therefore, specimens were also made from mortar slabs. These slabs were taken from masonry that cured under various conditions. They were tested in compression under various boundary conditions. The results showed a large variation, but still the effect of the curing conditions was obvious.

5.1 Introduction

First some general information of the mortars obtained with tests according to codes is discussed and then some results of tests on small specimens (15 mm in thickness) are presented. The latter tests were performed to investigate a) the effects of hardening conditions on compressive strength and b) the variation of properties over the joint.
These dedicated experiments were performed to establish the mortar mechanical properties in almost 'real life' conditions.

5.2 Mortar compressive strength according to NEN 3835

As for the establishment of unit-compressive strength, each code (country) also has specific rules for the establishment of the mortar compressive strength. Mostly, also in the Dutch code NEN 3835:1991, prisms with a dimension of 40 x 40 x 160 mm^3 are prescribed,. These prisms first have to be fractured in a three point bending test. Then, the remaining parts have to be loaded in compression via steel platens of 40 x 40 mm^2.
In Table 9 an overview of various typical Dutch mortar types used for building the wallettes mentioned in section 6.2 page 56, is given, together with their average properties and the type of brick with which they were combined. More details are given in Appendix A.2.
Mortar mix designs were specified in volume parts for cement, lime and sand. However, the mixture was made on the basis of the weight of the constituents. Therefore, the volume ratios were converted to weight ratios using the following values for the specific masses: cement 1250 kg/m^3, lime 600 kg/m^3 and dry sand 1400 kg/m^3.
The added amount of water was adjusted to the workability of the mortar, for which a flow according NEN 3835:1991, of 175 $\pm$ 10 mm was aimed for. A flow of 175 mm allows for good workability.

A hydrated shell lime was used and a hydrated lime with an air-entrainer (brand Mekal). In all cases Portland cement type A (brand ENCI) was used. This type of cement is now coded as CEM I 32,5 R, according to NEN EN 197-1:2000 [NEN 197-1].

Table 9 Overview of the mortars and their mean compressive strength according to NEN 3835: 1991 per test series and per unit type.

mortar (mix design in volume parts cement:lime:sand)	$f_{c,mor}$ N/mm^2	joint thickness mm	used in combination with unit types
GP 1:2:9	3.0	14	JG, VE
GP 1:½:6	4.5	14	JG, VE
GP 1:1:6 (lime + air entraining agent)	8.1	12,5	JG, RW
GP 1:½:4 ½	17.6	14	JG, VE
GP 1:½:2¼	37.5	14	JG, VE
TL (Ankerplast) batch 1	29.5	3-4	RW
TL (Ankerplast) batch 2	18.6	3-4	RW

TL: thin layer mortar (cement based, always prefabricated, factory made),
GP: general purpose mortar for a joint thickness of 12-15 mm, laboratory made,
The properties of the mortars used for ESPI testing are presented in Table 23.

5.3 Compressive properties of small sized mortar cylinders

The effects of hardening conditions on mortar strength were investigated experimentally. Test pieces made from mortar that hardened between bricks are more representative of mortar behaviour in masonry than larger specimens made in steel moulds. To obtain representative values for the behaviour of mortar in real masonry walls, specimens have to be cut from these walls, or the real conditions have to be simulated in the production process.

To produce the specimens the following method, adapted from [DGfM92] and [SCHu88] was used. Bricks, ground smooth and level, were covered with a special kind of paper – brand Schleicher & Schuell - to prevent mortar from bonding with the brick, but allowing the unit to absorb water from the mortar. Then, the quantity of mortar needed for one joint was placed and covered with paper. With the top brick the mortar was squeezed to the proper joint thickness. Therefore, wooden laths were placed at the end of the units, see *Figure 35*. The paper prevented mortar-brick bond, but allowed the unit to absorb water from the mortar. It is assumed that the paper did not affect the suction of the unit. In this way mortar slabs were made and cylinders and square prisms were cut out of these mortar slabs. Their height was 15 mm at most, because this is the largest bed joint thickness commonly used.

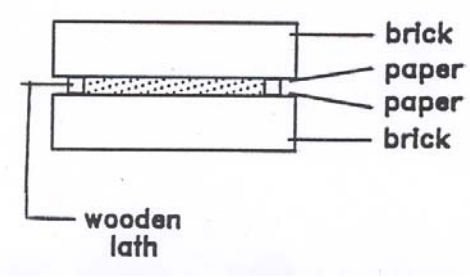

Figure 35. Mortar placed between two units, with porous paper to prevent bonding of the mortar but allowing the unit to absorb water from the mortar. Wooden laths to allow for the required joint thickness.

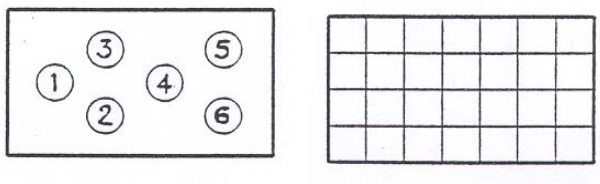

Figure 36 Position where cylinders were drilled from a slab, possible sawing lines for square specimens, 25 x 25 mm^2.

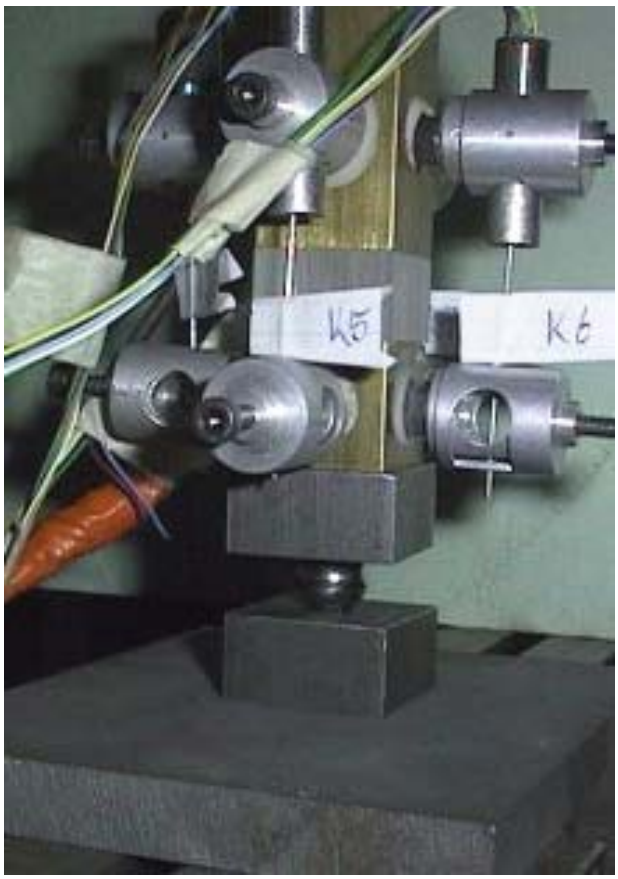

Figure 37 Load introduction and deformation measurement on a 15 mm thick mortar specimen.

The specimens were loaded via a brass bar, rigidly connected between the jaws of a loading machine. The specimens were supported by a brass prism, supported by a steel sphere in line with the vertical axis of the bras bar. Teflon was placed between the specimen and the brass load surfaces. The specimen's defor-mation was measured by means of four LVDTs as shown in Figure 37.

The following effects on mortar compressive strength were studied:
a) the capping materials and Teflon layers between cylinder and platens,
b) the mortar curing conditions (the moisture conditions of the bricks) and
c) the position of the cylinder in the mortar slab before drilling.

5.3.1 Curing conditions.

To investigate the effect of the moisture condition of the unit on the properties of the mortar, two types of mortar were used. Slabs were made of mortar 1:½:4½ (c:l:s) and 1:2:9. The slabs hardened for six to eight weeks between calcium silicate units having three moisture conditions: dry, medium (absorption rate 1.5 kg/m^2/min), and saturated. Cylinders with a diameter of 26 mm for the 1:½:4½ mortar and 35 mm for mortar 1:2:9 were drilled from the slabs and capped with gypsum. The averaged results of 108 compressive test on mortar cylinders are presented in Table 10.

The compressive strength established in tests according to NEN 3835 with prisms 40x40x160 mm^3 of the 1:½:4½ mortar was 12.2 N/mm^2, and 3.3 N/mm^2 for the 1:2:9 mortar. The mortar specimens from slabs were stronger than the prism strength for the 1:2:9 mortar; for the 1:½:4½ mortar this was the other way around. A large deviation of the E-moduli can be observed and so the relationship with the position in the slab and the mechanical properties of a specimen is not clear. One of the possibilities for the relative small ratio between E_{mor} and $f_{c,mor}$ (Table 10) is the way the deformations were measured, i.e. from brass bar to brass bar including two seams between specimen and loading surface, where also Teflon was present.

Table 10 Strength and E-modulus of strong and weak mortar cylinders 26 mm diameter, 15 mm high, cured under various moisture conditions, tested at an age of six to eight weeks.

Mortar type	moisture condition	Num-ber	$f_{c,mor}$ N/mm^2	C.o.V. %	E-modulus N/mm^2	C.o.V. %	E/$f_{c,mor}$	C.o.V. %
1: ½:4½	dry	18	10.20	28	1037	50	99	27
Strong	medium	18	10.80	24	1059	28	77	28
	saturated	18	8.87	23	815	50	67	32
1:2:9	dry	18	4.33	25	630	77	139	75
Weak	medium	18	5.56	22	700	62	128	70
	saturated	18	3.25	21	283	55	92	77

Together with the already mentioned strong (1:½:4½) and weak (1:2:9) mortar slabs, stack bonded masonry prisms of five bricks high were made with the same mortar. The averaged results of compressive tests on these masonry prisms are given in Table 11. For these specimens the moisture effects on strength and stiffness were clear, as also found in [KJA 91]. The saturated condition resulted in the lowest value for $f_{c,mas}$.

Mortar E-values were calculated by subtracting brick deformations from masonry deformations using E_{brick} = 6000 N/mm^2 (value for VE brick, see Table 5 page 40, and 50 and 15 mm for brick and joint thickness respectively, as explained in section 6.5.5, page 72. For the 1:2:9 mortar the E-values derived from masonry deformation are

roughly the same as the values found with cylinders drilled from slabs, except the saturated one. The 1:½:4½ mortar results show a greater difference, see Table 11.

Table 11 Compressive strength and E-modulus of masonry prisms that cured under various moisture conditions and mortar E modulus derived from it. E-values obtained from cylinders (Table 10) and the ratio between E values. Three specimens tested per type, at an age between six and eight weeks.

moisture condition		$f_{c,mas}$ N/mm^2	E_{mas} N/mm^2	$E_{mor,est}$ N/mm^2	$E_{mor,cyl}$ N/mm^2	$E_{mor,est}$ / $E_{mor,cyl}$
1:½:4½	dry	12.5	3020	1260	1037	1.20
strong	medium	13.3	3660	1530	1059	1.44
	saturated	11.1	3310	1340	815	1.64
1:2:9	dry	8.0	1830	617	630	0.98
weak	medium	9.0	2130	770	700	1.10
	saturated	6.2	1390	440	283	1.55

5.3.2 Effect of the position in a mortar joint on the compressive strength

Mortar strength may vary over the joint, as explained in section 2.4, page 15.

The effect of the position of small cylindrical specimens in mortar slabs was studied with a test series, which consisted of 29 tests on cylinders, 26 mm in diameter, drilled out of five mortar slabs that hardened between calcium silicate units, [AND 96]. The position where they were drilled out of the slab is shown in Figure 36. They were capped with gypsum and tested with the brass bar and a steel ball using Teflon, Figure 37. The test-method was similar to the method described by Schubert in [SCHu91].

The averaged compressive strength was 7.9 N/mm² and its C.o.V. = 24 %. The results ranged between 4.6 N/mm^2 and 13.3 N/mm^2. Averaged per slab the difference between the strongest and weakest cylinder was 2.1 N/mm^2. Cylinders drilled from the middle of the slabs were on average 1.2 times as strong as the cylinders drilled at the sides.

During testing, no cracks became visible. Afterwards, mainly vertical cracks were visible in the loaded, capped, surfaces, Figure 38. Few cylinder segments remained in the shape of columns. The rest of the specimen crumbled after the load platens were separated. From the mainly vertical running cracks it can be concluded that friction between platens and specimen is considerably reduced by the Teflon layers.

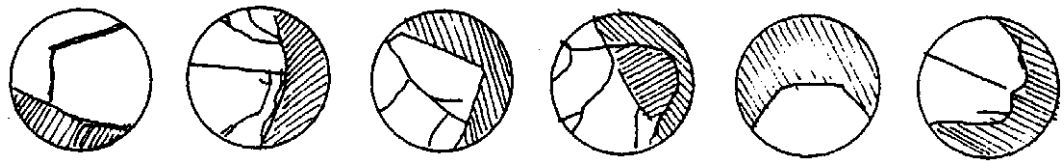

hatched areas are crumbled

Figure 38 Top view of cracking patterns of prisms of masonry cylinders.

5.3.3 Variation of properties

In section 2.4.2 three areas were recognised in the brick mortar contact zone and the ultra pulse velocity contours indicate variation of mortar properties over the joint.

Therefore, this possible variation of properties was tested with series D, a series of mortar specimens made of mortar slabs that were taken from a damage case with calcium silicate units, Table 12, [VMF 98].

Due to dry and warm conditions during erection, poor bond was obtained and slabs could easily be separated from the masonry wall. Square mortar prisms were sawn from three different slabs in order to get an impression of compressive strength and of variation of mortar quality over the walls. The results are given in Table 12.

With the same types of mortar and unit, bond wrench and cross couplet tests were subsequently performed in the laboratory, series L.

For series D and L the similar mortar mix designs of 1:¼: 4 were used.

Three hardening conditions were used: a) 30 % R.H., 30 °C, slab 1,

b) 90 % R.H., 30 °C, slab 2 and c) (30 % R.H., 30 °C, slab 3).

The strength results are summarized in Table 12. The effect of curing/hardening conditions on strength is obvious. In this series, the effect of the position of the prisms in the slabs could not be recognised.

Table 12 Compressive strength and E modulus of mortar prisms 25 x 25 mm^2 (15 mm thick) cut from slabs taken at positions D1, D2 and D3 from an existing building, damage case (1992). Per position three or four slabs were used to cut the specimens.

Series D	n for $f_{c,mor}$	$f_{c,mor}$ N/mm^2	C.o.V. %	n for E_{mor}	E_{mor} N/mm^2	C.o.V. %
slab D1	16	14.7	22	3	17300	28
slab D2	15	13.2	34	4	21500	12
slab D3	15	16.3	21	4	14700	61
averaged	46	14.7	26	11	17900	36
n: number of tests						

Table 13 Compressive strength of mortar prisms 25 x 25 mm^2 (15 mm thick) cut from laboratory made slabs, slabs were taken from rest pieces of bond wrench tests.

Series L			number of tests	$f_{c,mor}$ N/mm^2	C.o.V. %
slab L1	90 % R.H.	30 °C	6	19.7	6
slab L2	90 % R.H.	20 °C	5	19.9	7
slab L3	30 % R.H.	30° C	5	4.9	17

5.4 Conclusions

- Due to variation of the results, differences between the applied test methods could not be established clearly.
- The effect of curing/hardening conditions on mortar strength is clear:

  Curing under dry conditions considerably reduces mortar strength, in this study by a factor 4 if cured at RH = 30%, as opposed to RH = 90%.

  The difference in properties between steel mould prepared mortar and in-situ mortar showed clearly that the curing (moisture) conditions of the specimen affects the mechanical properties. Too dry or too wet both have a negative effect.
- Due to variation of strength and stiffness it is not possible to clearly recognise effects of the original position of the specimen in the slab. In one series, the central specimens seemed 1.2 times stronger than the edge specimens, which reflects the quicker drying conditions on the mortar at the wall face, than internally.
- The mortar E-values differed considerably, from 500-1000 N/mm^2 (Table 10 and Table 11) to 14000 to 17000 N/mm^2 in Table 12.

  The deformation measurements included Teflon and the seam between specimen and load platen, Figure 37, which affected the accuracy of the results negatively. On the other hand, the results in Table 10 agree well with the results calculated from measured masonry deformation, as shown in Table 11.

  These results emphasize the necessity to measure deformation in detail directly on masonry.
- Even when no paper was used, the mortar slabs used for making specimens could be taken from the brick-joint-brick couplet without damaging them, indicating poor mortar-brick bond.

6 Masonry properties

Abstract
In this chapter, the results of tests on various types of masonry, representing most of the types used in The Netherlands, are analysed. Test series A and B were made with general purpose mortar. Thin layer mortar was used to make series C.
For each compression test on a masonry specimen the load deformation diagram was recorded and a description of the observed fracture and cracking process noted. The subsequent analyses involved a comparison of the experimental results with analytical expressions.

First an overview of strength, stiffness and Poisson's ratios is presented. Then, the stress strain relationships and the failure process are discussed. The σ-ε diagram of a test can be described as a second degree parabola, with the strength and modulus of elasticity as key parameters. The statistical comparison of the results and the quest for trends between several mechanical properties, like strength versus E-modulus, showed tendencies for these parameters in relation to brick and mortar properties.

Fracture processes of masonry specimens are given and a few attempts to measure overall deformation beyond the peak are discussed.
Mortar E-values estimated from the difference between the estimated unit and the measured masonry deformation gave an indication of curing and hardening conditions.
Lateral deformation measurements gave insight in the effects of head joints on the failure process. A delayed brick deformation and the effects of fissures in the brick-mortar contact area were observed.

6.1 Introduction

In this chapter, the compressive responses of various masonry types are analysed.
The goal of the research program was to obtain more insight in the role of the brick-mortar contact surface on the mechanical behaviour of masonry under compression, and to acquire a database to be used in numerical simulations.

Three series of tests were performed to:

a) investigate mechanical properties of general purpose masonry, (series A and B),
b) investigate the effect, more in particular, of the specimen's length (series B), and
c) establish the mechanical properties of thin layer mortar masonry, (series C).

The analyses involved a comparison of experimental results with equations provided by mainly the ENV 1996-1-1:1996 for group 1 units. The following analyses are performed.

a) the relationship between experimental compressive strength and results obtained with the equation for masonry compressive strength given in [ENV 96],
b) the relationship between compressive strength and E-modulus of masonry,
c) the shape of the σ-ε diagram for the tested types of masonry.

6.2 Masonry specimens

In this section the making of masonry specimens, the test program, the measurements and the loading procedures are discussed. The properties of the bricks and mortars are given in the Chapters 4 and 5 respectively.

6.2.1 Making and storage of the specimens

All specimens were made in the laboratory and then covered with plastic sheets for at least the first three days after building. After that, some of them were stored in a climate room under 20°C and 60% R.H., the rest was stored in laboratory conditions under approximately 10-20°C and 30-45% R.H.

Where needed, half units were cut using a water cooled diamond circular saw. After cutting, the units were air dried.

Units were moisturized as follows. Soft mud units (RW and VE) were submerged in water for as long as needed to obtain an absorption rate (AR) during brick laying of approximately 1.1 kg/m^2/min for VE units and 1.4 kg/m^2/min for RW units. Initially, extrusion bricks were moisturized to an AR = 0.5 - 0.7 kg/m^2/min but in later tests prewetting of bricks of this type with an IRA = 0.9 kg/m^2/min was refrained from. The high strength extrusion bricks were not moisturized at all. The RW units used for the TL walls had no pre-treatment, only loose sand was rubbed off.

As usual in practice, cord guiding was used to obtain level and in plumb masonry. Special attention was given to the complete filling of the head joints.

Figure 39 Some specimens, being built and stored in the laboratory

6.2.2 Test program and specimen sizes

In series A 170 specimens of various sizes and various brick and mortar combinations were tested. In series B the same kind of specimens was tested, however, mainly the length of the specimens was varied. Finally, series C comprised tests on 630 mm square, bi-axially loaded specimens in combination with tests on stack bonded, uni-axially loaded specimens. These specimens were made using thin layer mortar. In general, two or three specimens were tested for each parameter. The size of the stack bonded specimens allowed for detailed deformation measurements.

The choice for the size of these specimens was based on the experimental findings of Rao [RAO 69], Man [MAN 94], and as described by Drysdale [DRY 93].

The top and bottom bricks of the first dozen stack bonded specimens were ground smooth and level. Later, the specimens were capped with 10 mm mortar. It is assumed that this difference in boundary conditions had no effect on the observed properties.

The thickness of all specimens was equal to the width of a unit, approximately 100 mm.

The height equalled 320 - 340 mm, 500 mm or 630 mm. With a slenderness h/t > 3 a uni-axial stress situation occurs in the centre of the specimen, e.g. [VMF 96 and 97b].

Specimens series A

Table 14 presents the number of tests for the various mortar-brick combinations used in series A. In total 170 specimens were tested. For brick and mortar properties see Chapter 4 and 5 respectively. Figure 40 shows stack bonded specimens of series A with LVDTs attached and their position in the testing machine. The glued-in 3 mm diameter bolds, used in the early series – see [ROT 97] - are shown on the photo at the left hand side. Later, glued-on nuts were used.

The results of 170 tests on more or less similar specimens were combined in order to find trends for strength, stiffness, deformation behaviour and brick-mortar interaction.

Table 14 Brick-mortar combinations and number of specimens, series A.

recipe	brick type												
mortar	JB		JG			ER	VE		Csi		PO		total #
	b	s	b	s	h	s	b	s	b	s	b	s	
1:½:1½	3	3	3	3			3	3					18
1:½:2½		3		3		3		3					12
1:½:3			3	3	3								9
1:½:4½	3	3	4	6		3	4	6	3	3	3	3	41
1:½:6		3		3		3		3					12
1:1:6									3	3			6
1:2:9			3	19			6	11		3			42
1:½:9				3	3		3	3	3		3	3	21
1:½:4½*			3	3	3								9
total		18		68		9		45		18		12	170

Sizes: s = 210 x 100 x 340 mm^3 b = 430 x 100 x 340 mm^3 h = 100 x 100 x 500 mm^3

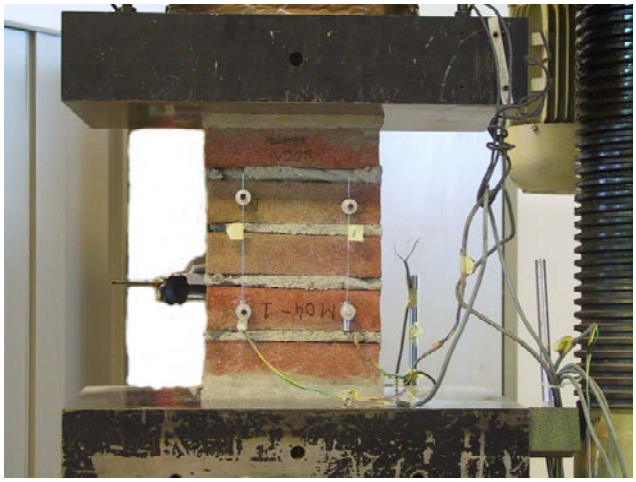

Figure 40 Stack bonded specimen of series A showing LVDT positions and specimen in 2.5 MN Schenck testing machine.

Specimens series B

The length of the specimens was the main parameter in series B. Table 15 presents the numbers of tested specimens for each boundary condition and their sizes. Series B consisted of eight specimens cut from clay-brick walls. These walls were made from soft mud RW-bricks using a 1:1:6 mortar. The RW-bricks had a compressive strength of $f_{c,Bo}$ = 17.0 N/mm^2 and an E_{Bo} value of 4000 N/mm^2 (Bolidt results). Poisson's ratio was 0.17 - 0.20. The mortar compressive strength according to NEN 3835 was 6.9 N/mm^2.

Table 15 Number of specimens, series B

Length	105	210	320	430	Σ
Number of tests	2	2	2	2	8

Specimen height 500 mm.

The loaded surfaces of the specimen were capped with a five mm thick gypsum layer.

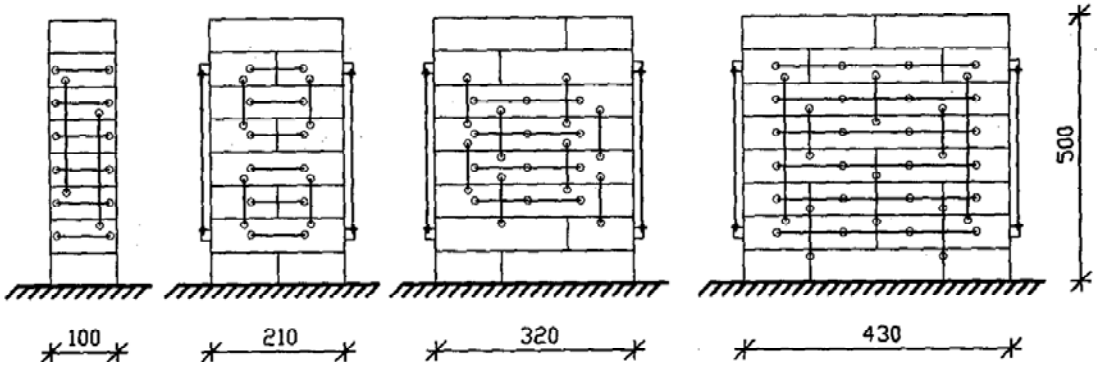

Figure 41 Specimens series B, sizes and position of measuring points

Specimens series C

In series C the height and length of the specimens were 630 mm. Table 16 gives an overview of the parameters used in series C and the numbers of tested specimens.
It was considered necessary that the specimen had at least two head joints per layer to be representative of a wall. Consequently, the specimen length equalled 630 mm, i.e. two and a halve brick. For symmetry reasons the height was taken 630 mm (10 layers) as well. These sizes were assumed to be large enough to produce a uniform stress distribution in the centre of the specimen. Stack bonded specimens (SBS) and wallette-like specimens (MTW) were cut from walls, see Figure 42, under angels of 0°, 22.5°, 45° and 67.5° with the bed joint.

Table 16 Number of RW thin layer mortar specimens, series C, wallette specimens were loaded equally in horizontal and vertical direction, SBS specimens were loaded uni-axially.

Head Joint	Bed Joint Orientation, MTW, 630 x 630 mm^2					SBS
	0	22.5	45	67.5	90	210 x 100 mm^2
Open	3	3	3	3	3	5
Filled	2	2	1	2	2	5

The specimens of series C were made of Rijswaard units. Table 5 gives the brick properties. Ankerplast BV provided the mortar for the series C specimens in two deliveries. Seven charges were made from the first delivery and four of the second. On average, the mortar compressive strength according to NEN 3835 was 29.5 N/mm^2 and 18.6 N/mm^2 respectively.

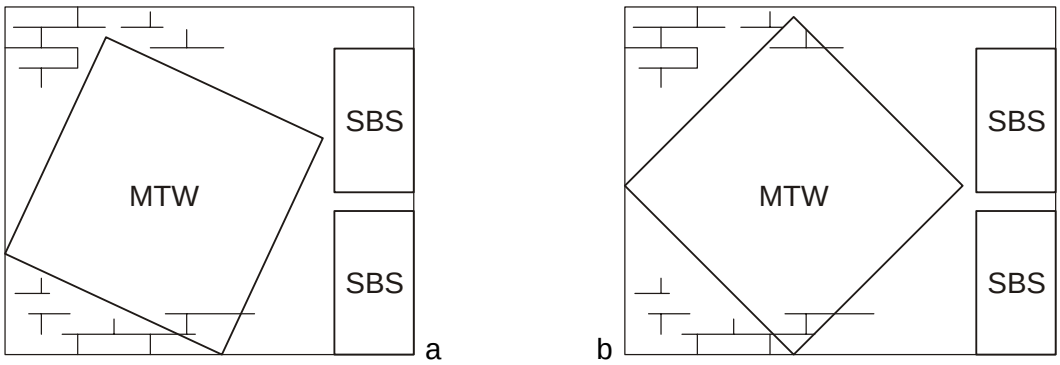

Figure 42 Cutting scheme for the specimens of series C with bed joint angles of 22.5° and 45°. Specimens with bed joint angles of 67.5° were cut similarly.

6.2.3 Experimental details

1. The experiments of series A

Using LVDTs, deformations were measured both vertically and horizontally. An overview of the positions where measurements on the stack bonded specimens were taken is given in Figure 43. The measurements on the specimens with other dimensions were done similarly.

Measurements were taken using LVDTs as follows:

a) between load platens,
b) over two joints, (gauge length 150 mm)
c) on the central brick vertically and
d) horizontally (gauge length 40 mm and 180 mm respectively).

Figure 44 right shows the 3 mm diameter bolts used for connecting the LVDTs. For later series, nuts were glued on the specimen. In a number of tests measurements were taken over an approximately 80 mm gauge length, including the edge of a unit, a joint, a unit, a joint and finally the edge of a unit again.

To investigate the behaviour of bricks separately, detailed measurements over 40 mm length with a clip-on instrument using strain gauges were performed, Figure 44.

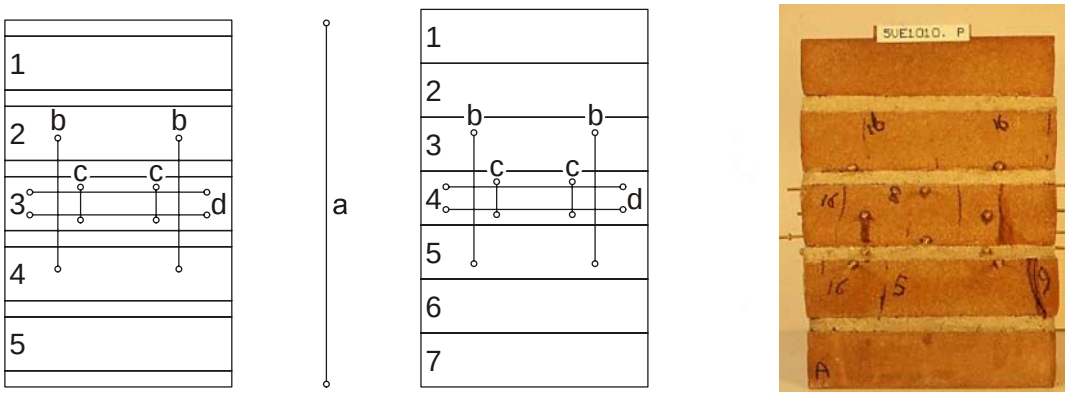

Figure 43 Scheme of the measurement positions on the five-brick stack bonded specimens in series A and a photograph after testing showing glued-in 3 mm diameter bolts. The seven brick specimen consisted of ground bricks with Bolidt adhesive.

The compression tests were performed in a Schenk servo-hydraulic 2.5 MN testing machine. The displacement speed of the top load platen was controlled using the built-in LVDT. Every specimen was pre-loaded to 50 kN and unloaded again to make the required adjustments and to control the equipment. This allowed the specimen to settle as well. Initial gaps and openings between the load platens and the specimen were closed and consequently, the initial part in the load deformation diagram was reduced.

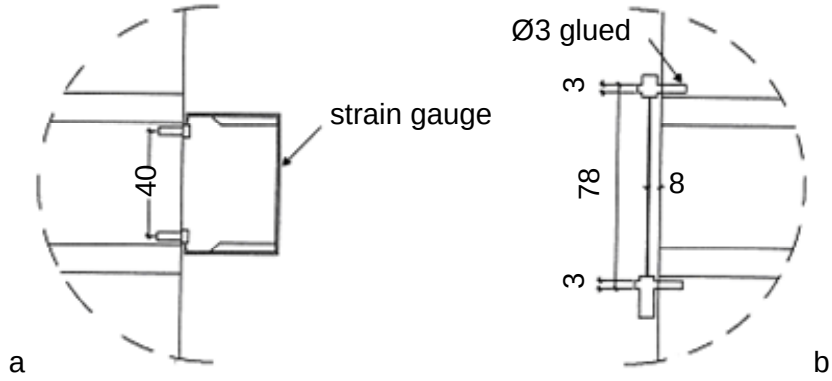

Figure 44 Instruments used to measure clay-brick deformation. a) Clip on instrument with strain gauges and b) LVDT mounted on glued in 3 mm diameter bolts, with 81 mm gauge length, measuring from brick edges over two joints. See also Figure 31b.

After this, the real test started. Usually it took about 15 to 30 minutes to reach maximum load. Testing was aborted when the load decreased below 80 % of the earlier recorded maximum load. This decrease often occurred within one electronic measuring cycle of 2 seconds.

2. The experiments of series B

In series B, LVDTs and Demec gauges [MORi90] were used to measure the deformations on more than 20 positions, both at the front and at the back. Figure 41 shows the position of the measuring points.

During the Demec measurements the moving speed of the loading platen was reduced to approximately one tenth of the original speed. A stand still of the load platen during a displacement controlled compression tests mostly results in a decrease of the load, or relaxation. By reducing the displacement speed of the load platen the decrease of the load is compensated by the increase due to the still, however slowly, moving load platen. Pre-loading and unloading was done as for the specimens of series A.

3. The experiments of series C

The stack bonded specimens (SBS) were tested in a 2.5 MN compression testing machine. Deformations were measured with two LVDTs on the front and two on the back. These tests were performed with a loading speed of 0.1 mm/min.

The wallettes of series C were tested in a specially designed and built test frame. The design was based on ideas from Page [PAG 88] and a 3D-test rig originally built to test concrete cubes, [MIE 84]. The columns and beams of this frame were made out of double HE300B steel profiles. Holes in these profiles allowed for simple and strong bolted connections.

Two times two 0.5 MN jacks were mounted in the frame, Figure 45. The load was transferred into the specimen using 'ball bearings' and steel profiles with a cross section of 100 x 100 mm^2. The four jacks (marked .5) were connected via a distribution unit to a 1 MN jack (marked 1 in Figure 45). This 1 MN jack was placed in a Schenck 2.5 MN testing machine and loaded, using the displacement control of this machine. Via the hydraulic system, all four jacks smoothly received the same oil pressure and consequently the specimen was loaded equally both horizontally and vertically.

In Figure 45, p is a sensor for the oil pressure, m is a manual oil pump and l indicates the position of the LVDTs on the specimen. The manual pump was used before the test started to bring the jacks in contact with the load platens.

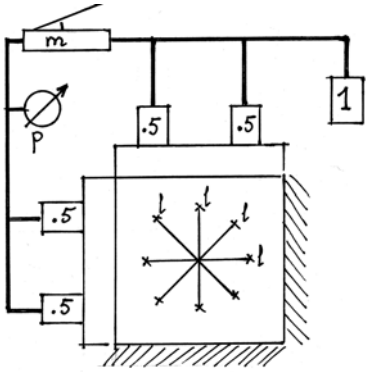

key to figure:
p = sensor for oil pressure
m = manual oil pump
.5 = 500 kN hydraulic jack
1 = 1000 kN hydraulic jack
l = LVDT length ~ 440 mm

Figure 45 Test rig and hydraulic system used for series C.

The opening between the load platens and the specimens was filled with a high strength pointing mortar after the specimens were positioned in the test set-up. The mortar compressive strength after 24 hours was at least 20 N/mm^2. Between the pointing mortar and the steel of the test machine, two layers of 0.05 mm thick Teflon sheeting and one layer of PVC sheeting were applied. The PVC sheeting protected the Teflon from damage. The Teflon was intended to reduce friction between specimen and steel loading platen.

In the wallete (MTW) tests, oil pressure in the system was recorded, in combination with the load applied on the 1 MN jack. Deformations of the MTW were measured with four LVDTs on the front and four on the back side, parallel and perpendicular to the bed joints and under an angle of plus or minus 45°.

6.3 Strength, modulus of elasticity and Poisson's ratio

Averaged compressive strengths of the masonry specimens of series A are presented in Table 17. The number of tests per combination is given in Table 14. No correction is made for size effect. Strong bricks in combination with strong mortar resulted in strong masonry, top left of Table 17. As expected, weak mortar in combination with weak bricks resulted in weak masonry. Detailed results of the tests of series A are given in Appendix A.5.5.

Table 17 Mean compressive strength of masonry specimens in N/mm^2 of series A

Mortar	brick type											
mix	JB		JG			ER	VE		Csi		PO	
design	b	s	b	s	h	s	b	s	b	s	b	s
1:½:1½	46.7	39.8	38.8	31.2			13.3	10.7				
1:½:2½		28.7		27.5		9.7		13.4				
1:½:3			26.9	21.5	23.2							
1:½:4½	23.7	20.9	18.2	15.8		8.3	11.1	9.1	19.4	19.6	5.4	5.1
1:½:6		20.5		16.8		7.4		10.2				
1:1:6									19.8	19.5		
1:2:9			9.0	8.8			7.5	6.5	14.9			
1:½:9				15.1	11.6		11.5	8.9		18.0	5.0	3.9
prefab			24.3	21.8	22.4							

Sizes: s = 210 x 100 x 340 mm^3 b = 430 x 100 x 340 mm^3 h = 100 x 100 x 500 mm^3

In Table 18 averaged compressive strengths and E-values of the specimens of series B are presented in combination with the width of the specimen, the height and the number of tests. E values were obtained with LVDT measurements and, in some cases, with a Demec gauge [MORi90]. The results of the latter were systematically smaller than the LVDT results. This may be because the Demec gauge covered relatively more 'joint' than the LVDTs. The 100 mm gauge length of Demec included two joints, 12.5 mm each, compared to the 375 mm LVDT gauge length, covering six joints. For Demec the joint-brick ratio was 1:3, for the LVDTs it was 1:4.

Table 18 Averaged compressive strength, E-modulus and Poisson's ratio of series B

width	number	height	$F_{c,mas}$	E_{LVDT}	E_{Demec}	ν
mm	of test	mm	N/mm^2	N/mm^2	N/mm^2	--
105	2	500	11,1	3300	3000	0,13
210	2	500	12,4	3900	3000	0,18
325	2	500	13,2	4100	3500	0,15
420	2	500	13,6	4000	3200	0,23
Avg.			12,6	3800	3200	

In Table 19 the strength in relation with the bed joint orientation of the specimens of series C is given. For comparison, the results of stack bonded specimens (SBS) are given. In this series, the effect of the loading direction on deformation was not so strong, therefore only an averaged value of the modulus of elasticity is given, both for open (non-filled) and filled head joint specimens.

Table 19 Averaged strength and E-values in N/mm^2 of wallettes.

Averaged strength (N/mm^2) versus bed joint orientation.

head joint	bed joint orientation to vertical axis											
	0		22.5		45		67.5		90		avg	
open	9.5	(3)	9.8	(3)	10.4	(3)	11.1	(3)	9.9	(3)	10.1	(15)
filled	12.9	(2)	11.3	(2)	7.9	(1)*)	11.7	(2)	12.3	(3)	11.6	(10)

Averaged strength and E-values (N/mm^2)

head joint		avg		[ENV 96]	SBS
open	strength	10.1	(15)		11.5
filled		11.6	(10)	10.0	13.4
open	E-values	5600			2990
filled		6500			3770

*) This specimen had poor bed joint filling.
Number of tested specimens between brackets ( ).

6.4 Measured versus calculated compressive strength

Building codes present expressions for the prediction of masonry strength, on the basis of the compressive strengths of the comprising units and mortar, as discussed in section 3.1.1. Reasonable consensus exists about the way safe masonry compressive strength values can be established (or better: estimated) for design purposes, using the tables or equations given in the codes. The following Equation (15) for the characteristic compressive strength of masonry according to Eurocode 6 [EC6 96] is appropriate for most types of masonry:

$$f_{c,k} = K\, f_{c,bri}^{\alpha}\, f_{c,mor}^{\beta} \qquad (15)$$

in which:

$f_{c,k}$ = characteristic masonry compressive strength

$f_{c,bri}$ = mean unit compressive strength of six units, corrected for the dimensions according to [EC6 96].

$f_{c,mor}$ = averaged value for six compression tests

In the 1996 version of the Euro code [EC6 96], the constants in Equation (12) are K = 0.60, α = 0.65 and β = 0.25 respectively for masonry of solid clay bricks. The version dated 2002 [EC6 02] prescribes the following values K = 0.55, α = 0.70 and β = 0.3. The

latter results in a 20 to 30% higher value for the estimated strength, compared with the 1996 version of EC6. In *NEN 6790:2004_concept 2004-08-11* [NEN 6790] the [EC6 96] values are given.
In Figure 46 the calculated value of $f_{c,k}$ is plotted versus the measured results of series A. The 'ideal' relationship is plotted as a dotted line as well.

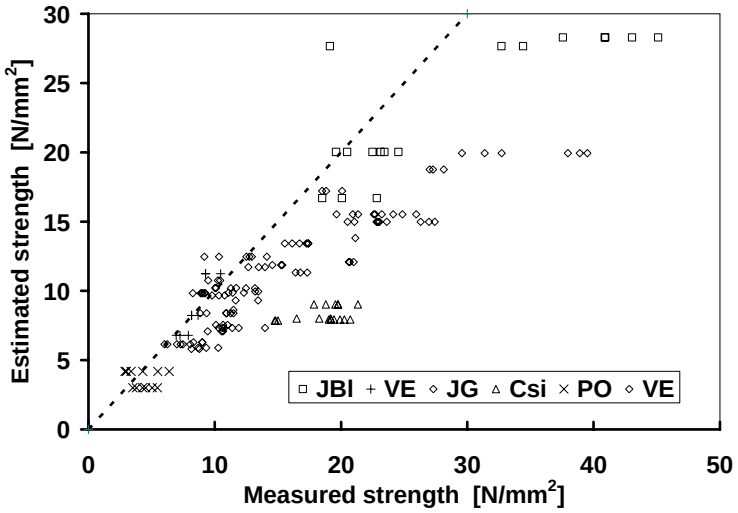

Figure 46 Estimated acc. [EC6 96] versus separately measured masonry compressive strength. A characteristic value versus individual results of experiments.

The basic assumption for establishing masonry compressive strength according to codes is that the result should never overestimate the actual strength, i.e. the measured strength should be larger than the calculated strength. In 87 % of the 170 test results in Figure 51 the estimated value was indeed conservative with the EC6:1996 parameters used in Equation (15).

Equation (15) shows that the most efficient way to improve the compressive strength of masonry is to use units with a higher strength. The effect of using a stronger mortar is much smaller. According to Equation (15) a mortar twice as strong will result in an increase of masonry strength of only 19 %. Consequently, the use of mortars that are too strong has little benefit.

For thin layer mortars the effect of mortar strength is not even taken into account, as shown by the next equation from [EC6 02]:

$$f_{c,k} = K * f_{c,bri}^{\alpha} \qquad (16)$$

with: K = 0.55 and α = 0.85.

In this test series however, the joint thickness was approximately 4 to 5 mm, while [EC6 02], refers to joint thicknesses smaller than 3 mm. Furthermore, the joints were not completely filled; the amount of filling varied considerably and no correction was made for the height over thickness ratio.

The way of filling the TL joints was similar to building practice where, for esthetical reasons, some recess is made by leaving the mortar free from the front of the facing masonry. In this way, the wall remains clean. Thus, real construction conditions were simulated.
The bending of the specimen due to eccentricities caused by the unfilled parts of the bed joint affected the results as well.

The general trend is that by using brick and mortar compressive strength, masonry strength can be estimated. Using the [EC6 96] equation, the strength is often underestimated. Better information can be obtained by doing tests. This is allowed in codes.

6.5 Deformation behaviour

6.5.1 General stress strain relationship

As an example, the measured strains are plotted versus the applied vertical stress in Figure 47. In general, the load deformation relationship can be subdivided into four parts, a, b, c and d, Figure 47, such as for concrete [DafSt 260] and [REI 85].

a) Due to the closing of gaps, fissures and openings, most of the load deformation diagrams showed an initial part. In Figure 47 this initial part can be recognised as a less steep part of the graph for the lower loads.

b) The initial part was followed by a more or less linear part b. Between approximately 15 and 80% of ultimate load the load deformation diagram was smooth and almost linear. This part was used for establishing the modulus of elasticity.

c) For loads above approximately 75 % of ultimate load the graph becomes non linear due to cracking. At the end of some tests, parts of the units came loose. In cases where LVDTs had been mounted on these parts, the gauge length changed in an uncontrolled manner and readings were no longer reliable.

d) After the maximum load is reached, the slope of the load deformation diagram changes considerably.

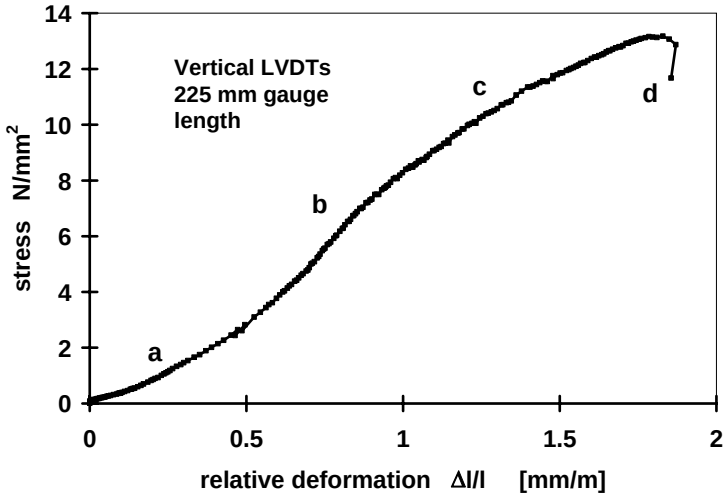

Figure 47 Example of a stress-strain diagram with phases a, b, c and d. Strain (relative deformation, Δl/l) measured in vertical direction.

6.5.2 The shape of the stress strain relationship for masonry.

For design purposes it is necessary to have a, preferably simple, mathematical description of the stress strain diagram. The results of the tests of series A were used to investigate whether the stress strain relationships could be represented as a second degree parabola like:

$$\sigma_r = A\,\varepsilon_r + B\,\varepsilon_r^2 \qquad (17)$$

where σ_r is the stress ratio, i.e. $\sigma_r = \frac{F}{F_{max}}$ with ε_r is the strain ratio i.e. $\varepsilon_r = \frac{\varepsilon}{\varepsilon_{90}}$ and ε_{90} is the strain that occurred when $\sigma_r = 0.90$. An example graph is given in Figure 48.

Only the smooth part b, approximately between 15-20 % and 80 - 90 % of failure load was used to establish the parameters A and B for each specimen separately. The least squares method was used to find the best fit as described in Appendix A.1.

On average, A equalled 1.32. Then, B equalled -0.42 because the lines were fit through the origin and the point: $\sigma_r = 0.9$ and $\varepsilon_r = 1$. Except for a few extreme values it showed that: $1 < A < 1.55$. Each σ-ε relationship gave a reasonable fit with $R^2 > 0.90$.

No relationship with strength or unit type used was found, while specimens of the same unit-mortar combination gave both high and low values for A. The position and height of the peak follow from the best fit according Equation (17). On average, the peak is positioned at $\varepsilon_r = 1.57$ and $\sigma_r = 1.035$.

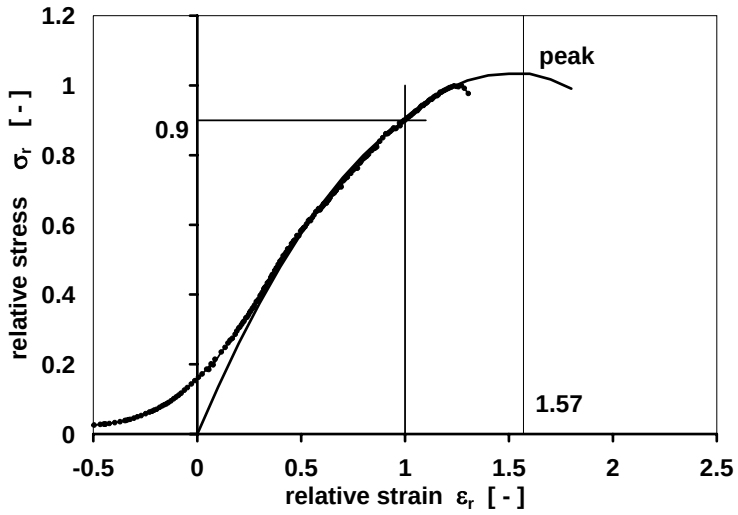

Figure 48 Stress strain diagram with relative values, $\sigma_r = F/F_{max}$ and $\varepsilon_r = \varepsilon/\varepsilon_{90}$

The parameters A and B in Equation (17) are based on the results of 170 tests, including 18 calcium silicate specimens for comparison.

To describe the overall σ-ε diagram in a more familiar way, the parameters A and B of Equation (17) were rescaled. Therefore, the ε_r values were divided by 1.57 which equalled the ratio between ε_{90} and ε_{max}.

After rescaling Equation (17) the overall σ-ε diagram can be represented by a parabola as follows:

$$\frac{\sigma}{f_c} = 2\frac{\varepsilon}{\varepsilon_{max}} - (\frac{\varepsilon}{\varepsilon_{max}})^2 \qquad (18)$$

with ε_{max} as the strain at ultimate load

This relationship is also given by Hendry [HEN 90]. As a restriction it should be mentioned that it concerns short term tests on laboratory made masonry.

6.5.3 Modulus of Elasticity for masonry

In the previous section the shape of the (parabolic) σ-ε diagram was studied. Using the same results, E_{33} values were established using a linear best fit as explained in Appendix A.1. In Figure 49 the resulting E-values are plotted versus compressive strength for each test separately, and some trend lines are drawn.

Using linear regression, the following relationship between E_{33} and $f_{c,mas}$ is found with a correlation (R^2) of 0.55:

$$E_{33} = 2140 + 340*f_{c,mas} \qquad (19)$$

This relationship is represented as line a in Figure 49.

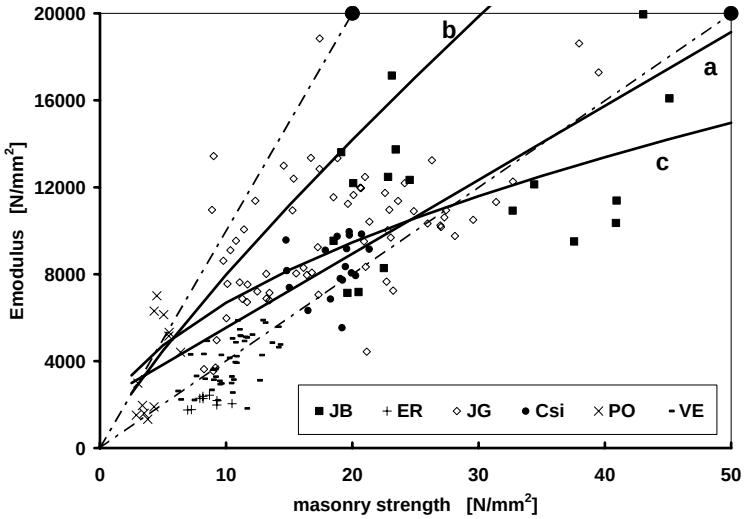

Figure 49 E_{33} versus masonry compressive strength, lines indicate trends

The following relationship (20) originates from NEN 6790 and is based on the averaged compressive strength in stead of the characteristic strength

$$E_{33} = S \bullet f_{c,mas} \qquad (20)$$

with S = 700.

The ratio between characteristic and averaged value is taken 0.7 based on a C.o.V. of approximately 20 %. With a C.o.V. of 20% the 95%-upper value for S according to NEN 6790, equals approximately 1000 and the lower value approximately 400.

Figure 49 shows that NEN 6790 overestimates the modulus of elasticity for the tested combinations. It is emphasized that this conclusion depends on the way “the” modulus of elasticity and “the” compressive strength are established or defined.

A ratio between E modulus and strength of S = 500 to S = 550 was found by Wolde Tinsae [WOL 93] based on an extensive literature review.

Salin [SAL 71] gave a ratio of S = 700. The most extreme ratios between E modulus and strength - S = 210 respectively S = 1670 - were found by Drysdale et.al. [DRY 93]. These results were based on an extensive study in the USA, with test results of many kinds of brick masonry.

For masonry made of concrete units [DRY 93] found the somewhat less extreme values of S = 400 and S = 1290. The tendency that E modulus increases less with higher strength can be represented using the exponential functions of Hendry:

$$E_{mas} = 1180 \bullet f_{c,mas}^{\ 0.83} \qquad (21)$$

$$E_{mas} = 2116 \bullet f_{c,mas}^{\ 0.50} \qquad (22)$$

[HEN 90], which are shown in Figure 49 as line b and c.

The size of the specimen has only a small effect on the E-modulus for the relatively slender specimens ($h/t > 3,5$) which were used.
The averaged stiffness of a small specimen may be assumed to be equal to the averaged stiffness of walls, as shown by tests on small and large specimens (shrinkage tests in [RAI 96] and shear tests in [VMF 93]). However, the duration of a test affects the result. Under dynamic loading the stiffness is higher, in long duration tests the stiffness will be lower due to creep effects.

Masonry stiffness varies considerably with strength, as shown by the large number of relationships found in literature. The presented relationships between $f_{c,mas}$ and E_{33} are found using quadratic best fit procedures for a cloud of points. Consequently, deviations for a (small) series may be considerable. The effect of high and low values should be studied in situations with a high sensitivity for material stiffness. Performing a series of tests can take away uncertainties.

6.5.4 Lateral deformation

The lateral brick deformation in stack bonded specimens was measured over a gauge length of 150 mm, see Figure 43. It was difficult to establish a Poisson's ratio from the results because lateral deformations started at various load levels. Initially, the deformation in the length direction of the brick (lateral to the load) is very small. The brick deformations differ considerably from the assumption based on a uniform stress distribution. Table 20 presents the Poisson's ratios obtained from measurements on units in the centre of stack bonded masonry and Bolidt specimens. To obtain the Poisson's ratio, the measured deformation was divided by the axial deformation that could be expected on the basis of the applied external load and uniform stress distribution, using the E-values from Bolidt tests.

Table 20 Mean Poisson's ratios for brick.

Type of brick	E_{bri} N/mm^2	ν a	ν b
VE	6050	0.14	0.14
JG	16700	0.28	0.28
JB	15400	-	0.19
KZ	13400	0.17	0.20

a) in masonry prisms made with 1:2:9 mortar and
b) in Bolidt specimens

The relatively small difference between the result from masonry and Bolidt specimens indicates that there is not a tensile splitting action yet at the stress level at which the Poisson's ratio was established (approximately 50% of the estimated strength).

For comparison, lateral deformation measurements were done on calcium silicate specimens [CUR 193]. Deformations were measured length wise (perpendicular to the loading direction) at the front and back side of the specimen and through holes in thickness direction, Figure 50.

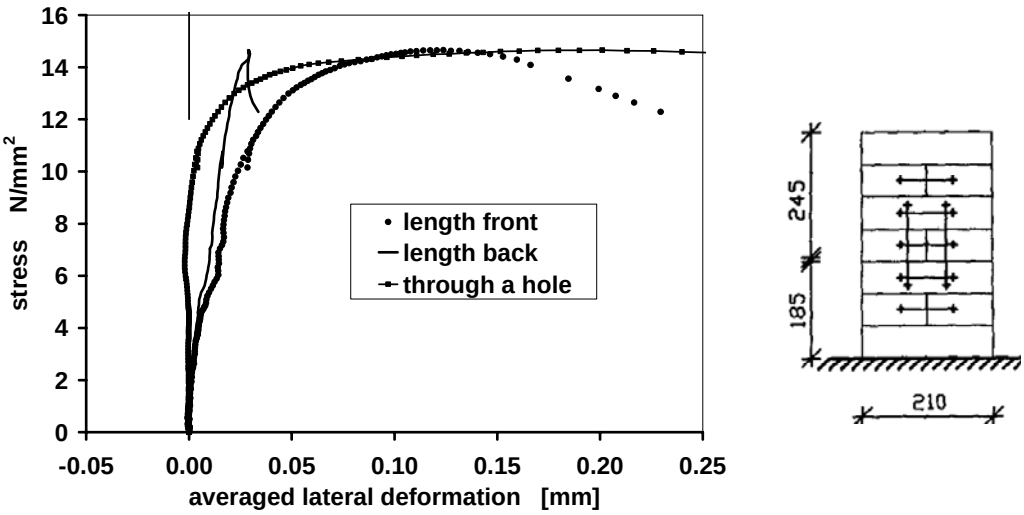

Figure 50 Averaged deformation in lateral (horizontal) direction of a 210 x 440 x 100 mm^2 (l x h x t) stack bonded specimen, tested with Teflon interfaces [CUR 193].

The results showed clear differences for measurements over head joints and measurements on one brick. This is indicated by the graphs in Figure 50 where the applied stress is plotted versus the deformation in lateral direction. Measured over a head joint, deformation is constant (vertical line), measured on a brick a much more fluent relationship was recognised.
Measurements in thickness (smallest) direction through a hole in the specimen are quite small compared to deformations in the longest lateral direction. Usually they are negligible until cracking starts. This image is similar to that of clay brick specimens.

Figure 51 shows large differences between measurements over a whole unit (smallest values) and over a head joint [CUR 193]. Averaged results of two times three LVDTs are used. Deformations were measured length wise (perpendicular to load direction) at the front and back side of the specimen and in thickness direction through holes in the wallette.

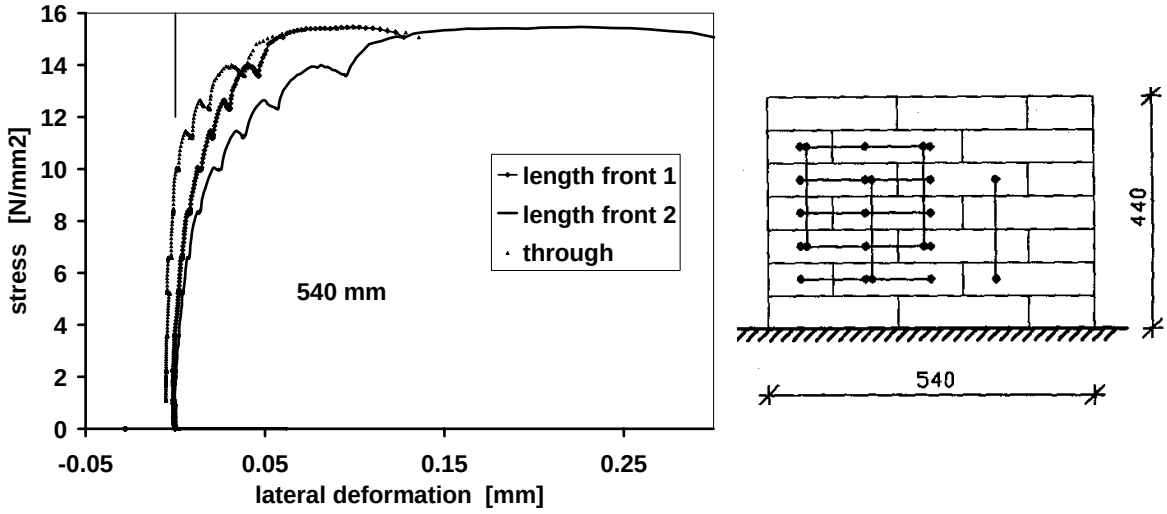

Figure 51 Averaged deformation in lateral direction of a 540 mm x 440 x 100 mm^2 (l x h x t) wallette tested with Teflon interfaces.

Results of lateral deformation measurements should be used carefully. Differences between lateral deformations are larger than those between vertical deformations. Often, only small lateral deformations were measured until, at loads of approximately 75% of failure loads, cracking started. Lateral deformations (strains) in length and thickness direction of a wall are unequal. This is confirmed by measurements through a hole drilled in the centre of the specimen as shown in Figure 50 and Figure 51.
These measurements also show that lateral deformations - Poisson's ratio - depend on the sizes of the specimen and the measuring direction. .

6.5.5 E-modulus of mortar in masonry specimens

The E-modulus of the mortar in the specimens (mortar hardened between bricks) was established by subtracting the proportion of the brick deformation (Δl_{bri}) from the measured masonry deformation (Δl_{mas}), as proposed by Drysdale et.al. [DRY 93].

$$\Delta l_{mas} = \Delta l_{bri} + \Delta l_{mor} \tag{23}$$

which results in:

$$\frac{h_{mor}}{E_{mor}} = \frac{h_{bri} + h_{mor}}{E_{mas}} - \frac{h_{bri}}{E_{bri}} \tag{24}$$

The deformation over a joint was also measured, as indicated in Figure 31b.
It is assumed that the brick deformation was linear with the applied load. In a few cases this resulted in (extremely) high or small E_{33}-values for the mortar. This effect was attributed to the fact that all (measurement) errors and uncertainties are assigned to mortar behaviour. Uncertainties are, for example, the assumption that brick deformation in a piece of masonry is the same as in a glued Bolidt specimen and that stresses are evenly distributed.

In Figure 52a, b and c the thus established E_{33} values of the mortars are plotted versus mortar prism compressive strength (acc. NEN 3835). Each group of points in the vertical direction are the results for the same kind of mortar.
The effect of curing conditions on the properties of mortar that hardened in masonry is considerable, Figure 52. The results of soft mud (VE) and extrusion (JO) bricks are given in separate graphs. $E_{33,mor}$ values are more or less comparable for both soft and strong mortars, that cured between this type of brick. For JG bricks, $E_{33,mor}$ in general is higher. It is assumed that mortar properties are affected by brick-mortar interaction, i.e. the brick-mortar-interface and fissures.
Table 21 presents the E_{mor} values obtained from masonry specimens. These results are more conclusive than Figure 52. It shows that for high mortar strengths, mortar stiffness depends on the bricks between it has cured.

No relationship between $f_{c,mor,NEN3835}$ and $E_{33,mor}$ was found. As discussed earlier in Chapter 5, the prism compression test (acc. NEN 3835) only gives the resistance of the mortar, but cannot be used for qualification; the test results (acc. NEN 3835) cannot be used in computer simulations of masonry behaviour. For that purpose, mortar should be tested separately and specimens should harden in conditions similar to those in practice, i.e. to the situation in a real wall. To measure this kind of mortar deformations ESPI was used as discussed in Part 3.

Table 21 Averaged E_{mor} in N/mm^2, of mortar cured in masonry specimens, calculated using the deformation measured over 120 mm.

	brick type →	VE	VE	JG	JG	JB
Mortar	specimen length, mm	430	210	430	210	430
1:½:9		1090		1770		
1:2:9			*2860		*14900	
1: ½:4½		1950	*1410	4510	*13300	5320
1: ½:1½		2120		12010		9330
* prefabricated industrial mortars, the rest: laboratory made mortars						

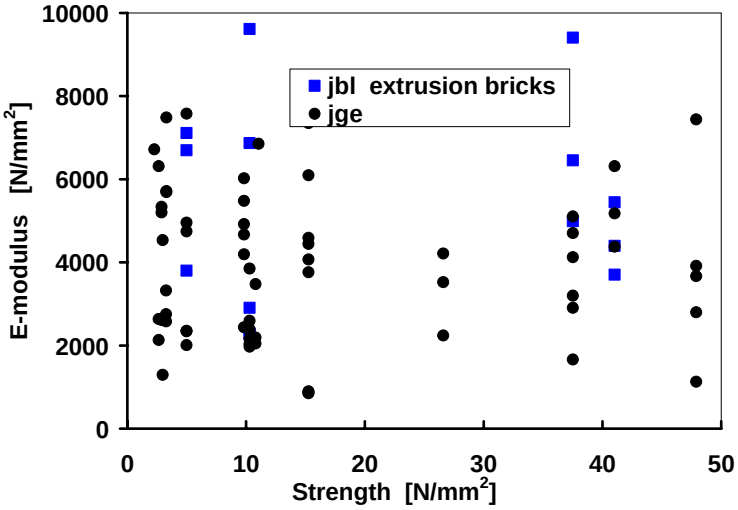

JG extrusion brick

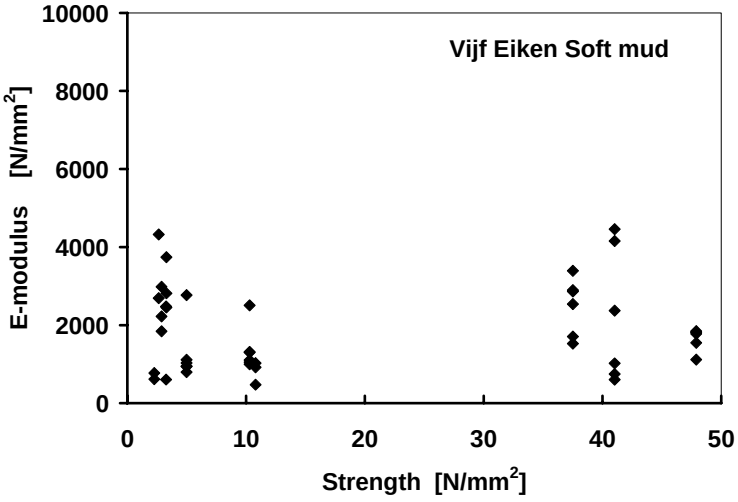

VE soft mud brick

Figure 52 Mortar modulus of elasticity versus compressive strength. $E_{33,mor}$ values obtained from measurements on stack bonded specimens and estimated brick deformations using $E_{BO,bri}$. A large variation and no relationship between $f_{c,mor,NEN3835}$ and $E_{33,mor}$.

6.5.6 Behaviour of brick in masonry

To investigate the behaviour of bricks separately, detailed measurements were done on stack bonded specimens with a clip-on instrument using strain gauges, (Figure 44) In Figure 53 the results are plotted for Vijf Eiken (soft mud sanded bricks) and Joosten (extrusion wire cut brick). From this figure it was concluded that, in a number of cases, the instrument only started to react after a considerable load was applied. This means that the outer part of a unit does not deform, while the inside central part has to carry all the load. This is an indication of the effects of the pillow shaped bed joints, a reason for the further investigation described in Part 3.

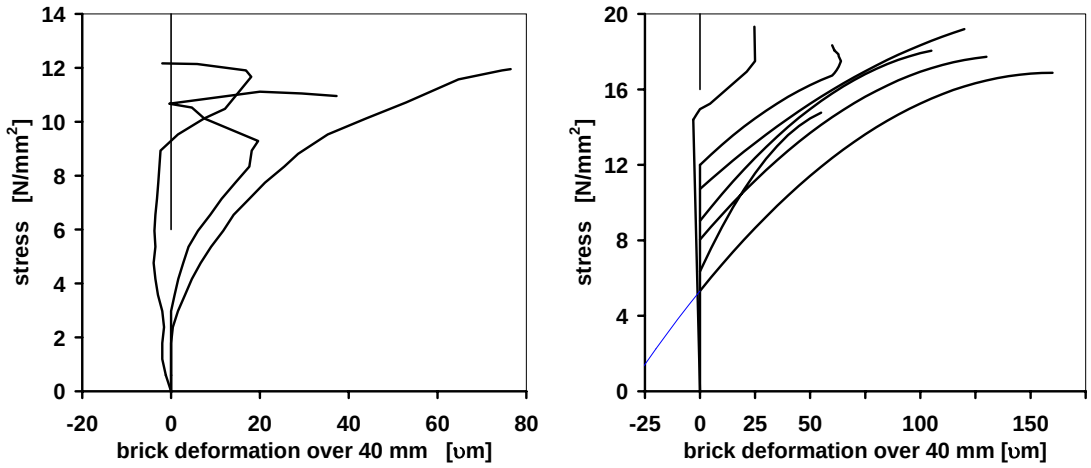

Figure 53 Brick deformation from detailed measurements using a clip on strain gauge instrument, VE and JG specimens.

6.6 Crack patterns

In this section the cracking behaviour of clay-brick GP mortar specimens of series A will be discussed and compared with the clay-brick wallette behaviour of series B. Then the fracture behaviour of the thin layer masonry wallettes loaded in two directions (series C) will be discussed.

6.6.1 Crack patterns of the specimens of series A

When cracking started hardly can be deduced from the load deformation graphs. In some cases one single LVDT recording acted odd. However, this could only be observed reliably after testing when analysing the results. At a load of approximately 75 to 85 % of failure load cracking became manifest, often only audible at first and visible later. Figure 54 gives an impression of observed crack patterns.

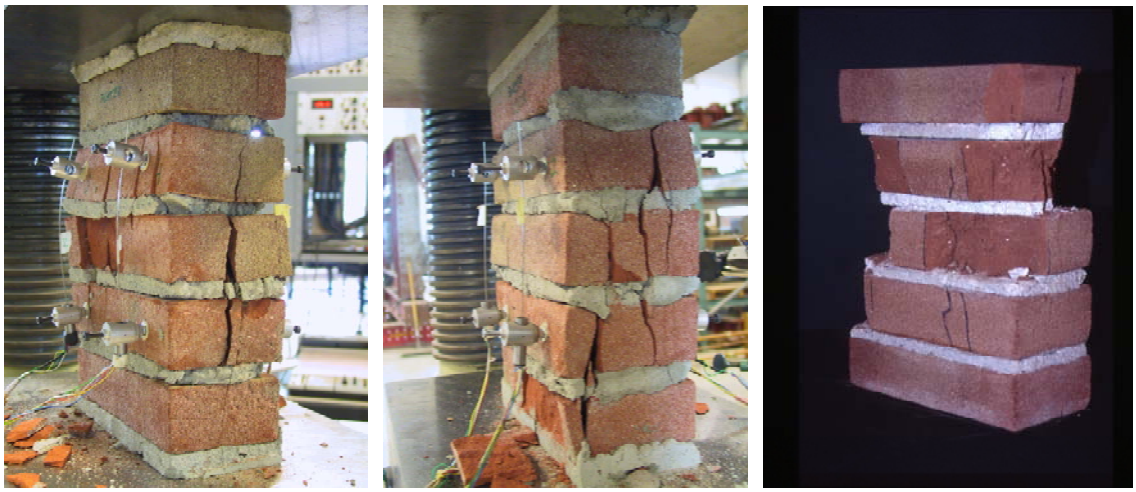

Figure 54 Stack bonded soft mud brick (RW) specimens built with general purpose mortar after testing beyond ultimate load. Splitting cracks and spalls are visible.

Especially in the case of the specimens made of harder extrusion bricks cracking noises were heard. In a single case cracking occurred very suddenly accompanied by a loud bang.

The almost straight cracks in each brick ran parallel with the loading direction. Spalls of 15 to 20 mm in thickness came apart, mainly in the second, third and fourth brick. At mid height, in brick number 3, second spalls were found subsequently, resulting in a pyramidal final shape. Over the joints, the crack often 'shifted' vertically over approximately the thickness of the joint. The structure of the brick became manifest, the 'vertical orientation' of the extrusion bricks was clear.

In specimens made of soft mud bricks the cracking process evolved more gradually. Spalls, separating from the specimen at the start of the cracking process are smaller. Also some fine grain shaped brick debris came free. Each time, a new load path is established inside the specimen when a spall comes loose. In some cases this can be recognised as a saw tooth line in the load deformation diagram. As an indication of the confining action of the load platens cracks sometimes ran under a 45° slope towards the corners of the top and bottom bricks. A pyramidal piece remained for the soft mud specimens as well. The material structure can be recognised in the crack surfaces.

6.6.2 Crack patterns of the specimens of series B.

The crack patterns of the RW-specimens are characterised by vertical cracks through head joints and bricks. Columns, half a brick wide (100 x 100 mm^2) developed, which finally cracked in two, following roughly the diagonal from bottom to top. Wedge shaped pieces remained. The head joint apparently had a considerable effect on the position where cracking started.

- One part of the 100 mm long RW specimens failed completely while the other part had hardly any visible damage. One pyramidal piece, approximately three bricks high and an number of smaller fragments remained.
- The 210 mm long RW specimens were cracked in two vertically, see Figure 55, on the right. One of the two parts failed completely as a result of a number of short, inclined cracks in a relatively small area of the specimen. In the example of Figure 55, this happened at the top, right. See the right front view in Figure 55.

Wedge shaped pieces remained and a similar pattern resulted as for the 100 mm wide specimens. This cracking pattern is contrary to the pattern of the specimens of series A, which had more diabolic shaped rest pieces. Probably, this deviant crack behaviour is caused by the load introduction via a thin gypsum layer instead of via one brick that was ground level.

- The 320 mm long specimens cracked vertically through the head joints which resulted in vertical columns that finally failed due to inclined cracking.
- The 430 mm long specimens had the same overall crack pattern as the shorter RW-specimens; that is, vertical cracks through head joints. In one of the specimens the left

top piece of 100 mm wide moved more than 2 mm horizontally while at the bottom right the material crumbled, see the left front view in Figure 55. A central part of two bricks wide remained and after the debris had been removed the inclined cracking surfaces ran under a slope of approximately 70°.

It may be clear that head joints affected failure. In longer specimens, the stiffness of the head joints is of importance, because then lateral expansion of the bricks is easier, Figure 50. The strength of such a specimen is lower than the strength of a specimen with stiffer head joint mortar. Usually, the mortar in the head joint is softer than bed joint mortar, the filling is less good at least. This was also recognised in the measurements of the lateral deformations depicted in Figure 50 and Figure 51.

Especially for the longer specimens it may have played a role that stress concentrations occurred due to the fact that the loaded surfaces were not absolutely level and that the capping thickness was not uniform over the whole surface. This may have caused peak loads at the edges of the top and bottom bricks.

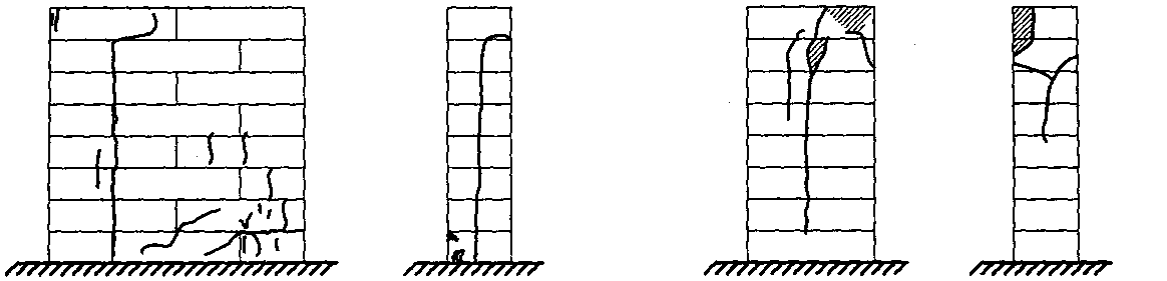

Figure 55 RW-specimens after testing. Left: front view and side view of a 430 mm long specimen. Right: front view and side view of a 210 mm long specimen

6.6.3 Crack patterns of the TL specimens of series C

The following three phenomena were observed in the failure process of the 630 mm by 630 mm TL-wallettes: a) Spalling of the bricks, with fragments of approximately 20 mm thick, b) bending of the specimen and c) vertical splitting of the specimen. Figure 56 shows remaining pieces after testing.

The following three remarks can be made.

a. As in practice, the joints were not completely filled to keep one surface of the wall clean. In this way, the recessed joints formed notches. Because a high strength thin layer mortar was used, it is assumed that stress concentrations occurred at the end of the mortar joint.

b. The joints were reasonably filled at the back of the wallettes. In combination with the already mentioned notch at the front side, the load was transferred with an eccentricity

of approximately 10 mm from the centre of gravity of each joint section. This caused the observed bending.

c. In specimens where the joints were better filled, less spalling occurred. These specimens were stronger. In those cases the more usual splitting failure could be observed.

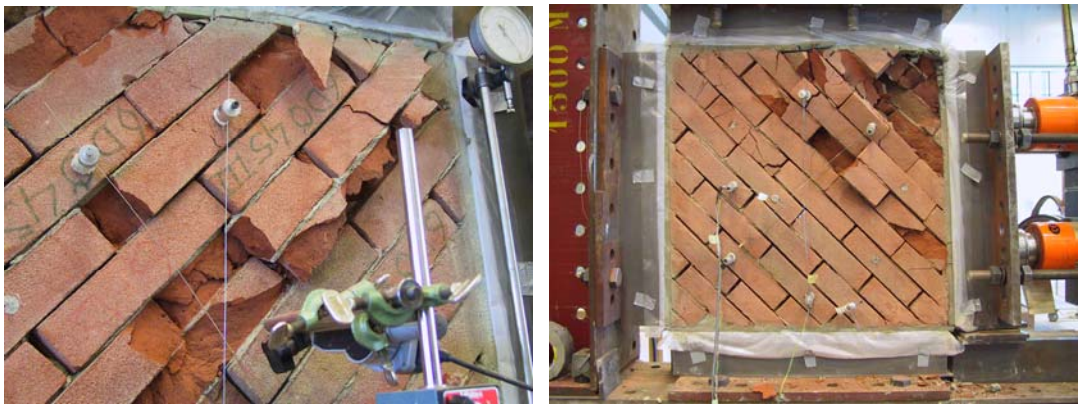

Figure 56 Remaining test pieces of thin layer mortar masonry after loading in two directions

The stress concentrations at the notch were confirmed by numerical simulations that showed that tensile stresses develop in the brick, as expected, [VMF 04]. The stress and strain distribution explained the observed spalling of the bricks. Averaged compressive stress in the bed joint equalled 12.69 N/mm^2 while the peak stress was 28,85 N/mm^2. The ratio between averaged stress and applied stress was 10.74/12.69 = 0.85, which is almost equal to the filling ratio. The tensile peak stress equalled 2.4 N/mm^2, the tensile strength of the bricks was 2.47 N/mm^2 see Chapter 4, Table 7.

6.7 Post peak behaviour.

In this section, post peak behaviour is discussed in more detail. In the discussion of cracking behaviour it was noticed that in some cases the LVDTs came loose from the specimen and consequently, their results were no longer reliable. Further, testing was aborted when the load dropped below 75 % of the registered maximum load to allow for the study of crack development. In this way, the specimen remained some coherence of the rest pieces. Even with this testing procedure, in a number of cases the specimens were completely destroyed.

When a structure is loaded over its maximum capacity it will fall apart completely, so stopping a test when the load has passed its maximum is sensible. However, in some situations, redistribution of the load is possible. For example, in a wall loaded diagonally in shear, it was observed that in the loaded corners brick and mortar crumbled and that the load introduction area consequently increased [VMF 93].

To allow for simulation of these effects in numerical simulations, knowledge of the post peak behaviour ('softening') is essential. To study this softening behaviour, three soft-mud-brick stack-bonded specimens were loaded in compression. The strains obtained from the results of LVDTs, are plotted versus average stress in Figure 57.

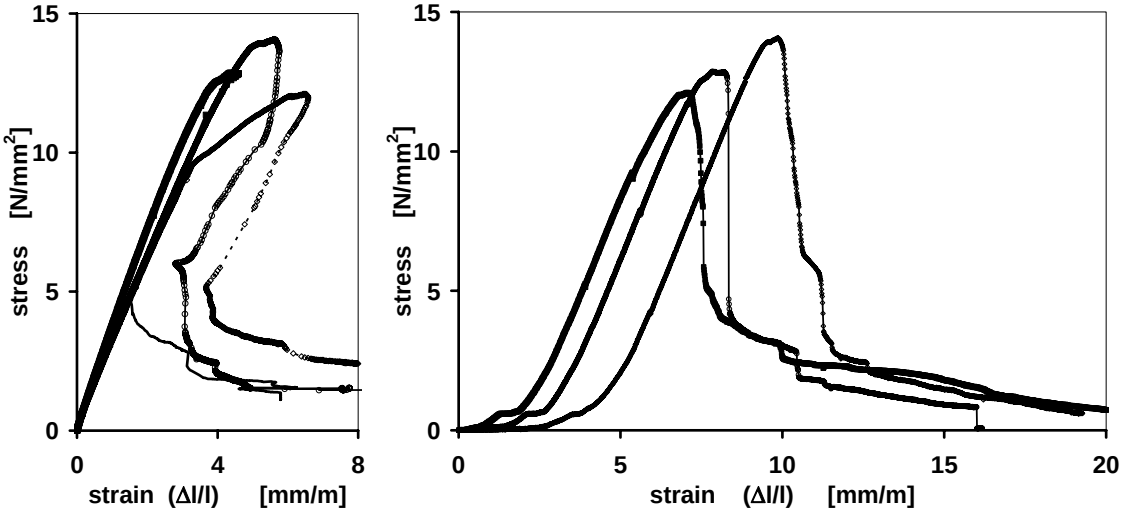

Figure 57 Stress versus relative deformation for three soft-mud-brick stack-bonded specimens. Results of LVDTs on the specimen (average of four, left) and an LVDT inside the machine (right).

Deformation was continued after the peak load was reached and testing was only stopped when the stress was below 1 N/mm^2. The displacement was controlled with the LVDT of the machine. The use of the LVDTs on the specimen to control the test was not possible because they could fall off prematurely. The three specimens behaved quite similar. In one test, a kink occurred in the measurements on the specimen itself. In the general observation with the LVDT inside the machine, that recorded load platen displacements, this effect could not be recognised.

The stress-strain diagram obtained from the results of the LVDTs on the specimen shows that after peak load relaxation occurred, including some snap back behaviour. The overall deformation however, obtained from the LVDT inside the machine, shows a steep drop back to a stress of approximately 3.5 N/mm^2 and then a slowly decreasing relationship for a large path. Each marker indicates one recording, and as recordings were taken every two seconds, an indication of failure speed can be obtained from Figure 57. This confirms that a parabolic approximation of the σ-ε curve according Equation (18) is not accurate after the peak.

6.8 Variation of axial deformation

Compression tests were carried out in a testing machine equipped with a spherical hinged top load platen. The freedom of rotation of this load platen allows for non parallelism of the surfaces of the specimens. In the beginning of almost every test the top load platen rotates, though, it was positioned – visually - parallel to the surface of the specimen. However, at a load of approximately 12 kN the play of the system was closed and further rotation prevented due to friction, Appendix A.2.3. Consequently, the increase of the rotation of the load platens is smaller for higher loads.

Specimens are not symmetric and systematic errors occur. Consequently, the load has some unintended eccentricity from the centre of gravity of the specimen. This is manifested by differences in measured deformations. The eccentricity will also be affected by the rotation stiffness of the spherical hinge, the rest of the structure of the testing machine and the bending stiffness of the specimen. The testing machine and the specimen will interact.
Differences in the results of the measurements of the four LVDTs mounted on the specimen showed to increase up to 15 % of the averaged values. From these results, load eccentricities were calculated, using double bending theory and assuming linear elastic behaviour. In addition it was assumed that the top load platen had settled at a load of 20 kN. By assuming that the material behaviour is linear elastic it is also assumed that all differences are caused by load eccentricity.
The largest eccentricity calculated from the strain differences equalled 5.4 mm in length direction and 0.5 mm in thickness direction.

The load platen displacement measurements also included the seam between the load platen and the specimen. After some initial effects, such as the mentioned ‘blocking’ at a load of ± 12 kN, the difference of the displacements of the corner points of the load platens in relation to each other shows to increase linearly with the load, which means that the eccentricity remained constant.

6.9 Discussion of the generalised stress strain diagram

For structural design purposes, the material strength, in combination with Young’s modulus and the shape of the σ-ε diagram is essential information, Figure 58.
The main result of a single compression test is the load deformation relationship, from which key values like the modulus of elasticity, the compressive strength and (if the set up allows for it) the post peak behaviour can be deducted. Besides that, fracture behaviour can be recorded by making notes and/or with a photo or video camera.
In this chapter, the results of 170 tests were compared and the relationships between the key values were established. A comparison with results from literature was made. Key values of each separate specimen of test series A are given in Appendix A.5.5.

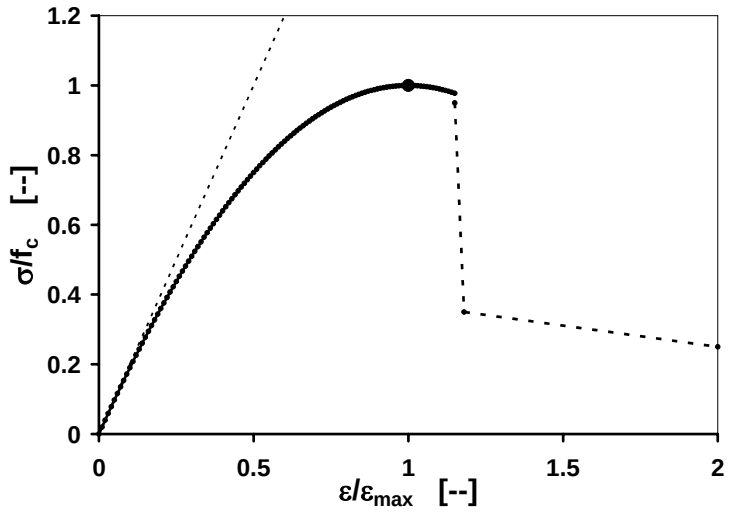

Figure 58 Generalized stress strain diagram, showing a parabolic part, the maximum value and post peak behaviour.

6.9.1 Prediction of masonry compressive strength

The general trend is that with given values for brick and mortar compressive strength, masonry strength ($f_{c,mas}$) can be estimated with Equation (15) [EC6 02].

Like with the similar approach of NEN 6790:1991 via tables, the strength for specific situations must be underestimated when the EC6 equation is used, while not all significant parameters are taken into account. Of course, the code will give a lower value approximation for safety reasons, because, code values have to be generally applicable for the many available unit en mortar types. Material safety factors, effects of test duration and other parameters should be used according to the applicable codes. As a better alternative, the strength, E-value and Poisson's ratio can be established with experiments. Both NEN 6790 and EC6:2002 provide for this.

6.9.2 The shape of the stress strain relationship

The σ - ε diagram under compressive loading can be described with:

$$\frac{\sigma}{f_c} = 2\frac{\varepsilon}{\varepsilon_{max}} - \left(\frac{\varepsilon}{\varepsilon_{max}}\right)^2 \qquad (25)$$

with $\sigma < 0.9\ f_c$

The ultimate strain ε_{max} follows from the strength, the parabolic shape and the modulus of elasticity. The shape of the tail is slowly descending after a steep drop.

6.9.3 The modulus of elasticity

The value for E can be estimated from the strength or from specific test results. As a tendency for the relationship between strength and E-modulus the following relationship, however different from the one given NEN 6790, was found:

$$E_{33} = 2140 + 340 * f_{c,mas} \qquad (26)$$

6.9.4 Experimental aspects

Three aspects are discussed.

a) Gauge length should be at least equal to two layers of masonry.

To be able to establish modules of elasticity and Poisson's ratios for masonry, the gauge length of the instrument should have a sufficient length. Otherwise, the behaviour is measured in too much detail, leading to much scatter in the results.

The number of measurements, in combination with gauge length determines the accuracy of the averaged results.

The stiffness of a specimen can best be judged using the results of sensors mounted onto the specimen itself. Measured load platen displacements may be disturbed by effects of the seam between specimen and load platen. On average, the results of the vertical deformation measurements on the specimen are consistent. However, differences between individual sensors on the same specimen may amount to a factor two to three. This is partly caused by unintended load eccentricities.

b) Deformations will vary around the outline of a specimen.

In each test the load platens will rotate for two reasons: load is not exactly concentric and consequently, the specimen is loaded in bending as well as compression. This causes deformation differences. From these deformation differences the load eccentricity may be computed.

Eccentricity effects should be taken into account when numerical simulations are undertaken. Then the load may be given a certain constant eccentricity from the beginning.

c) The coefficient of variation for compressive parameters

A coefficient of variation of 10 % for compressive strength should be taken into consideration. The C.o.V. on the modulus of elasticity should be 20 %. These values correspond with the values given by Lawrence [LAW 85].

In that respect, the number of the considered tests per specimen type was limited. However, the detailed measurements in the relatively large number of all tests gave a good indication of the scatter of the deformations measured on the surfaces of the specimens. A considerable deviation was found for each measurement separately, but on average, the resulting elasticity moduli and Poisson's ratios were consistent.

All conclusions are related to the type of solid clay-bricks used in this research.

Perforated bricks may give different results. Mortar properties depend strongly on curing conditions.

6.9.5 Course of a compression test

The following phases, as shown in Figure 59, are recognised in the failure process of masonry in compression. These phases coincide more or less with the phases a, b, c and d in Figure 47, page 67.

After an initial phase and a reversible linear elastic phase (a + b), local failure processes start (c) manifested by spalling of bricks and crumbling of mortar. Non-linear behaviour in the stress strain diagram becomes visible. Below 75 to 80 % no visual cracking is observed. Cracking noises indicate the beginning of cracking.

A key trigger for spalling was found to be the shape of the bed joint. In 12-15 mm thick GP-mortar joints, spalling occurred in chips of 10 to 15 mm thickness. The fissure of the pillow shaped bed joint induced peak strains. In TL-mortar joints, 3 to 4 mm thick, spalling was caused by the notch formed by the recessed joint. Then, the spalls had a thickness equal to the recess.

Phases in the course of a compression test
1) no visual cracking,
2) sounds / noises may be heard,
3) local cracking (start of non-linearity)
4) spalling, (shape of the bed joint)
5) increased spalling, vertical splitting into columns
6) shear of the columns.

spalls with a thickness equal to the recessing.

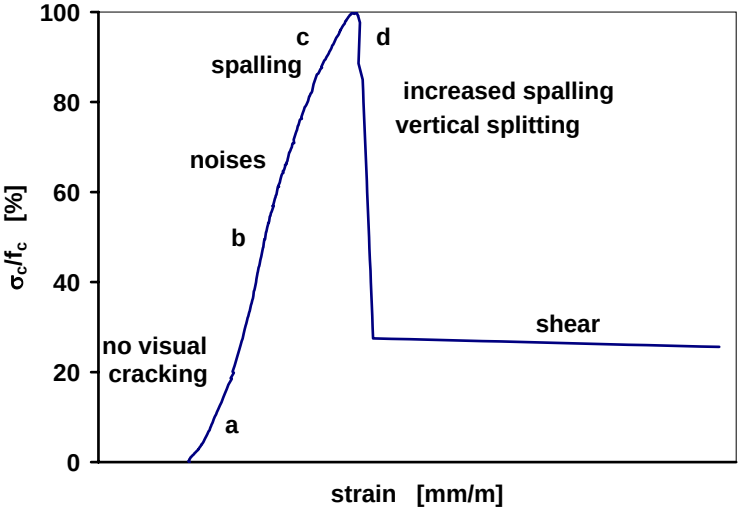

Figure 59 a) Phases in the failure process of a piece of masonry. b) Shear of a stack bonded specimen after spalling.

Subsequently, the reduced section of approximately 70 mm wide, shears diagonally under a 70° slope. The process may be affected by the boundary conditions of the test. When a gypsum capping was used, the top and bottom brick cracked, while these bricks were not damaged when a mortar capping was used. The head joints caused longer specimens to crack over the head joints.

After the peak load, increased spalling, vertical splitting into columns half a brick in section in longer wallettes and finally shear of the formed columns occurs. Head joints cause vertical splitting.

The following additional remarks are made.
a. The effect of lateral confinement could also be recognised in the crack pattern. Gypsum capped RW-specimens (length 210 mm or more) cracked vertically in thickness direction via the head joints. All specimens failed because inclined cracks developed in a small area as well. Specimens with head joints split over the full specimen height through these joints and, subsequently, the parts of approximately half the thickness sheared off under a 70° slope.

b. Specimens seem to be symmetrical, however, they are not. There is always some defect, on one side or the other and this activates the mentioned shear, as recognized by e.e. Vonk [VON 92] for concrete. In some processes shearing proceeds relatively slow, resulting in a long maximum load phase. This is usually the case in softer masonry, while masonry with well filled joints and high strength bricks fails more brittle.

c.The failure process of masonry prisms is similar to that of other stony materials like concrete and rock, [BAZ 94], [BAZ 97] and [GRA 70], but spalling of the unit is an additional effect in the failure process as a consequence of the layered structure. As long as only small spalls come loose from the surface of a specimen, a new way of load transfer is found.
The models discussed in Chapter 3 described failure and renewed load transfer, Figure 22 and Figure 23, page 27. In the experiments this effect is recognised as well. However, the causes are different. The models refer to the centre of the specimen. In the experiments, failure was initiated by spalling, followed by shear.

d. Post peak behaviour was studied in a few cases by continued testing much longer after passing the peak load, Figure 57. Actually, a special designed control system, using lateral deformations is required. As the shear process is dominated by lateral deformation due to increasing longitudinal deformation, lateral deformation controlled testing may be a useful idea, like in concrete [GEE 98]. However, this gives some complications in masonry, if the brick used to control the test spalls prematurely or not at all. In tri-axial testing the lateral load platen displacements can be used to control the test.

6.10 Conclusions

- In general, the compressive responses of the tested masonry types can be described with a second degree parabola ($\sigma < f_{c,mas}$).

  This outcome is based on a database which can be used in numerical simulations. However, due to the deviation in the results, only general trends can be given. The course of compression tests on masonry prisms is described in section 6.9.5.

- The brick-mortar contact surface played an important role on the mechanical behaviour of masonry under compression.

  A delayed reaction of the units (Figure 54) was observed.

  The LVDT readings varied, indicating that and uneven strain distribution, i.e. bending, occurred.

  Spalling occurred at the ends of the fissures (15 mm joints) or notches (3 mm TL joints).

- The compressive strength of masonry can be estimated with Equation (15).

  The relationship between experimental compressive strength and results obtained with Equation (15) for masonry compressive strength, [ENV 96], allows for the estimation of the compressive strength of masonry. For safety reasons, the estimation is conservative.

- A positive trend was found in the relationship between compressive strength and E-modulus of masonry, i.e. a higher E-value is found for stronger masonry.

- It was not possible to establish the modulus of elasticity of the mortar reliably.

Calculated results gave no correlation between mortar compressive strength (according [NEN 3835]) and mortar's E-value.

7 Test set up for brick-mortar interaction measurements

Abstract
In this Chapter the test set-up to study the brick-mortar interaction in detail is discussed. The ESPI system and its specific characteristics are explained together with the moving seating arrangement, developed to obtain appropriate results in combination with ESPI. The choice of the dimensions of the specimens is motivated and the method of specimen preparation discussed. The specimens were 25 mm thick pieces of masonry sawn from couplets, capped with gypsum.

7.1 Introduction

The main goals of the test program were to establish the brick-mortar interaction in compression and the behaviour of mortar and bricks separately in combination with the effects of joint imperfections due to the 'brick laying process' and shrinkage.
Joint deformation can be measured by LVDTs from the edge of one brick over the joint to the edge of the next brick. The results, as discussed in section 6.5.6, only gave some indication of the E-moduli of the mortar.

Better measurement results can be obtained using ESPI, a laser speckle technique which allows for the observation and accurate measurements of the deformation of surfaces of approximately 100 by 100 mm^2. The ESPI measuring equipment is discussed first.

To allow for measurement of the load transfer through the specimen, the test machine was provided with the moving seating arrangement presented in section 7.3. The applied boundary conditions are discussed in section 7.3.2.
The choice of the size of the specimens (a 25 mm thick, 100 mm by 115 mm slice of a two brick one joint couplet) is explained in section 7.4.

The results of concentric and eccentric tests are discussed in Chapters 8 and 9 and those on pointed specimens in Chapter10.

7.2 The ESPI measuring equipment

7.2.1 Introduction

ESPI is the abbreviation for **E**lectronic **S**peckle **P**attern **I**nterferometry [JON 83]. It is a non-contact, 3-D, displacement measurement system based on optical interference techniques that allows for the observation of deformation of surfaces. The ESPI instrument is presented in Figure 60.

The major advantage of using a laser-speckle system like ESPI over systems like LVDTs or Demec is that the displacement of a (theoretically infinite) number of points of a certain area can be observed while LVDTs only measure the displacement of two points in relation to one another.

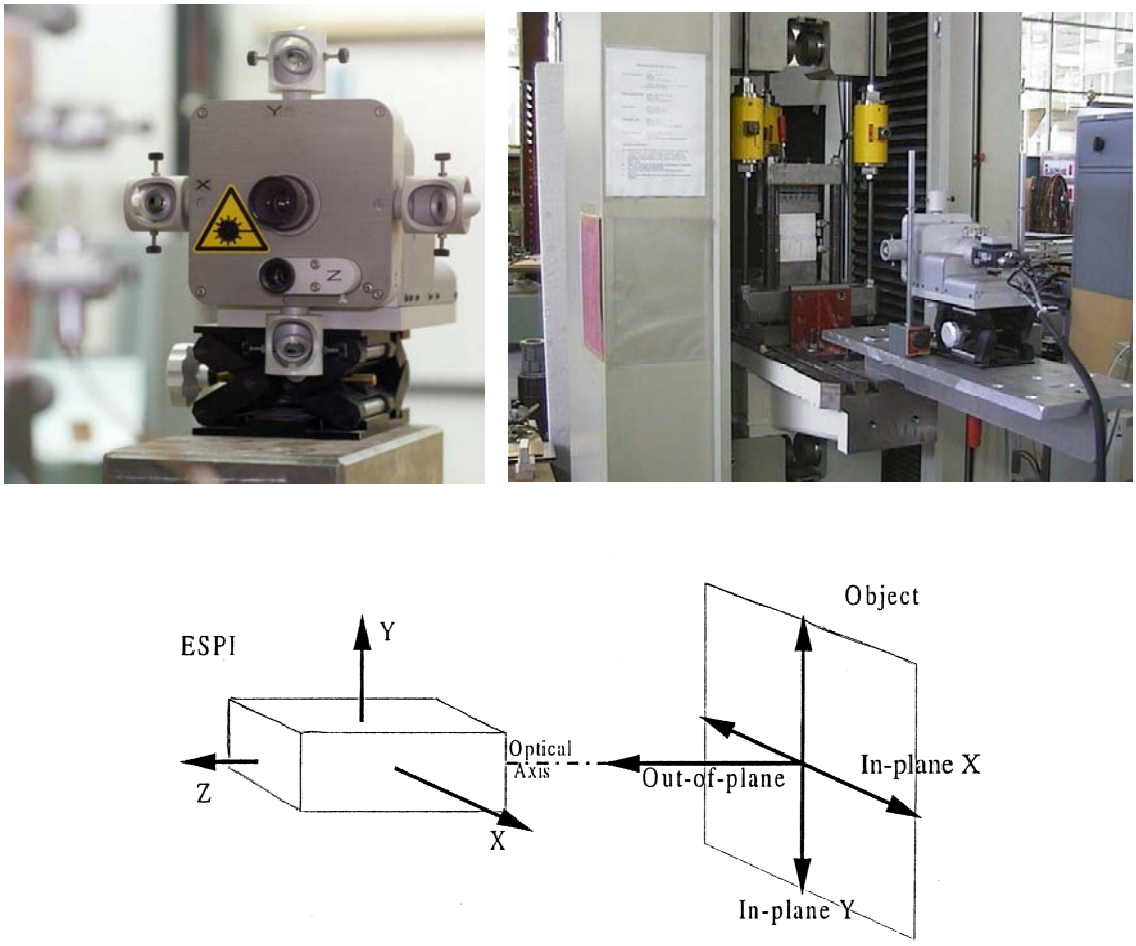

Figure 60 Front and side view of the ESPI apparatus, directions

7.2.2 Working of the ESPI system and method of data analysis

The working of the ESPI system and the method of data analysis will be explained in this section using the results of a concentrically loaded specimen as an example.
ESPI tests were performed on couplet-slices of 25 mm thickness. The front surface was observed. This surface measured approximately 100 mm wide (the width of the bricks used) and approximately 115 mm high, (twice the height of the brick and one joint).

The digital camera of the ESPI system can be used to take a photograph of the specimen, see Figure 61. A relationship between the real dimensions of the specimen and the number of pixels in the photograph can be established. This relationship is needed when measurements are analysed.

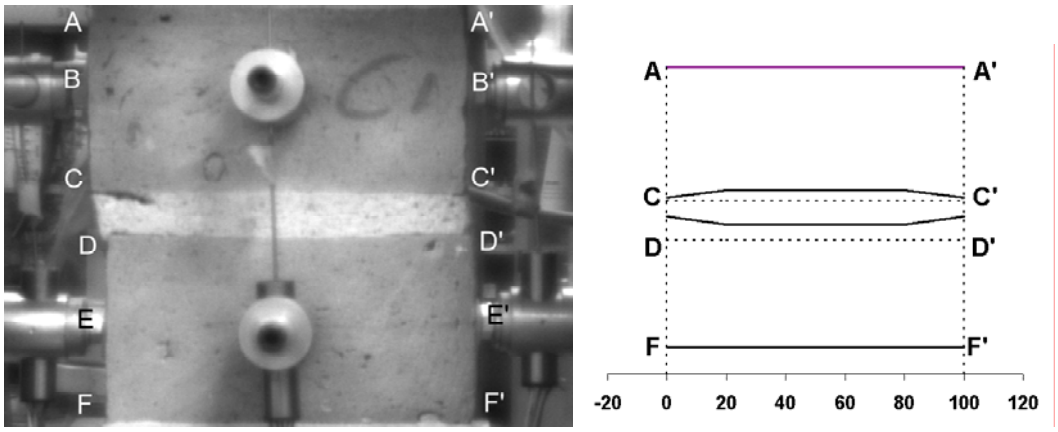

Figure 61 a) Photo of a specimen trough the lens of the digital camera. b) scheme of the deformed specimen.

The deformed specimen is shown schematically in Figure 61b.
The edge AA' is supported and the edge FF', is moved upwards. In a concentric test, the edges AA' and FF', will stay horizontal. Points on the observed surface near the line AA' will move slightly. Points close to FF', will move over almost the same distance as the points on line FF', when line FF' remains parallel with line AA' because of the imposed boundary conditions of the MSA. The joint is situated in the centre of the observed surface, the area CC'D'D in Figure 61b.

When the specimen is compressed, the brick corners C and C' will hardly move with respect to points A and A' respectively. However, C and C' will move over approximately the same small distance. In a similar manner, the distance of the points D and F and D' and F' will remain almost the same.

The speckle interferometry technique uses the interference characteristics of electromagnetic waves. It is based on the fact that an optically rough surface appears granulated when it is lit by two coherent light (laser) beams from two different positions. This phenomenon is called a speckle pattern and each individual grain is termed a speckle, Figure 62.
In the ESPI instrument, presented in Figure 60, the two coherent light beams are obtained by splitting the light beam produced by one laser diode. Then the two light beams are directed via mirrors onto the specimen. These two light beams interfere.

In the *first step* of the ESPI-process, the reflected light is captured with a charge-coupled device (CCD camera). The speckle pattern that is found, Figure 62, is stored in a computer.
Speckle patterns include the reflection information of points of the measured object. During a test, speckle patterns are taken at various load levels. In many cases in this thesis, speckle patterns were taken at a stress of approximately one third of the estimated strength of the specimen (load L1) and at a stress approximately 1 N/mm^2 higher (load L2).

In the *second step* interference fringes are formed by subtracting speckle pattern images taken at e.g. load L2 and load L1, see Figure 63. Specific software has been developed for the manipulation of such interference fringes [NEW 98]. The number of fringes and their widths are a measure of the displacements of points on the illuminated area.

Because the deformations, obtained from subtraction of two speckle patterns (step 2), have no relation with the specimen, an - arbitrary zero - displacement was assigned to a key point; a point that was assumed not to move. This has no further consequences for the following treatise.

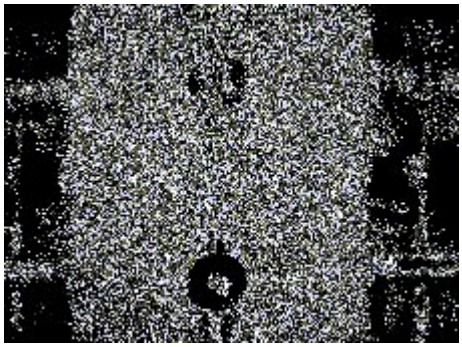

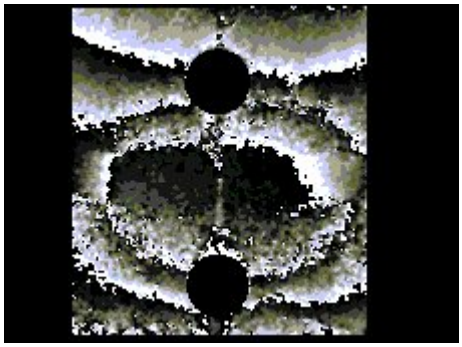

Figure 62 (left) Step 1 in the ESPI process: a speckle pattern image is obtained.

Figure 63 (right) Step 2 in the ESPI process: a fringe pattern is made by subtracting two speckle patterns. Masked circles appear, due to the attachment of an LVDT.

Thus the displacements of a large number of points, caused by a load increment (L2 - L1), were measured without any contact with the specimen. Surfaces up to 120 * 120 mm^2 were observed. However, (much) larger areas are possible, but with a decreased resolution and / or accuracy.
With the software, automatic evaluation of the measurements by real-time subtraction and phase-shifting algorithms is possible. From a fringe pattern of 572 by 768 pixels the displacement patterns can be established, however a data reduction to approximately 50 by 70 points was applied in the tests for this thesis.

In the *third step*, displacements were determined. By changing the polarity of the laser, displacements in X (horizontal) and Y (vertical) direction were obtained. A resolution of 10 nm was possible. Displacements in out of plane (Z) direction can be measured, although this was not done in this thesis.

In the *fourth step* the displacements were plotted. As an example, the vertical displacements of a specimen are plotted versus the X-position in Figure 64.
Lines AA' are almost straight, lines CC' and DD' have a kink. The distance between the displacement lines is a measure of the strain that occurred. In the centre, the strain is roughly the same for mortar and brick.
At mid height of Figure 64 the lines represent the displacements of points in the joint. Their distance is largest at the edges, from X between 0 and 20 mm and from X between 80 and 100 mm. The lines at the bottom and the top of the figure indicate the brick deformation, which is contrary to the joint.

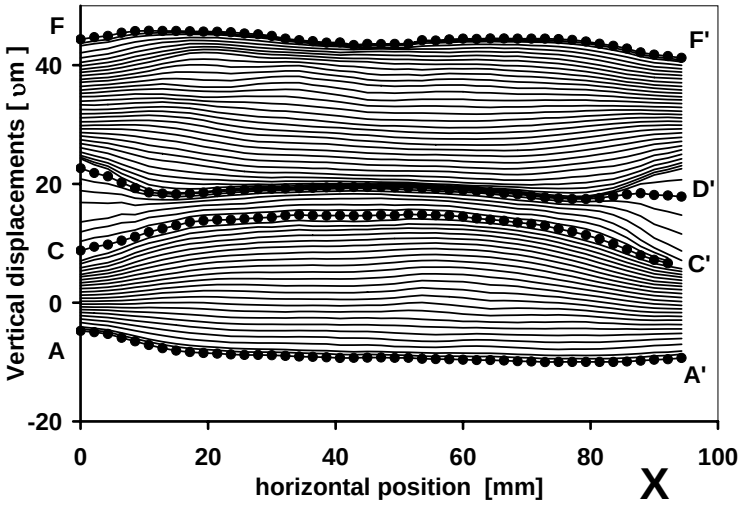

Figure 64 Step 4 in the ESPI process: Vertical displacements of points, plotted versus their horizontal position (X). Brick contours are indicated.

In the *fifth step* 'strains' were calculated from the measured displacements. Because the load increments at which deformations were obtained were different for each specimen, the specific strains ($\Delta l/l_{r,y}$-values) representing $\Delta l/l$ for a stress increase ($\Delta\sigma$) of 1 N/mm^2 were calculated using the following equation:

$$\Delta l / l_{r,y} = \frac{(v_i - v_j)}{(y_i - y_j) \cdot \Delta\sigma} \tag{27}$$

with:

$$\Delta\sigma = \frac{L_1 - L_2}{b \cdot d} \qquad \Delta l = v_i - v_j \qquad l = y_i - y_j \tag{28}$$

The variables v_i and v_j indicate displacements in vertical direction of node i and j respectively, y_i and y_j refer to the position in y direction of 'measuring' point i and j respectively. The gauge length for strain calculation is given by (y_i-y_j).

For each specimen, $\Delta l/l_{r,y}$-values were calculated over the top brick (y_i =0 mm; y_j = 48 mm) over the joint (y_i = 48 mm; y_j = 68 mm) over the bottom brick (y_i =68 mm; y_j = 105 mm) and over the same length as the LVDT measurements (y_i =25 mm; y_j =85 mm) indicated as specimen. These positions correspond with the height of lines AA' till FF' included, in Figure 61. Figure 65 shows an example of the results.

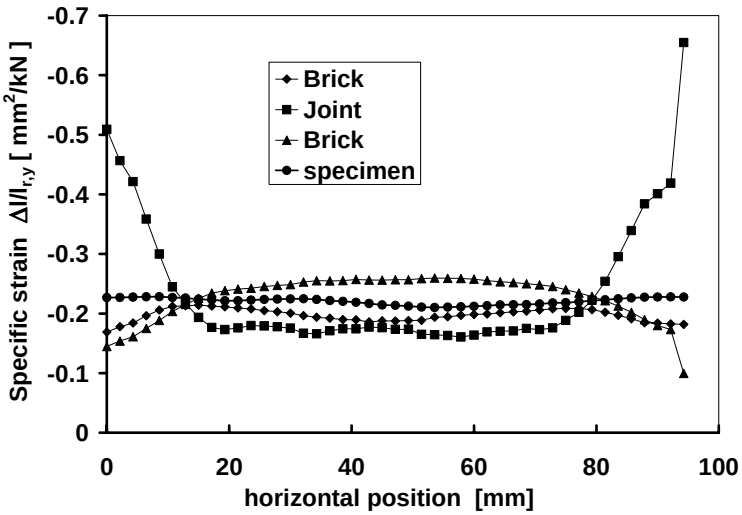

Figure 65 Step 5 Example of the $\Delta l/l_{r,y}$-value distribution over the width for a soft mud brick specimen with general purpose mortar.

At the edges AF and A'F', the deformation in the bricks is relatively small while there are hardly forces transmitted in that area. However, the 'strain' ($\Delta l/l$) over the joint is relatively large. As a consequence of the fissure, the stress is expected to be small and therefore the strain too. However, the shortening of the whole specimen, measured

between the lines AA' and FF', is (theoretically) equal over the full width, so locally a small brick strain has to be compensated by a large joint strain.
Actually, in this case, "mortar strain" results from both mortar deformation and the deformation of the fissure between mortar and brick.

The exact location of the fissure is unknown, so the real mortar strain can not be obtained in the fissure area while a measurement is taken over a void (the fissure).
For comparison between brick and mortar behaviour, values for $\Delta l/l$ are calculated.
Appendix A.1. gives some further remarks about the used stress and strain concept.

Finally, in the *sixth step*, the strain ratio for the joint was calculated. The strain ratio is the Δl between two certain points with the same X-value, divided by the averaged Δl in the central area of the joint, i.e. for 20 mm < X < 80 mm. Figure 66 shows an example of the results, which are approximately one in the central area.

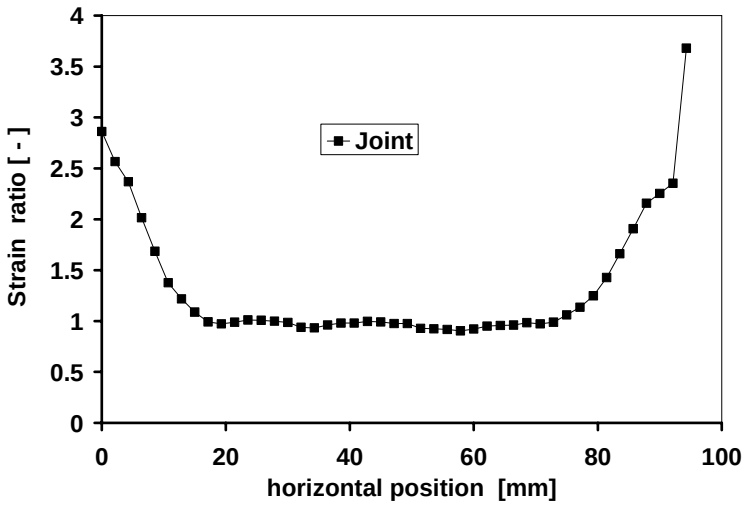

Figure 66 Step 6. Example of the strain ratio versus horizontal position.

7.2.3 Requirements for using ESPI

Some important conditions when using ESPI are:

- The surface has to be optically rough, which is the case for masonry and concrete.
- In masonry, the mortar has a different optical reflection than the units. Consequently, non-uniform illumination is possible. Therefore, a special spray ('paint') was used to prepare the specimens.
- The light intensity is a critical aspect too. In some cases there is too much sunlight and objects are overexposed. Then, blinding is necessary.
- Loading arrangement and specimen have to be stable. Often, in the beginning of the test, the specimen itself is not yet settled between the load platens. Therefore, most of the ESPI measurements were carried out at a load of approximately 1/3 of

the estimated failure load. Vibrations should be prevented, e.g. no heavy crane use during testing.
- ESPI measures the displacement differences of points of a surface, which is difficult if the whole body moves. A special test set-up with attachment of the ESPI-apparatus to the specimen itself can be a solution.

When these conditions are met, deformations in the order of 10 to 15 nm can be observed.

Like when using a photo-camera, the distance is of great importance for the image that is obtained. With a larger distance, a larger surface can be observed, however, the sensitivity of the measurement becomes smaller, the reflection weaker and measuring more difficult. For more details about the sensitivity of ESPI measurements, see Appendix A.4.

7.3 Moving seating arrangement

7.3.1 Principle of the moving seating arrangement

To analyse the ESPI results, it is desired to know the position of the line of thrust as accurate as possible. Therefore, the load transfer in the specimens was measured. A moving seating arrangement, (MSA, see Figure 69) was used, because in eccentric tests, the boundary conditions should give freedom of movement to at least one end of the specimen.

The moving seating arrangement (MSA) uses a (70 mm) steel plate that is suspended with three (16 mm) steel rods, 325 mm centre to centre, from the upper crossbeam of the Schenck tensile testing machine. The lower plate can move freely in the horizontal directions. The 25 mm thick specimen was positioned on this plate. Another (70 mm) plate above the specimen was mounted with three (32 mm) steel rods, 175 mm centre to centre, down to the bottom of the testing machine.

When the cross beam of the testing machine was moved upwards, the lower plate moved towards the top plate and the specimen was compressed. The reaction forces were measured with three load cells of 30 kN each, mounted in the middle of the 16 mm diameter rods.

For concentric testing it was desired that the two loaded surfaces remained parallel to simulate the situation in masonry loaded in compression as close as possible. Thus, the rotation of the moving seating should be minimal. This demand was taken into consideration designing the moving seating arrangement, Appendix A.2.
The loading speed of 0.1 mm/min was controlled via an inbuilt LVDT that measured the displacement of the upper cross beam from which the lower platen was suspended.

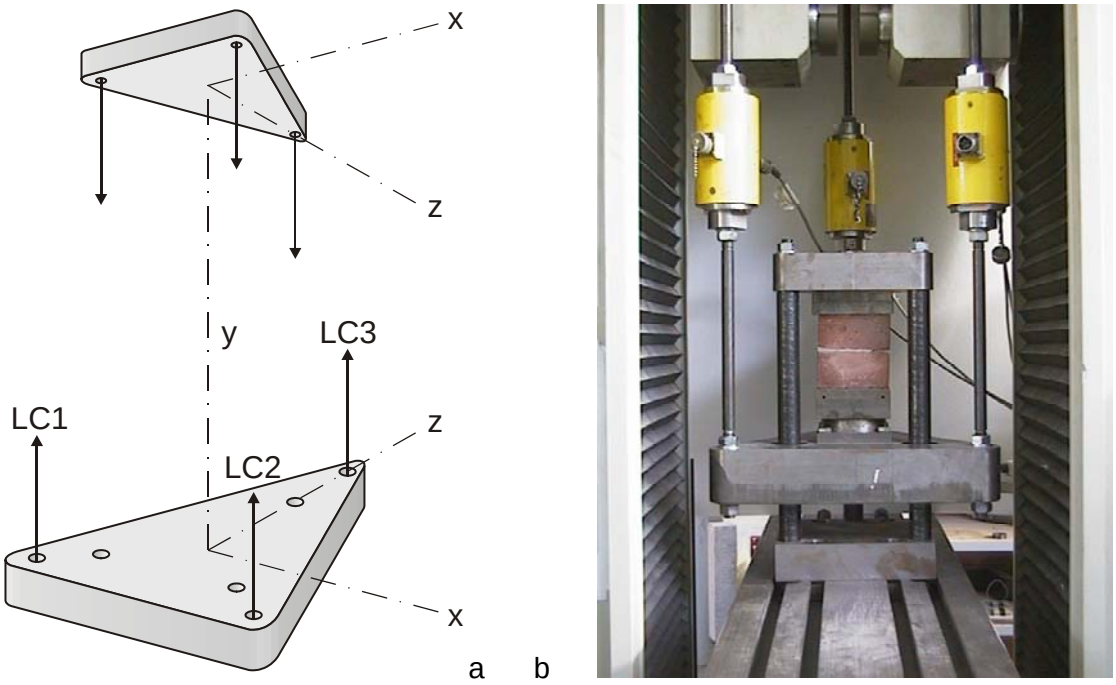

Figure 67 a) Moving seating arrangement, isometric scheme of top and bottom plate and photo showing top plate, suspension rods, load cells and bottom plate. Top plate supports run free through the bottom plate. b) Set-up with concentric loading condition.

To allow for the situation that the loaded surfaces of the specimens were not parallel, a ball bearing was used. Specimens were positioned on the ball bearing and rotated manually in order to get the top surface parallel to the top loading plate. By slowly closing the gap between loading plate and specimen and adjusting the position of the specimen at the same time, the load was introduced as evenly as possible.
When, during a test, the load increases, the ball bearing will increasingly be locked due to the increasing friction in the contact surfaces as explained in Appendix A.2.3.

7.3.2 Boundary conditions

All ESPI-specimens were gypsum capped. This made the surfaces to be loaded smooth and level and almost parallel to each other. The specimens were tested in the MSA with a) a free bottom plate or b) with the bottom plate supported in Z-direction. In all cases, specimens were loaded via steel blocks, in some cases with a tool to centre the loading. The pointed specimens were tested in a Schenck testing machine with standard load platens.
Pieces of steel were also used to obtain some distance from the larger load platens which otherwise would disturb the ESPI-view. This boundary condition could be described as the concentric loading condition. The bottom surface moved freely in the horizontal directions, while it displaced in vertical direction to the rigidly supported top surface.

In the tests described in Chapter 9 the specimens were loaded eccentrically and therefore the boundary conditions were changed. In these tests two steel blocks with slots were used to obtain a predetermined eccentricity. By positioning a steel 5 mm diameter bar in the slot, a 'hinge' was formed in one direction, while in the other direction rotation was still prevented. See detail A in Figure 67. This set-up was adapted to prevent the freedom of movement in the ESPI-view (Z) direction to allow for an optimal view of the effects due to bending of the specimen around the stiffest (Z-) axis.

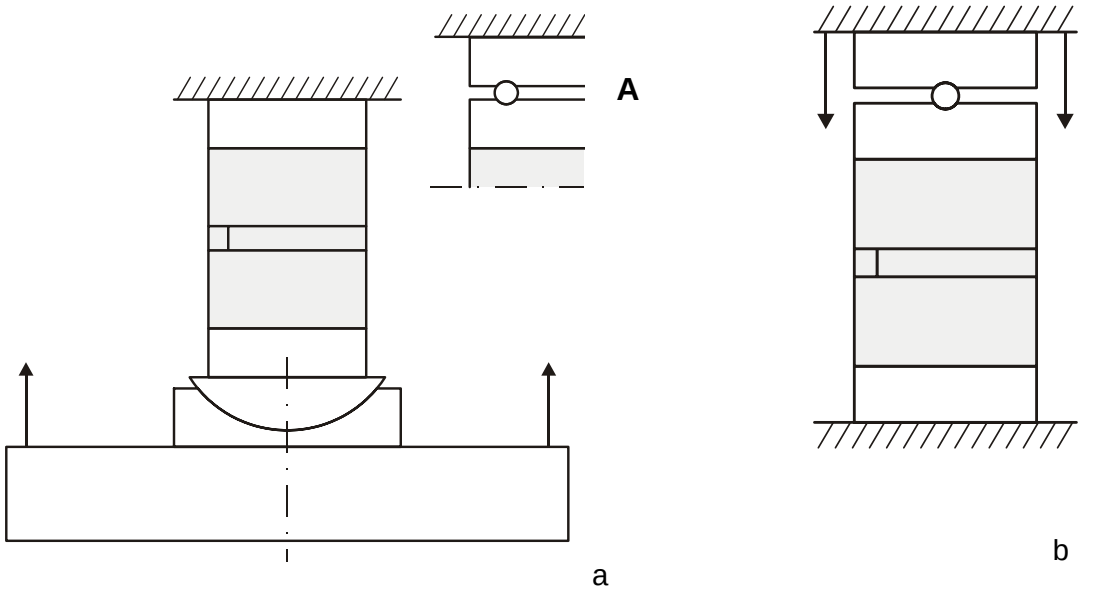

Figure 68 Boundary conditions in ESPI-tests. a) Concentric tests with a spherical seating used to allow for non-parallelism of the specimen and b) Eccentric test using hinged connection by means of a steel rod in slotted steel platens.

Movement of the lower plate was prevented in one direction through the use of ball-bearings and alternatively with a steel strip, see Figure 69.
These ball-bearings consist of a large number of steel balls fitted in a brass housing and placed between two steel plates. The ball-bearings were supported by steel supports connected to the bottom of the machine.
These measures were taken to reduce bending around the weaker axis. A view of the arrangement, a scheme of the loading system and the boundary conditions are given in Figure 69 and Figure 70 respectively.

The tests to study the effects of pointing of masonry, described in Chapter 10, were performed in a Schenck testing machine with standard load platens. In this series, steel blocks were positioned on the specimens. The steel sphere placed between two steel blocks gave some rotation possibilities, compensating when the surfaces were not exactly parallel. The loading platens of the machine gave no room for horizontal

displacements of the edges of the specimen. Figure 123, page 149 gives an impression. It was assumed that the machine load platen prevented the steel load blocks to rotate or to move vertically or horizontally, except for the top surface, which was moved downwards in order to load the pointed specimen.

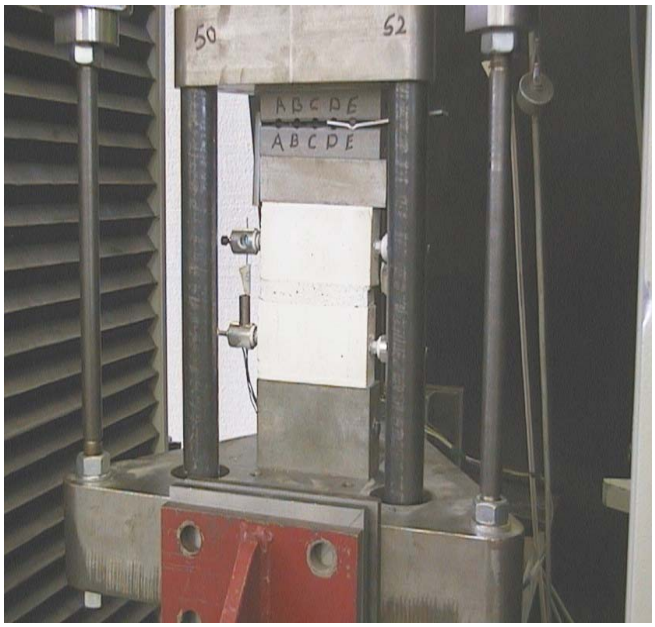

Figure 69 Specimen in the test set-up. Movement of the bottom plate was prevented in Z-direction using a ball bearing.

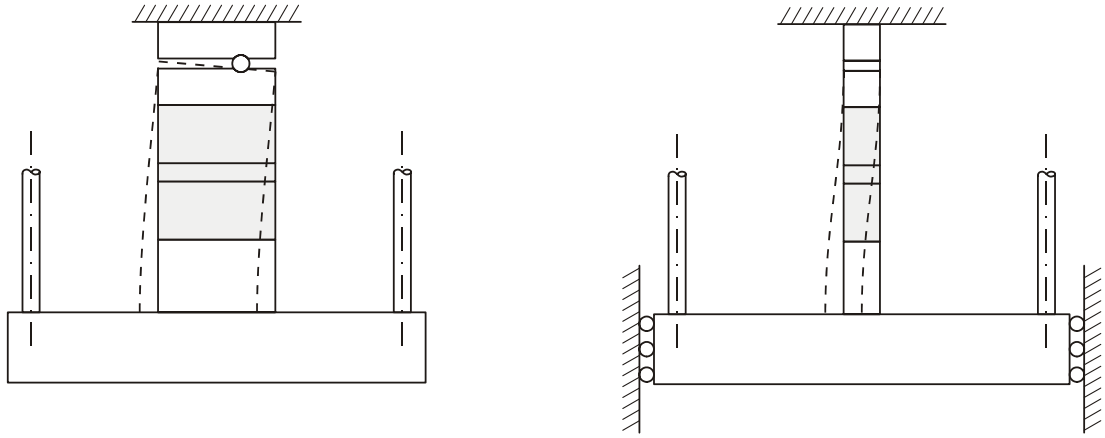

Figure 70 a) Scheme of the moving seating arrangement with the "hinge" used for eccentric loading. b) Horizontal movement was prevented in the Z-direction.

7.3.3 Load eccentricity in a concentric test

In a concentric test the load still may have some unintended eccentricity because:

a) The specimen is not symmetric, e.g. one joint is less filled than the other,

b) The specimen is not positioned in the exact spot, i.e. the centre of gravity of the tension bars. The (vertical) centre line of a specimen is not always the connection between the centres of gravity of each horizontal section and therefore it will not coincide with the system line of the test machine.

c) The specimen is not exactly rectangular. However, this is (partly) accommodated by the use of a ball bearing. Still, the top load platen does not touch the top surface of the specimen evenly, due to surface roughness. One point is always touched first.

d) Not every specimen is exactly straight, which fact is accepted as a characteristic of masonry.

The moving seating arrangement can be used to establish the load eccentricity using the measured forces in the three tension bars (LC_i) and their distance from the centre of the moving seating arrangement. Figure 71 shows a scheme of the bottom plate.

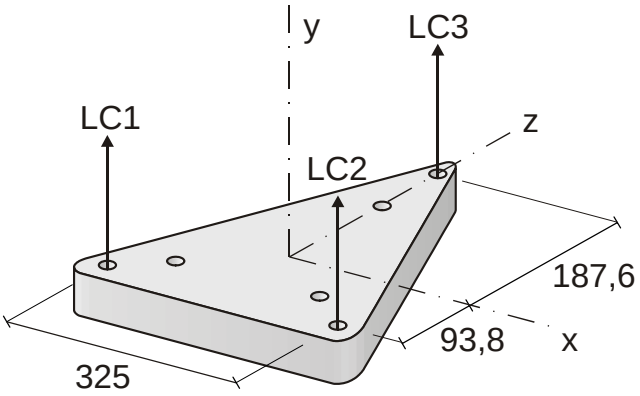

Figure 71 Isometric scheme of the bottom plate of the moving seating arrangement.

The weight of the bottom plate (W), together with the load cells and the tension bars, is approximately 600 N. With reference to Figure 71 the following relationships can be given:

$$Mz = -LC_1 \cdot 162.5 + LC_2 \cdot 162.5 \quad (29)$$

$$Mx = -(LC_1 + LC_2)\ 93.8 + LC_3 \cdot 187.6 \quad (30)$$

$$N = LC_1 + LC_2 + LC_3 + W \quad (31)$$

$$e_z = \frac{(LC_2 - LC_1)}{LC_1 + LC_2 + LC_3 + W} * 162.5 = \frac{M_z}{N + W} \quad (32)$$

$$e_x = \frac{-(LC_1 + LC_2) + 2 \cdot LC_3}{LC_1 + LC_2 + LC_3} * 93.8 = \frac{M_x}{N + W} \quad (33)$$

where:

N = axial force, sum of the forces in the load cells,
M = moment caused by the forces in load cells,
LC_i = the forces measured by the load cells, i = 1, 2 or 3,
e_X ; e_Z = eccentricity in X ; Z direction.

As an example, the measured moments M_X and M_Z are plotted versus N for a concentrically loaded specimen in Figure 72. For all specimens, the measured M-N relationship could be represented by:

$$M = N \bullet e + M_0 \tag{34}$$

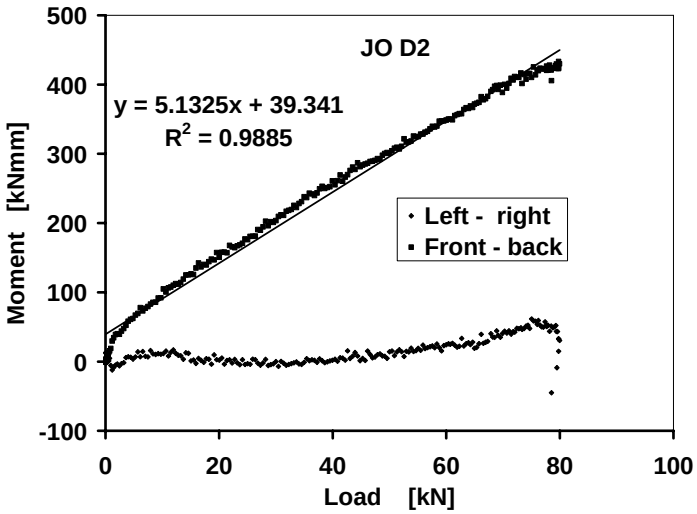

Figure 72 M-N diagram. After a begin-effect, an almost linear relationship is observed.

Equation (34) shows that in the initial phase of the test, the largest discrepancy of linearity occurs because the opening between the top load platen and the steel block on top of the specimen has to be closed. Moving the bottom plate up, one point will make the first contact and all (however small) forces have to be transmitted there, Figure 73. Then, the eccentricity is approximately half the width or half the thickness. Consequently, the specimen is compressed more at the side where the first contact is made. In this test-phase, the system is unstable, the specimen has to settle and find its position.

To close the opening, some accelerated rotation, i.e. a moment ($M \approx M_0$) is required and this explains why the M-N graphs had a steeper curved beginning, roughly until the total load equalled 2 kN. This first part of the M-N relationship was neglected when the best fit relationships in the almost linear part were established.

Actually, it holds:

$$e = \frac{M}{N} - \frac{M_0}{N} \tag{35}$$

That means, for small values of N, in theory the value of |e| will approach infinity. In the initial test-phase, variation in the (small) load cell recordings resulted in large variations of the eccentricity, which was not practical. Therefore, the use of M-N relationships rather than e-N relationships is preferred.
The linear M-N relationship only deviates at small loads (initial settling phenomenon) and at high loads (almost failure). The values for e were established using a best fit for the linear part in the M-N graph.

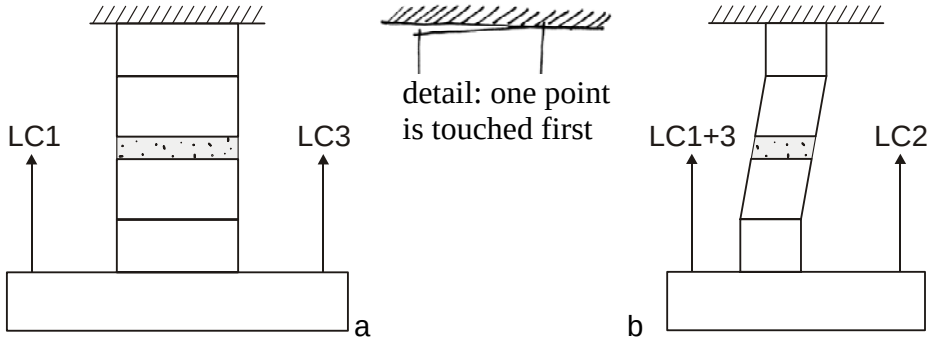

Figure 73 a) Position of the specimen at small loads. One point is touched first. Load cells and tension bars are not yet under stress and the bottom plate has to find its position. b) The loading may become skew in Z-direction.

7.3.4 Load eccentricity in an eccentric test.

In eccentric tests the load is introduced via a 'hinge' formed by two steel blocks with a small steel bar in-between. The blocks have grooves to guarantee the position of the steel bar. In Z-direction, parallel to this steel bar, which in its turn is parallel to the ESPI-view direction, the movement of the bottom plate was prevented. Consequently, only displacements perpendicular to the ESPI view direction (X and Y direction) were possible. As a result, the position of the load could not be established in Z-direction which was also the thickness direction of the specimen.

As an example, similar to Figure 72, the moment M is plotted versus the load N in Figure 74 for a specimen loaded eccentrically in position e (target value 32 mm). The almost linear relationship shows that the eccentricity was 33.1 mm and it remained almost constant during the whole test. The small off-set at the beginning may be attributed to the initial settling phenomenon.

The eccentricity during the ESPI measurements (N = 10 tot 12 kN) may be assumed constant. The best fit in Figure 74 has a relatively high correlation coefficient (R^2) and only a small off-set (M_0 = 10.4 kNmm). The best fit line intersects the N-axis at
N = – 0.314 kN.

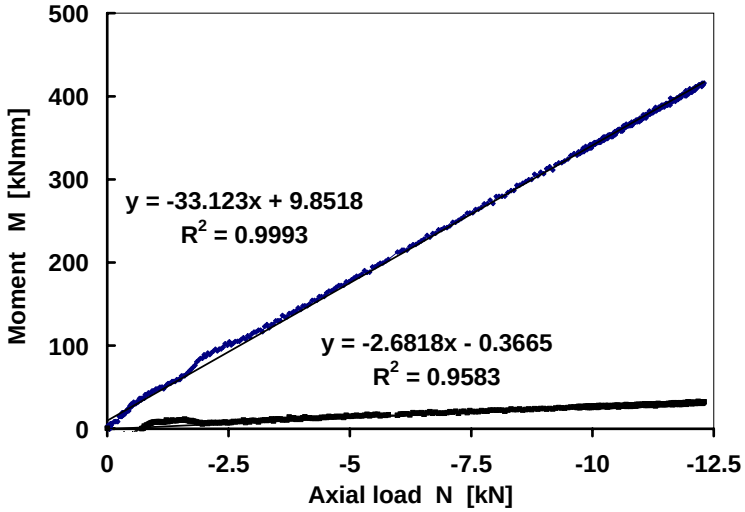

Figure 74 Example of a moment versus load relationship for a specimen loaded at position pos e, e_X = 33.1 mm and e_Z = 2.68 mm.

7.3.5 Rotation of the moving load platen

Rotation of the moving load platen was estimated from the force-differences in the tension rods measured by the load cells as explained in Appendix A.2.2.2.
With a modulus of elasticity of E_{spe} = 5000 N/mm^2 for the specimen it follows that the ratio between the rotation stiffnesses of the specimen and the MSA was 0.019 and 0.258 along the X and Z axis respectively. The shear deformation is neglected.

It may be clear that bending (deformation) of a specimen also causes some horizontal movement. The horizontal displacements (w) were estimated to vary between:
(0.25 and 1) times $M_X \cdot 10^{-6}$ in Z direction, and (44 and 174) times $M_Z \cdot 10^{-6}$ in X direction.
Appendix A.2.2.2. gives more details.
The horizontal displacements (in Z direction, i.e. thickness of specimen) disturbed test results in a number of cases (section 8.3.4).
The vertical and horizontal displacements, observed with the ESPI system, are discussed in Chapters 8, (concentric loading) Chapter 9, (eccentric loading) and Chapter 10 (pointed specimens).

7.4 Specimen preparation for ESPI testing

One of the conditions to obtain good results with ESPI is that the deformation at the observed surface of the specimen is representative for its behaviour. The ESPI technique requires specimens to be loaded preferably in plane stress. Therefore, small relatively thin specimens were used.

A specimen, cut as a slice of a couplet represents a sample of a joint, in combination with its adjoining bricks, Figure 76. With a thickness of 25 mm the specimen's slenderness of approximately 4.5 is enough to ensure that the boundary effects in the centre will be negligible [DUT 80] and [KHA 94]. Its cut surface will come under full compression and the effect of fissures and inhomogeneous joints still can be observed. With these specimen sizes a representative sample is obtained, in which a stress distribution can develop similar as in a real wall, which allows for accurate deformation measurements with ESPI.

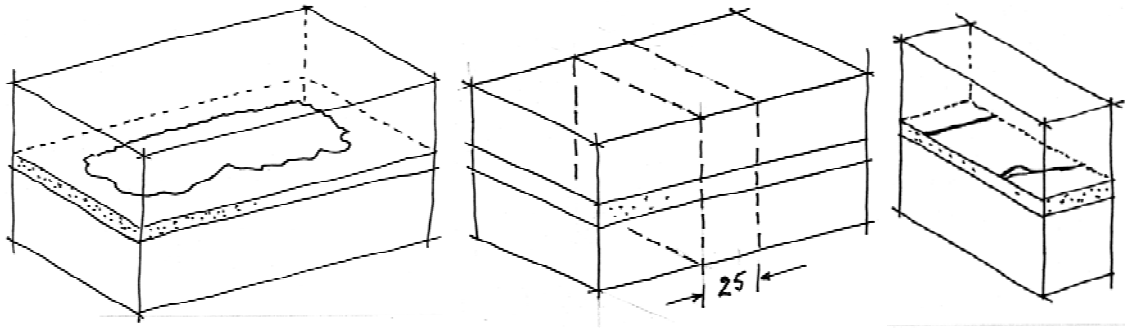

Figure 75 Schematic view of a couplet with the bonded area, the cutting position of a specimen, and a 25 mm thick specimen.

Figure 76 RW couplet, 25 mm thick specimen after testing, and capping of a specimen.

All ESPI specimens were capped with a thin layer of gypsum as follows. An amount of gypsum was prepared on a sheet of glass. The glass was oiled in order to prevent the gypsum from sticking to the glass. The specimen was pushed into the wet gypsum and placed in vertical position, Figure 76. After approximately one hour, when the gypsum was hardened, the specimen was taken from the glass sheet by moving it to the side. Then, the process was repeated for the other side of the specimen.
The capping procedure did not allow for absolutely parallel surfaces; this was compensated for by the use of a spherical seating, Figure 68.

8 Brick-mortar interaction in concentric compressed specimens

Abstract

In this chapter the brick-mortar interaction under concentric loading of fifteen combinations of five brick types and three bed joint thicknesses is discussed. Deformational results obtained by LVDT and ESPI measurements are presented and compared with each other. Results of numerical simulations with DIANA, are used to explain the expected deformations.

To study the progression of the strain distribution over the width of the specimen, ESPI measurements were taken at various load steps, i.e. stress levels.

The E-values of mortar and brick were of a comparable magnitude. The fissure at the end of the brick-mortar interface affected deformation of both brick and mortar.

In thin layer mortar specimens, the recessed joint, necessary to obtain a clean and esthetical appealing masonry surface, acts as a notch and so high levels of strain were found in that area. Lateral deformations show that both mortar and brick expanded. However mortar expanded less than brick.

8.1 Introduction

Knowledge of the brick-mortar interaction under compression and the resulting deformation of bricks and mortar separately is important for a reliable estimation of the capacity of a structure. For these estimations, analytical and numerical simulations can be performed, for which input results of detailed experiments are required.

In this chapter, the results of detailed deformation measurements on brick and mortar in masonry specimens are presented. ESPI was used to observe the brick-mortar interaction under concentric compression, using 25 mm thick specimens. LVDTs followed the deformation between two points over a 60 mm gauge length at both narrow sides of the specimen.

Besides specimens with traditional joint thickness (GP), specimens with joints of medium thickness (MM) and thin layer joints (TL) were tested.

Table 22 gives an overview of the brick-mortar combinations used.

The goals of the part of the thesis described in this section were:

a) to establish the axial and lateral deformation behaviour under concentric compression of mortar and bricks separately in combination with the effects of joint imperfections due to the brick laying process and shrinkage,
b) to establish the effects of joint thickness on deformation behaviour,

Table 22 Number of specimens and brick-mortar combinations for concentric ESPI tests.

Brick type [1])	Joint and mortar type		
	GP	MM	TL
JW	2*	2*	2
HE	2	2	2
HU	2	2	2
RY	2*	2*	2*
HY	2	2	2

* Additional specimens were used for specific tests, see sections 8.6 and 8.8 and Chapter 9

[1]) see Table 23

8.2 Experimental details

8.2.1 Material combinations and properties of materials used

The properties of the bricks, used for this part of the research, are summarised in Table 23. The bricks used were similar to the ones used for the wallette tests in Chapter 6 that were discussed in Chapter 4. In some cases they came from the same factory, however from a different delivery, so properties may be different. All bricks used were ± 210 × 100 × 50 mm^3.

The mortar properties, presented in Table 23, vary per brick type and joint thickness combination. Fifteen types of mortar were used.

Table 23 Brick and mortar properties according [PLU 99b].

Brick		Type	IRA	$f_{c,bri}$	$f_{c,brc}$	E_{bri}	$f_{c,mor}$		
							GP	MM	TL
				N/mm^2	N/mm^2	N/mm^2	N/mm^2	N/mm^2	N/mm^2
Joosten	JW	extrusion	3	141	70	29400	18.2	22.3	32.8
Heteren	HE	extrusion	28	72	36	15100	13.4	18.2	19.8
Huissenswaard	HU	hand mould	35	37	19	8000	13.0	15.9	9.4
Rijswaard	RY	soft mud	44	26	13	5460	9.6	9.4	10.1
Hylkema	HY	light weight	47	17	8.4	3600	9.9	10.3	9.2

$f_{c,bri}$ = brick compressive strength, according NEN 2489:1976, [PLU 99b],
$f_{c,brc}$ = $f_{c,bri}$ with correction for h/t = 0.5 to h/t = 4 [DUT 80],
$f_{c,mor}$ = mortar compressive strength NEN 3835, 1991,
IRA = Initial Rate of Absorption in gr/dm^2/min,
E_{bri} = from tests or estimated with: E = 430 $f_{c,bri}$ (Section 4.4).

8.2.2 Measurements

ESPI measurements were performed in the moving seating arrangement as described in section 7.3, page 94. LVDTs, used to observe the overall behaviour of the specimen, were fixed in the middle of the narrow sides of the specimen. In e.g. Figure 61, the nuts

are visible that were glued on the specimen to fix the LVDTs. The LVDTs measured over one joint with a gauge length of 50 mm or 65 mm. In a number of cases LVDTs were fixed at the back or at the front of the specimen. The LVDTs at the front obstructed the ESPI view, but allowed for comparison of the two measuring methods.
The load cells in the MSA measured the load transfer through the specimen as discussed in section 7.3. The built-in LVDT of the Schenck testing-machine measured the displacement of the traverse and the results were used to control the displacement speed of the traverse, which was set at 0.1 mm/min. The specimens discussed in this chapter were loaded concentrically in the moving seating arrangement with a free bottom plate. The applied boundary conditions are discussed more extensively in section 7.3.2.

8.3 Results of traditional measuring instruments

8.3.1 Strength

Averaged compressive strength and E-values of both ESPI specimens and wallettes, made at the same time, with the same materials, are presented in Table 24.

Table 24 Averaged strength and E-values of ESPI-specimens and TNO-wallettes for combinations of five brick and three joint thicknesses.

brick type ↓		strength N/mm²			E value N/mm²	LVDT-results	
mortar type →		GP	MM	TL	GP	MM	TL
JW	ESPI	43.1	46.5	59.3	14900	17300	22600
	Wallette	28.4	34.7	45.1	18000	18400	20800
HE	ESPI	29.8	31.2	48.9	6900	13400	14500
	Wallette	12.2	20.9	29.1	6000	13000	11000
HU	ESPI	11.3	16.5	17.2	1840	4120	4150
	Wallette	6.3	11.5	11.6	3310	4510	4060
RY	ESPI	12.1	16.3	12.6	3240	4300	4910
	Wallette	9.0	13.3	12.1	3760	4820	4000
HY	ESPI	11.8	10.4	7.6	4820	5120	4190
	Wallette	6.3	7.3	7.9	3370	4510	4400

ESPI : 25 mm thick, 100x115 mm^2, cut from a couplet
Wallette : 100 mm thick, 480x430 mm^3, tested at TNO [PLU 99a].

On average, the small ESPI specimen strength was 1.5 times the strength of the wallettes which were tested at TNO [PLU 99a]. Possible causes for strength differences are: a) the number of joints in the specimen, b) the specimen size, c) the type of joint filling and d) experimental conditions.
These causes will now be discussed.

a) Only one joint was loaded in the specimens. This is more favourable than the situation for a wallette where load is transmitted from one joint via brick to another. Irregularities in the transition from brick to joint influence stress transfer in the next joint and brick. Wallettes had relatively more bricks than specimens as well. Specimens had only one joint, wallettes had seven bed joints. Head joints in the wallettes made this situation even worse.
b) Specimen size effects were calculated according to Dutron [DUT 80] and Khalaf [KHA 94] as mentioned in Appendix A.3.2. In Table 25 strength ratios are presented. These theoretical considerations indicate that the differences in strength are not caused by dimension differences.
c) Another difference is the way the joints were filled. Couplets were made by pushing the top brick vertically into the mortar. This procedure was different from the making of the prisms. For couplets, the mortar was not scraped by the brick that was being placed as for wallettes (see brick laying process in section 2.2.3 on page 6).
d1) There was a difference in friction between load platens and specimen surface. The specimens were capped with gypsum, the prisms with masonry mortar.
d2) The tests where performed in different laboratories.

Table 25 Strength ratio for specimens and wallettes acc. [DUT 80] and [KHA 94]

Specimen size h × l × t		slenderness h/t	Dutron ratio	Khalaf ratio
ESPI specimen	113×100×25 mm^3	4.5	0.744	0.394
wallette	480×430×100 mm^3	4.8	0.716	0.391
Ratio specimen / wallette			1.04	1.01

8.3.2 Failure

In general, strong specimens failed much more suddenly than weak specimens. In particular for JW specimens the load displacement diagram did not give any indication of the moment of failure. Fracture had an explosive character. Pieces were blown away for meters. The LVDT measurements showed a faster deformation increase in the final seconds of the test, Figure 77, left. However, this could only be observed after testing.

The behaviour of weaker (RY) specimens was completely different. There, LVDTs gradually came loose from the surface of the specimens; see e.g. the right hand LVDT results in Figure 77. For this masonry type, failure could be predicted during testing on the basis of the load-displacement behaviour recorded by the LVDT in the machine and by cracking of the specimen. Another indication was that some LVDTs came loose from the specimen. At the end of the test, when LVDTs came loose, their results were no longer reliable. These results were not used for further analyses.

In specimens made from strong JW units and GP mortar, fracture lines were under a slope of 70° with the horizontal surface and in the length of the specimen. The confined mortar cracked as in confined concrete, [VON 93], Figure 78. Figure 79 shows an example with 70° fracture lines in the mortar and JW-bricks with a vertical fracture pattern.

The compatibility conditions at the mortar-brick interface lead to a tri-axial compressive stress state for the mortar. In the failure phase, shear surfaces will develop under a slope of 70°. This phenomenon was also recognised when masonry specimens were loaded in compression, section 6.6, page 75.

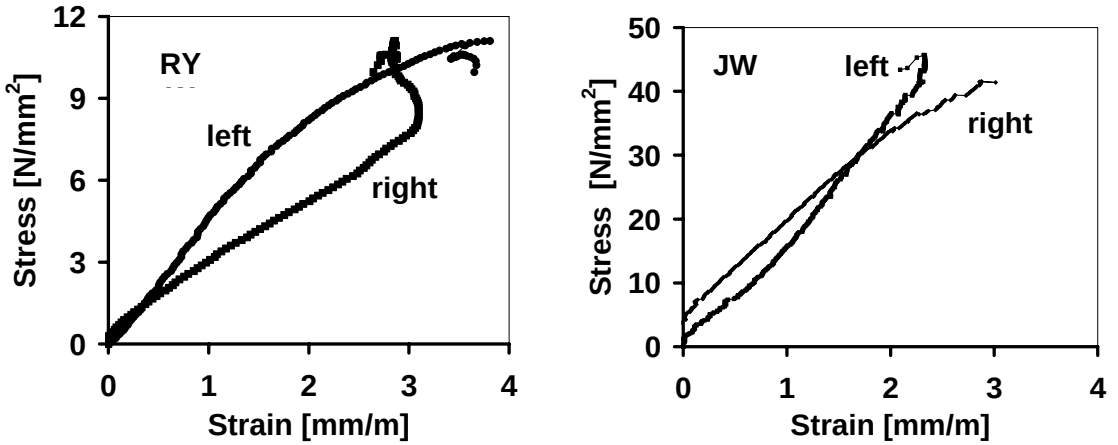

Figure 77 Stress-strain diagram for a RYGM specimen and a JWMM specimen obtained with one LVDT at the left and one LVDT at the right hand side of the specimen.

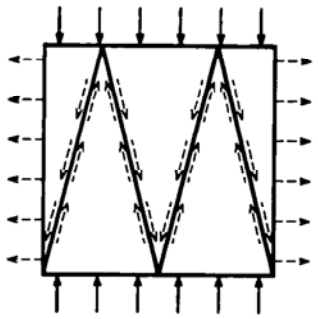

Figure 78 Fracture model of a concrete cube load in 3D compression [VON 92]

Figure 80 shows a diagonal cracked top brick and an unbonded part of the joint that initiated vertical cracking. In specimens made with softer bricks, e.g. RY, the crack ran right through the mortar into the brick and more diagonally through the specimen. In these specimens shear failure developed. Figure 80 also shows the unbonded part of the joint that initiated vertical cracking and spalling of the outer 20 mm of the specimen.

a

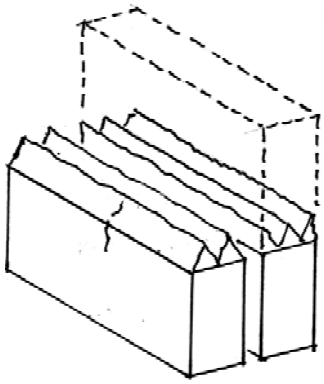

b

Figure 79 Top and bottom part of a fractured JW specimen (coded JOB1) showing inclined fracture surfaces in the mortar. Sketch, showing the top part positioned in front of the bottom part.

a

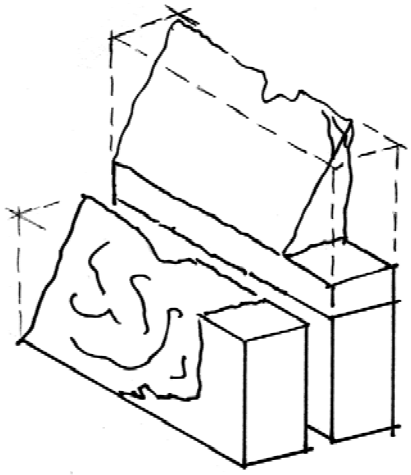

b

Figure 80. a) Top and bottom part of a fractured RY specimen (coded RWC2) showing diagonal cracking of the top brick and an approximately 20 mm deep fissure. b) Sketch of the top part put up-side down in front of the bottom part of the specimen.

8.3.3 Modulus of Elasticity

E-values were established from the averaged LVDT results as the secant of a representative part of the σ-ε diagram, as described in Appendix A.1.

TNO-wallettes and ESPI-specimens, made from the same materials, roughly had the same E-values, (Table 24). On average, the ratio E_{ESPI} : $E_{wallette}$ was 0.97. The lower value of $E_{wallette}$ can be explained by the fact that a wallette had five joints and an ESPI specimen only one.

The linearity of the σ-ε diagrams in the observed range was clear, the correlation coefficient (R^2) of the linear best-fit lines was more than 0.97 in all cases, Figure 81. Therefore, ESPI results were less sensitive for the stress level at which these measurements were taken.

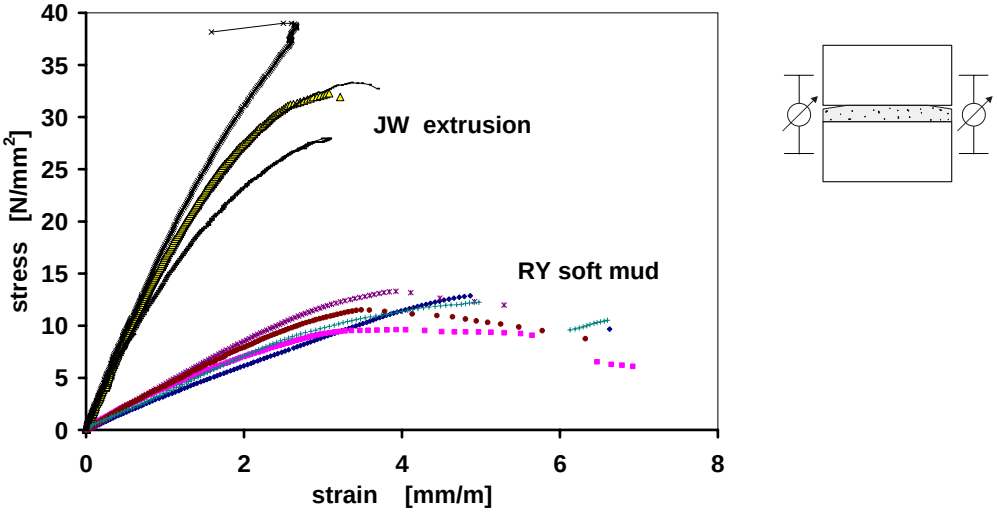

Figure 81 Examples of stress strain diagrams for JW and RY bricks. Average of the results of two LVDTs, illustrating linearity until approximately 80% of failure load.

8.3.4 Eccentricities

In all tests both LVDTs measured almost equal contraction at both sides of the specimen. In more than 50 % of the tests the difference was smaller than 10% of the averaged value. Differences in LVDT results indicate eccentricities of the loading and/or differences in material properties.

Load eccentricities also could be established from the reactions measured by the three load cells, section 7.3.2. The position of the axial load in relation to the assumed centre of gravity of the specimen was calculated for each specimen. As an example, the result of one RY specimen is presented in Figure 82. Eccentricities were considerably smaller in the direction parallel to the surface observed with ESPI (X-direction) than in the Z-direction. For all tests the eccentricity in X-direction was 1.02 mm on average. In thickness (Z) direction the averaged eccentricity equalled 5.34 mm. This caused the diagonal shear failure of the top brick in Figure 80. In many cases the X-eccentricity varied considerably during one load step, (Figure 82), indicating that spalling occurred in spalls of a few mm thickness.

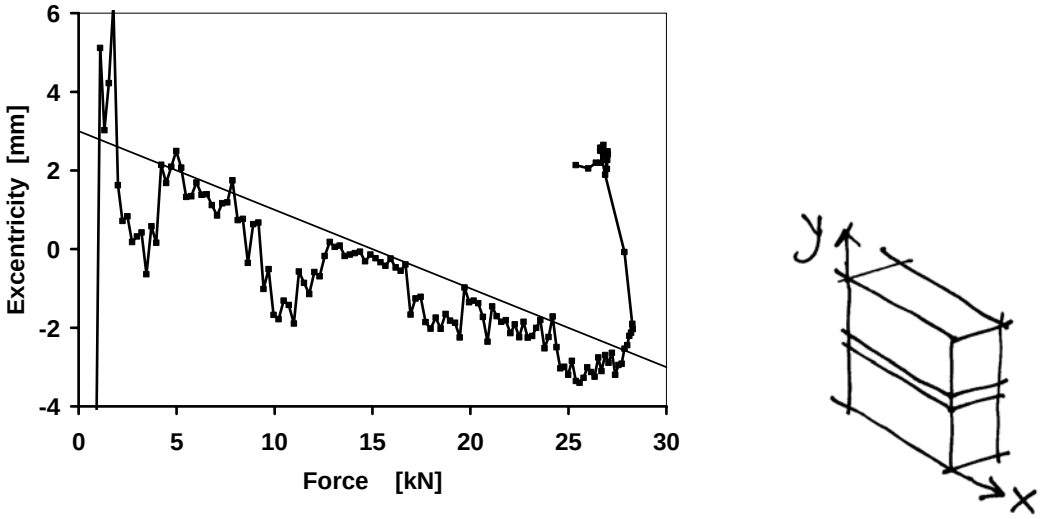

Figure 82 Eccentricity in X direction, after a begin-effect a decrease from e = +2 mm to e = –2 mm.

In the initial phase, lateral movements of the bottom plate of the MSA could freely occur in horizontal directions, (Figure 71, page 98).
After this phase, the specimen has settled and then it can be seen as a bar, rigidly supported at its ends. A horizontal movement will cause bending as indicated in Figure 83, and its effects can be seen in differences in brick deformation. For joint deformation, the effects are relatively small; the bending moment in the centre of the specimen, i.e. at joint height, is zero.
It is assumed that the load eccentricity is mainly caused by these lateral movements and that the largest movements occurred in the initial phase of the test, Figure 73, page 100.
Movements in X-direction were negligibly small. In the Z direction (weakest axis of the specimen) they caused the already mentioned eccentricities, bending and eventually the fracture according the mechanism shown in Figure 80.

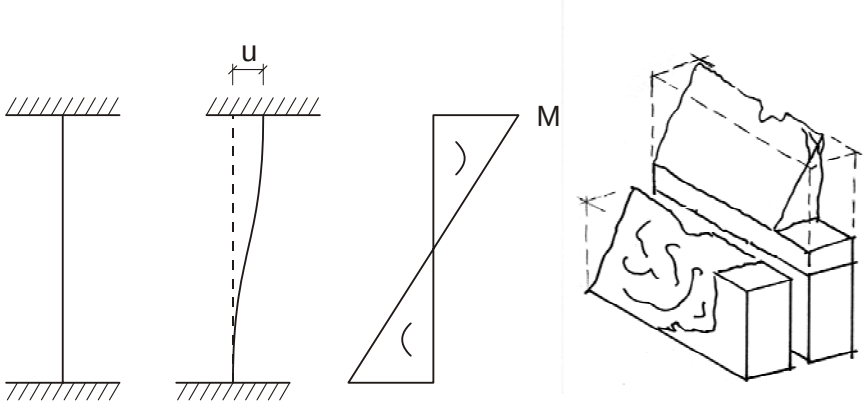

Figure 83 Bending in the specimen as a consequence of a lateral movement (u) and fracture of the top brick by diagonal shear.

8.4 Numerical simulations

The finite element program DIANA [DIA 96] was used for some explorative numerical simulations. Specimen's dimensions were as in the experiments except for the thickness for which one layer of elements of 10 mm thickness was used. The following values were used: E_{brick} = 4000 N/mm^2, E_{mortar} = 5000 N/mm^2, and for the interface layer E_{int} = 1000 N/mm^2. Poisson's ratios were 0.18 and 0.15 respectively. An interface layer of 1 mm thickness was modelled between mortar and top unit to simulate the contact layer. The fissures were modelled as 15 mm deep openings.
The specimen was loaded by assigning a 1mm displacement to two points on top of the steel block.
Figure 84 shows contour plots of the displacements and stresses of a concentrically loaded specimen with a fissure on either side. The parts of the specimen above and below the fissure remained without stress. Peak stresses occurred at the load introduction point and at the crack tips, (singularity, see also section 2.4.3). The vertical displacement of each node was plotted versus the X value of the node, (Figure 85), similarly to ESPI results, section 7.2.2, page 91.

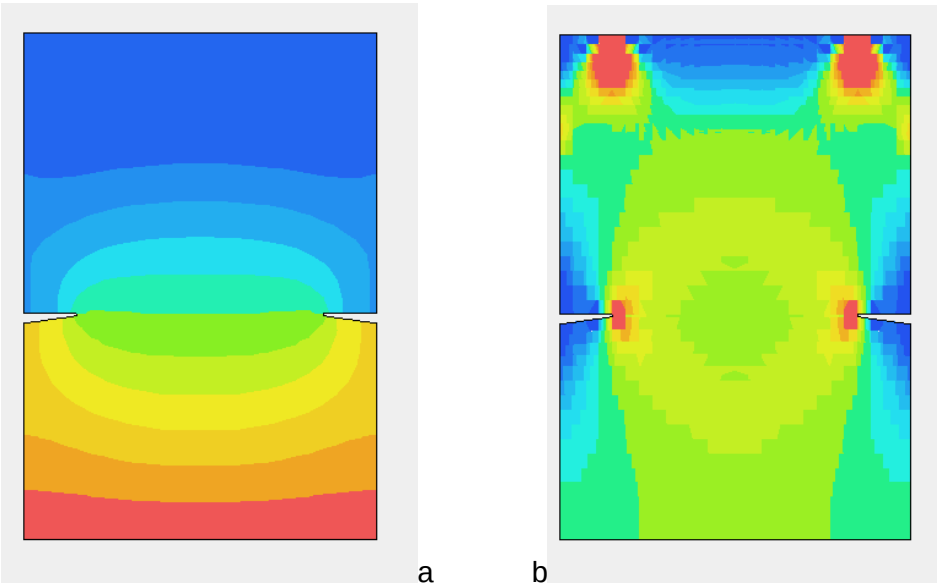

Figure 84 Deformation (a) and stress contours (b) of a concentrically loaded specimen, DIANA results.

The effect of the fissure is clear, Figure 85. The node displacements are smaller near these openings. Nodes of the bottom brick displace more and those of the top brick less than expected for a closed joint. The lines that are closer together represent the softer interface layer. The node displacement lines of this softer layer with smaller elements fan out at the end, near the fissure. Symmetry around the joint can be observed. This image is similar to the ESPI example given in Figure 64, page 91.

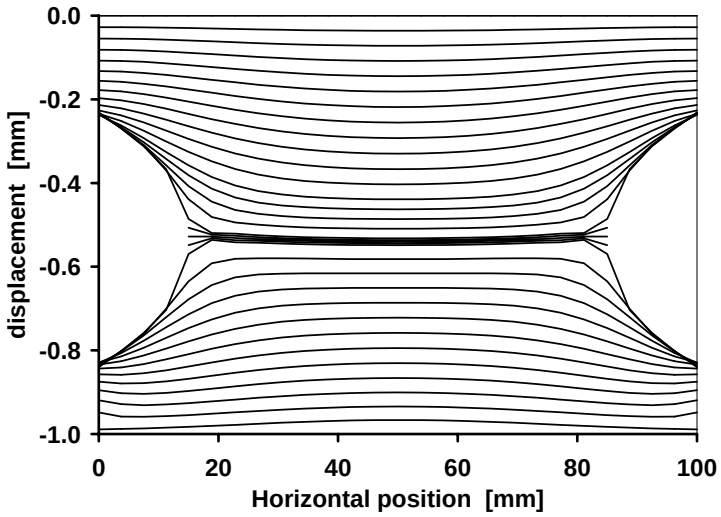

Figure 85 Vertical node displacements of a concentrically loaded specimen, DIANA results.

From node displacements at the edges of the bricks, strains were calculated for top and bottom bricks and for the joint with the method described in section 7.2.2, page 89, used for the ESPI results. In Figure 85, the strains were plotted versus their horizontal position in the model. Strains for the top and bottom unit are almost equal, as expected. The joint showed a high strain level near the fissures.

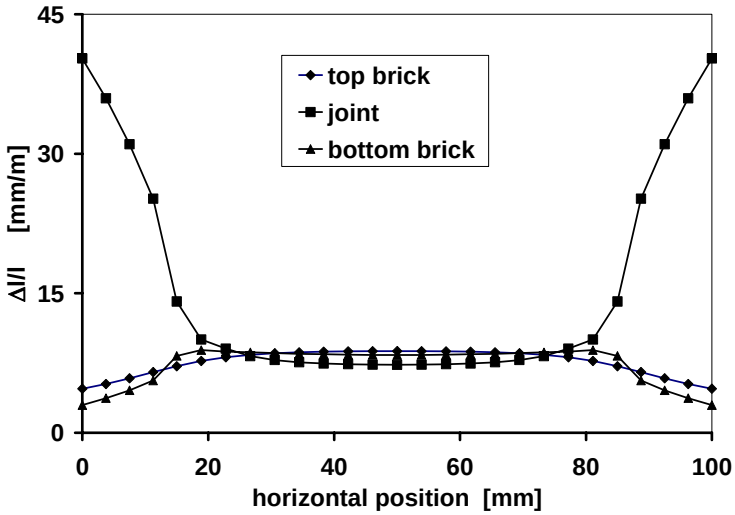

Figure 86 Vertical 'strains' (Δl/l) of a concentrically loaded specimen, DIANA results.

In Figure 87 the horizontal displacement of each node was plotted versus the Y value of the node. The image is almost symmetric around a vertical and a horizontal axis. Deviations are caused by the boundary conditions. The bottom nodes were confined both in vertical and horizontal direction. The top edge was loaded via a steel block, which results are omitted. The bricks expand laterally, the mortar is in compression.

The barrel ( ) shape in the bricks is the result of the boundary conditions and of the fissures modelled at brick mortar transition (Y = 65 mm).
Lateral stresses, plotted in Figure 88, show that the specimen is in compression in the centre, and that tensile stresses occur, in an area at 15 mm from the vertical edges of the specimen. The stress distribution is 'rounded', in contrast with the assumed 'blocked' stress distribution in the analytical model, Figure 20. The highest lateral stress (37.5 N/mm^2) occurred in the soft interface layer.

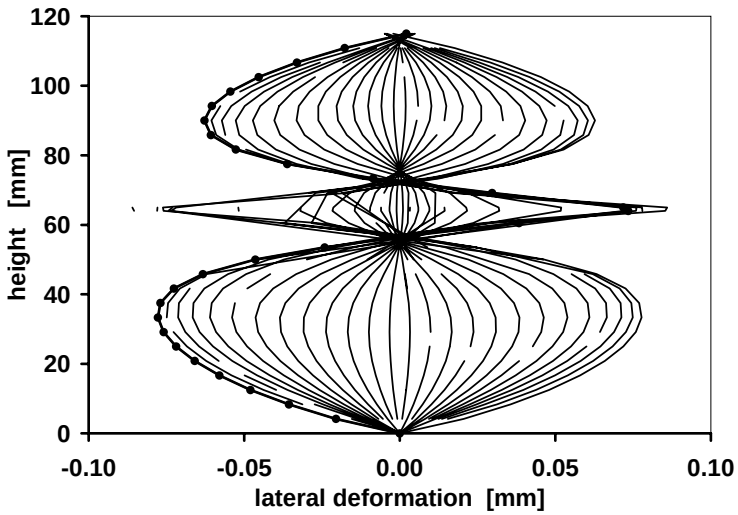

Figure 87 Horizontal node displacements of a concentrically loaded specimen, DIANA results. The bricks deform in a barrel ( ) shape.

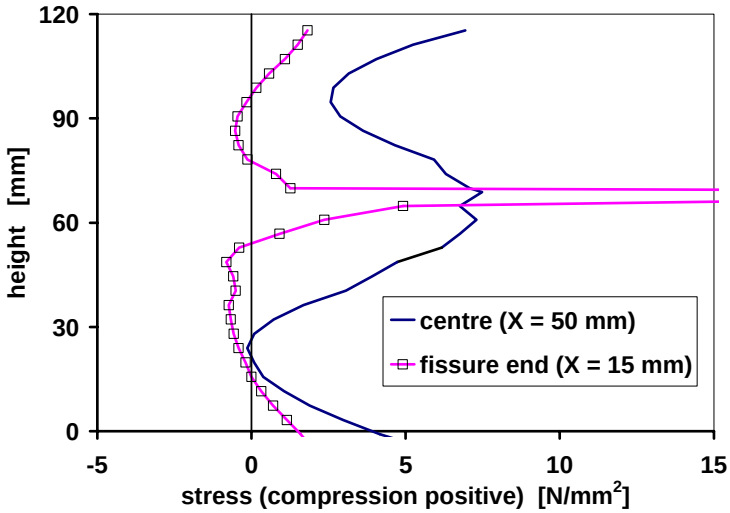

Figure 88 Horizontal stresses of a concentrically loaded specimen, in the centre and at 15 mm from the edge, DIANA results.

Note that strains and stresses in this section are obtained for a vertical displacement of 1 mm at the top edge, resulting in an averaged reaction stress of 29.8 N/mm^2 and an E-value of the specimen of E_{spec} = 3400 N/mm^2. This E-value was smaller than the E_{brick} of 4000 N/mm^2, due to the softer interface layer and the fissures in the model. The largest tensile stress occurred in the bottom brick - 15 mm from the edge - was 0.8 N/mm^2. The applied load was approximately three times the strength of this type of masonry.

8.5 ESPI results

8.5.1 General

As an example, the vertical ESPI-displacements of a JW specimen are plotted versus their X position in Figure 89. The deformation differences between brick and mortar are relatively small. The effect of a fissure at the edge is visible, indicated by the lines in the middle with a larger spacing. For comparison, another example is given in Figure 90, in which the joint deformation is more prominent.

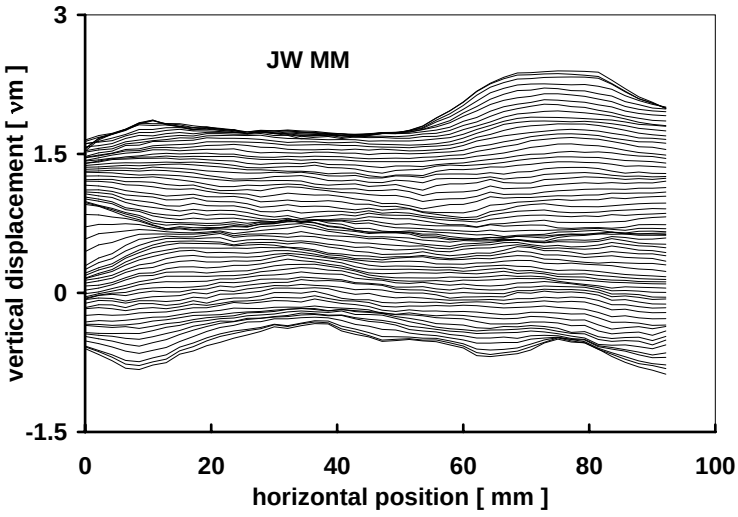

JW MM specimen

Figure 89 Vertical displacements versus horizontal position, $\Delta\sigma$ = 1 N/mm^2.

Depending on the brick mortar combination used, the 'joint' behaved more or less prominent. In general, in thin layer mortar specimens, the deformations were uniformly distributed over the width of the specimen. In specimens with thicker joints, deformation was more irregular.

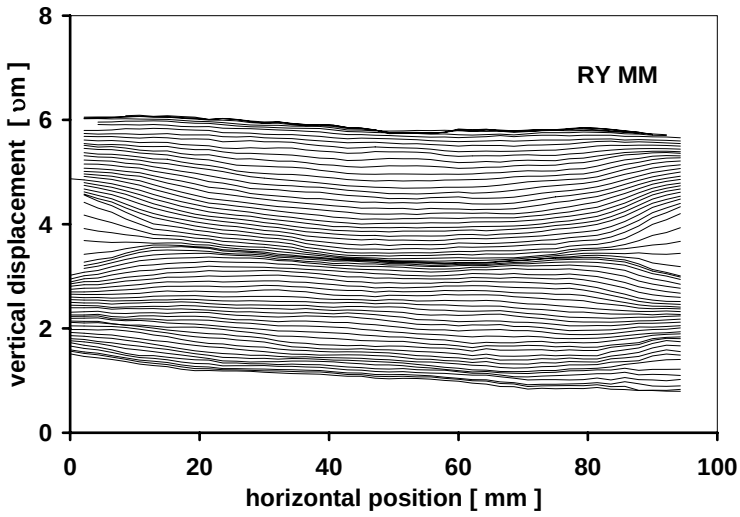

RY MM specimen

Figure 90 Vertical displacements versus horizontal position, $\Delta\sigma$ = 1 N/mm^2.

8.5.2 Comparison brick – mortar stiffness

In section 7.2.2 it is described how the ESPI results can be elaborated first to displacements, then to strains and finally to strains per N/mm^2 load. It is not clear where the fissure ends so in some cases, measurements are taken over the fissure i.e. a void. To prevent misunderstandings, strains per N/mm^2 load will be indicated as $\Delta l/l_r$. For further analyses, $\Delta l/l_r$ values were averaged over the width of the specimen, resulting in 'strain ratios' (SR), and where desired, E was calculated, ($E = 1/(\Delta l/l_r)$).

Table 5.3 in Appendix 5.3, lists the masonry deformation properties in more detail. Table 26 gives averaged strains ($\Delta l/l_r$) obtained for a stress increase of 1 N/mm^2 for brick, joint and specimen obtained at similar specimens.

Values for $\Delta l/l_r$ were obtained from brick deformation (lines AA'-BB' and CC'-DD'), from joint deformation (BB'-CC') and from specimen deformation between lines EE'-FF' in Figure 91. The $\Delta l/l_{r,mor}$ value was established including the brick-mortar interface, i.e. from the edge of one brick to the edge of the other brick, i.e. between lines BB' and CC' in Figure 91. The value $\Delta l/l_{r,spec}$ was established over joint and brick, lines EE'–FF' at a level comparable with the LVDT position.

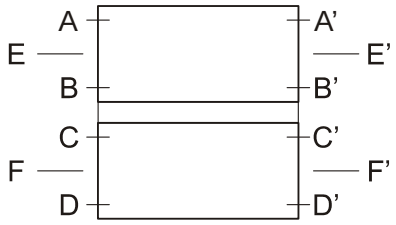

brick: level AA' BB'
joint: level BB' CC'
brick: CC' DD',
specimen: level EE' FF'

Figure 91 Levels used for the establishment E_{brick} and $E_{specimen}$.

The presented (averaged) strain values show the differences between mortar and brick properties. The ratios between mortar and brick strain, $\Delta l/l_{r,mor}$ /$\Delta l/l_{r,bri}$, are given in Table 26 as well. Largest ratios were found for HE and HY specimens, the smallest ratios for weaker brick types with MM and TL joints. The mortars used in combination with extrusion (JW and HE) bricks were relatively soft compared to brick stiffness (small ratios) and the mortars combined with relatively weak soft mud (RY en HY) bricks were relatively stiff (high ratios).

However, as all mortars were unique, a general tendency for the effect of joint thickness on mortar properties could not be established. Therefore, the same mortar should have been applied both for thick and thin joints. The 'averaged' brick mortar strain ratio equalled 0.63, Figure 92. Mortar 'strain' included interfaces, fissures and a few millimetres of the brick edges.
The LVDT measurements, obtained at the same load level indicate considerably smaller values for the modulus of elasticity of the specimen than the ESPI results, as shown in Table 26. The trend however is quite clear, R^2 = 0.96, indicating that LVDT values are 0.77 times the ESPI values.

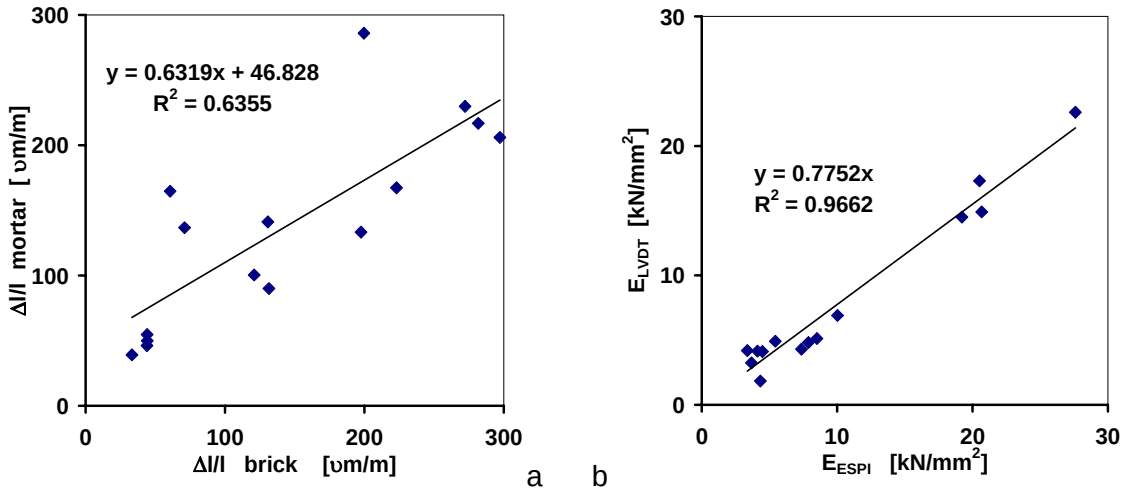

Figure 92 a) Averaged mortar strains ($\Delta l/l_{r,avg}$) versus averaged brick strains.
b) E_{LVDT} versus E_{ESPI} for comparison of the two methods.

Table 26 ESPI results (averaged). Relative strains ($\Delta l/l_r$) for brick, joint mortar and specimen. E values, ESPI results and LVDT results for specimen's deformation.

brick	AA'-BB' & CC'-DD'	joint BB'-CC'	specimen EE'-FF'	joint/brick ratio	$E_{specimen}$ ESPI *)	LVDT
	mm/m	mm/m	mm/m	--	N/mm^2	N/mm^2
JWGM	0.044	0.050	0.048	1.13	20677	14900
JWMM	0.044	0.046	0.049	1.05	20516	17300
JWTL	0.033	0.039	0.036	1.18	27601	22600
avg	0.041					
HEGM	0.061	0.165	0.100	2.72	10027	6900
HEMM	0.071	0.137	0.098	1.92	10174	13400
HETL	0.044	0.055	0.052	1.24	19216	14500
avg	0.059					
HUGM	0.200	0.286	0.231	1.43	4329	1840
HUMM	0.223	0.167	0.223	0.75	4484	4120
HUTL	0.282	0.217	0.243	0.77	4115	4150
avg	0.235					
RYGM	0.272	0.230	0.272	0.84	3675	3240
RYMM	0.131	0.141	0.136	1.08	7365	4300
RYTL	0.198	0.133	0.184	0.67	5433	4910
avg	0.200					
HYGM	0.132	0.090	0.127	0.68	7876	4820
HYMM	0.121	0.100	0.118	0.83	8505	5120
HYTL	0.297	0.206	0.297	0.69	3364	4190
avg	0.183					

*) $E_{spec,\ ESPI}$ from averaged $\Delta l/l_r$ values.

8.5.3 Vertical deformations and joint behaviour

In this section the deformation of the joint and, more specific, the effects of the fissures on the deformation are discussed.

In the previous section, the averaged $\Delta l/l_r$ values were used to establish the E-values presented in Table 26 in order to generally compare brick, mortar and masonry stiffness. This comparison only holds partly, because the strain distributions over the joint showed to be non-uniform, e.g. due to the fissures in the joint. Consequently, the strains at the edges do not give insight in the mortar stiffness.

Therefore, graphs that could explain the deformation distribution over the horizontal position in the specimen were made. These "strain ratio" (SR) graphs, presented in Figure 93 were made as described in section 7.2.2, page 93.

The SR-ratio is independent of the applied stress, but dependent of the dimension of the middle zone, which was based on experiences with fissure depth and visual observation of ESPI graphs. The chosen size of the middle zone shows the effects most clearly.

For specimens with TL mortar, the line oscillates around the value one over the full width of the specimen. These joints were completely filled. Specimens with GM and TL mortar have much larger values at the edges, indicating larger deformations.

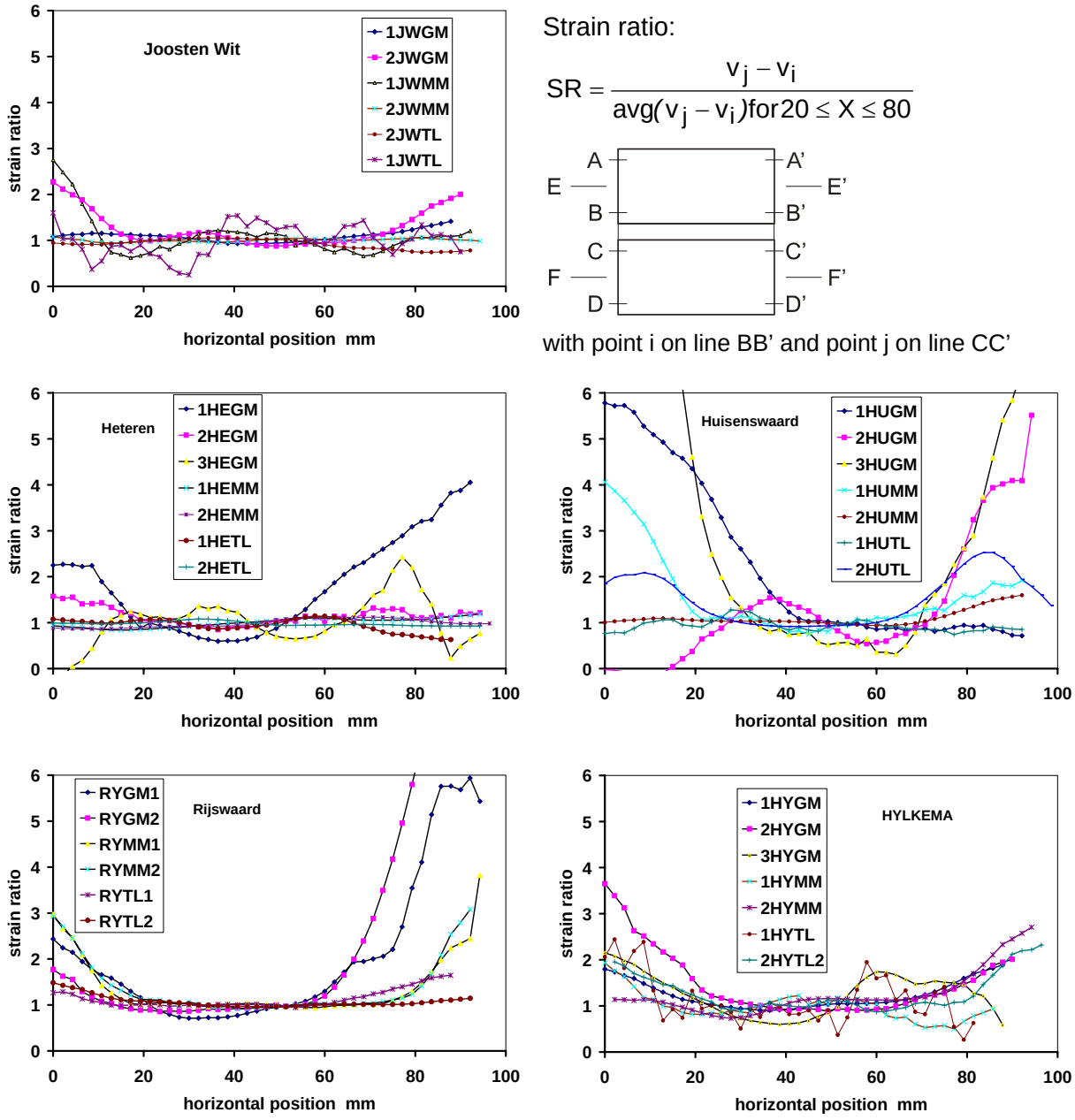

Figure 93. Strain ratio versus horizontal position for five brick types and 3 mortar types. The strain ratio is the ⊿l between two points with a certain X-value, divided by the averaged ⊿l in the middle of the joint (between 20 and 80 mm).

8.6 ESPI results obtained at various load levels.

Another important aspect is the evolution of strains and strain-distribution during a test. In most cases ESPI measurements were made at approximately one third of the estimated failure load. In a separate test series however, measurements were made in all stages of the test to follow strain development. For these tests, six specimens were made, with RY bricks, three with general purpose mortar and three with thin layer mortar. The general purpose mortar joints were 12 mm thick, the thin layer joints 3 mm.

The same procedure for determining $\Delta l/l_r$-values was followed as in section 8.5**.** In Figure 94 and Figure 95 $\Delta l/l_{r,mor}$-values are plotted versus horizontal position for the two times three RY specimens. The load levels at which the ESPI-measurements were taken, can be derived from the thicker parts in the stress-strain diagrams of Figure 94 and Figure 95.

The tendency of strain distribution is equal to the findings in section 8.5. However, the magnitude of the strain variation over the width, especially for RYTL, is larger because the thin-layer specimens had a recessed joint. The effect of this 'notch' can be seen in Figure 94 where the largest $\Delta l/l_{r,mor}$-values were found at this notch at the right hand side (80 mm < X < 100 mm).

The $\Delta l/l_{r,mor}$-value distributions for small and large loads differed most from the general trend. See e.g. the line for load step 4-6 in Figure 95 which deviates from the lines from the other load-steps. At small loads, instability effects of the moving seating arrangement are largest, see e.g. Figure 82, page 110.

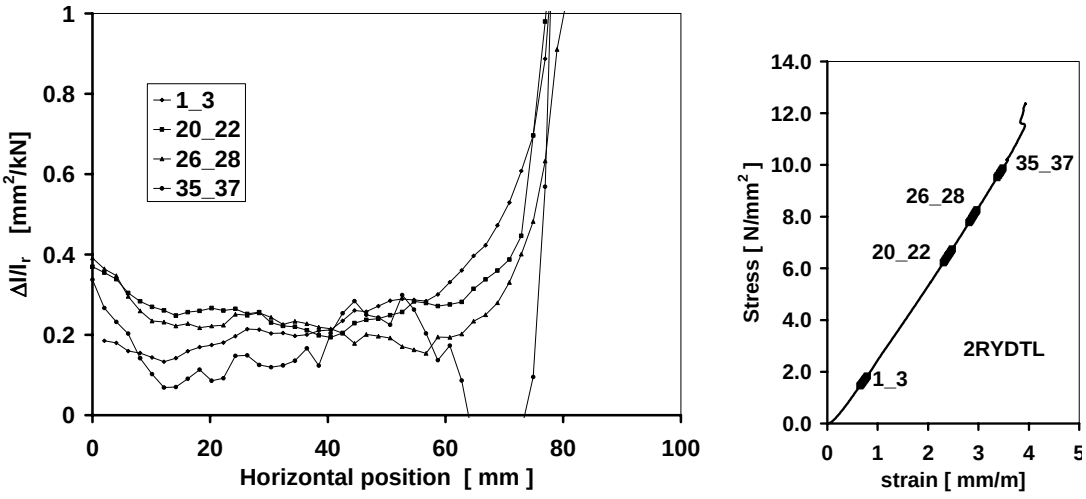

Figure 94 a) ESPI results, $\Delta l/l_{r,mor}$-values from measurements over the joint versus horizontal position. b) various load steps. RY specimen, TL joint.

When failure loads were almost reached, instability effects developed in the ESPI results, while the specimen started to crack and consequently, stress distribution through the specimens changed. This could be concluded from the variations in the N-M diagrams of e.g. Figure 82 and the σ-ε diagram of e.g. Figure 81.

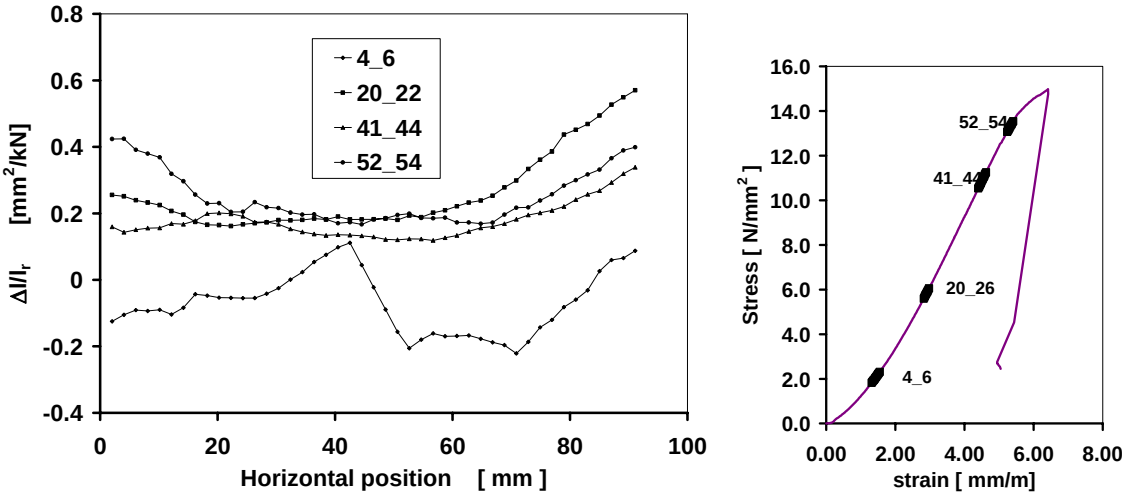

Figure 95 a) ESPI results, $\Delta l/l_{r,mor}$-values, from measurements over the joint versus horizontal position. b) various load steps. RY specimen, GP joint

8.7 Lateral displacements

When the behaviour of brick and mortar is modelled in detail, perfect interaction between brick and mortar is often assumed, e.g. Haller [HAL 58]. In these models it is assumed that the lateral expansion of both brick and mortar causes lateral tension in the brick and consequently failure. However, reliable values for lateral expansions are difficult to obtain from ordinary walls with LVDTs or Demec gauges. More insight in their magnitude is necessary to model masonry failure. Therefore, ESPI was used to measure the horizontal deformation of the specimens in the same way as the already discussed vertical deformations. Figure 96 shows an example of the horizontal displacements.

The data were handled in the same manner as the vertical deformations, as mentioned in sections 7.2.2 page 89. Now, the horizontal displacements of the grid points were plotted versus the Y-values of these points and the results of points with the same X values were connected with straight lines.

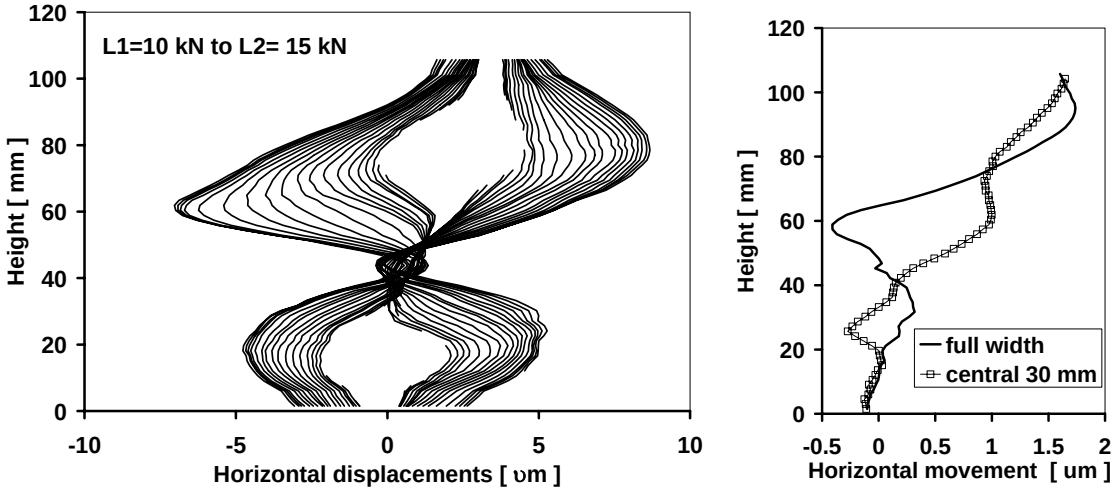

Figure 96 (left) Lateral displacements show a barrel ( ) shape in the bricks. (right) Movement of the centre of the specimen between lines GG' - KK' and HH' - LL' in the scheme of Figure 97.

In Figure 96 the horizontal movement of the specimen's centre is plotted versus height. The averaged displacement of the left hand side and the right hand side is calculated, i.e. $u_{avg} = (u_j-u_i)/2$ with point i on line GG' and point j on line KK', see Figure 97. As an alternative, the averaged displacement of two rows of points, one plus and the other minus 15 mm from the centre, lines HH' and LL', is calculated. The displacement lines in Figure 96 indicate that this specimen rotated during the test and kinked at joint height. Still, the similarity with DIANA results in Figure 87 is clear.

In most cases it became clear that the top brick rotated while the deformation of the bottom brick was more or less symmetric around the vertical axes. The top brick deformed more or less symmetric around an inclined line. Rotation of the top brick was already found when the vertical deformations were studied.
Figure 97 shows an overview of the horizontal strains, ε_r, for a specimen, calculated from:

$$\varepsilon_r = \frac{u_i - u_j}{(x_i - x_j)\Delta\sigma} \tag{36}$$

where (x_i-x_j) equals the width of the specimen. The strains, ε_r, are for a load increase $\Delta\sigma$ = 1 N/mm^2.
The strain distribution is influenced by the smaller deformations (and stresses) at the edges of the bricks, and of course by the difference in material properties. The position of the joints is clearly visible. The deformation lines suggest a 'barrel' ( ) shape as an effect of the confinement by the load platens and the joint. Not all tests gave reliable results, because horizontal deformations were too small.

Locally, strains will be much more irregular, as can be concluded from the distance between the displacement lines in e.g. Figure 96. In Figure 97 horizontal strains (ε_r-values) are plotted for three RY and four JW specimens respectively.

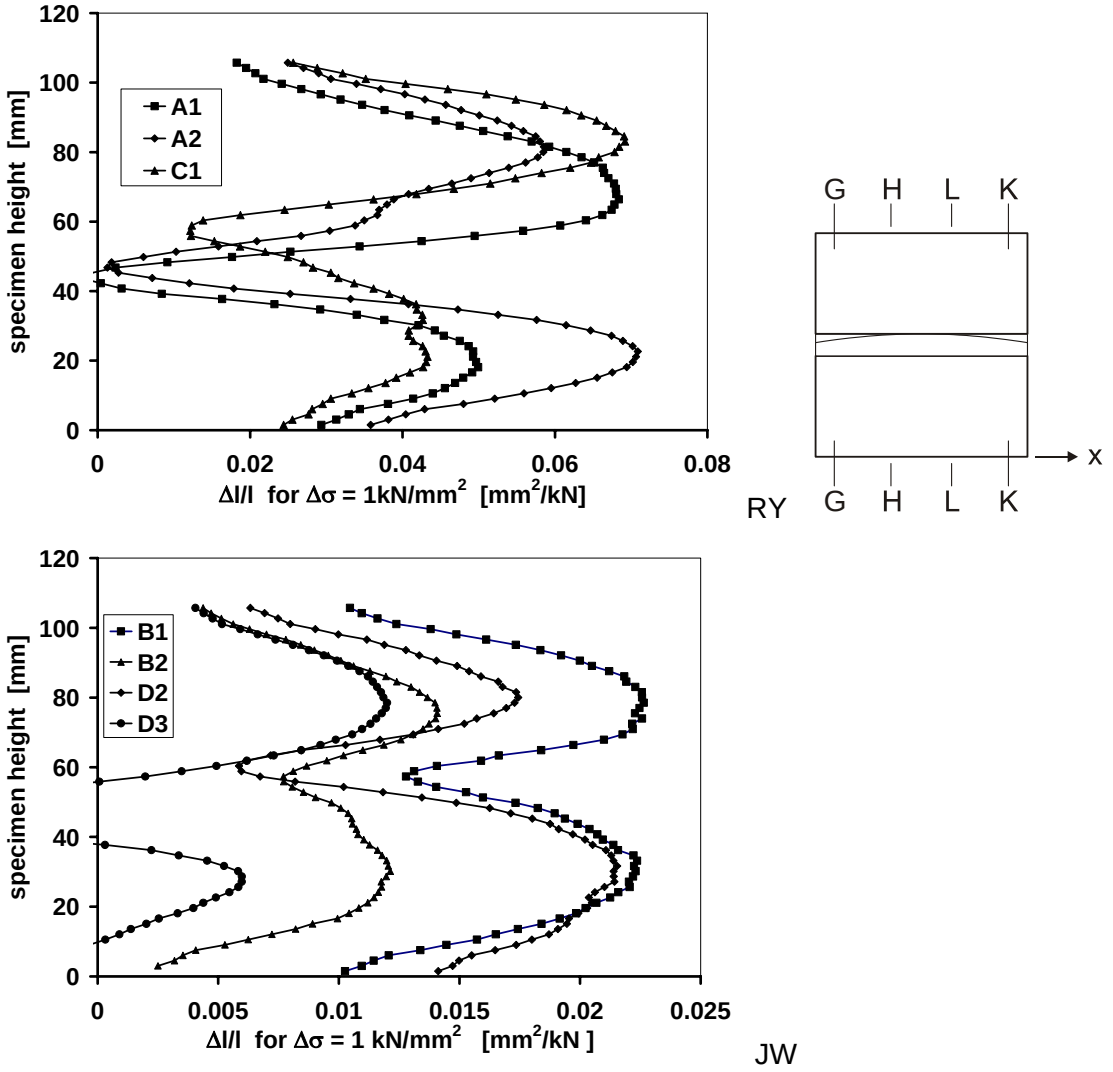

Figure 97. Examples of lateral strain distribution over height for RY and JW specimen. Strain calculated from displacement differences of points on line G and K.

Smaller ε_r-values were found at a height between 50 and 60 mm where the joint was situated. Probably, ε_r-values were smaller because the edges had smaller stresses than the central area. However, the shape and distribution of strains over the full width of the specimen and those over the 30 mm area were more or less equal, Figure 96. Consequently, an influence of stress differences between the outer and the central area could not be established.

The ε_r-values of the loaded top and bottom edges of the specimen were of the same order of magnitude as those of the joints, indicating that the confinement by the load platen (gypsum capping) was of the same order of magnitude as the confinement by the joint. Their magnitude also indicates that the confinement was not complete, contrary to the fully constrained boundary conditions in the DIANA simulation.

8.8 Comparison of ESPI results with LVDT results

8.8.1 General

A series of tests was performed to investigate the compatibility of ESPI and LVDT measurements. Therefore, measurements both with ESPI and LVDTs at one surface were carried out in order to allow for a good comparison between the results. Soft mud RY and extrusion JW specimens were used. The JW specimens were made with general purpose (GP) mortar, the RY specimens with GP and thin layer (TL) mortar. Two specimens for each parameter were tested, six in total.

For a comparison with ESPI, the LVDT results were added in the εr-graphs shown in Figure 98 and Figure 99. The $\Delta l/l_r$-values obtained with the left and right LVDT is presented by ♦ shaped markers and connected by a straight line. This line gives an indication of the rotation around the stiff (Z) axes of the specimen. Results of the LVDTs on front and back (X = 50 mm) were represented by a • and a ♦ marker respectively and their distance is an indication for the rotation around the weak (X) axes of the specimen.

The • marker is the $\Delta l/l_r$-value that was obtained from LVDT-measurements at the ESPI side (front) of the specimen from the centre of the top brick to the centre of the bottom brick. Ideally, this $\Delta l/l_r$-value (• marker) is on the line that represents the strain-distribution measured by ESPI between lines EE' and FF' in Figure 91. The marker should also be on the straight line between left and right LVDT. The distance between the • and the Δ marker is an indication of the difference between ESPI and LVDT results on the surface of the specimen.

The results of the left and right LVDTs (♦ marker) also should coincide with the line that represents the 'strain' of the specimen. In Table 26 the values of the LVDTs on the specimen's side were approximately 70% of the ESPI results. This confirms that the front surface of the specimens generally deformed most, probably due to bending effects, (Figure 83).

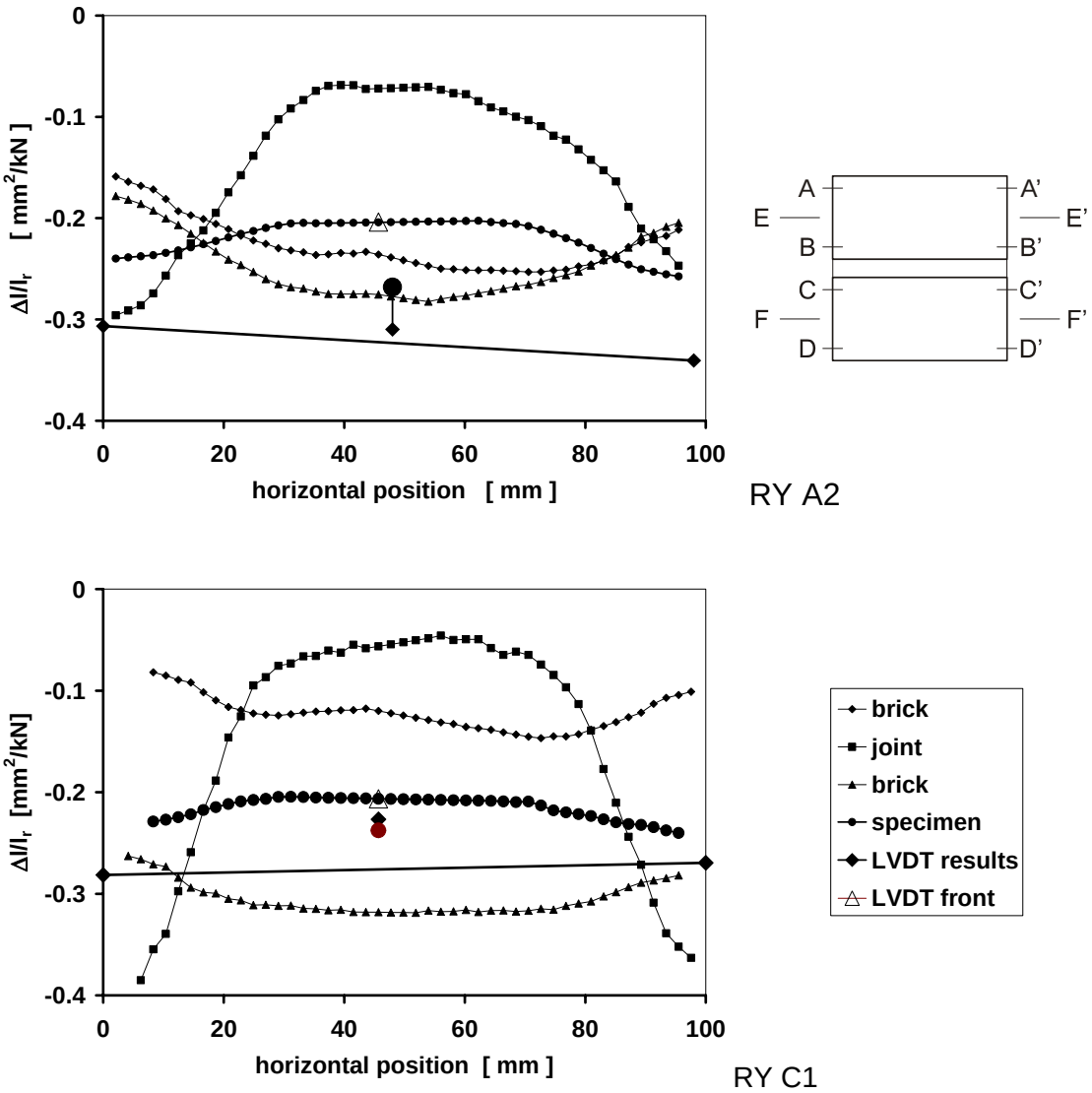

♦ = LVDT result, left, right, back. • = LVDT front. Δ interpolated value ESPI

Figure 98 Strain ($\Delta l/l_r$) versus horizontal position of RY specimens. Large differences in brick strain can be observed. Brick: level AA' BB' and CC' DD', joint: level BB' CC' specimen: level EE' FF'.

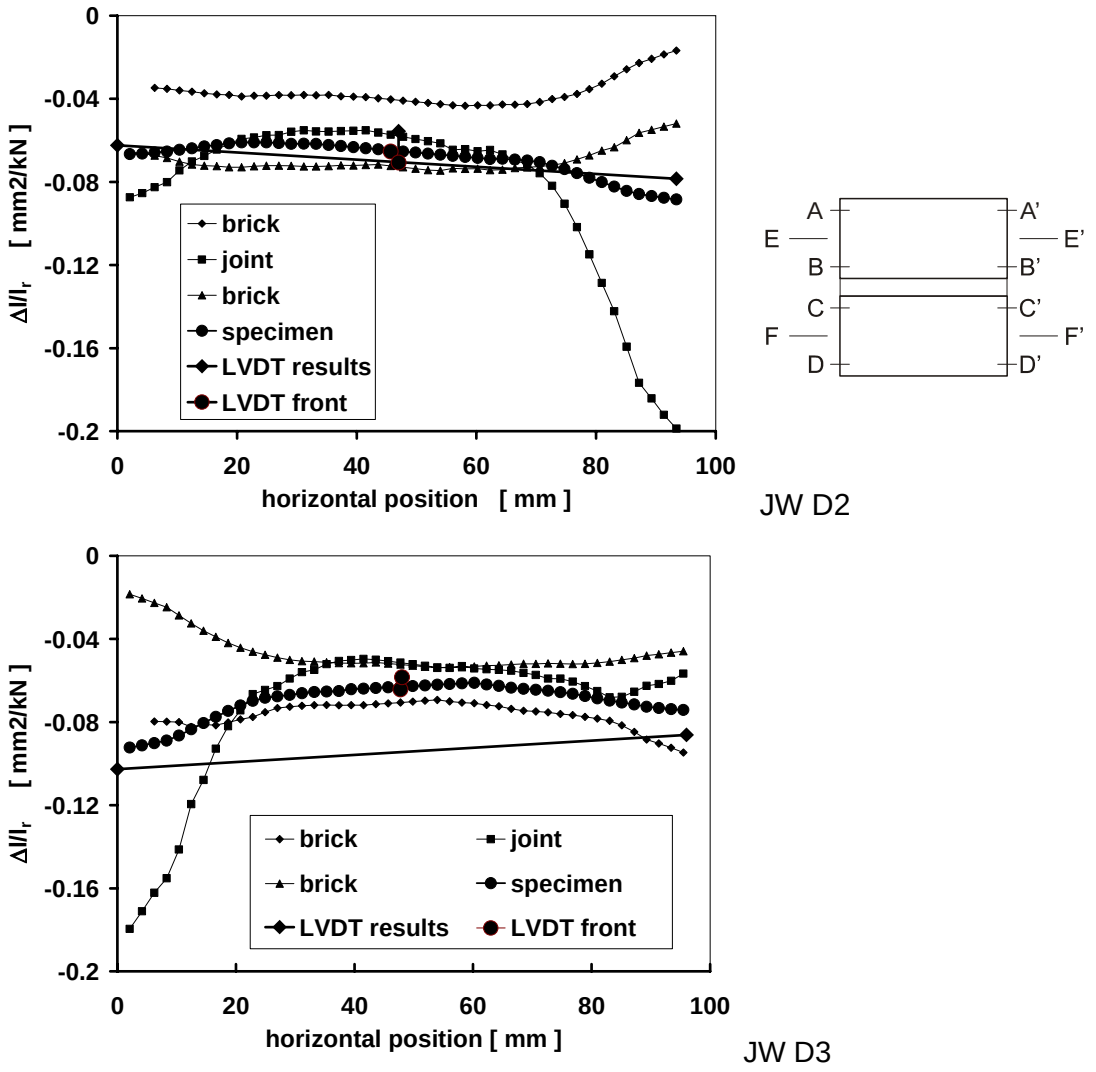

Figure 99 The $\Delta l/l_r$ distribution versus horizontal position of JW specimens. Smaller differences in brick strain can be observed compared to RY specimens.

Brick: level AA' BB' and CC' DD', joint: level BB' CC' specimen: level EE' FF'.

LVDT measurements also confirmed the directions of the eccentricities obtained from the forces measured with the three load-cells in the MSA discussed in section 7.3. Table 27 shows the $\Delta l/l_r$-values that were established with LVDTs and ESPI. The $\Delta l/l_r$-values of the LVDT results were calculated using the results of the same load increment (from L1 to L2 given in Appendix A.5.4.1) as used for the ESPI measurements. The ratio ESPI/LVDT varied between 0.76 and 1.10. In thickness direction, i.e. in the ESPI view direction, the eccentricity effects are larger as already noticed in section 8.3.

Table 27 Strains ($\Delta l/l_r$-values) in mm/m for LVDT and ESPI measurements

Specimen	LVDT	$\Delta\sigma$ = 1 N/mm^2			average	ESPI	ratio
	left	right	front	back	4 LVDTs	front	ESPI/LVDT
			A			B	*)
RYA1	0.386	0.414	0.235	0.390	0.356	0.2256	0.96
RYA2	0.307	0.341	0.268	0.310	0.306	0.2038	0.76
JWB1	0.081	0.083	0.052	0.104	0.080	0.0443	0.86
JWB2	0.024	0.076	0.060	0.054	0.053	0.0500	0.82
RYC1	0.281	0.269	0.238	0.227	0.254	0.2065	0.87
RYC2	0.333	0.252	0.185	0.281	0.263		
JWD2	0.062	0.079	0.071	0.056	0.067	0.0653	0.92
JWD3	0.103	0.086	0.058	0.062	0.077	0.0643	1.10

*) Values column A divided by values from column B

8.8.2 Joint and brick behaviour

As strains ($\Delta l/l_r$) for the joints varied most, these were isolated for similar specimens from the $\Delta l/l_r$-figures in Figure 98 and Figure 99 and collected in Figure 100 and Figure 101. As stated earlier in section 8.5.3, the $\Delta l/l_r$ values at the edges are larger for the joint and smaller for the bricks than averaged strain. The load was clearly transmitted through the central 60 to 70 mm of the specimen, caused by fissures in the bed joint.

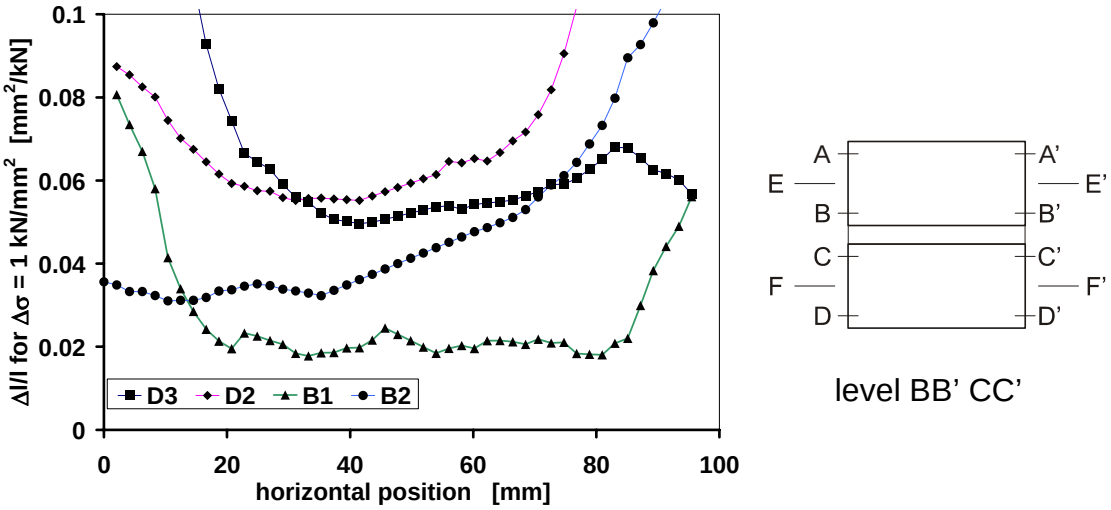

Figure 100 . Result for $\Delta l/l_r$-value distribution from vertical deformations of the joints for Joosten (JO) specimens. $\Delta l/l_r$-values.

For the JW specimens it is clear that the averaged E-value of the bedding mortar must be of the same order of magnitude as the E-value of the JW units while the measured strains are of the same order of magnitude, see Figure 101. Roughly, the E-value was 16,500 N/mm^2.

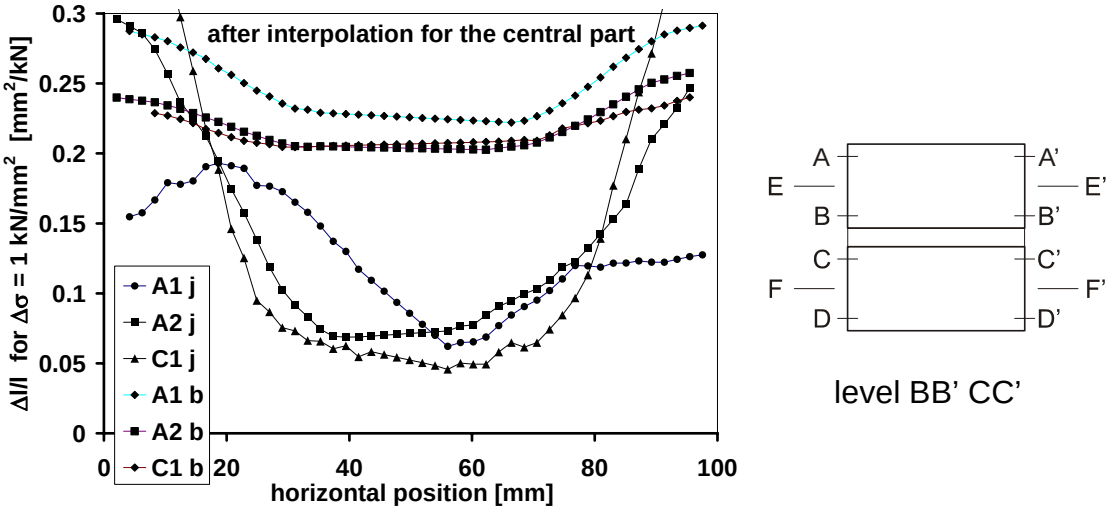

Figure 101 Result for $\Delta l/l_r$--value distribution from vertical deformation of the joints (j) and brick (b) for Rijswaard (RY) specimens

Strains for the top and bottom brick showed in some cases a considerable difference, maybe because of the bending effects as discussed earlier in section 8.3, page 110, due to the movement of the MSA bottom plate.
In Figure 101 not only joint, but also the averaged top and bottom RY brick 'strains' are plotted. The brick 'strains' were much more evenly distributed than joint deformations.

The RW brick strain was approximately 0.2 * 10^{-3} mm/m that means E = 5000 N/mm^2. The mortar strain was 0.075 mm/m or E_{mortar} = 13000 N/mm^2. The E-value of the brick was almost equal to the value in Table 23, which was obtained from tests on separate bricks.

8.9 Conclusions

• For GP and MM mortar joints, the ESPI measurements showed that the largest 'strains' occurred at the edges of the observed surface. For completely filled TL joints, strains were almost equally distributed over the full joint.

In each brick-mortar combination the E-values of brick and mortar were of the same order of magnitude, values found with ESPI resulted in E_{brick} = 1.14 E_{joint} on average, with 0.68 as the smallest and 2.72 as the highest ratio.

The $\Delta l/l_{r,mor}$-value distributions for small and large loads differed most from the general trend. At small loads, instability effects of the moving seating arrangement are largest.

- Mortar compressive strength according to [NEN 3835] is much smaller than brick strength (Table 23), however E-values (ESPI results) are almost equal.

  The tested mortar specimens hardened in a steel mould and consequently were mortar properties differed from the mortar that hardened between bricks.

  For each brick-mortar combination a different mix design was used. The effect of Joint thickness (mortar) had no effect on strength nor stiffness, except for the more uniform strain distribution in completely filled TL joints.

- Lateral deformations show effects of joint imperfections on the deformation of the joint.

  The order of magnitude of the lateral strain at a vertical load of 1 N/mm^2 is equal per brick type. As lateral deformations were smaller than the vertical ones, the results were less accurate. However, the horizontal movement of the specimens became clear.

- On average, the strength of the 25 mm thick specimens was 1.5 times the strength of masonry prisms made with the same materials.

  The main cause for this difference is the fact that a specimen only has one joint, compared to the seven joints in the prism. However, Young's modulus was the same for both specimen types. In general, 25 mm specimens behaved more brittle than masonry prisms, strong 25 mm specimens even 'exploded'.

- The load eccentricity followed from the three load cell recordings.

  Comparing ESPI and LVDT results, the effects of bending in the specimen were estimated. The horizontal movements of the bottom plate caused bending moments. The largest bending effects on strain distribution were found in thickness direction. Variations of load eccentricity (bending) in the widest direction were found when pieces of brick spalled (chips of brick came loose) from the specimens. Vertically, the load platens moved parallel to each other.

9 Brick-mortar interaction in eccentrically compressed specimens

Abstract

In this chapter, the results of tests on eccentrically loaded, 25 mm thick masonry specimens are discussed. The specimens were made from the same couplets as those discussed in Chapter 8. Locking of the bottom load platen in the appropriate direction reduced the effects of bending around the weak axis of the specimen. The deformations were observed with ESPI and LVDTs. M-N relationships are obtained from the measured deformations and compared with theoretical results. The results confirmed the expected uneven strain distribution. The fissures between brick and mortar affected bending stiffness. Together with the LVDT measurements, the ESPI results were compared with strain distributions obtained from numerical simulations with DIANA. Moment curvature diagrams showed a shift when changing from positive to negative rotations. Most of this rotation took place in the joint.

9.1 Introduction

The studies described in the previous section have shown that the fissures cause a non-uniform strain distribution in concentrically loaded specimens. In this section, the effects of load eccentricity on deformation are discussed. Therefore, specimens like the ones used for investigating the effect of joint thickness were loaded with certain predetermined eccentricities. The deformations were measured with LVDTs to study 'overall' behaviour and with ESPI for detailed behaviour. DIANA software was used to explain the expected behaviour.

9.2 Experimental details

9.2.1 Materials

Three wire cut- and three soft mud brick specimens 25 mm thick, with a joint thickness of 15mm and general purpose mortar were cyclically loaded with five eccentricities. The specimens were similar to the ones used for testing the joint thickness effects as described in Chapter 8. Brick and mortar properties are presented in Table 23.

The couplets made from soft mud bricks were broken before preparation into one 'clean brick' and one with all mortar attached to it. The two loose parts of the couplet fitted well to each other and were clamped together during cutting of the specimens. The specimens obtained in this manner were used to study the closing effect of cracks.

9.2.2 Eccentricities

Tests were carried out in a Schenck tensile testing machine using the moving seating arrangement (MSA), presented in section 7.3. Normally, the lower plate could move freely in all horizontal directions. In this case the movement of the lower plate was prevented in one direction, through the use of special ball-bearings.

The specimen was positioned on a steel plate connected with the lower plate of the moving seating arrangement. The specimen was loaded through a 30 mm thick steel plate and another two plates with slots in the appropriate positions to enable application of eccentricity through a pin. Using magnets, these plates were kept in position when changing the pin's position, in order to obtain the desired eccentricity. The five eccentricities used were: -32 mm, -16 mm, concentric, +16 mm, and +32 mm, measured from the centre in X-direction, and referred to as positions a, b, c, d and e, respectively.

Figure 102 Detail of eccentric load introduction using, a steel 7 mm diameter bar.

9.2.3 Measurements

The applied forces were measured with the three load cells of the MSA as described in section 7.3. The LVDTs positioned in the centre of the side surfaces of the specimen measured the deformations of the specimens. Their gauge length was 65 mm.

The ESPI equipment measured the deformation of a part of the specimen's front surface of approximately 100×100 mm^2.

Each specimen was loaded in 5 cycles, each cycle having a different eccentricity. At the end of each load cycle, ESPI measurements were made. Target values for the maximum load in each cycle and target values for stresses for ESPI measurements (according to linear elastic behaviour) are given in Table 28. When loaded at positions a and e, the JW specimens were considered to be uncracked, i.e. tensile stresses were considered possible. For the RY specimens the cracked situation was taken into account. Stresses were established as described in Appendix A.3.2.2 for the uncracked and for the cracked situation.

Table 28 Target values for maximum load (kN) and stress (N/mm^2) per cycle.

	Load position →	a - 32 mm	b -16 mm	concentric 0 mm	d 16 mm	e 32mm
JW	Load	12.5	15.5	30.0	15.5	12.5
	stress at left	-14.6	-12.0	12.0	0.0	4.6
	right	4.6	0.0	12.0	-12.0	-14.6
RY	Load	4.0	5.6	10.0	5.6	4.0
	stress at left	-5.9	-4.3	4.0	0.0	--
	right	--	0.0	4.0	-4.3	5.9

9.3 Numerical simulations

Similarly as for the concentric test series, DIANA was used for some explorative numerical simulations to obtain an indication of the expected deformations. Specimen's dimensions were as described in section 8.4. The same model was used; only one loading point was removed. Figure 96 shows contour plots of the displacements and stresses of the eccentrically loaded specimen.

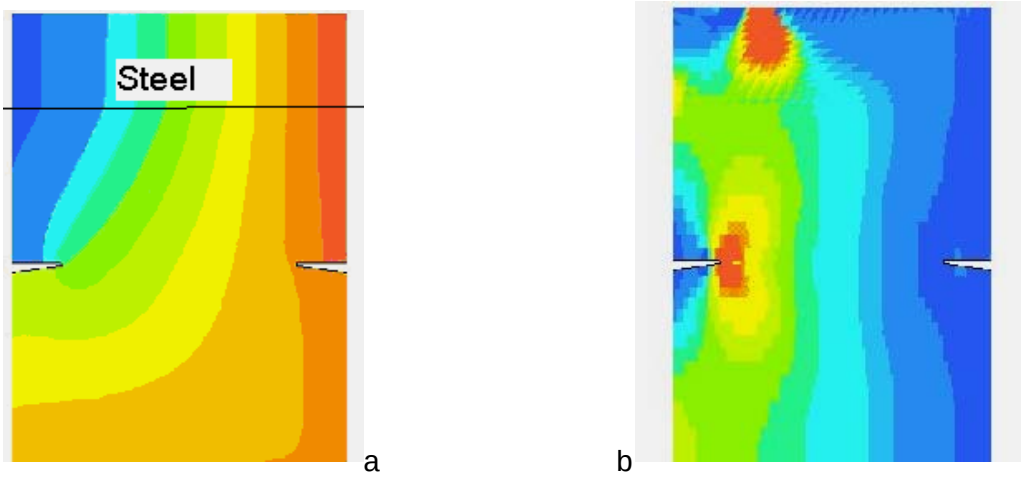

Figure 103 Vertical displacement a) and b) stress contour plots of an eccentrically loaded model, DIANA results.

Similar to the concentric loaded example, the parts of the specimen above and below the cracks remained without stress. Peak stresses occurred at the load introduction point and at the crack tips.

The vertical displacement of each node was plotted versus the X-value of the node, in in Figure 104. The marked dot in Figure 104 represents the displacement of 1mm of the load-introduction point. The horizontal line represents the displacement of the nodes in the bottom row. The most oblique line represents the displacements of the top row of nodes of the specimen. The deformation of the steel plate was omitted.

The effect of the joint with its fissures is similar to the concentric loaded case, i.e. displacements of nodes are smaller near the open joints. The displacements fan out at the end near the fissure. Nodes of the bottom brick displace more and those of the top brick less than expected for a closed joint. Symmetry around the joint can be observed, as in the concentrically loaded model.

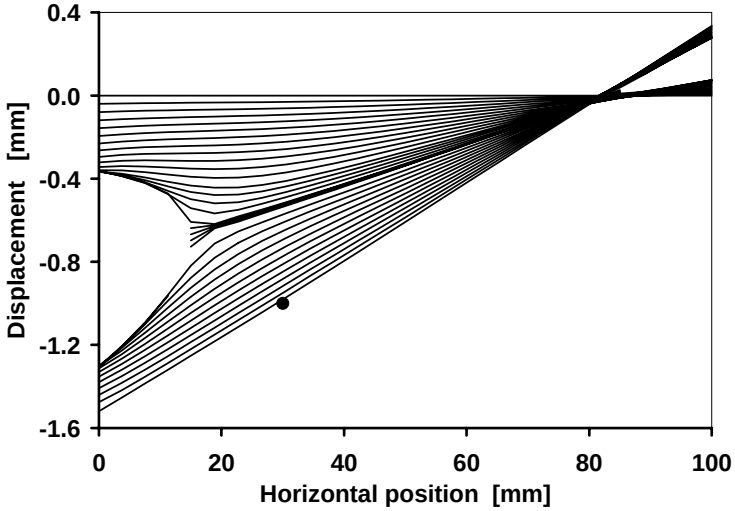

Figure 104 Vertical node displacements for an eccentrically loaded specimen, DIANA results.

From node displacements at the edges of the bricks, strains were calculated for top and bottom units and for the joint with the method described in 7.2.2, page 92, used for the ESPI results.
In Figure 105, the calculated strains are plotted versus their horizontal position. Strains for the top and bottom unit are almost equal. The joint showed a high strain level near the open cracks and positive strain at the unloaded, right hand side.
The DIANA-stresses at the brick edges near the loading plates, are linearly distributed over the width. Near the joint, peak stresses can be observed, especially at the crack tip in the softer interface layer, as expected from the theories described in section 2.4.3, page 17.

Results of numerical simulations may be used for comparison with ESPI results. The stress distribution is almost linear for X between 10 and 90 mm. The averaged stress (σ = N/A) for the (eccentric) simulation was 21.48 N/mm^2. The position of the resultant of the stresses in Figure 106 coincided with the applied eccentricity of 30 mm.
The strain distribution at the horizontal edges of the specimen edges is linear, Figure 105. In combination with an averaged strain of 0.0053 mm/m - obtained with a displacement of 1mm (the dot in Figure 104) and a 'length' of 115 mm - results in a modulus of elasticity of E_{spec} = 4053 N/mm^2.

The E value is of the same order of magnitude as E_{brick}. Differences are caused by the stiffer mortar, the modelled fissures and the interface layer with an $E_{interface}$ = 1000 N/mm^2.

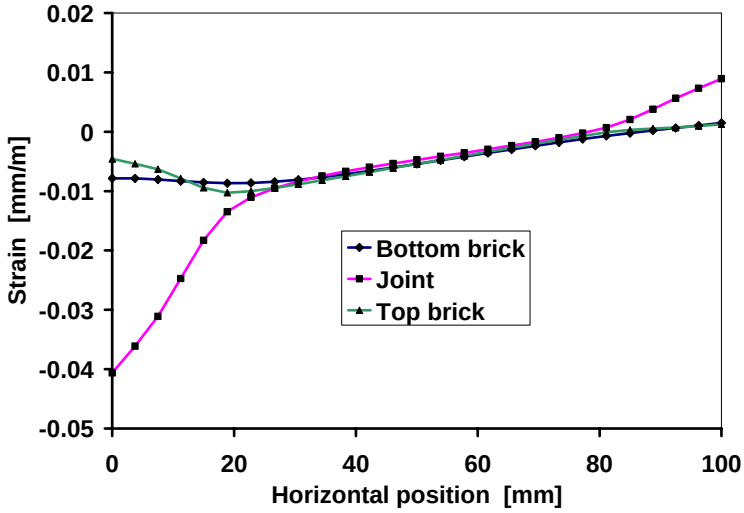

Figure 105 Strain distribution versus horizontal position, DIANA results.

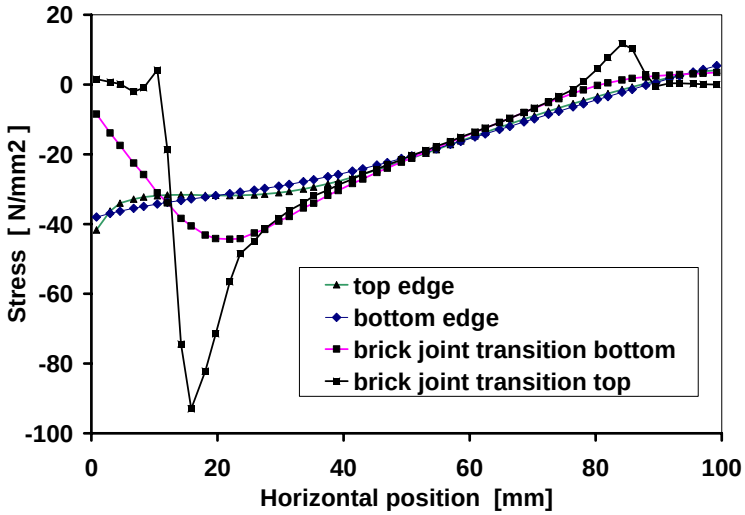

Figure 106 Stress distribution versus horizontal position, DIANA results.

9.4 Results of LVDT measurements

9.4.1 Strength and Young's modulus

In each load cycle, deformations were measured with two LVDTs in the centre of each of the narrow sides of the specimen. The Joosten graphs showed that some force had to be applied before deformations started. The surface of the specimen, where the LVDTs have been positioned, is not in full stress right from the start of the test, possibly due to cracks but also because of the fact that the loaded surfaces were not exactly

parallel and load platens were not in full contact. Another cause may be the friction in the LVDT. The steel core of the LVDT may have experienced some friction which could have caused an interruption in the measurement when changing from 'shortening' to 'elongation'. This will be discussed further in section 9.4.4, page 139, along with the M-φ effects.

The RY graphs show that the specimens can be deformed quite easily at the start. For larger loads, (stresses larger than 1 N/mm^2) a more or less linear relationship for the RY specimens was found.

Loaded concentrically (position c), the E-values presented in Table 29 were obtained from the linear parts of the graphs. The mentioned starting effects were neglected. Both for the wire cut and for the soft mud specimens, one odd E-value was found. It may be remembered that the applied stresses were smaller than 1/3 of estimated failure load and, as a result, cracks and fissures were probably not fully closed yet.

Table 29 E values from specimens loaded concentrally in pos c.

Specimen	$E_{specimen}$ N/mm^2	Specimen	$E_{specimen}$ N/mm^2
JW 1	21400	RY 1	3000
JW 2	15350	RY 2	1130
JW 3	22750	RY 3	2900
DIANA result	page 114	RY	3400
DIANA result	page 132	RY	4053

Loaded eccentrically, the slope in the JO σ-ε graph decreases with larger eccentricity where specimens were uncracked at the end of the test. A decreasing stiffness could indicate some effect of cracking on averaged strain.

In cracked sections, like for RW, the gross stress (σ_{gr}) is less than half the maximum compressive stress ($\sigma_{c,c}$), Figure 107. The ratio between the maximum compressive stress and the gross stress for cracked sections, depends on the ratio between the 'depth' of the section (d) and the size of the stress area (x) and equals 2d/x, (Figure 107). For eccentricities of 1/3 of the width, this ratio is 4. The equations used are given in Appendix A.3.2.2.

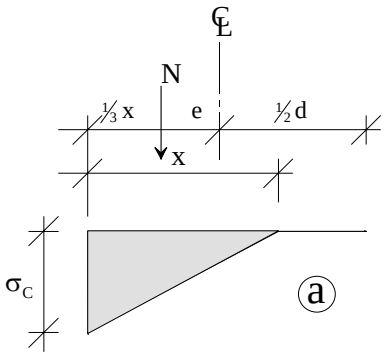

Figure 107 Stress distribution in a cracked section.

In general, σ-ε diagrams for RY were much more irregular than for JW specimens. Figure 108 shows the $\sigma_{gr}/\varepsilon_{avg}$ diagrams for specimen RY 3. In these diagrams the averaged strain was plotted versus the averaged gross stress.

After some initial settlement, the σ_{gr}-ε_{avg} diagrams for the specimen loaded in positions pos a and pos e are almost vertical. This means that no increase in average strain occurred. For an eccentricity of 32 mm, which is almost 1/3 of the width, x = 0.5 d. Consequently, the tension strain at one side (ε_t) is almost equal to the compression strain at the other side ($\varepsilon_{c,c}$) and consequently, averaged strain equals almost zero.

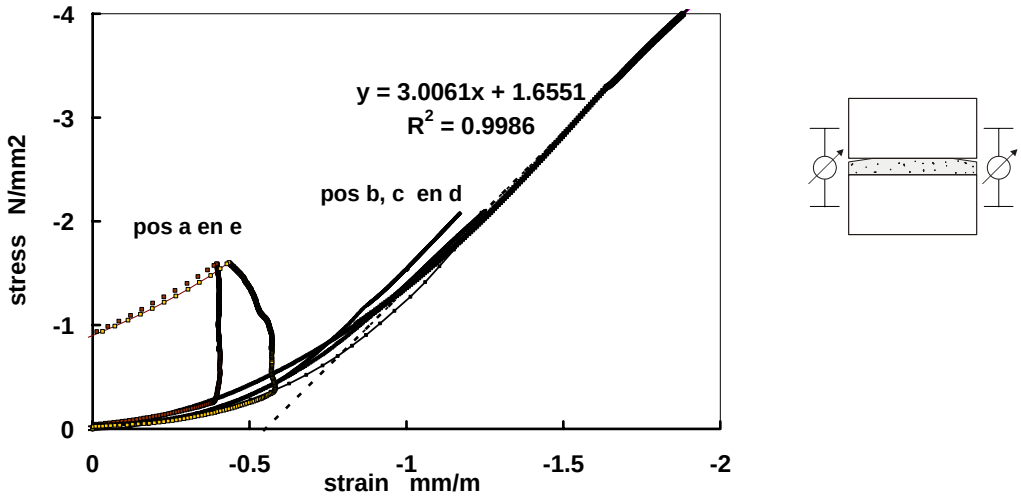

Figure 108 Overview of σ-ε diagrams for various eccentricities (LVDT results, RY3).

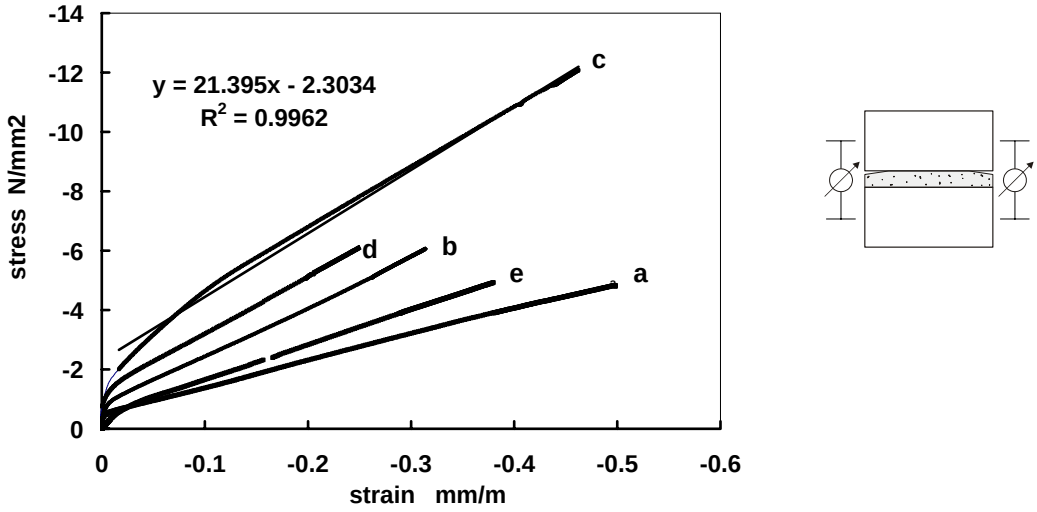

Figure 109 Overview of σ-ε diagrams for various eccentricities (LVDT results, JW1).

9.4.2 M-N diagram

The use of load cells allowed for the establishment of the bending moment from the difference of load cell results and their distance. The relationship of moments (M) to normal forces (N) is of the form:

$$M = N\,e + M_0 \qquad (37)$$

as discussed earlier in section 7.3.3, page 98. Figure 110 shows an example for RY1. The factor M_0 is 23.4 kNmm on average for the three JW specimens. The value of M_0 represents the moment that has to be applied at the start of the test, (N = 0 means: M = M_0). Specimen and test set-up interact and settle. This is a phenomenon similar to the one, explained in section 7.3.3 for concentric testing, but that phenomenon is mainly caused by the fact that one corner of a specimen is touched first when the test starts. This 'settling' could be (part of) the explanation of the horizontal part in the M-φ diagrams, (section 9.4.4).

For the RY specimens the intersection of the best fits through the linear parts of the graph is situated at – 0.3 kN and a moment of 20 kNmm. A similar value for M_0 as for the JW specimens, was required. Although some irregularities were observed at the start of the tests, the M-N relationship could be established accurately using a linear best-fit relationship for the measured data.

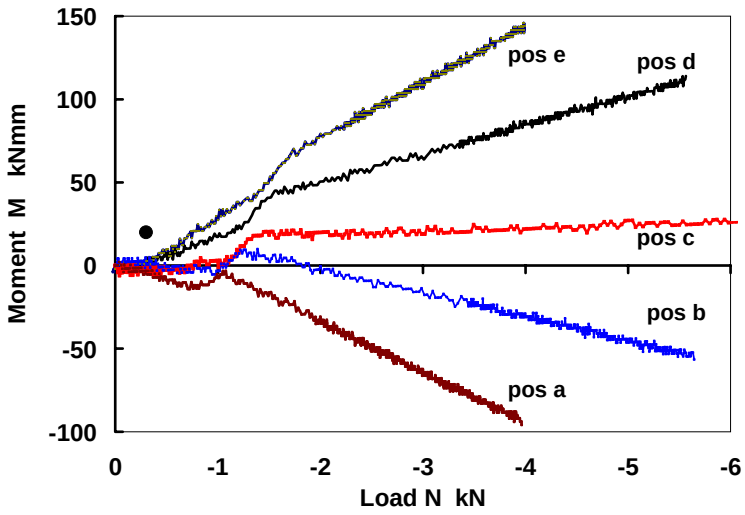

Figure 110 M-N diagram for RY1 for various eccentricities. After some initial effects a linear M-N relationship.

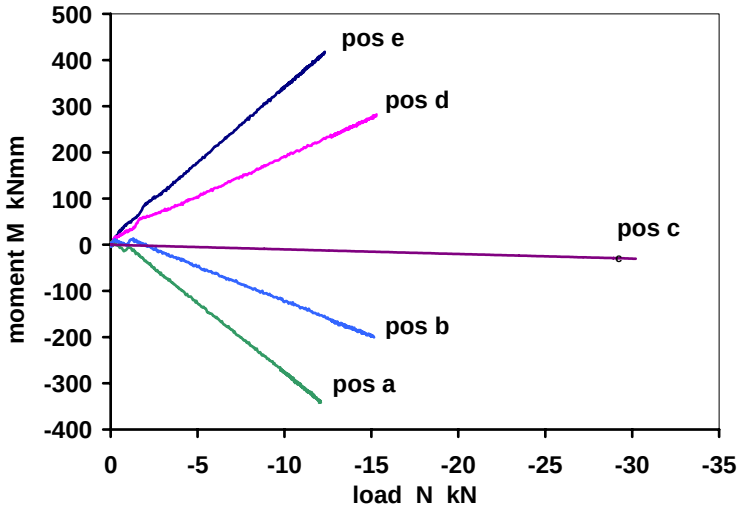

Figure 111 M-N diagram for JW 1 for various eccentricities. Hardly any initial effect and linear relationship, i.e. constant eccentricity.

9.4.3 Eccentricities during ESPI measurements

For each ESPI measurement the first speckle pattern was taken at load L1 and after some increase the second pattern was taken at load L2. An almost constant ratio between M and N was observed in e.g. Figure 110 and Figure 111.

In Figure 112 the target values for the eccentricity are plotted versus the measured values. For the RY specimens the relationship between realized (e_{real}) and desired (e_{desi}) eccentricity was:

$$e_{real} = 0.874\, e_{desi} + 5.63 \qquad (38)$$

For JW specimens the relationship was:

$$e_{real} = 0.96\ e_{desi} + 2.35 \quad (39)$$

These (relatively minor) deviations between realized and desired eccentricities may be caused by a) measure deviations in the system, b) errors arising from the positioning of the specimen. c) interaction between the system and the specimen and d) the out of line position of the specimen.

The latter means that the system line of the moving seating arrangement did not coincide exactly with the centre of gravity of the specimen. This may be considered as a systematic error. Moreover, the middle of the width of the specimen was not necessarily the centre of gravity of the specimen.

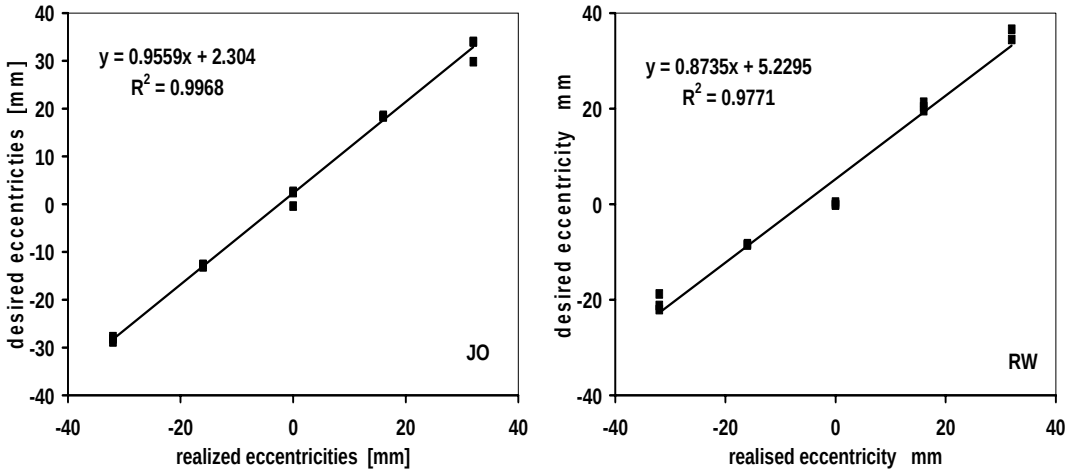

Figure 112 Desired versus realised eccentricities, $e_{desired}$ versus $e_{realized}$.

9.4.4 Moment rotation diagram

The eccentricity of the applied load produced a bending moment and the loaded surfaces rotated. From the difference in LVDT results the rotation angle φ was established. M-φ relationships are presented in Figure 113 for JW and RY respectively. In the results of the φ calculations, the effect of the closing of the crack over the full width is apparent in all RY cases.

As mentioned earlier, these specimens were broken in two, a piece with most of the mortar connected to it and the other one almost clean. These two pieces fitted closely, however, some contact had to be restored.

When the load increased, stiffness increased and σ-ε relationships became almost linear. The RY3 specimen gave the best (smoothest) M-φ relationship. Analysing the results using the equations in Appendix A.3.2.2 gave an E-value of 2100 N/mm^2. This value is smaller than the experimental values presented in Table 29, page 134.

For JW an E-value of 16700 N/mm^2 was found from the M-φ relationship. This value is of the same order of magnitude as the values presented in Table 29.

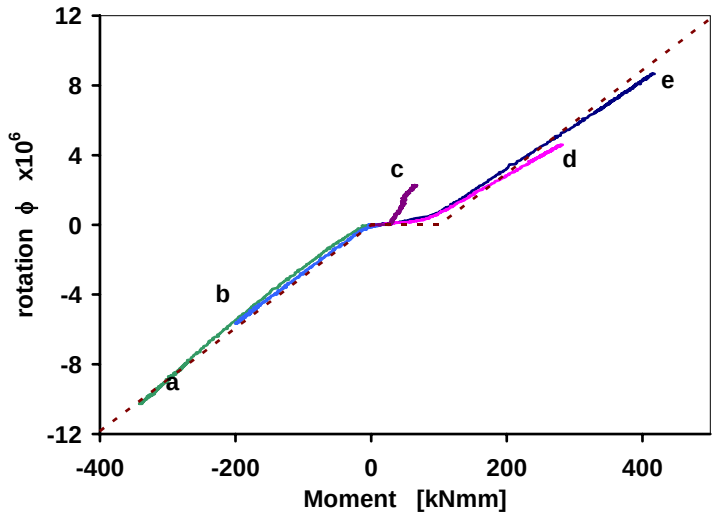

gauge length 65 mm

$$\varphi = \frac{\Delta l_{left} - \Delta l_{rigth}}{65}$$

JW1

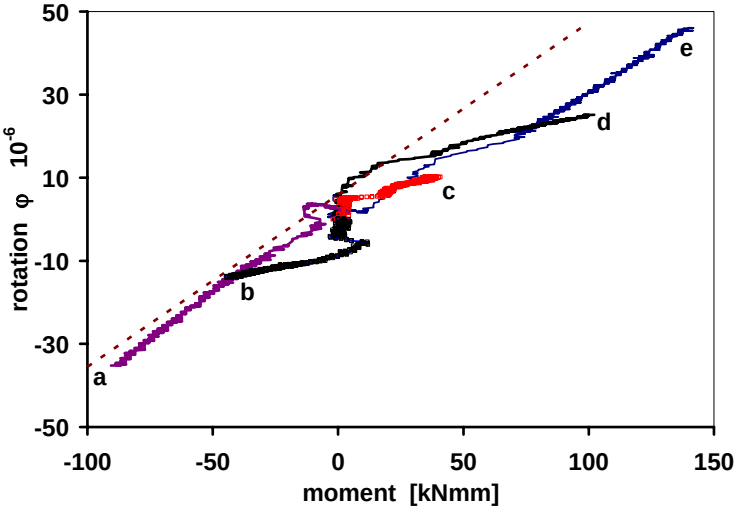

RY 3

Figure 113 M/φ diagram for JW1 and for RY3

The shift from positive to negative rotation may be caused by friction in the LVDTs as mentioned in section 9.4.1. However, all specimens showed some irregularities around the origin, both for loads and deformations, so the 'instability' of the moving seating arrangement may have been a cause as well. It takes some force to become a 'stable' situation and after that, curves become smooth. The system - specimen and MSA - reacts more or less at random at first.

Another aspect is the opening and closing of the fissures, see section 2.4.3, page 17. Loaded concentrically, both fissures are in compression and 'closing'. Loaded eccentrically, one fissure is 'closing' the other one is 'opening' (cracking). Changing eccentricity, from negative via concentric to positive, causes the effective joint area to shift from left to right.

In the concentric situation, the behaviour was less stable than in the eccentric situation. Loaded in position c, (concentrically) the M-φ relationship was odd. Ideally, both M and φ should have been zero. Initial effects were observed in the σ-ε diagram as well, Figure 109. However, the unintended eccentricity and the higher load caused some moment and rotation. This again shows that the centre of the loading system did not exactly coincide with the centre of gravity of the specimen.

9.5 ESPI results

9.5.1 General

As an example, the vertical ESPI-displacements of specimens RY3 and RY2 are plotted versus their X position in the Figures 114, 116 and 117. The deformation differences between units and joint are clear. The lines in the middle with the largest spacing correspond with the brick mortar transition in the specimen. It has been previously stated that the RY specimens were cracked before testing. RY specimens also had a sanded surface and as a result, the deformation in the transition area is larger. Compare the ESPI-results in Figure 114, 116 and 117 with Figure 104, the DIANA result and the resemblance becomes clear.

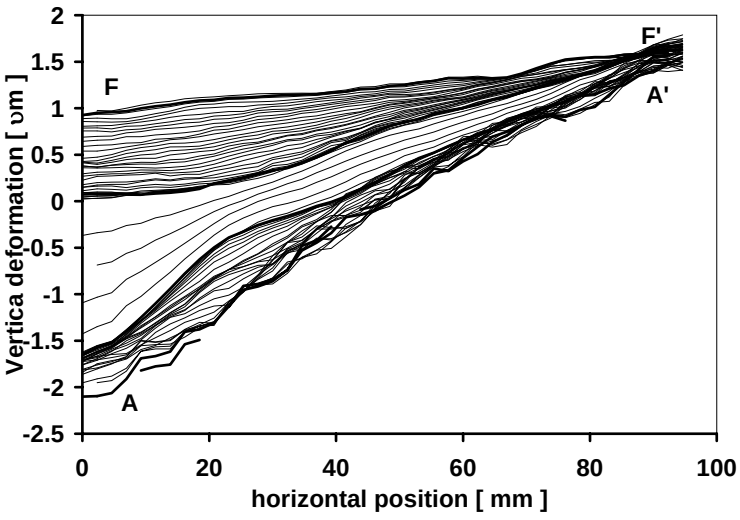

RY 3 eccentricity pos b.

Figure 114 Vertical displacements obtained with ESPI in eccentric load situation pos b versus horizontal position.

Figure 115 shows an example for JW3. The JW specimens were whole even after testing. However, the large spacing of the displacement lines is because the edges had – visible – fissures, as a result of the brick laying process, as stated in the introduction, section 2.2.3.

In all RY-displacement figures, the central area at mid height showed the largest deformation due to the fact that the specimens were cracked in two before testing started.

The mortar-brick gap in the RY specimens can be observed in Figures 114, 115 and 117. The displacement lines obtained in the brick mortar transition have a larger spacing.

It is not possible to point out one specific row of points with ESPI values that could indicate the original crack. However, the few lines with a larger distance indicate that locally large displacements occurred. The original distance between the rows of points is approximately 1.75 mm and each line in e.g. Figure 117 represents the displacements of points on one row.

The groups of lines close together represent the displacements of points on the bricks.

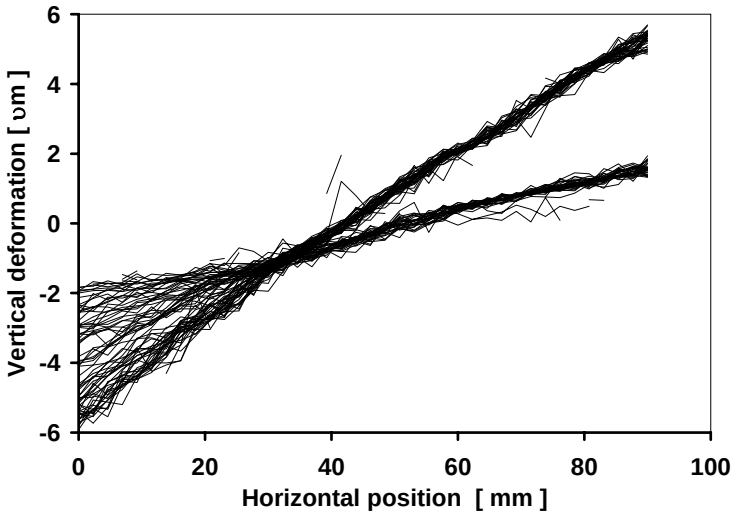

JW 3 eccentricity pos a

Figure 115 Vertical displacements obtained with ESPI in eccentric load situation pos a versus horizontal position.

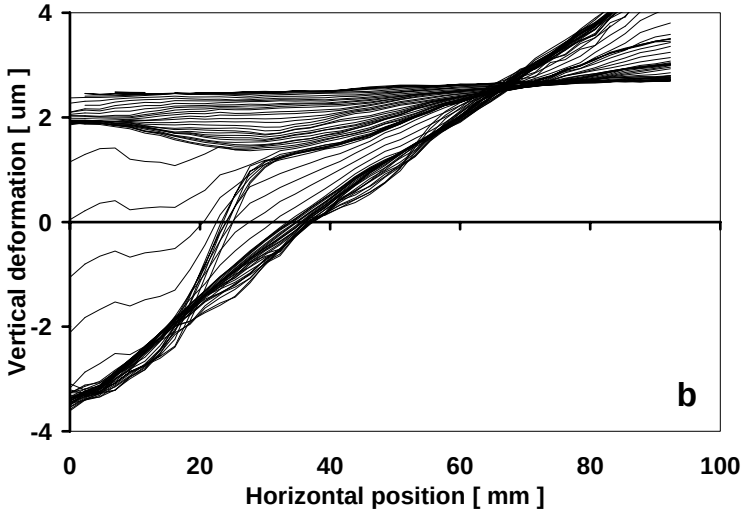

RW 2
eccentricity pos b
(e = -16 mm)

Figure 116 Vertical displacements obtained with ESPI in eccentric load situation pos b versus horizontal position for an RY specimen to show effects of the pre cracked joint.

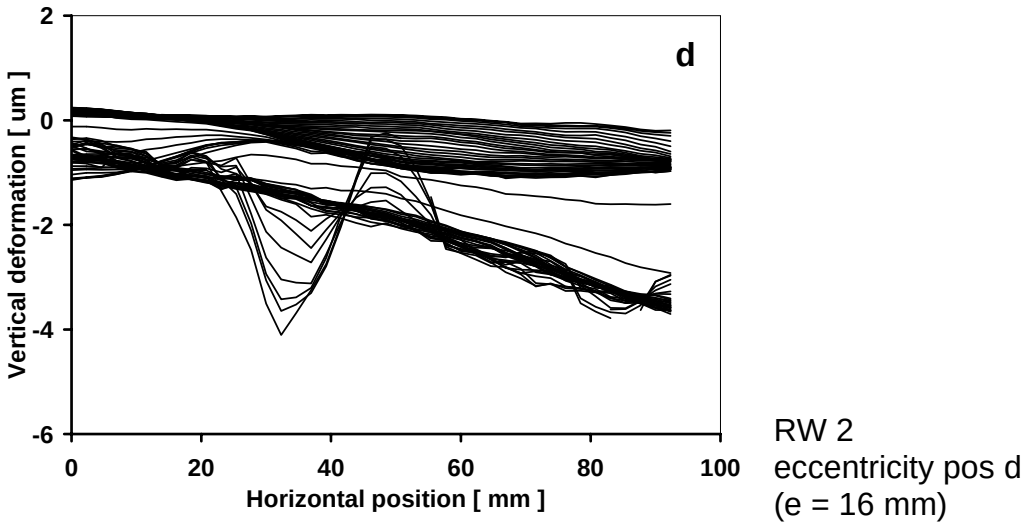

Figure 117 Vertical displacements obtained with ESPI in eccentric load situation pos d versus horizontal position for an RY specimen to show effects of the pre cracked joint.

9.5.2 Overview of vertical deformations

Each of the three specimens gave five strain distribution curves ($\Delta l/l_r$-values). The results for each eccentricity of the three specimens were averaged. Figure 118 shows the results for the JO specimens and Figure 119 those for the RW specimens. The $\Delta l/l_r$-values obtained from the displacements of points in the middle of the top brick (y_i = 25 mm) and the bottom brick (y_j = 85 mm) were used. The JW graphs are smoother than the RY graphs.

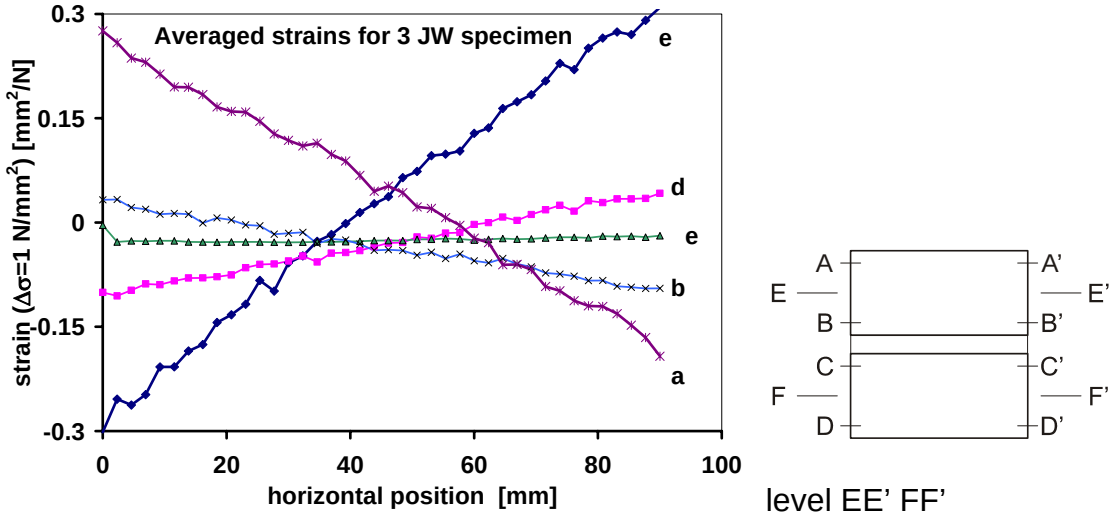

Figure 118 Averaged strains for three JW specimens

Each strain curve also represents a stress distribution over the width of the specimen, assuming $\sigma = E * \varepsilon$. The centre of gravity of the stress block for the JO specimen did not coincide with the load introduction point, assuming that the tensile strains provided tensile stresses. The specimen was whole, however there was visible poor bond at the edges. This effect was most clear for the results of load eccentricities a and e.

The averaged $\Delta l/l_r$-value distribution of the RY specimen, plotted in Figure 119 is less linear than the one for JW. However, the tendency is the same.

The RY specimens were cracked before testing, therefore stresses were zero in the tensile strain area, and consequently a better resemblance for the centre of gravity of the stress block and the load-eccentricity was found.

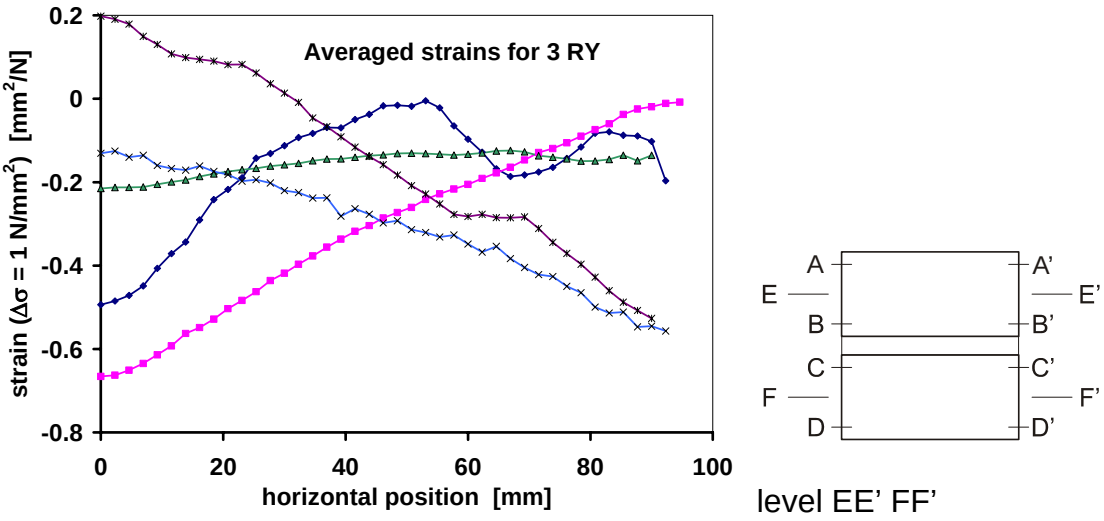

Figure 119 Averaged strains for three RY specimens.

9.5.3 Horizontal displacements

In a similar manner as for the vertical deformations, the ESPI results were processed to obtain horizontal displacements. Two examples are given.

Example 1.

Figure 120 shows as an example the results of RY1, one of the eccentrically loaded RW specimens. The displacement of the centre of the specimen is plotted versus the height. The average of the displacements of the rows of points at the utmost right and left of the specimen were used, $u_{avg} = (u_j - u_i)/2$, with i the first set of points (X=0) and j the last set of points (X = ~ 100).

For eccentricities b, c and d, the specimen stayed almost straight. A large difference in movements was observed for eccentricities a and e. There was an obvious kink in position e where rotation had occurred mainly in the joint. The curve for position a was corrected in the top brick by using results of a row of points that was situated more to the centre of the specimen.

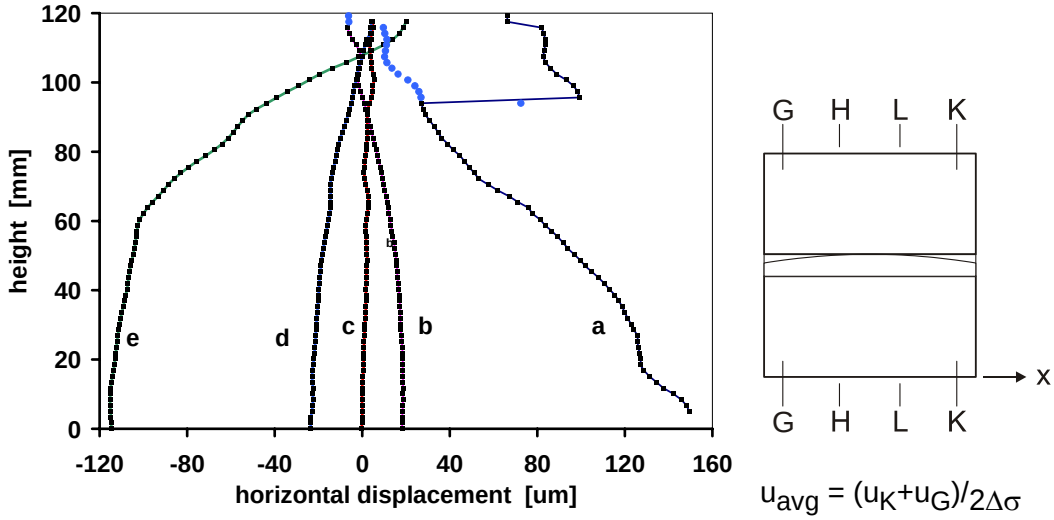

Figure 120 Horizontal displacements (u_{avg}) over height, RY1, ESPI results

Example 2

In Figure 121 the horizontal displacements for concentric and eccentric loaded specimens are plotted versus the height of the specimens. These specimens were similar to the ones discussed earlier in this section. Concentrically loaded, horizontal movements are small compared to the movements of the eccentrically loaded specimens. The latter show kinks at mid height, indicating that most of the rotation occurred in the joint. Specimen B3b showed largest displacements, and was also deviant in its M-N and M-φ relationships.

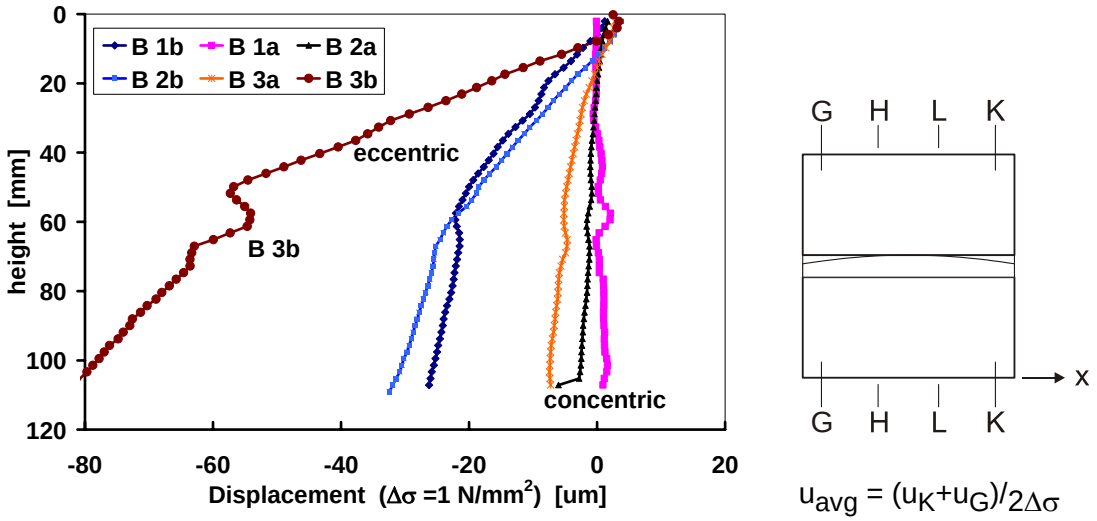

Figure 121 Horizontal displacements (u_{avg} in X-direction), ESPI measurement results, for a stress increase of 1 N/mm^2.

The horizontal strains for the six specimens of this example are plotted in Figure 122. Due to the measurement accuracy of these micro deformations, it is not appropriate to interpret these horizontal strains in detail, probably because the load increment was relatively small (0.2 N/mm^2). Nevertheless, a trend is seen that in position a and e (largest eccentricity) horizontal strain in the top brick is largest.

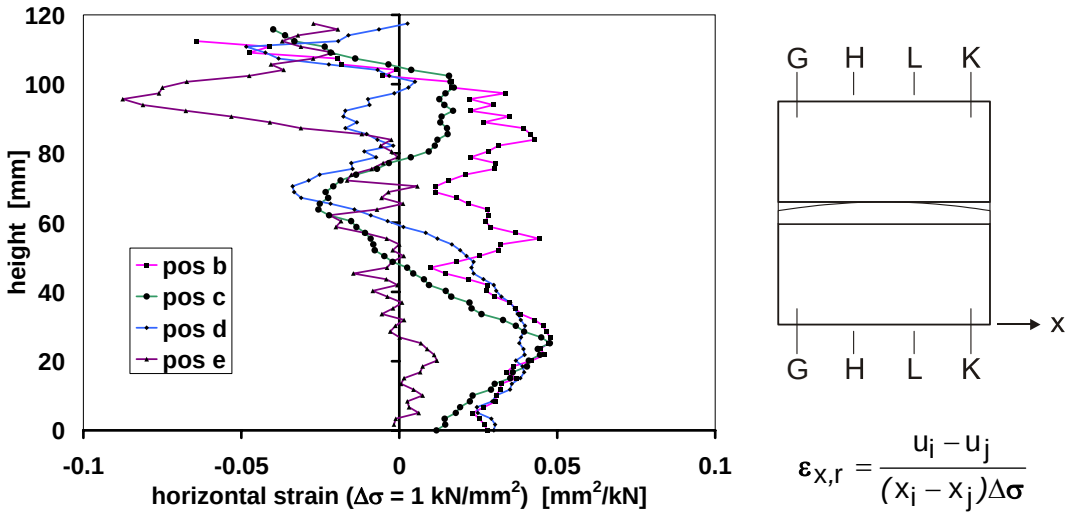

Figure 122 Horizontal strains ($\varepsilon_{x,r}$), ESPI measurement results.

9.6 Conclusions

Relationships between σ and ε, N and M, and M and φ, are established.

- For larger loads, linear relationships are found, but there are disturbances at the onset of all tests.

  RY specimens consisted of two pieces that were broken before testing started, but still fitted well onto each other. The effect of the relative soft intermediate layer between the two pieces was recognised in all test results. JW specimens were intact at the start of testing and still after tests.

  Closing of cracked interfaces was recognized in vertical ESPI deformation graphs, however, not in stress strain relationships.

  Due to the fact that detailed laser speckle (ESPI) measurements were made at one third of failure load, the early phase of the test became of more importance. In other cases when loaded to failure, the offset in the beginning of the test can be neglected.

- The shift in the M-φ diagrams when changing from negative to positive rotation was caused by the change of the position of the effective area due to the opening and closing of the fissures.

  The slope in the positive and the negative part of the graph was the same.

Friction in the core of the LVDTs and properties of the test equipment, e.g. friction in the hinge, may have had a minor effect.

Loaded concentrically (in position c) some questions about the observed, unintended rotation remain, because the effect of bending around the weak axes, in combination with torsion in the specimen could not be estimated accurately. For the other loading positions, these effects were smaller compared with the applied eccentricity around the stiff axes.

- The eccentricity of the load was almost constant while ESPI measurements were done, as is concluded from the measured forces and using Equation (65).

  The detailed behaviour of each specimen separately was often irregular. However, these irregularities are explained by taking into account the shape and the irregularity of the specimen, the measured forces and the deformations.

- Averaged over three tests, the strain distribution found with ESPI was reasonably linear across the width.

  For the JW specimens, the position of action line of the resultant of the stresses does not coincide with the position of the action line of the axial loading, when linear elasticity is assumed. In the cracked RY specimens they coincided better.

10 Strains in eccentrically loaded, pointed masonry.

Abstract

This chapter presents the results of investigations into the mechanical behaviour under compressive loading of two combinations of pointing and bedding mortars used in combination with two types of bricks. The specimens were loaded in a standard testing machine via steel blocks. At the top, two steel blocks with an inserted steel ball were positioned, in order to centre the load and to allow for some rotation.

Special attention is paid to stress concentrations due to the mechanical incompatibility of the bedding and pointing mortar. In particular, “hard” pointing material applied on “soft” bedding mortar shows a high degree of mechanical incompatibility.

10.1 Introduction

Pointing masonry means that a new material is added. When the masonry wall is loaded, the different materials interact. The mechanical properties of the pointing mortar mostly diverge from those of the bedding mortar and the units. The interaction between brick, bedding mortar and pointing mortar causes irregularities in the stress and strain distribution and consequently there is an effect on durability.

Specimens made of RW and JG bricks were used in combination with a) strong pointing and weak bedding mortar and b) weak pointing and strong bedding mortar.

The preparation and sizes of these specimens were similar to the specimens discussed in Chapters 8 and 9. However, they were loaded in a standard Scheck testing machine and bricks of the same factory but from another delivery were used.

10.2 Experimental details

10.2.1 Specimen preparation

Brick-joint-brick couplets were made from soft mud (RW) and extrusion (JG) bricks in combination with weak and strong bedding mortar. Couplets with weak bedding mortar were pointed with strong mortar (A1 and A2, see Table 30), those with strong bedding mortar were pointed with weak mortar (A3, A4 and B3, B4). The strong mortar had a compressive strength of 20 N/mm^2. For the weak mortar it was 2 N/mm^2. Soft mud bricks, type RW, with a $f_{c,bri}$ = 27 N/mm^2 and extrusion bricks, type JG, with a $f_{c,bri}$ = 66 N/mm^2 were used, (Table 1, page 35). The same bricks were used as for the masonry tests described in Chapter 6.

Table 30 Overview of specimen types and materials used.

	specimen types		
brick type	bedding mortar	pointing mortar	number of tests
RW	weak	strong	2
RW	strong	weak	2
JG	strong	weak	2

The pointing mortar reached approximately 15 mm deep. Specimens were cut from the couplets with a water-cooled diamond saw and left to dry before testing. The size of the specimens was approximately 100 mm wide (the width of the brick used), 112 mm high (two times the thickness of a brick and one joint) and 25-27 mm thick.

10.2.2 Measurements

LVDTs were connected in the middle of the left and right hand side of the specimen. Their gauge length was 50 mm and included the joint, (Figure 123). ESPI was used to observe the behaviour of a part of the front surface which measured ±85 by ±110 mm^2.

10.2.3 Load introduction

The load was applied via steel blocks of the same section (25 x 100 mm^2) as the specimens, and 60 mm in height. The complete height of steel blocks and specimen was 235 mm. The specimens were capped with a thin layer of gypsum. Specimens were positioned between machined steel blocks with no support horizontally. However, due to friction, horizontal displacements were not absolutely free, which may have caused additional horizontal stresses in the specimen.
In order to centre the load, a steel ball, 10 mm in diameter was placed in a hole in the top plate. This steel ball enabled the steel top plate to rotate and ‘forced’ the position of the load. However, any unintended load eccentricity, especially in thickness direction, was not measured.

In the case of soft pointing mortar and the strong bedding mortar, Figure 123 right, the centre of gravity of the joint did not coincide with the line of thrust of the load. Consequently, there is an eccentricity to the right when it is assumed that the pointing mortar has a small stiffness compared to the bedding mortar.
In the case of strong pointing mortar the eccentricity is to the left, Figure 123 left. The strong pointing mortar acts as a ‘rigid point’. The soft bedding mortar is compressed heavily and the top unit and the steel block above rotate.

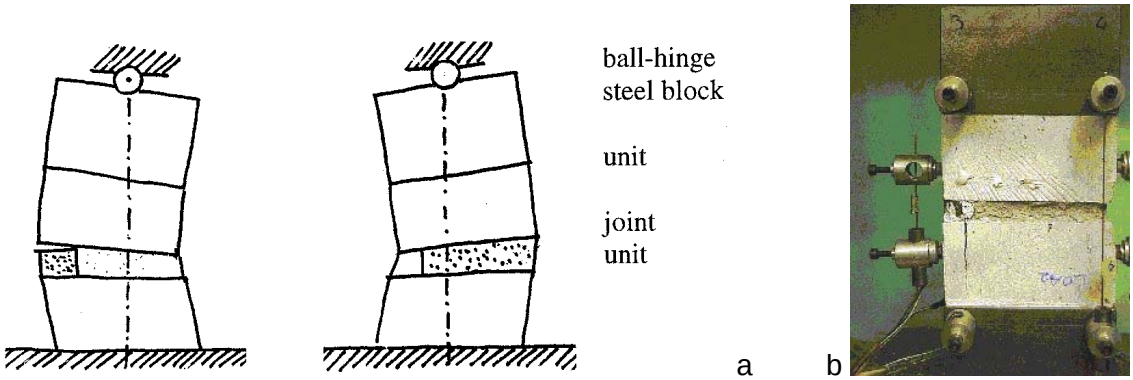

Specimens were only laid on machined steel blocks without horizontal support.

Figure 123 a) Deformation of specimens, to the left with strong pointing mortar and to the right with weak pointing mortar. b) Photo of a specimen with LVDTs.

10.3 Results from traditional measuring instruments

10.3.1 Strength and E modulus

The expected strengths, based on the results given in section 4.4 and Table 17, are given in Table 31.

Table 31 Expected material strengths for pointed masonry

Brick type	bedding mortar	c:l:s	$f_{c,mor}$; NEN 3835 N/mm^2	$f_{c,mas}$; Table 17 N/mm^2
VE brick	soft	1:2:9	3	6.5
VE brick	strong	1:½:4½	17.6	9.1
JG brick	strong	1: ½:4½	17.6	15.8
The properties of VE bricks are comparable with those of RW bricks.				

After the ESPI measurements, the specimens were loaded to failure, perpendicular to the bed joint. The strength of each specimen is given in Table 32. It showed that the strength of the bedding mortar had a large influence on the strength of the specimen. Effect of brick type was negligible. Compare A3 and A4 results with results of B3 and B4. The deviation of similar specimens was small.

The ratio between strength and elasticity modulus is hard to establish while joints have completely different properties. For the RW specimens E_{mas} was approximately 700 times $f_{c,mas}$, as expected. For the JG specimens, E_{mas} equaled approximately 500 $f_{c,mas}$.

Table 32 Codes of the six specimens that were tested, their strength and E modulus

Specimen code *)	Bedding mortar	Pointing mortar	$f_{c,spec}$ N/mm^2	E_{spec} **) N/mm^2	Stress levels for ESPI measurements	N/mm^2
A1	Weak	Strong	6.4	4640	2.83	3.24
A2	Weak	Strong	6.5	5440	0.21	0.40
A3	Strong	Weak	24.3	6250	0.83	2.20
A4	Strong	Weak	24.6	6670	2.64	3.20
B3	Strong	Weak	26.0	7940		
B4	Strong	Weak	27.0	6670		

*) A: soft mud brick, RW, B: extrusion brick, JG

**) E from LVDT measurements on specimen

10.3.2 Fracture behaviour.

The specimens failed due to vertical cracking. In some cases the effect of the confinement by the load platens was visible in the cracking pattern. Weak bedding mortar was completely crushed and crumbled after testing. It behaved like sand with no bonding. In specimens with strong bedding mortar, cracks ran straight through the mortar from brick to brick.


A1


A2

Figure 124 Specimens A1 (left) and A2 after testing


A3

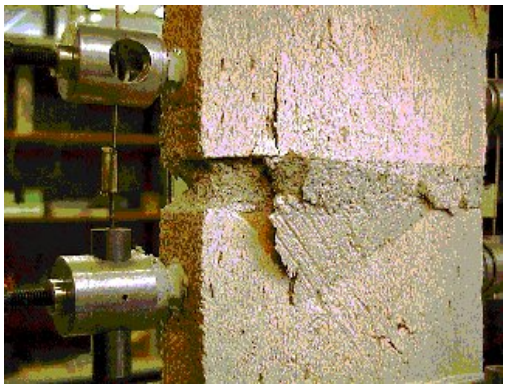
A4

Figure 125 Specimens A3 (left) and A4 after testing

At the end of the test of specimens A1 and A2, (Figure 124), with soft bedding mortar and strong pointing mortar it became visible that the top brick rotated and the bottom brick moved to the left. As expected, vertical and horizontal stresses concentrated just beneath the strong pointing mortar where specimens A1 and A2 cracked.
Specimens A3 and A4, (Figure 125) had soft pointing mortar and strong bedding mortar. Stresses were largest just behind the pointing mortar, 15 mm from the left. Spalling of the specimen occurred, as is visible in Figure 125. This spalling is similar to the spalling of stack bonded specimens as discussed in e.g. section 6.6.

10.3.3 LVDT measurements

Deformations measured by the LVDTs over a gauge length of 50 mm are plotted versus applied averaged stress in Figure 126 for specimens A1, weak bedding mortar, and A4, strong bedding mortar. The LVDT measurements confirmed that the top brick rotated in most cases. For A1 and A2 (weak bedding mortar) the rotation was clock wise. The displacement of the left LVDT is almost zero. For the specimens with strong bedding mortar the rotation is counter clock wise, while the left LVDT shows the largest deformation. The side that was observed with ESPI was considered as the front and left and right are related to this way of observation.

Estimations for E values were made. These values were computed by taking the average of the LVDT measurements (left and right hand side) and performing the linear procedure given in Appendix A.1. The results are given in Table 32.

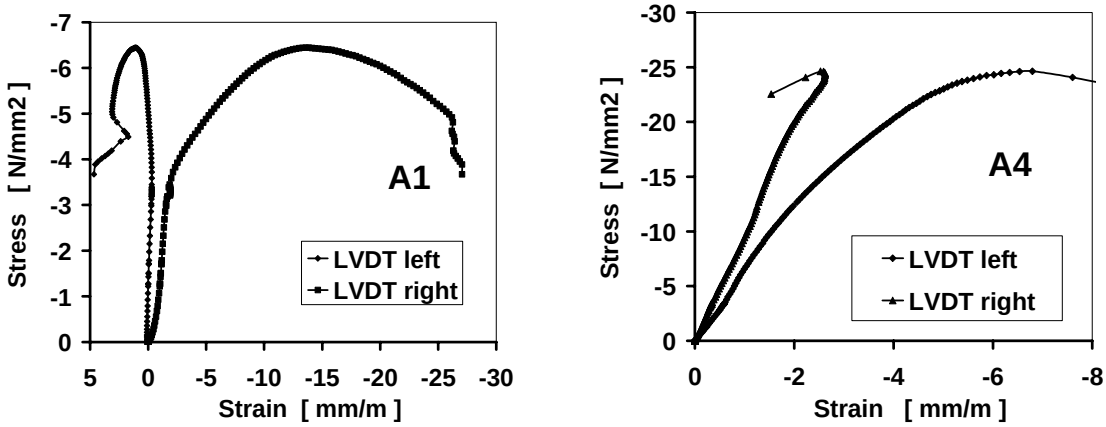

Figure 126 Results of LVDT measurements for specimen A1 and A4

10.4 ESPI results

The stress levels for these tests by merely dividing force by sectional area are given in Table 32. The loaded area measured approximately 25 mm by 96 mm.

10.4.1 Vertical displacements

In Figure 127, left, the vertical displacements of each of the observed points of specimen A3 are plotted versus their X value. Displacement-values were 'scaled' to a stress increase of 1 N/mm^2. Points with the same Y value were connected, resulting in more or less parallel lines in the graph. The distance between these lines is an indication for the stiffness of the materials used. Deformation at the left was larger than at the right, indicating an eccentricity of 7 to 8 mm to the left. This was expected because of the weak pointing mortar.

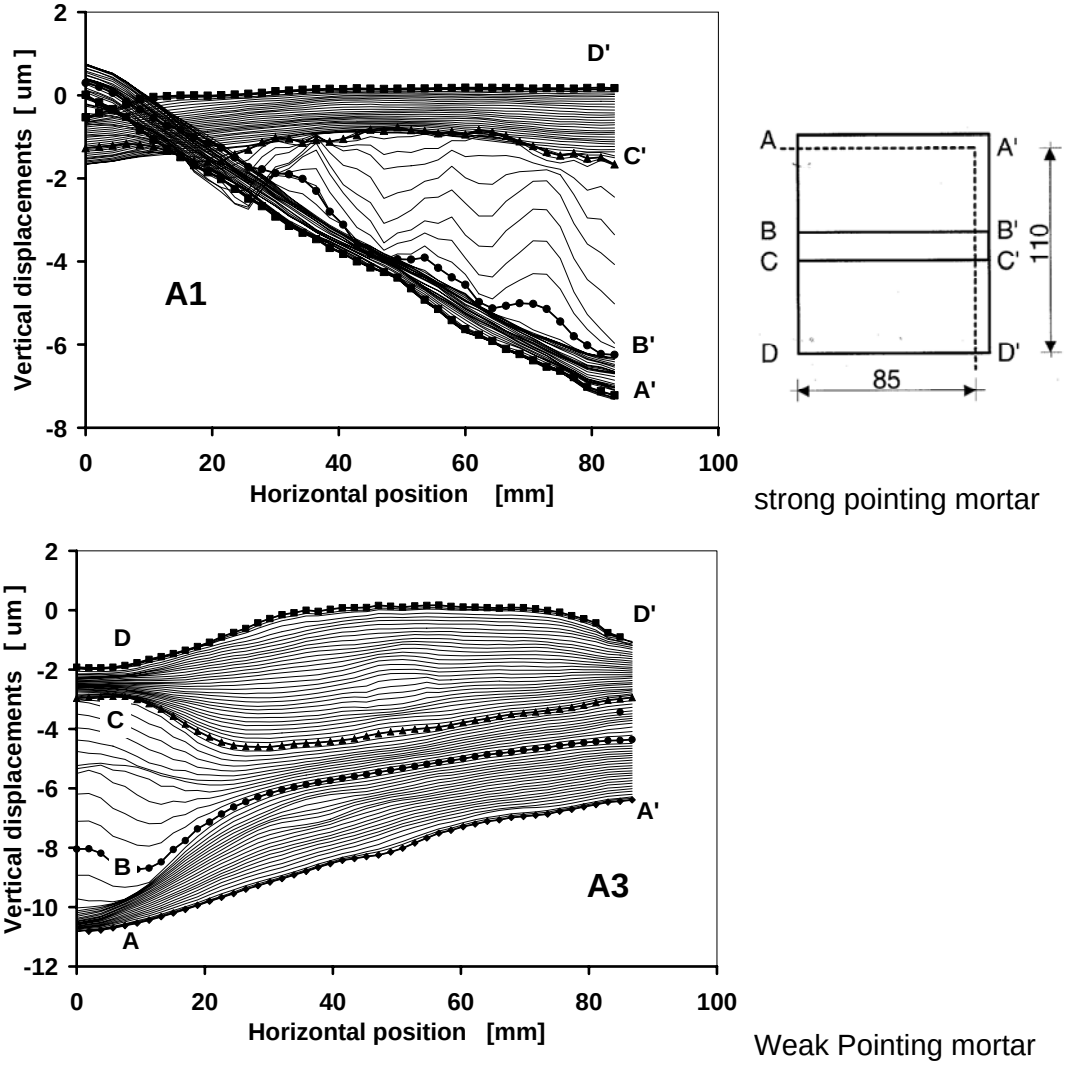

Figure 127 Vertical displacements of specimen A3, (weak pointing mortar) and of specimen A1, (strong pointing mortar), for a stress increase of 1 N/mm^2.

The graph of specimen A3, Figure 127, shows that brick deformations were much smaller at the left than at the right hand side. This means that the pointing mortar at the left deformed much more than the masonry mortar at the right.
For the strong bedding mortar the stiffness of brick and mortar was of the same order of magnitude. For the specimens with soft bedding mortar the graphs show that their stiffness was much smaller than for the bricks (larger line spacing). See the graph of specimen A1 in Figure 127, where also rotation is clear.

The top edge, line AA', did not move at the left hand side, while the right hand side moved considerably. At the left, the points at the bottom edge of the top brick, line BB', had positive displacements, which means tensile stresses. Probably, bending around the X-axis occurred as well. In this case, the top brick reacted 'stiffer' than the bottom brick which can be concluded from the spacing between the displacement lines.

The effect of the strong pointing mortar is clear at the left hand side of Figure 127. Lines AA' and DD' cross each other at a few mm distance from the left edge. Lines BB' and CC' indicate tension at the left edge.
To compare the effect of eccentricity, the displacements of the points at the top edge (lines AA') of all six specimens are plotted in Figure 128.

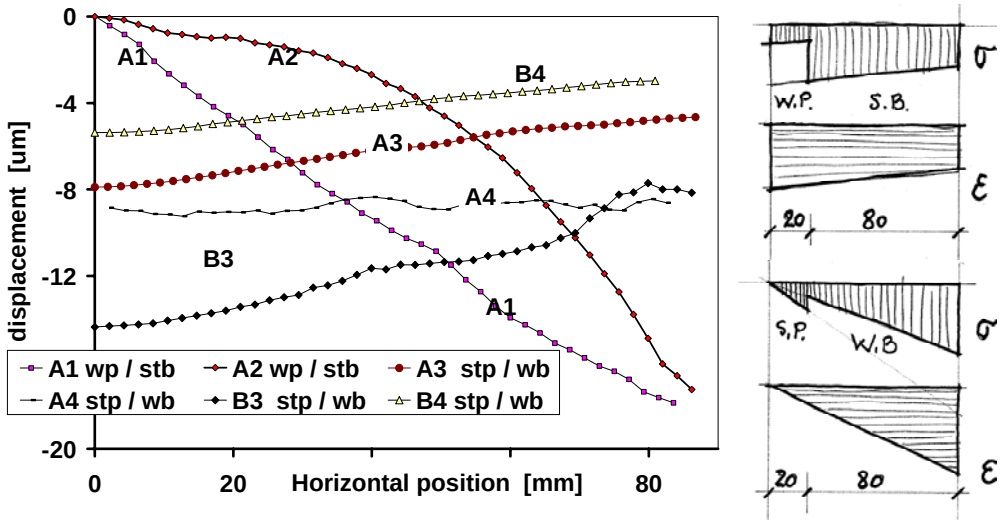

code for mortars used: w = weak, st = strong, b = bedding, p = pointing

Figure 128 Displacement of upper edge (lines AA') of specimens (normalised to 1 N/mm^2) and schematic view of assumed joint stresses, right.

The lines of specimens A3, A4, B3 and B4 indicate larger strains at the left hand side and load eccentricity to the right. Specimens A1 and A2 have hardly any deformation at the left and large deformation at the right, due to the strong pointing mortar.

10.4.2 Horizontal displacements

Horizontal displacements are plotted as a function of vertical position (Y) of the points, see Figure 129. In most cases it is clear that the top brick rotated. In the specimens with weak bedding mortar the strong pointing mortar acts as a stiff point of rotation as already recognised in the graphs with the vertical displacements. In the specimens with the strong bedding and weak pointing mortar, rotation is much smaller.

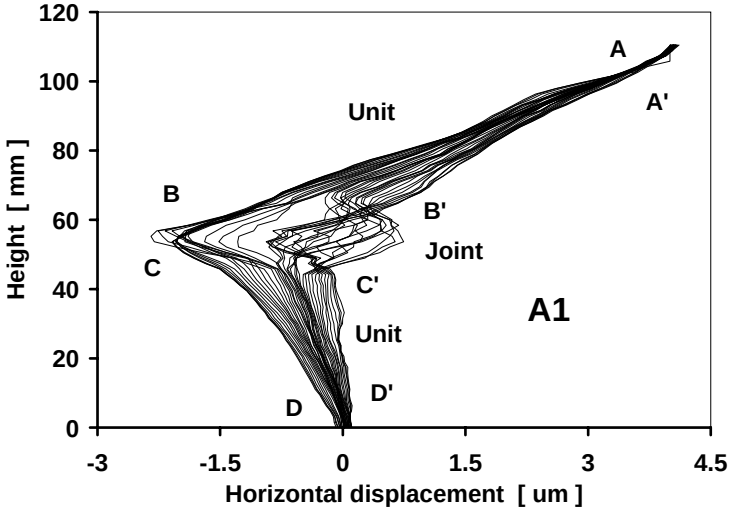

Figure 129 Horizontal displacements for specimen A1, $\Delta\sigma$ = 1 N/mm^2

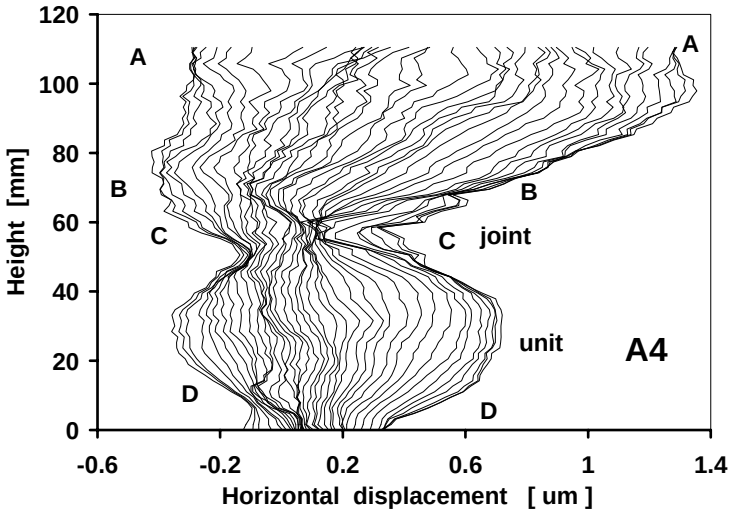

Figure 130 Horizontal displacements for specimen A4, $\Delta\sigma$ = 1 N/mm^2

In Figure 130, specimen A4 shows a nice example in which the effect of the strong bedding mortar on the horizontal confinement can be observed. The deformation of the bottom brick shows a barrel shape as an effect of the confinement by the load platens. In the cases with the strong bedding mortar the middle of the bricks deformed more than their ends, both at the loaded side and on the mortar side.

For specimen A1, most of the deformation occurred in the joint, Figure 129, i.e. the opposite effect of that of a strong bedding mortar.

10.4.3 Strains in mortar and unit and their stiffness

From the vertical displacements 'strains' were obtained as described in section 7.2.2, page 89. For joint behaviour, relative displacements between unit edges, measured over mortar joints were used, see the lines BB' and CC' in Figure 127.
The strains were plotted versus horizontal position in Figure 131.

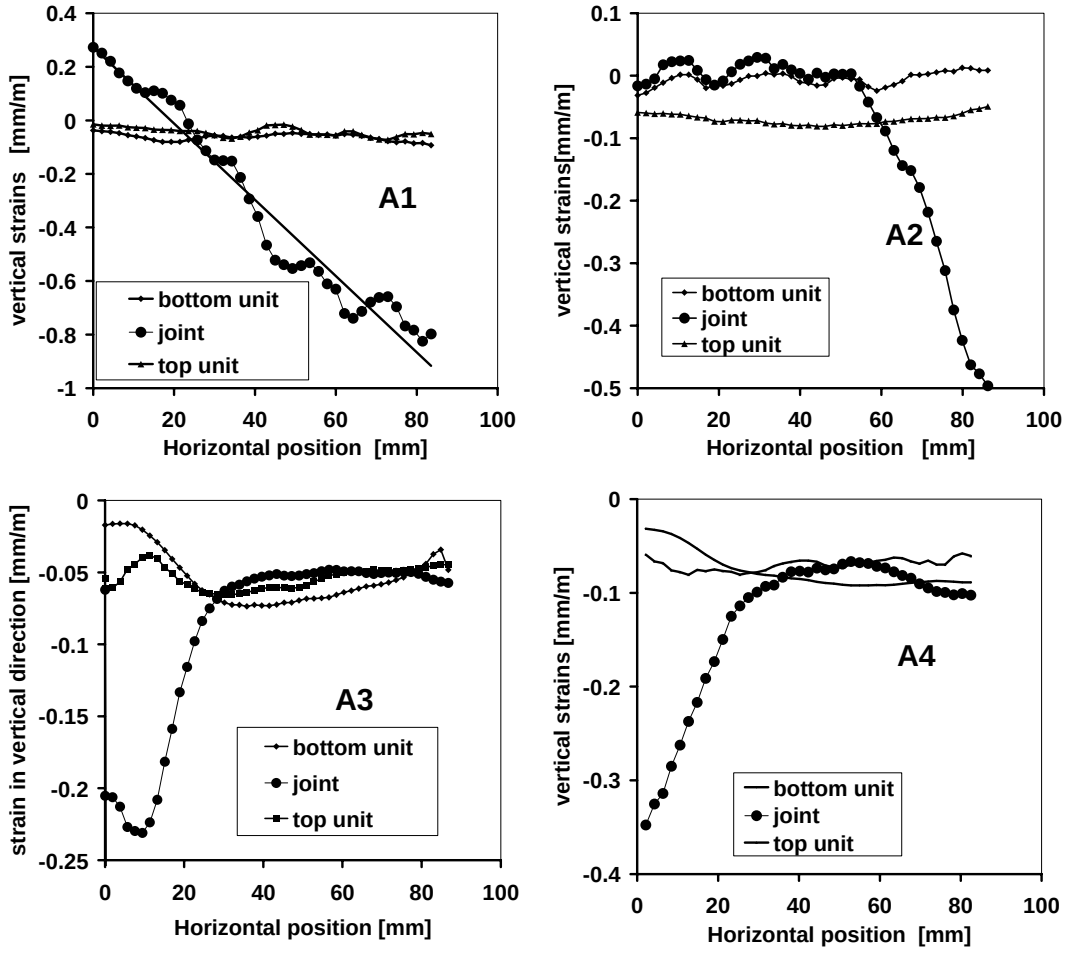

Figure 131 Vertical strains for a load increase of 1 N/mm^2.

The tensile strains in the strong pointing mortar of A1 are clear. Large compressive strains in the soft bedding mortar are clear too. In specimen A2, this effect is much less visible, perhaps due to a lesser stiffness of the pointing mortar. In this specimen the pointing mortar was perhaps not pushed in as hard as in specimen A1 or it had more shrinkage.
The strains of the bedding mortar of specimens A3 and A4 are of the same order of magnitude as those of the units. The pointing mortar strains, however, are much larger.

It is not easy to obtain a reliable modulus of elasticity from these graphs. Strains vary over the width of the specimen. Further, stresses at the outside of a specimen do not equal the averaged stress that was applied. It is clear that the E-value of the strong (bedding) mortar is of the same order of magnitude as the E of the units. The E-value of the soft mortar is considerably smaller.

10.5 Comparison of E-values

The measured soft-bed mortar E-values were between 2200 N/mm^2 and 4600 N/mm^2. In Figure 131, mortar strains for strong mortar (specimen A3 and A4) are of the same order of magnitude as unit strains.
Bending effects make it difficult to obtain reliable E-values. See e.g. specimen A2 with positive strains for the upper unit. Only trends can be established.
The E_{bri}-values are larger than expected from Bolidt tests. When the $E_{bri,Bolidt}$ values are used, the trend of the estimated value for E_{mor} corresponds reasonably with the trend of the measured values.

Table 33 Comparison of E-values.

Specimen	E masonry	E_{bri}		E bed mortar	
	(LVDT 50 mm)	ESPI	Bolidt	ESPI	Estimated
	A		B		
A1	4640	19800	6050	2240	2490
A2	5440	12300	6050	4600	3960
A3	6250	18600	6050	16000	7120
A4	6670	13700	6050	11700	10800

Estimated with: $\frac{13.5}{E_{mor}} = \frac{63.5}{E_{mas}} - \frac{50}{E_{bri}}$; E_{mas} from column A and E_{bri} from column B

10.6 Conclusions

- The centre of the loaded area did not coincide with the centre line of gravity in the specimen due to the two types of mortar used, but also due to flaws in units and mortar.
- Soft pointing mortar hardly effects the strain distribution in the specimens while its Young's modulus is small compared with that of the brick and the strong bedding mortar.
- Strong pointing mortar in combination with soft bed mortar acts as a hinge.
- The results from the LVDT measurements are in reasonable agreement with the ESPI results, considering that the ESPI results showed a large variation over the joints.

11 Synthesis of results and findings

In order to place the findings of this thesis in a larger framework, this section is organised around three statements. These are:

a) The brick-mortar contact area is the weakest link.
   Spalling of the unit initiates failure as an additional effect in the failure process of layered, stony materials. Recessed joints in thin layer mortar reduce strength.

b) A few tests are better than an empirical formula to predict compressive strength.
   Testing may be optimised with respect to specimen size, testing apparatus and measurements.

c) ESPI results are superior to LVDT results.

d) Numerical simulations can support the analysis of ESPI results

11.1 The brick-mortar contact area is the weakest link

Four phases may be recognised in the behaviour of masonry in compression up to failure. These phases are: an initial phase, a reversible linear elastic phase, a spalling-cracking phase and finally, a post peak phase.
After the initial phase and reversible linear elastic phase, local failure processes start. In masonry specimens spalling occurs first, followed by diagonal shear. Spalling of the clay-brick units, as a consequence of the layered structure, is an additional effect in the failure process of masonry compared to the processes occurring in more homogeneous materials like rock and concrete. This is discussed more extensively in section 6.9, under point c, on page 84. Some additional aspects are discussed below.

a) The models of Haller and his successors use the stiffness of the unit and the mortar and their Poisson's ratios to predict the resultant (lateral) stresses. The interaction between mortar and brick, later completed with more detailed failure criteria, are used to predict the strength of the brick-mortar composite. Brick and mortar stiffnesses are the main parameters, in combination with brick and mortar joint thicknesses. Some doubt may be cast on the assumptions about lateral stress and strain distribution over the height.

b) Stress and deformation of the joints were calculated with numerical models by Rots [CUR 193], and Sabha and Schöne [SAB 94].
Sabha en Schöne [SAB 94] proposed a model to be used for natural stone. With this model, vertical peak stresses were found at a distance approximately equal to the joint thickness, from the outside of the wall. The mortar bulges out. Consequently, lateral stresses will be present.

c) In the brick-mortar interface of contemporary masonry three areas may be recognised, as discussed in section 2.4, page 15. An outer edge area without bond (bleeding water), an inner area with bond and an intermediate area where bond is broken due to e.g. shrinkage are shown in Figure 132.
The wall-effect in the mortar against the brick decreases the properties of the interface as well. Grains of sand of sanded soft mud bricks act as a kind of insulation, while small mortar particles (cement) are prevented from moving to the solid brick surface. The grains of sand may be bonded to the mortar. However, the sand is only poorly bonded to the brick, and in all cases, the packing effect of grains to a large surface (wall effect) as discussed in section 2.2.5, page 8, occurs there.
These joint imperfections cause stress variation, both in axial and in lateral direction.

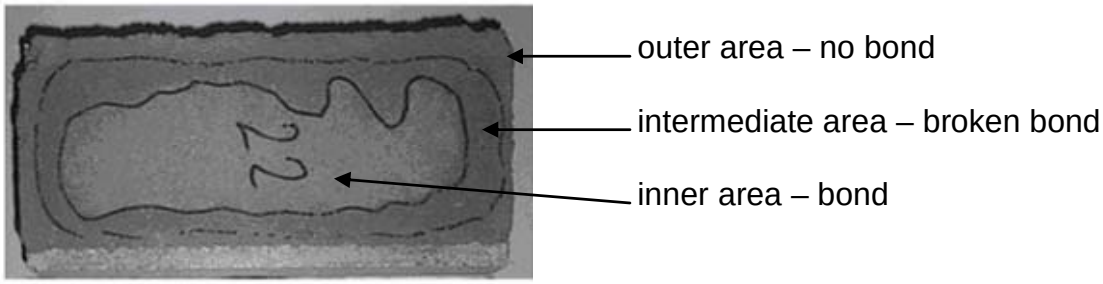

Figure 132 The brick-mortar contact areas.

d) New mortar application techniques may result in not uniformly filled joints, which cause additional stresses. In tests on specimens with recessed thin layer mortar joints, for example, the effect of notches was evident. (see e.g. section 2.4).
For thin layer mortar the wall-effect may be of minor importance, the particle size is much smaller than in general purpose mortar. Thin layer mortar has a relatively high cement content compared with GP mortar. Because additives are added, the mortar is more retentive of water and so water transport is reduced and better bond is obtained.
Loads are smoothly transmitted through the joint, however, near the end of the notches peak (lateral) stresses result.

e) Spalling of brick pieces 10 to 15 mm thick, parallel to the loading direction, may be explained by the Sabha model in combination with the strain distributions observed using ESPI. Vertical peak strains were recorded indicating the position of the end of the fissure, (Chapter 9).
The effects of the pillow shape of traditional mortar joints (fissures) and the notch in thin layer joints were similar, although pronounced for thin layer joints. The highest strain levels were observed at the end of the notch, indicating that high lateral stresses could occur there.

11.2 A few tests are better than an empirical formula to predict compressive strength

11.2.1 Tests, equations and codes

Building codes aim at guaranteeing some safety. Therefore, a lower bound, conservative approach is followed. This means that, when doing a few tests, the resulting strength is at least equal to the predicted strength and probably a higher strength is obtained.
In 87% of the 170 tests, described in Chapter 6, the estimated value was indeed conservative with the [EC6 96] result.
Tests usually indicate higher strengths than equations and a provision is given in the Dutch and other codes to use test results for masonry design. Codes prescribe the minimum number of tests (usually 6). The C.o.V. of the compressive strength in series of tests is usually around 10 %. The C.o.V. of the modulus of elasticity is usually around 20%.

Many equations exist to establish masonry compressive strength based on brick and mortar compressive strengths, e.g. [SCHb82]. Equations and tables in codes use the compressive strengths of unit and mortar to predict masonry strength. The unit and mortar strengths are established according to national codes. The third important parameter, which is becoming more important as the popularity of thin layer mortar is increasing, is the joint thickness. [EC 6 02] provides parameters for this type of material. The ratio between joint thickness and unit size is important too. Compare, for instance, a brick sized unit with 15 mm thick joints, with 600 mm high calcium silicate elements with 3 mm thick joints.

11.2.2 Dimensions of specimens

When the purpose of the test is to find the appropriate mortar for a certain type of brick, the following minimum specimen sizes, based on the test results described in Chapter 6, are proposed: A length of one brick, a thickness equal to the width of the brick, and a height of five times the brick thickness, or three layers. The minimum height over thickness (h/t) ratio is 3.5.

The lack of head joints in this type of stack-bonded specimens results in an overestimation of masonry compressive strength. However, the effect of the length of the specimens, studied with the specimens of the B-series [VMF 97b], proved to be small. Load transfer via head joints is small, when the filling is poor. If the gross sectional area of a wall is reduced by the area of the head joint(s), - when loaded perpendicular to the bed joint - head joint effects are taken into account reasonably.

In codes (e.g. NEN 6790, EC6) dimensions are prescribed for specimens that are used to establish masonry compressive strength. These specimens should have head joints to represent reality in a certain way. The thickness of the specimen is usually equal to the width of a unit. The dimensions (especially the length of the specimen) of the specimens is often too large to be tested in the machines originally intended for testing concrete(cubes). The strength of code-specimens may also exceed the capacity of the test machine.

The main advantage of stack bonded specimens is that they are manageable, especially when they have to be made on site and transported to a laboratory for testing. Making specimens on site may give a better similarity between test results and real properties. Quality control with this type of specimens is better than with tests on brick and mortar separately.

11.2.3 Symmetry in specimens

The behaviour of specimens is not symmetric, due to geometrical imperfections, variation of material properties and the fact that they are not positioned perfectly in the centre of the loading machine. One of the geometrical imperfections is the contact area in the joint, (Figure 132). Therefore, deformations measured in the loading direction will not be the same all around the specimen. This may indicate that the load has some eccentricity when it is assumed that all fibres follow the same σ-ε relationship. However, fissures affect the σ-ε relationship.
When test results are meant to be used to control structures loaded both in compression and in bending, the compression tests should be performed with a certain predetermined eccentricity.

11.3 ESPI results are superior above LVDT results

The largest benefit of ESPI is that measurements are performed by ‘taking pictures’ of a surface during the course of a test. The surface is not touched and no further instrumentation is required. After data reduction, the displacements of a grid of roughly 50 by 70 points are stored in a data base. Between each pair of grid points the strain can be calculated. Compared to the limited number of LVDTs that can be attached to a surface of such a size, the increase in information is manifold.
As ESPI follows deformation over a short gauge length, the modulus of elasticity of mortar can be established under the assumptions made for the stress distribution.

In this way, the ESPI results are superior to traditional results from LVDTs because ESPI gives more information about the behaviour of a surface than the measurements by LVDTs. This makes ESPI objective in the presence of fissures at the brick mortar interface and other material imperfections. ESPI allows for observation of lateral deformations, one of the main assumptions in the traditional models for masonry

strength (section 3.2, ‘sandwich model’) and shows that no shift occurred at the brick mortar transition.
The strains per specimen or per measurement varied considerably. In ‘real’ masonry this variance fades out, because measurements are taken over several bricks and joints. Then, a more ‘averaged’ result is obtained.

In ESPI concentric tests, the vertical deformations confirmed the effect of the fissures in the brick-mortar interface. The horizontal strains showed a B-shape over the height of the ESPI specimens indicating that the bricks expanded more than the mortar.
A possible stress distribution (DIANA-result) is presented in section 8.4, page 111.

In ESPI eccentric tests, a similar image as in concentric tests was found. It showed that most rotation occurred in the joint, possibly, but not completely confirmed, in the brick-mortar interface with the fissures. This was the interface that developed during positioning of the brick being laid in the fresh mortar.

Lateral deformations were clear from ESPI measurements, although, it was not possible, to accurately establish the Poisson’s ratio of brick or mortar due to uncertainties in the stress distribution. From wallette test results, an estimation is presented in Table 5, page 40.

11.4 Numerical simulations can support the analysis of ESPI results

ESPI measurements and finite element (FE) calculations produce similar results. In experiments (ESPI) the material variations may blur the result. In numerical work the material properties are uniform if so specified.
In both methods the displacements of a number of points on the surface of a specimen are found. The data format of ESPI and FE simulation software (X, Y coordinates and displacements) are similar.

In a specimen some irregularities are always present, which may be simulated in an FE model by assigning material properties more or less randomly to the elements of the model, as suggested by van Geel and Van der Pluijm [GEE 94] and [PLU 96b].
In ESPI-specimens, size may play a role while a 3D stress situation occurs. This should be kept in mind in FE simulations. In thinner specimens the stresses are more uni-axial than in thicker specimens [VMF 97b].

Explorative numerical simulations of the behaviour of the ESPI specimens were made with DIANA. Both the simulation and the ESPI results showed that stresses are concentrated, as expected, in the centre of the specimen, due to the fissures in the bed

joints. The observed B-shape for the strain distribution over the height (Figure 133) is almost the same for strains a) calculated with the full width of the specimen as gauge length and b) calculated over a central 30 mm wide band, as discussed on page 121. The resemblance to the DIANA result is evident.
The input data used for the DIANA calculations were: E_{brick} = 4000 N/mm2, E_{mor} = 5000 N/mm^2, 1 mm thick interface layer $E_{interface}$ = 1000 N/mm2. More details are presented in section 8.4, page 111.
The ESPI results are taken from an RY specimen with medium thickness mortar. Similar graphs are given in section 8.7, page 121.

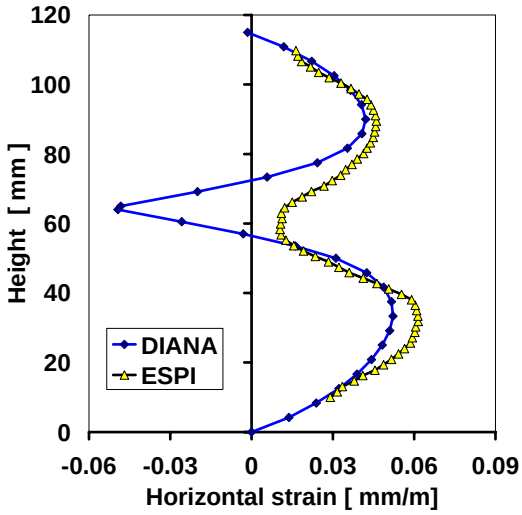

Results of ESPI (specimen 1RYMM) and DIANA for a stress increase of $\Delta\sigma$ = 1 N/mm^2
DIANA simulation details are given in section 8.4, page 111.

Figure 133 Lateral strains versus height.

The coinciding stresses computed with DIANA are shown in Figure 134. The (stiffer) mortar joint experiences a larger compressive stress than the bricks. The stress distribution in this model has a rounded S-shape, unlike the assumed blocked distribution of the sandwich model.

The stress distribution is affected by the confinement of the load platens. The mainly compressive stresses are counterbalanced by the (horizontal) friction forces at the loaded surfaces of the specimen. When these forces become smaller, the lateral stresses will reduce, as indicated by the dotted line in Figure 134. Consequently, assuming that the lateral stress distribution over the specimen height does not change, the mortar would be in compression while the bricks will be in tension. This situation is probably more representative for ‘real’ masonry where a load platen effect is not present in the centre of a wall.

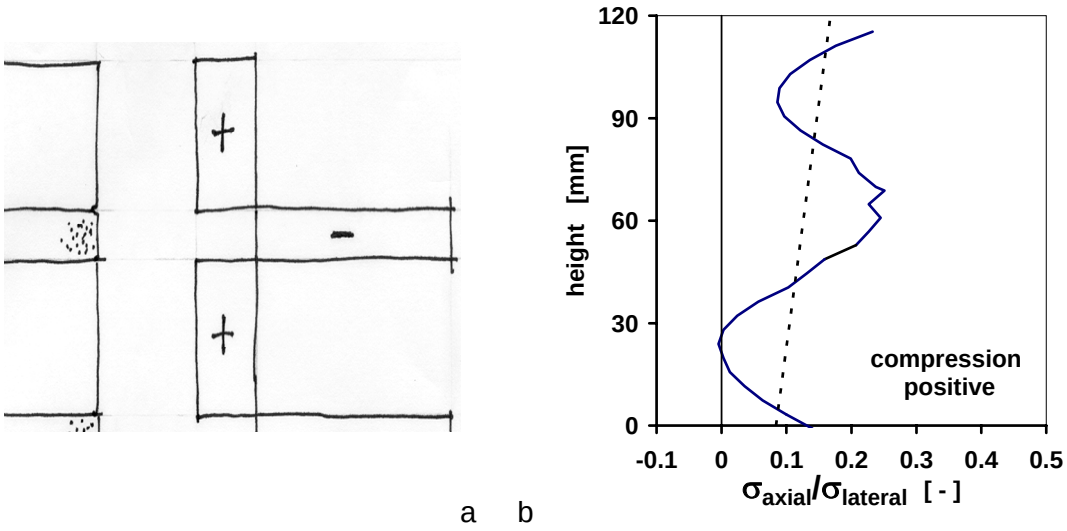

Figure 134 Stresses versus height, a) according the sandwich model b) DIANA result.

Strain distributions recorded by ESPI and calculated with DIANA are similar. The advantage of a numerical simulation over experiments is that stresses can be calculated as well. The DIANA-stresses in the centre of the specimen, although affected by the imposed boundary conditions, show a curved distribution over the specimen's height, different from the block distribution assumed by Haller, (3.2.1, page 22). At the end of the fissures (15 mm from the masonry surface) lateral tensile stresses in the brick were calculated

Through the possibility of accurate, detailed measurement by ESPI, this research has shed light on this important failure mechanism in masonry under compression. More research is needed to revise analytical models for prediction of compressive resistance.

12 Conclusion

In this section, concluding remarks, proposals for further research and recommendations are given.

12.1 Concluding remarks

- The deformation behaviour of masonry in compression is established.

  In the load deformation graph, a reversible, almost linear part is followed by a non linear part. Cracking marks the transition of these two parts. After peak load, a sudden drop of the load is followed by an almost constant load part.

  The compressive strength and E-value of the masonry specimens depend on the mechanical properties of the bricks and mortar used as confirmed by empirical equations given in codes. However, a few tests are better to be used for the prediction of masonry compressive strength than an empirical equation.

  The data base, given in Appendix A.5.5 can help to obtain an impression for a given brick-mortar combination.

- In masonry loaded in compression, joints are weak links and initiate failure.

  Contact areas are created when bricks are laid in mortar. When masonry specimens are tested in compression, spalling occurs as a result of the shape of the contact area. In this area, fissures are present at the masonry surface. ESPI measurements showed the effects of the fissure in the contact area between bricks and general-purpose bed-joint mortar on vertical deformation. The load was transferred through the central 60 to 70 mm of the 100 mm wide specimens.

  In thin layer mortar masonry, the recessed joint causes high levels of strain at the end of the recess (notch). This ‘notch’ in thin layer joints, has negative consequences for the load bearing capacity. In facades, with a low axial load, its effects should be anticipated, especially when loaded in bending (wind loads).

- Lateral strains indicate expansion in both mortar and brick.

  The experimental lateral-strain versus height relationships resemble the ones found in numerical simulations. Stresses obtained with numerical simulations show a distribution like a sinus over the height of the specimen. This distribution is different from the block distribution assumed in the sandwich model.

  Both in the experiments and in the (explorative) simulations the stress distribution is affected by the boundary conditions. Without friction at the loaded ends the ‘zero-stress line’ has to shift to obtain equilibrium.

Both for general purpose bed joints and thin layer mortar bed joints, the measured strain distributions confirmed the experimentally observed spalling of the bricks in masonry specimens.

12.2 Further research

• Non linear numerical simulation of the brick mortar interaction in combination with softening processes may be considered to improve the numerical simulations of masonry structures. In structures, like shear walls, locally masonry fracture can occur, however, some load bearing resistance remains due to redistribution of the load. For this kind of situations, knowledge of post peak behaviour is essential.

• Softer masonry mortar could allow for some more movement in facade masonry.

A higher mortar strength (and consequently a stiffer mortar), often considered as an advantage, decreases the flexibility and increases the risk of cracking. The “Coat or Harness” concept could be elaborated further. This concept is based on two extremes. A facade may be subdivided into relatively small pieces that move like the units of a stiff harness or, completely the opposite, the facade may be built so flexible that it can follow all movements like a coat. In the first situation, the facade is 'pre-cracked' by the expansion joints.

• Further (experimental) research is required for Poisson’s ratio, (lateral deformation of specimens), and softening.

The results of tests, where post peak behaviour was observed, are indicative. It seems that the residual strength of a specimen, after having passed the peak load, is approximately 30% of the peak load. Control of lateral deformation is needed for the study of softening.

• Further research into shear, using ESPI may be considered.

The effect on shear strength of pre-compression and pre-tension needs attention.

Forces concentrate in a part of a shear loaded wall where both axial and shear forces have to pass, [ZIJ 01]. For design purposes, in most cases, the material section is assumed to be fully loaded in compression. The shear capacity is checked through a separate calculation.

Shear tests are performed on uncracked specimens, although, the critical section in a structure may be cracked e.g. by (reversed) wind loading.

• The reasons for the top bricks becoming loose from masonry should be investigated further.

It is postulated that this is caused by a combination of shrinkage, carbonation and changes of temperature and moisture conditions.

12.3 Recommendations

• In numerical simulations of the structural behaviour of masonry the data given in Appendix 5 can be used.

From the data given in Table A.5.5, strength and stress strain relationships can be reconstructed. Poisson's ratios for brick are given as well. In more detailed simulations, the shape of the brick mortar contact area should be taken into consideration. The linear elastic simulations given in Chapters 8 and 9 show the possibilities.

• The mortar application method needs improvement to optimise masonry compressive behaviour.

An option is to level the (GP) mortar before laying the brick. Further, the bond strength may be improved by removal of sand hanging on the units, by impregnating the surface or other methods of surface preparation in order to obtain a better load transfer.

Pouring mortar into the joints, like is done in prefabricated masonry, produces better filled homogeneous joints with less fissures. This kind of masonry is produced on its flat face and consequently, the action of gravity is positive since the freshly poured mortar is in compression.

The recess of TL mortar joints needs extra attention. A complete fill of the joint for structural TL masonry is advantageous. The problem, however, is how to keep the wall clean and aesthetically appealing.

• For structural clay-brick-masonry jointing is needed. Curing of fresh masonry is recommended to prevent formation of fissures.

The improvement of quality due to jointing instead of (re)pointing is underestimated. The way the appearance of pointed masonry can be made more uniform over a facade is a point for further research.

More compaction and pointing pressure on the mortar after the joint is completed can improve the brick-mortar contact considerably. In The Netherlands, it is a tradition to point the masonry after construction. If a mechanical vibrating pointer is used, the bond may turn out to be good (at least on that side of the masonry). Any subsequent shrinkage may reduce the bond, i.e. curing of the fresh work is recommended.

Abstract

Masonry is an age-old building material. Evidences may be found all over the world.
When walls are being built, bricks are laid one on top of the other, with mortar in between. The brick mortar interaction is considered of paramount importance with respect to the mechanical behaviour of masonry.

This study focuses on the role of the brick-mortar interaction. To do so, a novel experimental research technique (ESPI) is employed to measure and visualize the interaction on the mortar joint level. The further developments of this laser speckle technique enabled the observation of unit-mortar interaction in detail.

New developments are the use of high quality factory made mortars and the use of thin bed joints. The brick mortar interaction plays an important role in the transition of loads.
Making masonry and the role of mortar is discussed. Unit types and the processing of units and mortars and esthetical qualities of the joints are discussed.

The structure of unit and mortar is of importance for deformation and fracture behaviour. Both unit and mortar are solid, however porous. Stress concentrations around the pores may initiate failure (cracking). In mortar, stronger (stiffer) grains of sand are present which causes stress concentrations as well.
The mortar joint, as an interface between units, is formed during the brick laying process and positioning of the unit. Normally, the unit absorbs water from the mortar. This changes the properties of the mortar, especially near the contact area with the unit. The interface between brick and mortar forms a weak spot.

Theories to predict masonry compressive strength are based on the layered structure of masonry and use the brick mortar interaction as a basis. As traditionally mortar was relative soft compared to the units, it was assumed that the mortar was squeezed out from between the units. Consequently, the unit was under lateral tension and the mortar under (three axial) compression. Relationships were drawn up for the relationship between applied stress and lateral stresses in unit and mortar. In these relationships, unit and mortar modulus of elasticity and Poisson's ratio and unit and mortar-joint thickness are taken into account. Then, failure envelopes for both unit and mortar can be used to estimate the failure stress.

Detailed unit and mortar tests were performed to establish the mechanical properties. Bricks showed some dependency on 'manufacturing method' and mortar properties depend on the curing conditions. Specimens were taken from pieces of masonry, and not as usual, from mortar that hardened in a steel mould.

The masonry test program comprised tests on pieces of masonry from various sizes, ranging from stack bonded specimens, one brick in section, to 630 mm square specimens. All masonry specimens were half brick in thickness.
Several sub series were tested including six clay-brick types, with multiple sand lime cement ratios for the mortars. Experiments on masonry wallettes gave detailed material properties for both new and traditional materials that can be used in numerical simulations. Trends between properties are established and compared with information from literature.
Strength, modulus of elasticity and Poisson's ratios were established and relationships between strength and test parameters were obtained. Crack development and patterns were recorded. Post peak behaviour was observed in a few dedicated tests. The evolution of the tests indicated the important role of the brick mortar interface.

Dedicated test equipment, like laser speckle equipment, ESPI, was used for measuring the clay-brick-mortar interaction in detail. To allow for the detailed measurements of the force transfer, a moving seating arrangement (MSA) was developed. The MSA measured the reactions, which allowed for the estimation of the eccentricity of the axial load.
To investigate the effect of joint thickness, specimens were loaded concentrically and eccentrically. The effect on deformation of pointed masonry was also studied.
Five clay-brick types in combination with three bed joints thicknesses (15 combinations) were tested and their behaviour was analysed. Clearly the pillow shape of the bed joint affected the strain distribution over the joint.
The axial load in a masonry structure usually acts with some eccentricity. Therefore, specimens were loaded with various predetermined eccentricities. The strain distribution was observed with ESPI and compared with LVDT and DIANA results. It showed that most of the rotation occurred in the brick-mortar interface, especially due to the pillow shaped bed joint.
In pointed masonry when strong pointing and weak bedding mortar is used the pointing mortar acts as a hinge. The edge of the pointing mortar initiates failure cracking. In strong bedding and weak pointing mortar specimens some eccentricity was observed.

Further research is required for the magnitude of Poisson's ratio, (lateral deformation of specimens), and softening. In both cases, control of the lateral deformation is demanded.
The shear mechanism in masonry can further be examined using ESPI.
The shape of the joints, pillow shaped or recessed, has a negative effect on load transfer. Improvement of the method of mortar application and / or preparation of the bedding surface of the bricks can improve the load transfer. Improvements which may become essential in the modern age of performance based structural design, ensuring that masonry as a structural material remains relevant.

Samenvatting

Metselen is een eeuwenoude techniek waarvan de resultaten overal in Nederland te zien zijn. Bouwen met metselwerk is mogelijk doordat de drukweerstand goed is.
Bij het metselen worden stenen op elkaar gelegd en daarbij wordt mortel gebruikt. De interactie tussen de stenen en de mortel is van groot belang voor het mechanisch gedrag van metselwerk.

Recente ontwikkelingen zijn het gebruik van industrieel vervaardigde mortels van hoge kwaliteit en uitmuntende verwerkingseigenschappen en het gebruik van lijmmortels die met een spuitpistool worden aangebracht. Het metselproces en de rol daarbij van de mortel worden besproken. Ook komen de gangbare steensoorten, het verwerken van de stenen en de mortelsoorten aan bod en worden de esthetische kwaliteiten van de voegen belicht.

Nieuwe ontwikkelingen zowel op experimenteel als op numeriek gebied motiveerden nieuw onderzoek dat zich richtte op de rol van de interactie tussen stenen en mortel. Het gebruik van de laser spikkeltechniek (ESPI), maakte de gedetailleerde observatie van de steen mortel interactie mogelijk.
De vorm van de voeg, - met spleten bij traditioneel metselwerk en terugliggend bij modern lijmwerk - zorgt er voor dat er van de stenen schijfjes afsplijten. In combinatie met de interactie tussen proefstuk en lastplaten bepaalt dit effect het breukgedrag van gemetselde proefstukken.

Ook kennis van de (micro)structuur van (bak)stenen en mortel zijn van belang bij het verklaren van het vervormings- en breukgedrag. Zowel de stenen als de mortel zijn vaste maar poreuze stoffen en de spanningen die rondom de poriën optreden kunnen breuk inleiden. In de mortel zijn sterkere (stijvere) zandkorrels aanwezig die eveneens spanningsconcentraties veroorzaken.
De voeg wordt tijdens het metselen bij het positioneren van de stenen gevormd. Gewoonlijk onttrekken de stenen water uit de mortel waardoor de morteleigenschappen veranderen, vooral in het contactvlak tussen steen en mortel. Daardoor vomen deze overgangen zwakke plekken in het metselwerk.

De druksterkte van metselwerk kan met empirisch opgestelde formules worden voorspeld als de mechanische eigenschappen van de stenen en de mortel bekend zijn. Theorieën, gebaseerd op de gelaagde structuur van metselwerk, gaan uit van de interactie tussen steen en mortel. Uitgangspunt was daarbij dat de mortel veel zachter was dan de stenen. Bij zachte mortel ontstaan er in de steen trekspanningen in dwarsrichting, de materialen komen in een drie dimensionele spanningstoestand.
Bij meer recente modellen worden bezwijkomhullenden voor steen en mortel gebruikt om de metselwerksterkte te voorspellen.

De mechanische steeneigenschappen bleken af te hangen van de gevolgde vervaardigings-methode. De morteleigenschappen zijn vooral afhankelijk van de verhardingscondities. De mortelproefstukken werden zoals gebruikelijk in een stalen mal gemaakt maar ook van mortelschijven die uit metselwerk werden genomen.

Proeven op gemetselde prisma's van verschillende afmetingen en gemaakt van diverse soorten baksteen en mortels met verschillende samenstellingen resulteerden in een schat aan materiaaleigenschappen voor gebruik bij numerieke simulaties van zowel nieuwe als traditioneel bekende materiaalcombinaties. Met de gevonden resultaten werden trends onderzocht en vergeleken met uit de literatuur bekende informatie voor sterkte, E-waarden en dwarscontractiecoëfficiënten van metselwerk.
De verbanden tussen sterkte en proefparameters en het scheurvormingsproces en de scheurpatronen werden vastgelegd. Ook werd met enkele proeven het post-peak gedrag bepaald.

De belangrijke rol van de steen-mortel interactie werd gedetailleerd met proeven op 25 mm dikke proefstukken vastgesteld, die zowel centrisch als excentrisch werden gedrukt. Met ESPI en LVDT's werden de vervormingen bepaald. Om de krachtsverdeling door een proefstuk te kunnen vaststellen werd een opstelling met een bewegende onderplaat ontwikkeld.

Het ESPI test programma omvatte proeven op vijftien soorten metselwerk, gemaakt met vijf steensoorten elk in combinatie met drie mortels.
Uit de analyse van de ESPI-resultaten kwam duidelijk de invloed van de vorm op de rekverdeling over de voeg naar voren. Bij het excentrisch belasten bleek het grootste deel van de kromming van het proefstuk te worden veroorzaakt door de vervorming in de voeg overgang van steen naar mortel.
Ook in gevoegd metselwerk blijkt het voegmaterial het krachtenspel aanzienlijk te beïnvloeden.

Verder onderzoek kan zich richten op de grootte van de dwarscontractie-coëfficiënt en op softening. Voor beide gevallen is het meten van de dwarsvervorming voor de sturing van de proef van belang. Het (b)lijkt dat de reststerkte van een gemetseld proefstuk ongeveer 30% bedraagt van de piek belasting.
Ook het schuifmechanisme in metselwerk kan in detail verder worden onderzocht met ESPI.
Terugliggende voegen hebben een negatieve invloed op de krachtsoverdracht. Door de mortel anders aan te brengen en door het (voor)bewerken van het vlijvlak kan de krachtsoverdracht via de voeg worden verbeterd.

References

AND 96 Anderson, N., 1996, Investigation into the Effects of Brick Moisture content on the compressive behaviour of masonry mortar, Project Rapport TU/e.

ANS 64 Anson, M, An investigation into hypothetical deformation and failure mechanism for concrete, Magazine of Concrete Research, Vol. 16, no 47, pp. 73..82.

ATK 83 Atkinson, R.H., Noland, J.L. and Abrams, D.P., 1985, A proposed failure theory for brick masonry in compression, Proc. 3th Can. Mas. Symp., Edmonton, Canada, pp. 5-1..5-7.

ATK 85 Atkinson, R.H., Noland, J.L. and Abrams, D.P., 1985, A deformation failure theory for stack-bond brick masonry prisms in compression, Proc. 7th Int. Brick Block mas. Conf. Melbourne pp. 577..592.

BAL 91 Balen, K. van, 1991, Karbonatatie van kalkmortel en haar invloed op historische structuren, Thesis, Kath. Univ. Leuven, 1991.

BAZ 94 Bazant, Z.P., Ozbolt, J., Eligehausen, R., 1994, Fracture size effect: Review of Evidence for Concrete Structures, Journal Str. Eng. Vol. 120, no. 8.

BAZ 97 Bazant, Z.P., Xiang, Y., Size effect in compression fracture: splitting crack band propagation, Journ. Eng. Mechanics, 1997, pp. 162..172.

BERs91 Berndt, E. and Schöne, I, 1991, Tragfähigkeitsversuche am Naturstein-Mauerwerk aus Sächsischen Sandstein zur Beurteilung historischer Konstruktionen, Proc. 9th IBMaC, Eds. Glitza, H. and Göbel, K., Bonn, DGfM, pp. 1449..1456.

BER 91 Beranek, W.J. and Hobbelman, G.J., 1991, A mechanical model for brittle materials, Proc. 9th IBMaC, Berlin, Eds. Glitza, H. and Göbel, K., Bonn, DGfM, pp. 694..701.

BET 95 Betzler, M., 1995, Untersuchungen zur Auswirkung unterschiedlicher Formen von Versuchskörper bei der Ermittlung der Drukfestigkeit von Mauerwerk, Dissertation, Darmstadt.

BIE 91 Bierwirdt, H., Dialer, Ch., Stöckl, S. and Kupfer, H, 1991, Development of a test equipment for triaxial loaded mortar specimens, Proc. 9th IBMaC, Berlin, pp. 584..593.

BOT 94 Bottger, K.G., Mehlmann, M., Knöfel, D., 1994, Influence of Additives on Compressive Strength of Joints of Hardened Masonry Mortars, Proc. 10th IBMaC, University of Calgary, pp. 1367..1376.

BOR 01 Bormans, P., 2001, Keramiek, van steen tot synthetisch bot, Van Veen magazines, Amsterdam, ISBN 90 73035 79 1.

BRO 00 Brocken, H.J.P., Van der Pers, N.M. and Larbi, J.A., 2000, Composition of lime-cement and air-entrained cement mortar as a function of distance to the brick-mortar interface: consequences for masonry, Materials and Structures, Vol. 33, pp. 634..646.

CAR 66 Carputi, U., 1966, De mechanische sterkte van dragend metselwerk, KNB, De Steeg, The Netherlands, translation from: Sulla resistenza meccanica della murature portani in mattoni, Costruire, no 35.

CUR193 Vermeltfoort, A.T. and Pluijm, R. van der, 1999, Materiaalparameters voor constructief metselwerk, CUR Gouda, ISBN 90 376 0300 9.

DaFSt 232 Wittman and Zaitsev, 1974, Bestimmung physicalische Eigenschaften des Cementsteins, pp. 1..64, Verformung und Bruchvorgang beim

Poröser Baustoffe bei kurzzeitiger Belastung und Dauerlast, pp. 65..145, Berlin, Ernst, ISSN 0171-7197.

DaFSt 260 Eibl, J. and Ivanyi, G., 1976, Studie zum Trag- und Verformungs-verhalten von Stahlbeton, Berlin, Ernst, ISBN 3-433-00747-0.

DGfM92 /...../, 1992, Vorläufige Richtlinie zur Ergänzung der Eignungsprüfung von Mauermörtel, Deutsche Geselschaft für Mauerwerksbau e.v.

DIA 96 De Witte, F.C. (editor), DIANA – Finite Element Analysis, TNO Building and Construction research, Delft, 1996.

DRY 93 Drysdale, R.G., Hamid, A.A. and Baker, L.R., 1993, Masonry structures, behaviour and design, Prentice Hall, Englewood Cliffs, New Jersey

DUT 80 Dutron, 1980, in: Ontwerp en berekening van Metselwerk. Belgisch Instituut voor normalisatie. Belgium Building Code. NBN 24-301.

EC6 88 /...../, 1988, Eurocode No. 6. Common unified rules for masonry structures. Commission of the European Communities.

EC6 96 /...../, ENV 1996-1-1: 1996, Eurocode No. 6. Common unified rules for masonry structures. Commission of the European Communities.

EC6 02 /...../, ENV 2002-1-1: 2002, Eurocode No. 6. Common unified rules for masonry structures. Commission of the European Communities.

ENV 96 /...../, ENV 1996-1-1: 1996, Eurocode No. 6. Common unified rules for masonry structures. Commission of the European Communities.

EUR 96 /...../, 1996, European Committee for Standardization, juni 1996, prEN 772-1, Methods for test for masonry units, Determination of compressive Strength (draft), Brussel.

FRA 71 Francis, A.J., Horman, C.B. and Jerrems, L.E., 1971, The effect of joint thickness and other factors on the compressive strength of brickwork, Proc. 2nd Int. Brick Block Mas. Conf. Stoke on Trent, pp. 31..37.

FRA 91 Franke, L., Deckelman, G., Goretzky, 1991, Influence of material spread on the strength of brickwork–theoretical and experimental studies. Proc. 9th IBMaC, Berlin, pp. 180..187.

GEE 94 Geel, H.J.G.M. van, Pluijm R. van der, 1994, The Variability of Tensile and Flexural Bond Strength, Proc. 10th IBMaC, Calgary, Canada.

GEE 98 Geel, H.J.G.M., 1998, Concrete behaviour in multiaxial compression. Experimental research, Bouwsteen 48. Thesis, TU/e.

GRA 70 Gramberg, J., 1970, Klastische en kataklastische processen en hun betekenis voor de gesteentemechanica: inleiding tot breukmechanica voor gesteente, Thesis, TU Delft, published by: S.I. Pasmans.

GRO 88 Groot, C.J.W.P., 1988, Aspects of mortar brick bond. Proc. 8th Int. Brick/Block Masonry Conf. Dublin, pp. 175..181.

GRO 93 Groot, C.J.W.P., 1993, Effects of water on mortar-brick bond, PhD Thesis, Delft.

HAL 58 Haller P., 1958, (Dutch translation 1967), Die technische Eigenschaften von Backstein, Schweizerische Bauzeitung, 1958.

HAY 04a Hayen R., Van Balen K. and Van Gemert D., 2004, The mechanical behaviour of mortars in triaxial compression. In: C. Modena, P.B. Lourenço and P. Roca (eds.), Proc. 4th Int. Seminar on Structural Analysis of Historical Constructions, Padova 2004: vol.1, pp. 611..617.

HAY 04b Hayen R., Van Balen K. and Van Gemert D., 2004, The mechanical behaviour of historic masonry structures. In D. Martens & A. Vermeltfoort (eds.), Proceedings of the 13th International Brick/Block Masonry Conference, Amsterdam 2004: pp.1147..1157.

HEN 87 Hendry, A.W., Sinha, B.P. and Davies, S.R., 1987, Load Bearing Brickwork design, 2nd edition, Ellis Horwood Ltd, ISBN 0 745 0183

HEN 90 Hendry, A.W., 1990, Structural masonry, Macmillan Education Ltd, ISBN 0-333-49748-1.

HIL 69 Hilsdorf, H.K., 1969, Investigation into the failure mechanism of brick masonry loaded in axial compression, Designing Engineering and construction with masonry products Johnson F.B. Gulf publishing Texas pp. 34..41.

HIL 76 Hillerborg, A., Modéer, M. and Petersson, P.E., Analysis of crack formation and crack growth in concrete by means of fracture mechanics and finite elements, Cement and Concrete Research, 6, pp. 773..782.

HOB 91 Hobbs, B., 1991, Development of a construction quality control procedure using ultrasonic testing, 9th IBMaC, Berlin, pp. 636..644.

HOD 93 Hodge, J., 1993, Brickwork for apprentices, 4 Rev.ed, Hodder Headline PLC, Kent, Great Britain, ISBN 0-340-55641-1.

HUI 66 Huizer, A., 1966, A non Standard Tensile Splitting Test for Clay Brick Masonry. Newsletter no 30, Brick Development Research Institute, 1966, University of Melbourne, BDRI, Australia.

JON 83 Jones, R. and Wykes, C., 1983, Holographic and Speckle Interferometry, 2nd edition, Cambridge University Press, Cambridge, ISBN 0 521 23268 6.

KAS 90 Kasten, D., 1990, The Compressive Strength of Masonry Units Determined According to Different European Standards. Masonry International, Vol 4, No2.

KAS 94 Kasten, D. and Eden, W., 1994, The influence of the compressive strength of the mortar on the compressive strength of masonry, 10th IBMaC, Calgary, Canada, pp. 1407..1413.

KHA 90 Khalaf, F.M. and Hendry, A.W., 1990, Effect of bed face preparation in compressive testing of masonry units. Brit. Mas. Soc. Proc. No 4, pp. 129..130.

KHA 94 Khalaf, F.M. and Hendry, A.W., 1994, Masonry unit shape factor from test Results, Proc. 3th Int. Mas. Conf., Stoke on Trent, pp. 136-140.

KHO 72 Khoo, C.L., 1972, A failure criterion for brickwork in axial compression, PhD Thesis, Univ. of Edinburgh.

KJA 91 Kjær, E., 1991, The influence of suction from masonry units upon the strength of the hardened masonry mortar, 9th Int. Brick/Block Mas. Conf., Berlin pp. 1356..1363.

LAR 91 Larbi, J.A., 1991, The cement paste aggregate interfacial zone in concrete, Dissertation, TU Delft.

LAW 85 Lawrence, S.J., 1985, Random Variations in Brickwork Properties, Proc. 7th IBMaC, Melbourne, Australia, pp. 537..547.

MAN 94 Mann, W. and Betzler, M., 1994, Investigations on the effect of different forms of test samples to test the compressive strength of masonry. Proc. 10th IBMaC, Calgary, pp. 1305..1313.

MAS 96 Maso, J.C. (ed.), 1996, Interfacial transition zone in concrete, Rilem, report 11, E&FN Spon, ISBN 0 419 20010 X.

MCN 85 McNary, W.S. and Abrams, D.P., 1985, Mechanics of masonry in compression, Journal of structural engineering.

MIE 84 Mier, J.G.M. van, 1984, Strain-softening of concrete under multiaxial loading conditions, PhD thesis, TU/e, Eindhoven, The Netherlands.

MIE 97 Mier, J.G.M. van, 1997, Fracture processes of concrete. Assesment of material parameters for fracture models, CRC Press, Boca Raton, ISBN 0-8493-9123-7.

MORi90 Morice P.B. and Base, G.D, 1990, The design and use of a demountable mechanical strain gauge for concrete structures, Cement and concrete association research and development division. Magazine of concrete research, August 1953 vol. 5 no 13 pp. 37..42.
Base, G.D., 1955, Further notes on the demec, a demountable mechanical strain gauge for concrete structures, Magazine of concrete research, March 1955, vol. 7, pp. 35..38.

MUL 94 Muller, Ch. and Meier, U., 1994, Influence of unit and mortar properties on the compressive strength of mortar in vertically perforated clay-brick masonry, Proc. 10th IBMaC, Calgary, Canada, pp. 1423..1432.

NBN 80 /……..…/ 1980, Ontwerp en berekening van metselwerk NBN 24-301, Belgisch Instituut voor Normalisatie, Belgium Building Code, see [DUT 80]

NEN 197-1 NEN EN 197-1:2000, Cement - deel 1 : Samenstelling, specificatie en conformiteitscriteria voor gewone cementsoorten. Nederlands Normalisatie Instituut, Delft.

NEN 2489 /...../ 1976, Bricks of fired clay for masonry, Nederlands Normalisatie Instituut, Delft.

NEN 2871 /……./ 1975, Test methods for building materials. Mechanical properties, Nederlands Normalisatie Instituut, Delft.

NEN 3835 /...../ 1991, Mortars for masonry of bricks, blocks or elements of fired clay, calcium silicate, concrete and aerated concrete. Nederlands Normalisatie Instituut, Delft.

NEN 6790 /…… / 1991, Steenconstructies TGB 1991, basiseisen en bepalingsmethoden.
/.... .../ 2004, NEN 6790:2004_concept 2004-08-11, Steenconstructies. Nederlands Normalisatie Instituut, Delft.

NEW 98 Newport, 1998, 'Brochure of the ESPI SD-30 system', Newport Instruments AG Giessenstrasse 15, CH-Schlieren, Switserland.

NIE 95 Nieuwenhuys, M.H.M., 1995, Innovations in the brick laying process on the building site, Proc. 4th Int. Mas. Conf. London, pp. 180..182.

OHL 86 Ohler, A., 1986, Zur Berechnung der Druckfestigkeit von Mauerwerk unter Berücksichtigung der mehrachsigen Spannungszustäde in Stein und Mörtel, Die Bautechnik 63, 1986 Heft 5, pp. 163..169.

PAG 85 Page, A.W. and Marshall, R., 1985, The influence of brick and brickwork prism aspect ratio on the evaluation of compressive strength. Proc. 7th IBMaC, Eds. T. McNeilly and J.C. Scrivener, Melbourne, pp. 653..664.

PAG 88 Page, A.W. and Shrive, N.G., 1988, A critical Assessment of Compression Test for Hollow Block Masonry. Mas. Int., Vol. 3, No.3, pp. 64..70.

PEL 95 Pel, L., 1995, Moisture transport in porous building materials, PhD Thesis, TU/e.

PLA 86 Plas, J.C. van der, and Gielgens, F.H.P., 1986, Economische bouwtechniek voor parkeergarages, Cement Jrg. 38, nr. 3, pp. 46..53.

PLU 92 Pluijm, R. van der, 1992, Material Properties of Masonry and its Components under Tension and Shear, Proceedings of the 6th Canadian Masonry Symposium, Saskatoon, Canada, pp. 675..686.

PLU 96a Pluijm, R. van der, 1996, Deformation controlled tensile and flexural tests on clay brick and calcium silicate masonry, TU/e rapport TUE/BKO/96.2, Eindhoven.

PLU 96b Pluijm, R. van der, and Naaktgeboren, N.M., augustus 1996, Spreiding in hechtsterkte en buigtreksterkte, een numeriek stochastische gevoeligheidsanalyse, TNO Bouw rapport 95-CON-R1640.

PLU 97 Pluijm, R. van der, 1997b, Non-linear Behaviour of Masonry under Tension, Heron, Vol. 42, No.1, ISSN 0046-7316, pp. 25..54.

PLU 99a Pluijm, R. van der, Korteduur- en langeduurgedrag van baksteen metselwerk, TNO Rapport 1999-con-R3020

PLU 99b Pluijm, R. van der, 1999, Out-of-plane bending of masonry. Behaviour and strength, Thesis, TU/e.

POL 67 /...../ 1967, Polytechnisch zakboekje, PBNA, 255ste t/m 285ste duizendtal, Argus, Amsterdam.

PRO 81 Probst, P., 1981, Ein beitrag zum Bruchmechanismus von zentrisch gedrücktem Mauerwerk, München, PhD thesis.

RAI 96 Raijmakers, T.M.J., 1996, Onderzoek van het krimp- en kruipgedrag van metselwerk, meetrapport, in opdracht van de leerstoel Stapelbouw, TU/e rapport TUE/BKO/96.03.

RAO 69 Rao R.N.S. 1969, Experimental investigation on structural performance of brick masonry prisms, Designing Engineering and construction with masonry products, Johnson F.B. Gulf publishing Texas pp. 74..79.

REI 85 Reinhard, H.W., 1985, Beton als constructiemateriaal, eigenschappen en duurzaamheid, Delftse Universitaire pers.

ROT 92 Rots, J.G., Numerical simulation of cracking in structural masonry, Heron, vol. 36 no. 2. pp. 49..63.

ROT 97 Rots, J.G. (editor), 1997, Structural masonry. An experimental / numerical base for practical design rules, CUR Gouda, A.A.Balkema.

SAB 94 Sabha, A. and Schöne, I., 1994, Untersuchungen zum Tragverhalten von Mauerwerk aus Elbesandstein, Bautechnik (Ernst & Sohn Verlag) Nr 71, pp. 161..166.

SAB 98 Sabha, A., 1998, Eccentrically loaded historic masonry, Masonry 8, Proc. 5th Int. Mas. Conf. London, West, H.W.H., ed., Brit. Mas. Soc., Stoke on Trent, pp. 176..181.

SAL 71 Salin, S., 1971, Structural Masonry, Prentice-Hall, Inc. Englewood Cliffs, New Jersey.

SCHb82 Schulenberg, W., 1982, Theoretische Untersuchungen zum Tragverhalten von Zentrisch gedrücktem Mauerwerk aus künstlichen Stein unter berücksichtigung der Qualität der Lagerfugen, Darmstadt, PhD thesis.

SCHu88 Schubert, P., 1988, The influence of Mortar on the Strength of Masonry, Proc. of the 8th IBMaC, Trinity College, Dublin, Ireland, pp. 162..174.

SCHu91 Schubert, P., 1991, Properties of Masonry, Masonry Units, Masonry Mortar, Proc. 9th IBMAC, Berlin, ed. DgfM, pp. 101..108.

STO 94 Stöckl, S., Bierwirth, H. and Kupfer, H., 1994, The influence of the test method on the results of compression tests on mortar, Proc. 10th IBMaC, ed. Shrive, N. and Huizer, A., Calgary, Canada, pp. 1397..1406.

SYM 90 Sym, R., A Study of the Dimensional Deviations of Clay Bricks. - Part I and II - Masonry International, Vol 4, No1, 1990.

TOR 89 Torrenti, J.M., Desrues, J. Acker, P. and Boulay, C., Application of stereogrammetry to the strain localization in concrete compression, in: Cracking and Damage, eds. J. Mazars and Z.P. Bazant, Elsevier Applied Science, London, pp. 30..41.

VER 97 Vervuurt, A.H.J., 1997, Interface fracture in concrete, Technische Universiteit Delft, PhD thesis.

VIN 01 Vintzileou, E., 2001, The effect of deep rejointing on the compressive strength of brick masonry, Mas. Int. Vol. 15 No. 1, pp. 8..12.

VMF 91 Vermeltfoort, A.T. and Pluijm, R. van der, 1991, Strength and deformation properties of masonry to be used in computercalculations. Proc. 9th IBMaC, Berlin, pp. 244..251.

VMF 93 Vermeltfoort, A.T., Raijmakers, T.M.J. and Janssen, H.J.M., 1993, Shear tests on masonry walls, Proc. 6th North American Mas. Conf., Philadelphia, USA, pp. 1183..1195.

VMF 96 Vermeltfoort, A.T., 1996, Effects of boundary conditions on compressive properties of brittle materials, Proc. 7th North Am. Mas. Conf. pp. 1130..1142.

VMF 97a Vermeltfoort, A.T., 1997, Properties of Some clay bricks under varying loading conditions, Mas. Int. Vol. 10, No. 3, pp. 85..91.

VMF 97b Vermeltfoort, A.T., 1997, Effects of the width and boundary conditions on the mechanical properties of masonry prisms, 11th IBMaC, Shanghai, China, pp. 385-395.

VMF 98 Vermeltfoort, A.T., 1998, Mechanical compressive properties of small sized mortar cylinders, 8th Can. Mas. Symp., Jasper, pp. 336..347.

VMF 04 Vermeltfoort, A.T., 2004, Shear, bond and 2D compressive properties of thin layer mortar masonry. In D. Martens & A. Vermeltfoort (eds.), Proc. of the 13th Int. Brick/Block Masonry Conf., Amsterdam 2004: pp.73..82

VON 92 Vonk, R., 1992, Softening of concrete loaded in compression, PhD. Thesis, TU/e.

WAT 59 Waters, E.H., 1959, A note on the tensile strength of concrete across construction joints, Mag. of Concrete Research, Vol. 11, no. 3, pp. 163..164.

WIJF 04 Wijffels, T., 2004, Bond strength in calcium silicate brick masonry, 13th Int. Brick Block Masonry Conference, eds. Martens D.R.W. and Vermeltfoort A.T., TU/e, Eindhoven, ISBN 90-90-18294-2, pp. 903.. 914.

WIN 89 Winslow, D., 1989, Some experimental possibilities with mercury intrusion porosimetry, Roberts L.R. and Skany, J.P. eds. of Pore structure and permeability of cementitious materials, Mat. Res. Soc. Symp. Proc. Vol. 137, pp. 93..103.

WOL 93 Wolde-Tinsae, A.M., Atkinson, R.H., and Hamid, A.A., 1993, State-of-the-Art Modulus of elasticity of Masonry, Proc. of the 6th NAMC, Drexel University, Philadelphia, Vol. 2, pp. 1209..1220.

ZIJ 01 Zijl, G.P.A.G. van, Rots, J.G. and Vermeltfoort, A.T., 2001, Modelling shear-compression in masonry, 9th Can. Mas. Conf., Fredericton, Canada, on CD.

Variables, Symbols and Notations

A	loaded gross cross-sectional area, b*d,	mm^2
A	parameter for strain	
A	age of a specimen	days
a	half of crack length	mm
b	length of loaded section	mm
B	parameter	
C	stiffness of a tension bar in combination with a load cell	kN/mm
d	depth of loaded section, measured perpendicular to loading direction	mm
e	eccentricity	mm
e_x	eccentricity in X direction	mm
e_y	eccentricity in Y direction	mm
e_{real}	realised eccentricity	mm
e_{desi}	desired eccentricity	mm
E	modulus of elasticity	N/mm^2
E_{33}	modulus of elasticity at 1/3 of ultimate load, (Appendix A.1)	N/mm^2
E_{Bo}	modulus of elasticity of brick, Bolidt test	N/mm^2
E_{bri}	modulus of elasticity of brick	N/mm^2
EI_x	bending stiffness of the specimen, X-axis	N/mm^2
EI_z	bending stiffness of the specimen, Z-axis	N/mm^2
E_{mas}	modulus of elasticity of masonry (measured in a test)	N/mm^2
E_{mor}	modulus of elasticity of mortar	N/mm^2
E_{spe}	modulus of elasticity of the specimen (form 1000 to 25000 N/mm^2)	N/mm^2
F	Force, applied load	kN
F_{max}	maximum force recorded in a test	kN
f_c	compressive strength	N/mm^2
$f_{c,1}$	uni-axial compressive strength	N/mm^2
$f_{c,1,\ cyl}$	uni axial compressive cylinder strength with lateral compression	N/mm^2
$f_{c,2}$	compressive strength under bi-axial condition	N/mm^2
$f_{c,200}$	compressive strength for a cube with ribs of 200 mm	N/mm^2
$f_{c,avg}$	compressive strength, averaged value	N/mm^2
$f_{c,BO}$	brick compressive strength, Bolidt tests result	N/mm^2
$f_{c,bri,EC6}$	averaged, normalised brick compressive strength, acc. EC6	N/mm^2
$f_{c,bri}$	averaged unit compressive strength of six (or more) units	N/mm^2
$f_{c,con}$	biaxial compressive strength of a laterally confined cylinder	N/mm^2

$f_{c,k}$	characteristic masonry compressive strength in	N/mm^2
$f_{c,tlm}$	compressive strength of thin layer masonry	N/mm^2
$f_{c,mas}$	masonry compressive strength	N/mm^2
$f_{c,mor}$	mortar compressive strength, averaged value for six tests	N/mm^2
$f_{c,spec}$	compressive strength of a specimen with dimensions h and d	N/mm^2
f_{ref}	strength of a reference sized specimen	N/mm^2
f_t	tensile strength	N/mm^2
$f_{t,1}$	uni-axial tensile strength	N/mm^2
$f_{t,2}$	tensile strength under bi-axial condition	N/mm^2
$f_{t,bri}$	uniaxial tensile brick strength	N/mm^2
f_{test}	strength of a specimen with certain dimensions	N/mm^2
h	height of a specimen parallel to the loading direction	mm
h_{bri}	height (thickness) of the brick	mm
h_{mor}	thickness of the mortar bed	mm
h_{spe}	height of the specimen	mm
I_{spe}	second moment of inertia, 1/12 b.d^3	mm^4
k	factor, depending on brick and mortar properties	
l	length of a specimen measured perpendicular to the loading direction	mm
L_1	Load at level 1	kN
L_2	Load at level 2	kN
LC_i	force measured by Load Cell i, where i = 1, 2 or 3	kN
M	Moment (result of load cell measurements)	kNmm
m_{mor}	parameter for mortar in failure envelope	
M_0	initial moment	kNmm
M_x	Moment around X axis	kNmm
M_z	Moment around Z axis	kNmm
n	exponent, n = 0.546	
N	Normal or axial force	kN
O	bed joint orientation	rad
R^2	square of the Pearson product moment correlation coefficient	
r	radius at crack tip	
S	ratio between strength and modulus of elasticity	
SR	Strain Ratio	
scf	size correction factor, scaling of results of different sized specimens	
std	standard deviation	
sv	scaled value	
t	specimen’s thickness, measured perpendicular to the loading direction	mm
t_{bri}	thickness for brick (vertical)	mm

t_{mas}	thickness of masonry (vertical gauge length)	mm
t_{mor}	thickness mortar joint (vertical)	mm
U	non uniformity coefficient [HIL 67]	
u_i ; u_j	displacement in horizontal direction of node i, j	mm
v	displacement measured during a certain stress increase	mm
v_i ; v_j	displacement in vertical direction of node i, j	mm
w	width of the specimen	mm
w_x, w_z	displacement of bottom plate of the MSA	mm
W	wind load	kN
W	weight of the load platen of the MSA	kN
x_i, x_j	position in X direction of 'measuring' point i, j	mm
y_i, y_j	position in Y direction of 'measuring' point i, j	mm
(y_i-y_j)	gauge length for strain calculation, ESPI results	mm

Greek symbols

α, β	parameter	
δ	error	
ε	strain	
ε_{max}	strain at ultimate load, after correction for initial effects	mm/m
ε_r	strain for a $\Delta\sigma$ = 1 N/mm^2	mm^2/N
$\varepsilon_{r,y}$	strain per N/mm^2 stress variation, in Y direction	mm^2/N
$\varepsilon_{x,bri}$	strain in x direction in brick	mm/m
$\varepsilon_{x,mor}$	strain in x direction in mortar	mm/m
ε_{90}	strain that occurred for σr=0.90	mm/m
ΔF_i	load level difference during an ESPI measurement	kN
Δl_{bri}	shortening under compression of brick	mm
Δl_{mas}	shortening under compression of masonry	mm
Δl_{mor}	shortening under compression of mortar joint	mm
$\Delta l/l_r$	strain (possibly measured over a void (fissure) for a $\Delta\sigma$ = 1 N/mm^2	mm^2/N
θ	variable (angle)	rad
$\Delta\sigma$	stress increase during an ESPI measurement	N/mm^2
σ	stress	N/mm^2
σ_c	compressive stress in axial direction	N/mm^2
$\sigma_{c,2}$	lateral confinement stress	N/mm^2
σ_t	tensile stress	N/mm^2
σ_{gr}	gross stress increase	N/mm^2
σ_r	stress ratio F/F_{max}	
σ_2	lateral confinement stress of a cylinder	N/mm^2

σ_x	stress in x direction (lateral)	N/mm^2
$\sigma_{x,brir}$	stress in brick (lateral)	N/mm^2
$\sigma_{x,mor}$	stress in mortar (lateral)	N/mm^2
σ_y	stress in y direction applied stress, working stress	N/mm^2
$\sigma_{y,mor}$	working stress in the mortar (applied stress in Y direction)	N/mm^2
$\sigma_{z,bri}$	stress in z direction in brick	N/mm^2
$\sigma_{z,mor}$	stress in z direction from mortar	N/mm^2
τ_{xy}	shear stress	N/mm^2
ν	Poisson's ratio	
ν_{bri}	Poisson's ratio for brick	
ν_{mor}	Poisson's ratio for mortar	
$\varphi_{x,s}$	rotation around the X-axis of the load platen	rad
$\varphi_{x,spec}$	rotation around the X-axis of the specimen	rad
$w_{x,spec}$	horizontal displacement in X direction of the specimen	mm
$\varphi_{z,s}$	rotation around the Z-axis of the load platen	rad
$\varphi_{z,spec}$	rotation around the Z-axis of the specimen	rad
$w_{z,spec}$	horizontal displacement in Z direction of the specimen	mm

Subscripts

0	number, indicating initial situation
33	refers to a situation at 1/3 of ultimate load
200	refers to the size of a reference cube
bri	clay-brick unit
c	compression
cyl	cylinder
Dut	Dutron [DUT 80]
EC6	Euro Code 6
ESPI	Electronic Speckle Pattern Interferometry
gro	gross
i, j	variable,
k	characteristic
Kha	Khalaf [KHA 94]
mor	mortar
mas	masonry
max	maximum
r	relative ($\Delta\sigma$ = 1 N/mm^2)
spe	specimen
TL	thin layer masonry
t	thickness
x, y, z	directions

1 Analysis of traditional measurement results

1.1 About stresses and strains.

In referring to applied stresses and the resulting strains, it is noted that actual stress and strain distributions inside a specimen may be unevenly. This is because of several factors, such as, for instance, the presence of weak spots, fissures and stiffer grains of sand.

In this thesis, applied stress, σ is defined as averaged forces per unit area of the loaded surface and the resulting strain, ε as average change in length per unit initial gauge length. Thus σ = N/A where N is the applied load and A is the gross sectional area.

Strain (ε) is per definition the change in length (Δl) divided by the initial gauge length (l) despite of any fissures, voids etc., occurring within the considered area. Thus, the ε results describe the local behaviour of the part of the specimen included between two measuring points under the (global) applied stress (σ).

1.2 Establishment of E-values and Poisson's ratios

The modulus of elasticity is defined as the ratio between an applied stress and the strain that consequently occurs. Usually, linear elastic behaviour is assumed, i.e.

$$\Delta l = \frac{Fl}{EA} \text{ or } \sigma = E\,\varepsilon \qquad (1)$$

with:

σ = F/A, and ε = Δl/l.

However, when the behaviour is non linear, the definition could be adjusted to:

$$\Delta l = \frac{\Delta F l}{E_S A} \text{ or } \Delta\sigma = E_S\,\varepsilon \qquad (2)$$

The modulus of elasticity (E_S) represents coefficient of proportionality (CoP) of the tangent to the stress strain relationship at a certain stress level. Other definitions for the modulus of elasticity are a) the CoP obtained with a linear best fit to (a part of) the σ-ε diagram, b) the tangent to the σ-ε diagram in the origin, (or any other point) or c) by using the CoP of the connection line between a point on the σ-ε diagram and the origin.

In this thesis, linear and quadratic approximation procedures are used. For both procedures the method of least squares is used to fit the best fit to the measured curve. From these best fit relationships, E-values were derived.

1.2.1 Procedure Linear.

The linear procedure is as follows.

1. Plot the load versus the deformation for each LVDT.
2. Correct or omit deviations in LVDT results.
3. Calculate strain from the averaged LVDT results and plot the σ-ε diagram.
4. Establish a linear best fit with e.g. the best fit procedure of the Excell software, as:

$$\sigma = E\,\varepsilon + \delta. \quad (3)$$

Use a (linear) part of the diagram. Usually, a part between 15% and 75% of ultimate load will give an acceptable (linear) fit. In some cases these boarders must be changed in order to obtain a better fit (R^2 closer to one).

5. In a similar way, Poisson's ratio (ν) can be established from lateral strain with:

$$\nu = E_{ax}/E_{lat} \quad (4)$$

with:

E_{ax} = E-value from axial measurements and

E_{lat} = E-value form lateral measurements.

1.2.2 Procedure Parabolic

The following parabolic best fit method has been used to establish the shape of the σ-ε diagram.

1. Plot load versus deformation for each LVDT.
2. Correct or omit deviations in LVDT results.
3. Calculate strain from the averaged LVDT results and plot the σ-ε diagram.
4. Normalise the values to $\sigma_r = F/F_{max}$ and $\varepsilon_r = \Delta l/\Delta l_{max}$

Δl_{max} is the deformation that occurs at F_{max}.

5. Describe the curve between $\sigma r = 0.15$ and $\sigma r = 0.9$ with a second degree parabola of the form:

$$\sigma_r = P\varepsilon_r^2 + Q\varepsilon_r + R \quad (5)$$

(The parameters P, Q and R were established, separately for each specimen, using a quadratic best fit procedure, Appendix A.5.5 gives data).

6. Establish the modulus of elasticity in the origin (E_0) with the secant to the quadratic best fit through the results between $\sigma r = 0.05$ and $\sigma r = 0.15$. The "real" origin (point O) is found by intersecting this second degree function with the X-axis.
7. Establish the value of E_{33}, i.e. the modulus of elasticity at one third of ultimate load. Use the "real" origin. Fit a straight line through the results between $\sigma_r = 0.25$ and $\sigma_r = 0.50$, to find E_{33} in the 'exact' point were $\sigma_r = {}^1/_3$.

E_{90} was established similarly for $0.70 < \sigma_r < 0.90$ as $E_{90} = 0.90 f_{c,mas}/\varepsilon_{90}$.

8. Make corrections when the first part is concave. Omit the results in the lowest part of the curve and establish the best fit again. Repeat this process until the best fit is convex.
9. Omit error readings from LVDTs that got loose due to spalling. Then, an elongation is measured while the relaxing parts move away from each other.
10. Normalise equation (5). The function then goes through the point S ($\varepsilon_r = 1$; $\sigma_r = 0.9$) and the earlier mentioned origin point O.
Equation (5) changes to:

$$\sigma_r = A\ \varepsilon_r 2 + B\ \varepsilon_r \qquad (6)$$

in which A + B = 0.9 while the point S ($\varepsilon_r = 1$, $\sigma_r = 0.9$) is on the original curve.

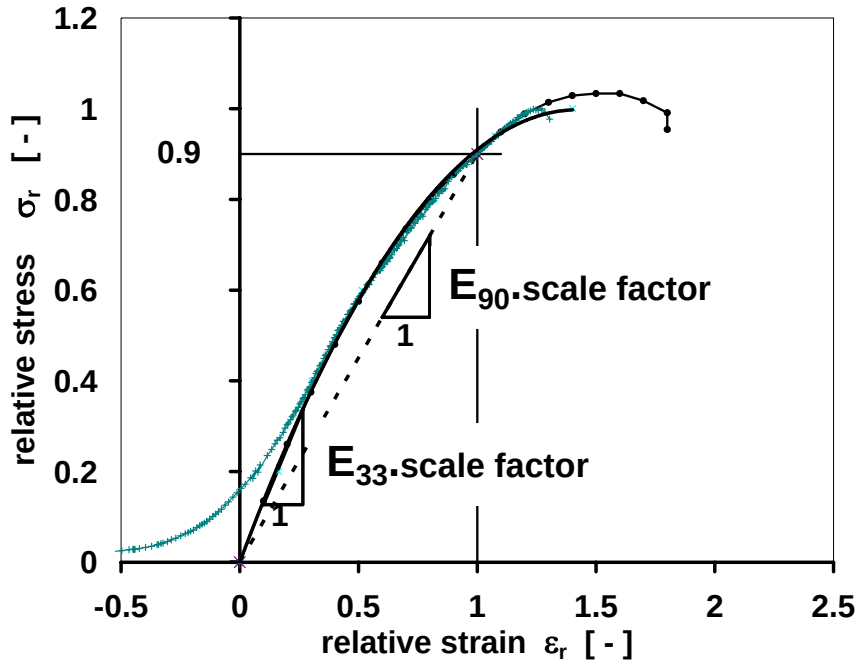

Figure 1 Normalised stress strain diagram with definitions for the modulus of elasticity. The scale factor is equal to $f_{c,mas.}/\varepsilon_{90}$.

In section A.5.5. some key values of each separate test are given. The measured stress strain diagram can be reconstructed with these values. With the value B of the function $y = A x^2 + Bx$ the normalized graph can be plotted, Figure 2a.
Given the values: $Y = \sigma/f_{c,mas}$ and $X = \varepsilon/\varepsilon_{90}$ the 'real' σ ε diagram can be reconstructed, Figure 2b. The strength ($f_{c.mas}$) is used to establish the values along the Y-axis. With the value of E_{90} the X-axis values can be calculated, while $\varepsilon_{90} = 0.90.f_{c,mas}/E_{90}$. Other values, like E_0 and E_{33} can alternatively be used to establish the X-axis (strain) values or for comparison with the other values.

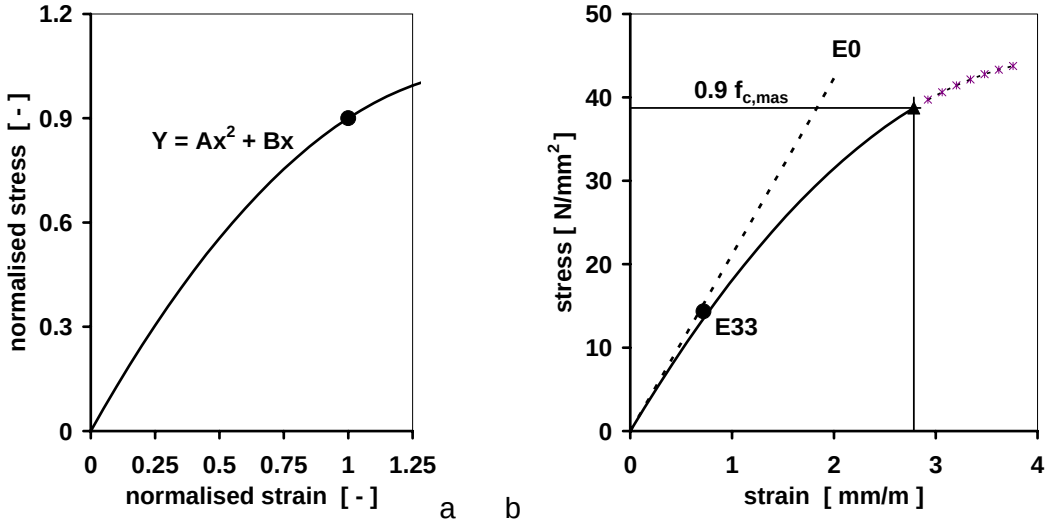

Figure 2 Reconstruction of the measured stress strain diagram using the key values given in Appendix A5.5. a) Normalised diagram. b) Reconstructed σ-ε diagram.

2 Design of the moving seating arrangement

2.1 General

One of the aspects in the design of the moving seating arrangement was “parallel movement of the load platens”, to apply a uniform displacement field.
However, differences in reactions, measured by the load cells, causes differences in elongation of the three tensile bars and consequently rotation of the load platens.

a) A large difference in load cell readings gives a higher accuracy of the measurement. Therefore, the tensile bars have to be placed a close together as possible.
b) For practical reasons, the specimen should remain visible, distance at least 120 mm.
c) The smallest rotation is obtained when the distance is as large as possible but the distance between the columns of the 2.5 MN Schenck testing machine is limited.
d) The tensile bars of top and bottom load platen have to pass.

This resulted in a centre to centre distance of the tensile bars for the top load platen of 175 mm, and 325 mm for the bottom load platen.
The bars of the top load platen run through holes in the bottom load platen.
A surface is determined by three points, therefore it was decided to use three tension bars positioned in an equal sided triangle.

2.2 Key values

In the initial phase of testing, differences in the reactions measured by the load cells are relatively small and consequently the accuracy is a point of concern. Further, the accuracy of the load eccentricity is discussed.

2.2.1 Sensitivity of the moving seating arrangement

In the initial phase of a test the precision of the load cells is of importance for an accurate estimation of the load eccentricity.
The force difference of each individual load cell (ΔF_i) can be established with the following Equations.

$$N * e_z = \frac{325}{2} * (LC_1 - LC_2) \quad (7)$$

$$N * e_x = \frac{325}{2\sqrt{3}} * \left(\frac{(LC_1 + LC_2)}{2} - LC_3 \right) \quad (8)$$

$$\Delta F_i = LC_i - \frac{(LC_1 + LC_2 + LC_3)}{3} \quad (9)$$

with:

e_x ; e_z = eccentricity in X ; Z- direction

LC_i = the forces measured by the load cells, i = 1, 2 or 3

N = $LC_1 + LC_2 + LC_3$

In view of the Equations (7)-(9) the following observations about the expected forces can be made.

1. To obtain an eccentricity where stresses are zero at one side of the specimen, i.e. $|e_z|$ = 16.25 mm, a difference between the forces in the left and right load cell of approximately one tenth of the total load is required (Equation 7).
Since LC_3 is equal to the averaged value of the three load cell recordings, LC_1 and LC_2 both will have a deviation (ΔF_i) of 5% of the total load or 1.66% of the averaged force in each tensile bar. For similar reasons, LC_3 only has to deviate 2.22 % from the averaged value to obtain a stress free front or back surface, i.e. a load eccentricity in thickness direction of $|e_x|$ of 4.17 mm, (Equation 8).

2. The force difference that has to be measured is relatively small in comparison with (one third of) the total load. As an example, ΔF_i is plotted versus N/3 in Figure 3. Two forces (load cells LC_1 and LC_2) increased linearly, one force (LC_3) remained more or less constant during the test. The rimples in the graph indicate that the sensitivity of the measurements is far below 100 N. Detailed observation showed that the load cells could distinguish a force variation of approximately 12.5 N. This sensitivity of the load cells was sufficient, while it allowed for the measurement of moments of minimal 4.15 Nm, which is a relatively small value compared with the measured values.

As stated earlier, M-N relationships were almost linear, except in the beginning of a test, and deviations from the best fit line were small. Using best fit methods, the values of M_0 and e could easily be established. The use of M-N relationships and linear best fit techniques improved the accuracy of the estimation of the load eccentricity considerably.

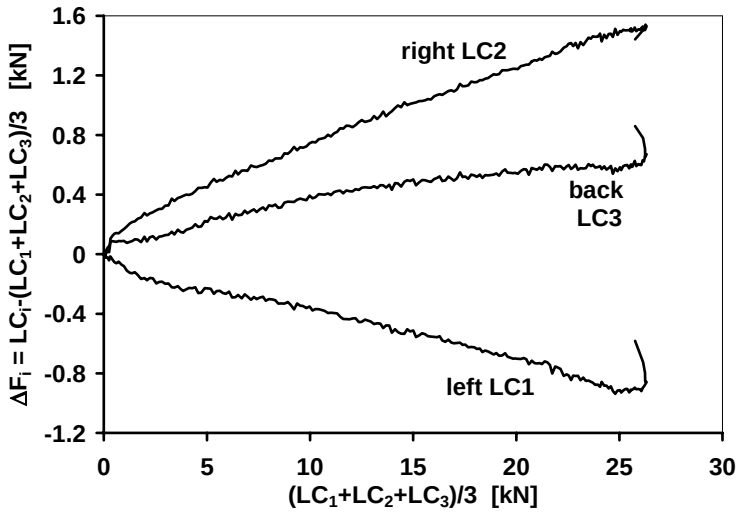

Figure 3 Example of ΔF_i versus N/3.

2.2.2 Rotation of the moving load platen

Rotation of the moving load platen may be estimated from the force-differences in the tension rods measured by the load cells.

The mechanical scheme of the moving seating arrangement is given in section 7.3.3., Figure 72. The stiffness of each tension bar, together with the corresponding load cell was established experimentally and equals C = 150 μm/kN. The 1 m long, 16 mm diameter bars itself have a stiffness of 24 μm/kN.

Forces in the tension rods will be unequal when the load is eccentric. The elongation of the bars will be different, and consequently the moving load platen will rotate. The rotation (φ) is equal to the difference in bar elongation divided by their distance, (325 mm centre to centre). The force difference in the tension bars is equal to the moment M divided by their distance. Rotation of the moving load platen (φ) may be estimated from the force-differences in the tension bars measured by the load cells as follows:

$$\varphi_{z,sys} = (LC_1 - LC_2) * \frac{C}{325} = \frac{2 \cdot M_z * C}{325^2} \tag{10}$$

$$\varphi_{x,sys} = \left(\frac{(LC_1 + LC_2)}{2} - LC_3 \right) * \frac{C}{281} = \frac{3 \cdot M_x * C}{281^2} \tag{11}$$

The rotation stiffness of an uncracked specimen equals:

$$\varphi_{z,spec} = \frac{M_z \bullet h_{spec}}{E_{spec} I_{spec}} \tag{12}$$

$$\varphi_{x,spec} = \frac{M_x \bullet h_{spec}}{E_{spec} I_{spec}} \tag{13}$$

with:

φ = the rotation of the load platen is $\varphi = \Delta L/d$,
M = the moment $M = \Delta L*C*d$.
C = the stiffness of a tension bar with load cells included
d = 325 mm.
The deformation of the steel components and shear deformation of the specimen are neglected.

From (10), and (12) respectively (11), and (13) it follows that the ratios between the rotation stiffness of the system and that of the specimen are:

$$\frac{\varphi_{z,sys}}{\varphi_{z,spec}} = \frac{2 \bullet C \bullet EI_{z,spec}}{325^2 \bullet h_{spec}} \quad \text{or} \quad \frac{\varphi_{z,sys}}{\varphi_{z,spec}} = 0.019 \tag{14}$$

$$\frac{\varphi_{x,sys}}{\varphi_{x,spec}} = \frac{2 \bullet C \bullet EI_{x,spec}}{281^2 \bullet h_{spec}} \quad \text{or} \quad \frac{\varphi_{x,sys}}{\varphi_{x,spec}} = 0.258 \tag{15}$$

With E_{spe} = 5000 N/mm^2 it follows that the rotation stiffness ratio equals 0.019 around the Z-axis and 0.258 around the X-axis.

Bending (deformation) of a specimen also causes some horizontal movement. The horizontal displacements (w_y and w_x) can be estimated with:

$$w_{z,spec} = \frac{M_z \bullet h_{spec}^2}{2 \cdot E_{spec} \cdot I_{z,spec}} \quad \text{or} \quad w_{x,spec} = \frac{M_x \bullet h_{spec}^2}{2 \cdot E_{spec} \cdot I_{x,spec}} \tag{16}$$

Where $w_{x,spec}$ and $w_{z,spec}$ are the horizontal displacements in X or Z direction of the specimen respectively. Using the values given earlier, the horizontal displacements may be estimated to vary between:
$w_z = 0.25 \times 10^{-6}$ and 1×10^{-6} times M_z in Z direction, and
$w_x = 44 \times 10^{-6}$ and 174×10^{-6} times M_x in X direction.

In section 7.3.3. the closing effect between specimen and load platen is discussed. The horizontal displacement of the bottom plate is equal to:

$$w = \varphi \, h/t \tag{17}$$

in which:
φ = the angle between the specimen's surface and the load platen, (Figure 73).
h = the height of the specimen and load platen (215 mm), and
t = the thickness (or length) of the specimen (100 mm).

Assume the opening at one side is 0.5 mm wide while the other corner touches the load platen. This is a pessimistic assumption because the specimen can be adjusted in view of the light opening between the two surfaces and this non parallelism of the specimen's surface and load platen is clearly visible.
The value of φ_Z is equal to 0.005 rad, (or φ_X = 0.020 rad). The horizontal displacements are: w_Z = 0.01 mm and w_X = 0.04 mm, which are minor contributions compared to the observed contribution due to the settling of the specimen.

2.3 Friction in a hinged connection

In tests often a hinged connection is required. A hinge functions perfectly when it is not loaded, but needs moment to rotate when loaded, due to the friction between the contact surfaces.
The vertical load will cause friction between the bar and the load platens, in peculiar when slots are used to position the bar.
In the eccentric ESPI tests, a hinge was formed, by putting a steel bar between two steel platens. This 'connection' can be compared with a lever arm that rotates around an axis with radius r, for which the following holds:

$$F = G\frac{l \pm r\,sin\,\varphi}{l \mp r\,sin\,\varphi} \qquad (18)$$

or $M = (F\,l - G\,l)\,r\sin\varphi = N\,e$ (19)

with:

φ = the angle of internal friction, $\varphi = 6°$, for a coefficient of friction of μ = 0,1.

N = F - G

For as long as $M < N\,r\sin\varphi$ the hinge will not rotate, (the moment equals M = N x e). This means that for eccentricities $e < r\sin\varphi$ no rotation will occur.
Vonk [VON 92] assumes, as a reasonable assumption, that the moment needed to rotate the hinge, is in the order of αRN and states that for a Teflon coating α= 0.02.

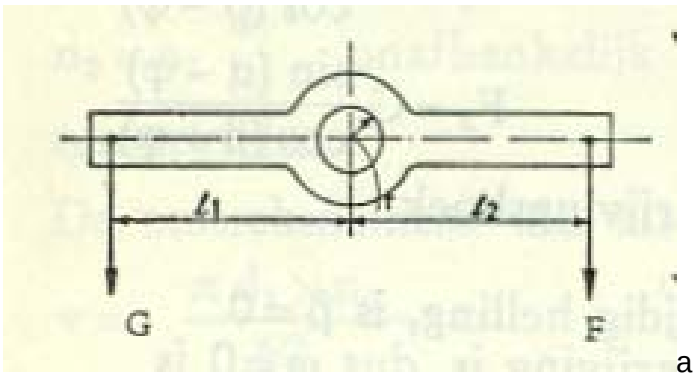

a

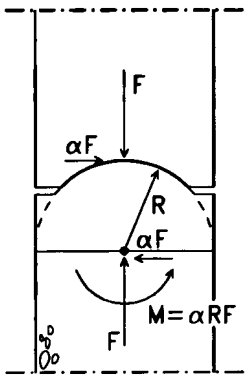

b

Figure 4 a) Forces applied on an axis via two lever arms. A difference between the forces G and F will cause friction and probably rotation, [POL 83]. b) Forces in a spherical seating [VON 92].

2.3.1 A bar between steel blocks

In the ESPI tests, a hinge was formed with a 7 mm diameter bar placed in slots between two steel blocks. The axial load (N) on this connected could go up to 30 kN, resulting in an averaged stress in the bar of 240 N/mm^2, almost the yielding stress of the steel platens. Rotation would occur when M = N . e or e = 5sin6° = 0.52 mm.

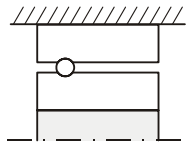

Figure 5 Hinge in detail, formed by a bar between two steel platens with slots

2.3.2 Spherical seating

To position the ESPI specimens a spherical seating was used. The radius was 150 mm. The friction was reduced as much as possible by making the surfaces of the seating as smooth as possible and by using bearing grease. The estimated coefficient of friction was μ = 0,1 or φ = 6°. This means that the bearing block will not rotate as long as the eccentricity e is smaller than 150.sin6° or 16 mm. In concentric testing, the eccentricity was intended to be negligible and so the seating blocked.

3 Models

3.1 Some aspects of the sandwich model

The sandwich model is based on the elastic properties of brick and mortar. The basic idea is that when a combination of layers of alternating soft material (mortar) and stiffer material (clay-brick) is compressed, the materials will deform both in the loading direction and in the lateral direction, as discussed in section 3.2.1. The lateral stresses induced in the central brick and adjacent mortar beds are indicated in Figure 6.

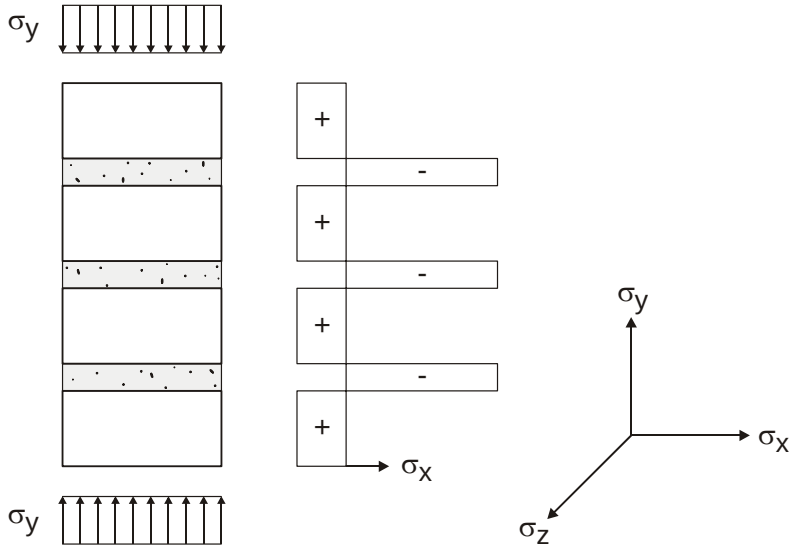

Figure 6 Stresses in unit and mortar, Haller model from [HIL 69].

For equilibrium, the total lateral tensile force in the unit is equal to the total lateral compressive force in the mortar; hence:

$$\sigma_{x,mor} * h_{mor} = \sigma_{x,bri} * h_{bri} \tag{20}$$

Only the x direction is considered. The derivation for stresses and strains in the z direction is similar. The lateral strains in the unit in the x direction are:

$$\varepsilon_{x,bri} = \frac{1}{E_{bri}}\left[\sigma_{x,bri} + \nu_{bri}\left(\sigma_y - \sigma_{z,bri}\right)\right] \tag{21}$$

Similarly, the strains in the mortar joint are derived:

$$\varepsilon_{x,mor} = \frac{1}{E_{mor}}\left[-\sigma_{x,mor} + \nu_{mor}\left(\sigma_y - \sigma_{z,mor}\right)\right] \tag{22}$$

Because the units and the mortar are assumed to be in full contact in the interface the lateral strains must be the same, i.e. $\varepsilon_{x,mor} = \varepsilon_{x,bri}$. Then, the following relationship may be derived from Equations 20, 21, and 22,

$$\sigma_{x,bri} = \sigma_y \cdot \frac{\upsilon_{bri} \cdot \frac{E_{bri} \cdot \nu_{mor}}{E_{mor} \cdot \nu_{bri}} - 1}{\frac{E_{bri}}{E_{mor}} * \frac{h_{bri}}{h_{mor}}(1-\nu_{mor}) + (1-\nu_{bri})} \quad (23)$$

Equation (23) is theoretical and only gives an impression of the stresses that occur in the unit and the mortar as a ratio to the applied vertical loading (σ_y). The following remarks are made.

a) When $E_{bri} = E_{mor}$ and $\nu_{bri} = \nu_{mor}$ which could be the case for contemporary masonry, where the mortar is well tuned to the properties of the type of brick, no additional stresses are assumed to happen. However, the result of Equation (23), depends on the ratio between the brick and mortar height, i.e.

$$\sigma_{x,bri} = \sigma_y \cdot \frac{h_{mor}}{h_{bri} + h_{mor}} \quad (24)$$

On the other hand, in traditional masonry, where the brick is much stiffer than the mortar, i.e. $E_{bri} \cdot \nu_{mor} >> E_{mor} \cdot \nu_{bri}$ Equation 5 can be simplified to:

$$\sigma_{x,bri} = -\frac{h_{mor}}{h_{bri}} \cdot \frac{\nu_{mor}}{1-\nu_{mor}} \cdot \sigma_y \quad (25)$$

b) Stresses become smaller when higher bricks and / or thinner joints are used. For joints with zero thickness there would not be lateral stresses.

In Figure 7 the ratios between lateral stress and applied vertical stress are plotted versus joint thickness and versus E_{brick}. These graphs show that:

a) joint and unit thickness have a considerable influence on the lateral stress ratio, Figure 7a.

b) the E-values and Poisson's ratios of units and mortar considerably determine masonry compressive strength, i.e. the lateral stress ratio, Figure 7b.

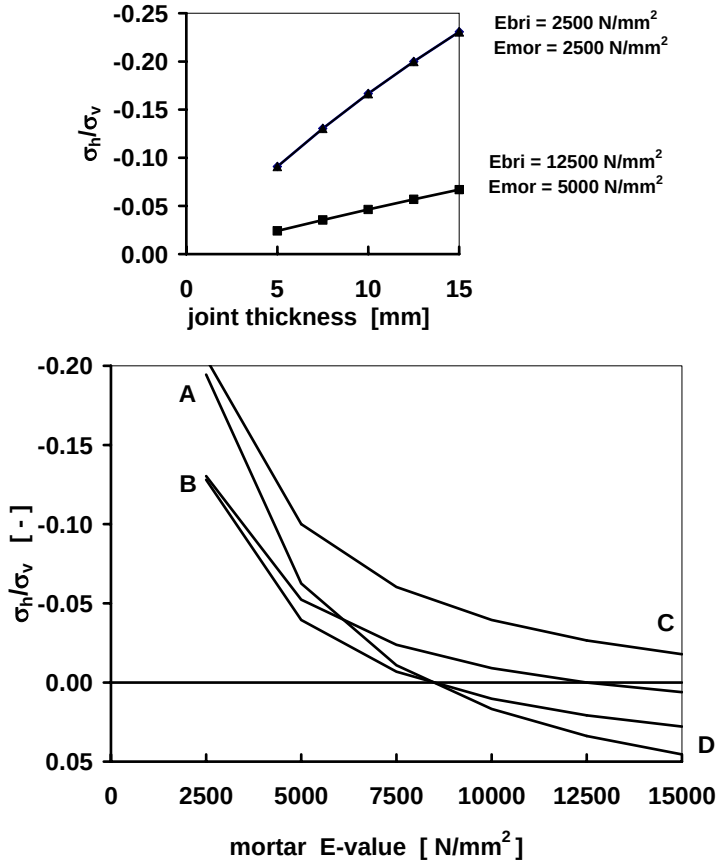

E_{bri}	ν_{bri}	h_{bri}	E_{mor}	ν_{mor}	h_{mor}	σ_h/σ_v	*)
2500	0.2	50	2500	0.1	12.5	-0.205	A
2500	0.2	50	2500	0.3	7.5	-0.128	B
15000	0.2	50	2500	0.1	12.5	-0.018	C
15000	0.2	50	2500	0.3	12.5	0.045	D
2500	0.2	50	2500	0.2	12.5	-0.200	
2500	0.2	50	2500	0.3	12.5	-0.194	
15000	0.2	50	2500	0.2	12.5	0.010	
15000	0.2	50	2500	0.3	7.5	0.028	

*Figure 7 Ratio between horizontal and vertical unit stress according to Equation 23 a) for various joint thicknesses and b) for various brick and mortar properties. Key values are given in the Table. *) letters refer to letters in figure b.*

3.2 Specimen geometry

The relationship between the dimensions of a specimen and the compressive strength is especially important for units and masonry because a large variety of dimensions is available. Masonry specimens will have different dimensions while the specimen should have a representative number of bed and head joints when it is supposed to represent wall behaviour. For economical reasons, it was attempted (in most codes) to prescribe a specimen as small and simple as possible.

For tests to investigate the interaction between mortar and units, e.g. when a new mortar is developed, a relatively small specimen will satisfy, certainly when the results are only used for comparison. In those situations the use of a five-brick stack bonded specimen can be considered [HEN 87, 90], [DRY 93].

To allow for an objective design parameter, read 'the compressive strength', the test results have to be 'scaled' for slenderness, i..e. the ratio between length and thickness and possibly the volume of the specimen. The strength of a specimen with certain dimensions ($f_{c,test}$) is normalised to the strength of a reference sized specimen ($f_{c,ref}$) using a slenderness correction factor (scf), according to:

$$f_{c,ref} = scf * f_{c,test} \tag{26}$$

It is emphasized that the reference specimen size is different in almost every method. The factor scf not always incorporates all dimensional effects. In some methods, only the effect of slenderness is taken into account. In other methods also the thickness and the length are taken into consideration.

3.2.1 Effect of slenderness

The slenderness is the ratio between the height (h) and the smallest lateral dimension i.e. the thickness (t). Sometimes however, instead of the thickness (t), the average of width and thickness (l+t)/2, or the square root of the loaded area $\sqrt{(l*t)}$ is taken into account.

The effect of slenderness is accounted for using the factor scf in the formula (16) mentioned above. Implicitly, it is assumed that only the height varies and that the other dimensions remain unchanged.

Correction factors are plotted versus slenderness *h*/*t* with *t* = 100 mm in Figure 8. As mentioned earlier, not all methods have the same slenderness range and the size correction factor depends on the size of the reference specimen. Therefore, the slenderness *h*/*t* = 3 with a correction factor of 0,8 is taken as the reference point in Figure 8. In literature, this reference (*h*/*t* = 3 and scf = 0.8) is more often used e.g. by Page [PAG 85]. In Figure 8 the scf values are normalised to the value 0.8 at a h/t ratio of 3. Therefore, each value for a certain method is multiplied by 0.8 and divided by the value of the scf when h/t = 3.

Some methods work with δ factors. For comparison, the inverted value of δ ($1/\delta$) should be used in combination with scf-factors.

In Figure 8, a width of 100 mm is used for scaling the values given in pr EN 772-1 [EC 6]. The h/t ratio in [EC 6] is limited to 5 for the smallest width.

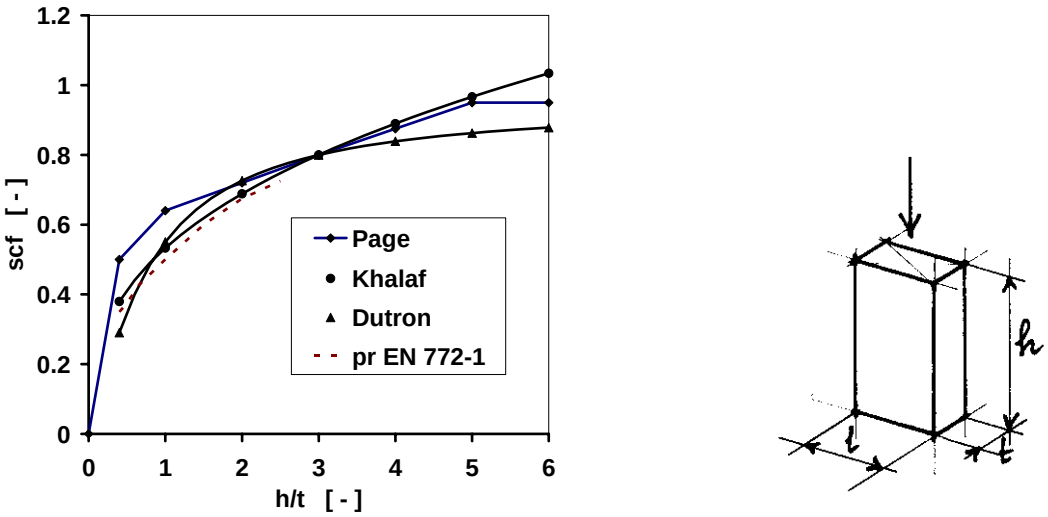

Figure 8 Correction factors (scf) for compressive strength as a function of slenderness (h/t) according various researchers.

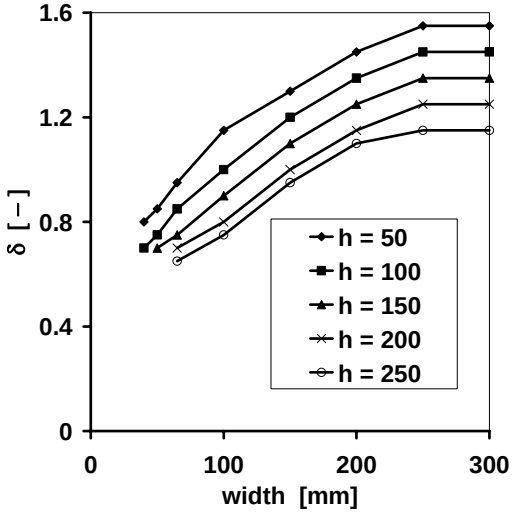

Figure 9 Shape factor, δ to allow for the tested dimensions of the specimens after surface preparation, [EC6 02].

As can be seen in Figure 8, the effect of the boundary conditions on strength is less for higher slenderness. Buckling effects may be considered negligible small for the considered h/t values.

When the strengths of two specimens with approximately the same h/t ratio are predicted, the result will only slightly depend on the method used, while the slope of the

graphs is roughly the same. However, when the difference in h/t ratio is larger, the scf-factor found with one method or the other may differ up to 35%.
Page [PAG 85] postulates that many correction factors originate from the same source: a series of tests on masonry columns performed by Krefeld in 1938.

Page [PAG 85] experimentally established correction factors for calcium silicate units and masonry specimens.
The Belgian masonry code [NBN 80] uses the next equation:

$$scf_{Du} = \frac{f_{c,spec}}{f_{c,ref}} = 0.65 \frac{0.70}{1 + \frac{l+t}{400} + \left(\frac{2 \cdot h}{l+t}\right)^{1.25}} \qquad (27)$$

in which:
$f_{c,spec}$ = result of a compression test using a specimen with dimensions d and h;
$f_{c,ref}$ = reference compressive strength; cube of 200 mm ribs
Equation (3) was originally proposed for concrete by Dutron. As a reference, the compressive strength that would have been found when a cube made of the same material with ribs of 200 mm was used for $f_{c,ref}$.
In Equation (2), besides the slenderness effect in the term *h*/(l+t) also the volume effect in the term *(l+t)*/400 can be recognized.

The work of Khalaf and Hendry [KHA 94] resulted in the formula:

$$scf_{Kha} = 0.533 \left(\frac{\sqrt{A}}{h}\right)^{0.37} \qquad (28)$$

in which A represents the cross section area of the specimen, A = l * t.
The correction factor table in EC6 [EC6 88] is based on formula (4). The only difference is the exponent of 0,38 in stead of 0,37 in [KHA 94]. EC6 limits the *c*-factors for larger h/t ratios and consequently a constant value of 0,7 for *h*/*t*>3 should be found. For clarity, this reduction is not used in Figure 8.

The effect of the slenderness on strength is also determined by the interaction between the material that is tested and the used capping. Large differences may occur. Therefore, according to a.o. Page [PAG 85], it is probably not sufficient to use one single set of correction factors.
The effect of the load introduction reduces when the slenderness is higher, therefore it is advisable to make the specimens as slender as possible. However, an upper limit of h/t = 5 to 6 should be used to avoid that buckling should become to dominant.

3.2.2 Stress distribution in an eccentrically loaded specimen

To assist with the understanding of the behaviour of cracked and uncracked specimens, the following equations may be considered. Linear stress/strain behaviour is assumed, while in cracked sections eccentricity must be accepted as being of considerable importance.

A	= sectional area	= b * d = 24 * 100 mm^2	1
σgr	= gross stress	= N/(b*d)	2
	Cracked section, Figure 10a and b		
σc,c	= compressive stress	= 2N/(x*b)	3
εavg	= averaged strain,	= ½ (-εc + εt)	4
		= ½ (-εc + (d – x)/x * ε)	
φcr	= curvature	= σcc / (E*x)	5
		= 2N/(E*x^2*b)	
		= 2M / (E*e*x^2*b)	
	Uncracked section, Figure 10b and c		
φuc	= curvature	= M/EI = 12 N*e / (b*d^3)E	6
εavg	= averaged strain	= ½ * (-εc + εt) = σgr / E	7
σt	= tensile stress	= εt * E	8
		= -N/(b*d) + 6*N*e / (b*d^2)	
σc,u	= compressive stress	= εc * E	9
		= -N/(b*d) - 6*N*e / (b*d^2)	

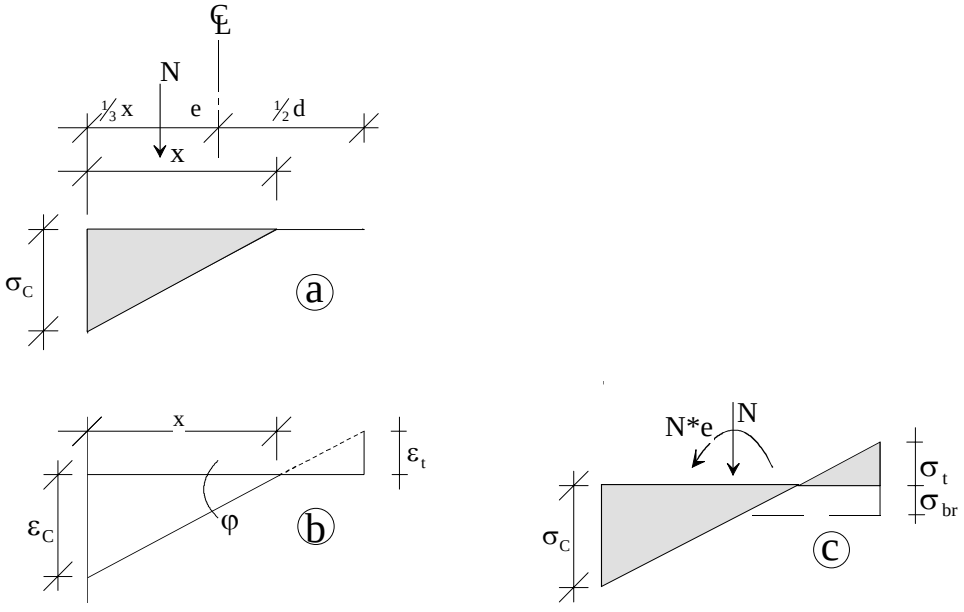

Figure 10 Stresses and strains in cracked and uncracked sections

4 ESPI Sensitivity

Like when using a photo-camera, the distance is of great importance for the image that is obtained with the ESPI equipment. With a larger distance, a larger surface can be observed, however, the sensitivity becomes smaller, the reflection weaker and measuring more difficult.

The sensitivity (ψ) of the ESPI system depends on the wave length (λ) of the light produced by the laser diode and on the illumination angle of the laser-beams (i.e. the distance d1 between two mirrors), Figure 11. In equation:

$$\psi = 2\frac{\lambda}{sin(\alpha)} \tag{29}$$

where, for the angle α the following holds:

$$\alpha = arctan\left(\frac{d1}{2 \cdot d2}\right) \tag{30}$$

In this thesis the following data apply:

λ = 783 * 10^{-3} μm

d1 = spherical mirror distance = 200 mm

d2 = object distance, ranging between 600 and 800 mm

From these data it follows that the sensitivity ranges between 2.4 μm and 3.2 μm.

Usually, sensitivity in ESPI is referred to as the required object deformation to produce one additional fringe. Roughly one fringe (produced by a deformation of 2.4 to 3.2 μm) is represented by 256 colours, which means that the resolution, that is the minimal deformation to produce a signal that can be measured, was approximately 10 to 13 nm.

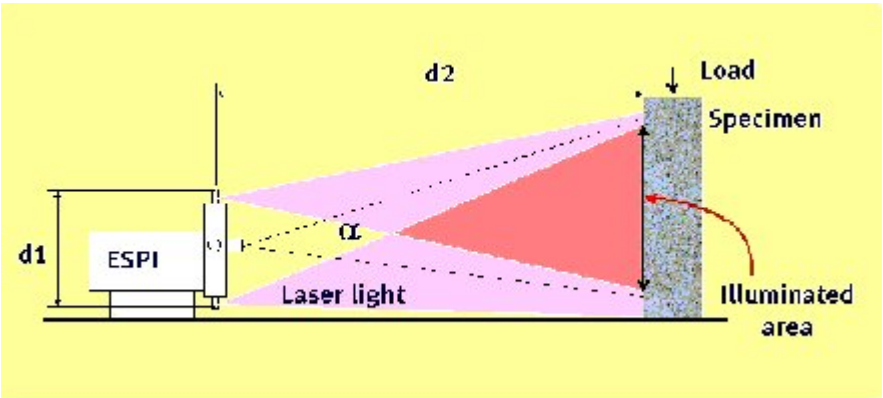

Figure 11 Scheme of the light beams to explain sensitivity

5 Material properties and experimental data

5.1 List of brick properties

Bricks of the same type were used in various series of tests over considerable periods of time. The bricks were delivered in various batches, which explains the differences between some of the properties of bricks from one factory. It also indicates the variety between batches from one factory. Not all properties were established in al sub-series, which explains for the blanks in the table.

Part 1		dimensions			water	f) free absorption		
		l	w	t	IRA *)	a)	b)	sp.mass
		mm	mm	mm		%kg/kg		Kg/m^3
Extrusion wire cut bricks								
Joosten Geel	JG	204	98	50	0.9		7.3	1994
Joosten Geel	G1	204	98	50	0.9	4.4		1897
Joosten Geel	G2	204	98	50	0.9	4.8		1900
Joosten wit	JW	206	98	50	3.0			2040
Joosten wit	JW	205	96	50	3.0			2040
Joosten blauw	JB	210	97	50	0.3		3.7	2053
Heteren roze	HE	210	101	50	28.0			
Soft-mud machine-moulded bricks								
van Erp	ER	212	99	51		13.6		1750
Hapert	HA	210	100	50	4.5	13.5	23.6	1750
Huissenswaard	HU	214	102	53	35.0			
Hylkema	HY	237	97	139	47.0			
Rijswaard	RW	206	96	50		15.5		1630
Rijswaard	RY	210	99	50	4.4	13.5	22.6	1630
Rijswaard	RW	210	99	50	4.4	13.5	22.6	1630
Vijf Eiken	VE	208	98	50	4.2	10.8		1610
Poriso	PO	cut to brick size					25	1356

f) free absobtion of water:

a) prewetted situation during building

b) brick is submerged in water for 24 hours

*) IRA initial rate of absorbtion: one surface in contact with water for 1 minute, kg/m^2/min

Part 2	$f_{c,bri,code}$ N/mm^2	$f_{c,bri}$ N/mm^2	$f_{c,Bo}$ N/mm^2		E_{Bo} N/mm^2	Poisson's ratio a)	b)	tensile strength N/mm^2
Extrusion wire cut bricks								
Joosten Geel	50.0	66.0	35.8		16700	0.28	0.28	
Joosten Geel	50.0	60.0	33.0		15400	0.28		1.13
Joosten Geel	50.0	60.0	26.7		13900			1.82
Joosten wit	61.0	81.0	68.9	2)	19900			
Joosten wit	141.3		70.0		29400			
Joosten blauw	90.0	120.0	64.8		15400		0.19	
Heteren roze	71.6		36.0		15100			
Soft-mud machine-moulded bricks								
van Erp	21.0	27.0	12.0		4500			
Hapert		19.0	10.6		3200			
Huissenswaard	37.2		19.0		8000			
Hylkema	17.0		8.6		3600			
Rijswaard	21.0	27.0			5460			
Rijswaard	26.3		13.0		5460			
Rijswaard		27.0	17.0	1)	4000		0.13	1.09
Vijf Eiken	25.0	33.0	14.2		6050		0.14	
Poriso			10.5		7110			

$f_{c,bri,code}$: $f_{c,bri}$ corrected according to code for height — estimated value

$f_{c,bri}$: brick loaded in compression on bed side, surfaces ground level, height 50 mm

$f_{c,bri,7}$: result of test on a 7 bricks high specimen — 2) 43x43x145 mm^3

$f_{c,bri,Bo}$: result of Bolidt test — 1) 95x95x280 mm^3

a) Poisson's ratio in masonry specimen

b) Poisson's ratio in Bolidt specimen

The normalised compressive strength values $f_{c,bri,code}$ were calculated using the values of $f_{c,bri}$ according code for clay-brick: NEN 2489:1976 with the conversion table of prEN 772-1:1995. This conversion is intended to give a strength value for the unit with a normalised height of 100 mm.

5.2 List of mortar properties

The tables below give an overview of the various types of mortars used a) in the masonry tests, b) in the detailed tests on mortar specimens and c) in the ESPI tests.

Part 1. Mortars used for masonry specimens (Chapter 6).

mix design in volume parts c : l : s	$f_{c,mor}$ N/mm^2	joint thickn. mm	used in combination with unit types
GP 1:1:6	8.2	14	Csi
GP 1:2:9	3	14	JG, VE,
GP 1:½:4 ½	17.6	14	JG, VE
GP 1:½:6	4.5	14	JG, VE,
GP 1:½:2¼	37.5	14	JG, VE,
GPl 1:1:6	8.1	12.5	JG, RW
TL (Ankerplast) batch 1	29.5	4	RW
TL (Ankerplast) batch 2	18.6	4	RW

Part 2. Mortars used for detailed experiments (Chapter 5).

	condition	$f_{c,mor}$ N/mm^2	CoV %	$f_{c,mor}$ N/mm^2	CoV %
GP 1:½:4 ½	dry	10.2	28	1037	50
	medium	10.8	24	1059	28
	saturated	8.87	23	815	50
GP 1:2:9	dry	4.33	25	630	77
	medium	5.56	22	700	62
	saturated	3.25	21	283	55
damage case in labo		7.9	24	700	77
damage case from site		14.7	26	17900	36
series Og		19.8	6		

	joint thickness in mm
GP: General Purpose mortar, laboratory made	15
GPf: General Purpose mortar, factory made	15
GPl: General Purpose mortar, lime + air entraining agent	15
MM: Medium joint thickness Mortar, factory made	9
TL: Thin Layer mortar, cement based, always prefabricated, factory made	4
$f_{c,mor}$ according NEN 3835	

Part 3. Mortars used for ESPI measurements (Chapters 8, 9 and 10)

			$f_{c,mor}$ N/mm^2	joint thickness
Joosten	JW	GPf	18.2	15
Heteren	HE	GPf	13.4	15
Huissenswaard	HU	GPf	13	15
Rijswaard	RY	GPf	9.6	15
Hylkema	HY	GPf	9.9	15
Joosten	JW	MM	22.3	9
Heteren	HE	MM	18.2	9
Huissenswaard	HU	MM	15.9	9
Rijswaard	RY	MM	9.4	9
Hylkema	HY	MM	10.3	9
Joosten	JW	TL	32.8	4
Heteren	HE	TL	19.8	4
Huissenswaard	HU	TL	9.4	4
Rijswaard	RY	TL	10.1	4
Hylkema	HY	TL	9.2	4

	joint thickness in mm
GP: General Purpose mortar, laboratory made	15
GPf: General Purpose mortar, factory made	15
GPl: General Purpose mortar, lime + air entraining agent	15
MM: Medium joint thickness Mortar, factory made	9
TL: Thin Layer mortar, cement based, always prefabricated, factory made	4

$f_{c,mor}$ according NEN 3835:1991

5.3 Strains obtained from concentric ESPI tests

The table below gives strains ($\Delta l/l_r$ *10^{-3} mm/m) obtained for a 1 N/mm^2 stress increase for separate specimens for brick, joint and specimen.
Values for $\Delta l/l_r$ obtained from brick deformation (lines AA-BB and CC-DD) from interface plus joint deformation (BB-CC) and from specimen deformation between lines EE-FF. Large strains around fissures were omitted. LVDT results at the same load level are given as well.

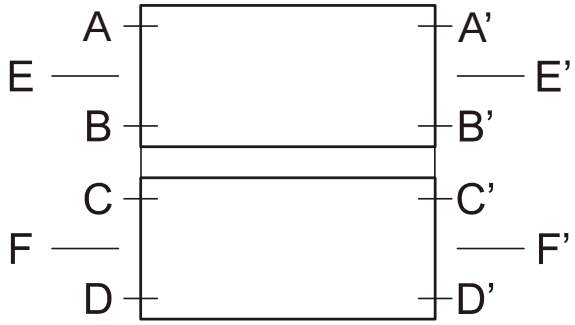

Figure 12 Levels for strain calculations.

Strain for $\sigma\Delta$ = 1 N/mm^2 in 10^{-6} m/m

	brick AA'-BB'	joint BB'-CC'	brick CC'-DD'	specimen EE'-FF'	LVDT left	LVDT right
1JWGM	-51.6	-71.5	-68.3	-64.2	-91.3	-75.9
2JWGM	-27.0	-28.3	-30.3	-32.6	-54.2	-66.6
1JWMM	-26.5	-20.7	-27.8	-26.5	-59.3	-71.2
2JWMM	-51.6	-71.6	-70.1	-71.0	-53.5	-56.7
1JWTL	-35.4	-33.0	-27.5	-32.5	-53.2	-49.2
2JWTL	-34.8	-45.2	-35.1	-39.9	-31.4	-40.6
1HEGM	-53.0	-245.1	-84.5	-132.6	-263.8	-156.5
2HEGM	-40.4	-40.9	-65.2	-54.2	-72.4	-67.9
3HEGM	-51.1	-208.1	-69.3	-112.4	-556.2	-580.4
1HEMM	-51.4	-41.8	-56.3	-55.4	-72.3	-60.1
2HEMM	-93.4	-231.6	-83.0	-141.1	-220.0	-125.3
1HETL	-46.4	-63.3	-56.8	-57.3	-67.1	-62.3
2HETL	-28.6	-46.0	-44.7	-46.8	-72.6	-59.6
1HUGM	-243.4	-505.3	-193.1	-312.6	-179.2	-500.5
2HUGM	-73.1	-124.7	-185.1	-119.3	-583.1	-375.7
3HUGM	-183.7	-228.1	-319.5	-261.0	-556.2	-580.4
1HUMM	-314.1	-135.3	-148.7	-223.8	-96.0	-314.9
2HUMM	-122.5	-135.6	-282.2	-203.4	-426.6	-168.2
1HUTL	-349.7	-114.4	-267.8	-217.5	-182.8	-398.4
2HUTL	-258.8	-319.1	-250.4	-268.6	-338.2	-206.7
1RYGM	-318.8	-198.6	-269.8	-297.0	-473.9	-258.0
2RYGM	-244.6	-261.0	-255.3	-247.3	-426.4	-273.7
1RYMM	-197.2	-237.9	-227.7	-220.8	-252.0	-252.0
2RYMM	-50.6	-44.5	-47.2	-50.8	-268.6	-186.6
1RYTL	-174.5	-135.3	-239.6	-201.7	-245.5	-172.1
2RYTL	-208.1	-131.3	-168.2	-166.4	-150.1	-166.3
1HYGM	-103.1	-87.2	-106.3	-96.8	-234.1	-206.8
2HYGM	-189.9	-128.5	-154.6	-173.9	-174.3	-302.0
3HYGM	-89.8	-54.5	-145.6	-110.2	-208.6	-161.0
1HYMM	-250.3	-135.9	-98.5	-167.3	-288.8	-256.7
2HYMM	-65.1	-65.0	-69.9	-67.8	-219.8	-103.3
1HYTL	-211.7	-298.1	-603.8	-472.6	-356.6	-356.0
2HYTL	-95.0	-113.8	-278.2	-122.0	-234.2	-190.7

5.4 List of data from ESPI specimens

Values of specimens used for concentric ESPI tests. Results LVDT measurements.

Overview 1

Mortar type	size mm x mm	height mm	TNO N/mm^2	ESPI N/mm^2	E modulus N/mm^2	E modulus LVDT's N/mm^2	LVDT's averaged N/mm^2
1JWGM	26 x 98	115	28.44	43.552	5359	12412	**11958**
2JWGM	25 x96	115	28.44	42.649	14154	17983	**17918**
1JWMM	26 x 96	112	34.67	45.674	10143	16134	**16524**
2JWMM	26 x 97	112	34.67	47.265	9956	19038	**18079**
1JWTL	25.5 x 96	106	45.10	50.874	10176	16667	**18797**
2JWTL	24.5 x 96	106	45.10	67.641	12410	26901	**26322**
1HEGM	26 x 99	116	12.16	31.570	7225	4883	**4747**
2HEGM	25 x 100	116	12.16	43.006	9600	13140	**12928**
3HEGM	26 x 100	116	12.16	14.698	4245	2656	**2952**
3HEGM							**2952**
1HEMM	26 x 100	109	20.89	46.000	13968	14620	**14743**
HEM1	26 x 99.5	109	20.89	18.801	25952	18000	**16195**
2HEMM	25 x 100	109	20.89	46.063	14130	15325	**16716**
HEM2	26 x 100	109	20.89	14.108	8188	5357	**6008**
1HETL	26 x 99	104	29.10	48.461	16980	13250	**13485**
2HETL	25 x 100	104	29.10	49.368	11487	15289	**15460**
1HUGM	26 x 100	118	8.43	17.599	3311	2884	**3448**
2HUGM	26 x 100	118	8.43	12.831	4391	2293	**2219**
3HUGM	26 x 100	118	8.43	14.732	2954	1683	**1698**
1HUMM	26 x 100	114	11.46	15.030	3569	4405	**3290**
2HUMM	26 x 100	114	11.46	18.146	4007	3926	**4953**
HHM1	26 x 102	114	11.46	16.413	4560	4598	
1HUTL	26 x 100	108	11.62	16.784	3153	2986	**4432**
2HUTL	26 x 100	108	11.62	17.527	3195	2900	**3872**
1RYGM	26 x 98	113	9.03	11.099	2954	3200	**3333**
2RYGM	25.5 x 97	113	9.03	13.070	2835	3160	**3149**
1RYMM	26 x 97	110	13.29	16.406	4168	4100	**4101**
2RYMM	26 x 97	110	13.29	16.194	3913	4370	**4492**
1RYTL	26 x 98	105	12.14	13.951	3467	4421	**4535**
2RYTL	25 x 97	105	12.14	11.651	2143	5240	**4766**
3RYTL	26 x 97	105	12.14	12.452	2681	4976	**5372**
RYT1	25.7 x 98	105	12.14	12.370	4129	4450	**4969**
1HYGM	24.5 x 95	125	6.28	12.329	5367	5300	**4346**
2HYGM	25 x 95	125	6.28	11.577	5952	4283	**4321**
3HYGM	24.5 x 95	125	6.28	11.525	4386	4947	**5049**
1HYMM	26 x 97	112	7.34	8.287	3785	4652	**4474**
2HYMM	25 x 98	112	7.34	12.481	4723	4733	**5765**
1HYTL	26 x 96	105	7.91	4.299	2206	3781	**3071**
2HYTL	27 x 96	105	7.91	10.877	4549	4878	**5305**

Overview 2

Concentric ESPI tests

Concentric ESPI tests Results LVDT measurements				DETAIL stress strain curve between L1 - L2	
	LVDTs avg	E modulus LVDT's left	LVDT's right	E modulus LVDT's left	LVDT's right
Mortar type	N/mm^2	N/mm^2	N/mm^2	N/mm^2	N/mm^2
1JWGM	11958	12464	11452	10956	13171
2JWGM	17918	15813	20023	15021	18461
1JWMM	16524	14901	18148	14037	16858
2JWMM	18079	18754	17404	17627	18686
1JWTL	18797	20018	17577	20328	18807
2JWTL	26322	25451	27193	24647	31850
1HEGM	4747	5688	3806	6388	3791
2HEGM	12928	13317	12539	14724	13807
3HEGM	2952	3949	1955	4577	
3HEGM	2952			5044	1566
1HEMM	14743	15653	13833	16641	13826
HEM1	16195	18612	13777		15846
2HEMM	16716		16716	21769	15433
HEM2	6008	7960	4057	7978	4545
1HETL	13485	13087	13884	16050	14905
2HETL	15460	17256	13664	16775	13771
1HUGM	3448	2027	4870	1998	5580
2HUGM	2219	2728	1710	2662	1715
3HUGM	1698	1655	1740	1723	1798
1HUMM	3290	3201	3379	3176	10420
2HUMM	4953	7355	2551	5945	2344
HHM1				4714	3312
1HUTL	4432	3115	5750	2510	5469
2HUTL	3872	4648	3097	4838	2957
1RYGM	3333	4348	2318	3876	2110
2RYGM	3149	3914	2384	3653	2345
1RYMM	4101	3997	4205	3969	3969
2RYMM	4492	5363	3620	5358	3723
1RYTL	4535	4094	4975	5810	4073
2RYTL	4766	5466	4066	6662	6012
3RYTL	5372	6092	4652	3957	5576
RYT1	4969	4263	5675		
1HYGM	4346	4754	3938	4835	4271
2HYGM	4321	3284	5357	3311	5736
3HYGM	5049	5896	4202	6210	4794
1HYMM	4474	4791	4157	3895	3463
2HYMM	5765	7910	3619	9683	4549
1HYTL	3071	3027	3115	2809	2804
2HYTL	5305	5983	4626	5244	4269

Averaged values, part 1

				E value		
	SR	strength TNO N/mm^2	ESPI N/mm^2	LVDT's N/mm^2	LVDT's N/mm^2	LVDT's averaged N/mm^2
JWGM	1.52	28.44	43.10	9757	15198	14938
JWMM	1.34	34.67	46.47	10050	17586	17302
JWTL	1.31	45.10	59.26	11293	21784	22560
HEGM	2.45	12.16	29.76	7023	6893	6876
HEMM	1.50	20.89	31.24	15560	13326	13416
HETL	1.68	29.10	48.91	14234	14270	14473
HUGM	1.79	6.32	11.29	2664	1715	1841
HUMM	1.44	11.46	16.53	4045	4310	4122
HUTL	1.48	11.62	17.16	3174	2943	4152
RYGM	1.34	9.03	12.08	2895	3180	3241
RYMM	1.23	13.29	16.30	4041	4235	4297
RYTL	1.04	12.14	12.61	3105	4772	4911
HYGM	1.88	6.28	11.81	5235	4843	4572
HYMM	1.41	7.34	10.38	4254	4693	5120
HYTL	0.96	7.91	7.59	3378	4330	4188
	1.49					
	0.35		SR: strength ratio ESPI / TNO			

Averaged values, Part 2.

	E values LVDT's left N/mm^2	LVDT's right N/mm^2	E values LVDT's left N/mm^2	LVDT's right N/mm^2
JWGM	14139	15738	12989	15816
JWMM	16828	17776	15832	17772
JWTL	22735	22385	22488	25329
HEGM	7651	6100	8563	5866
HEMM	14075	12096	15463	12413
HETL	15172	13774	16413	14338
HUGM	1603	2080	1596	2273
HUMM	5278	2965	4612	5359
HUTL	3882	4424	3674	4213
RYGM	4131	2351	3765	2228
RYMM	4680	3913	4664	3846
RYTL	4979	4842	5476	5220
HYGM	4645	4499	4785	4934
HYMM	6351	3888	6789	4006
HYTL	4505	3871	4027	3537

5.4.1 Experimental data of six specimens.

Specimens were instrumented with four LVDTs for comparison of LVDT and ESPI results.

Specimen	Brick type	Loaded area mm x mm	L1 kN	L2 kN	Strength N/mm^2	E modulus N/mm^2
A1	RW	94 x25	10	15	12.87	2807
A2	RW	96 x 25	10	13	9.62	3266
B1	JO	96 x 25	43.1	48	32.29	12526
B2	JO	96 x 25	10.05	20.12	38.99	18727
C1	RW	94 x 25	16.5	18.9	13.29	3941
C2	RW	95 x 26	--	--	11.51	3805
D2	JO	96 x 25	24.6	34.5	33.31	14970
D3	JO	96 x 26	15.1	25.1	27.97	12945

L1 force at start of ESPI measurements

L2 force at end of ESPI measurements

The E modulus was established in the LVDT-stress-strain diagram between L1 and L2 as a linear best fit. Strain was calculated from the averaged results of four LVDTs.

5.4.2 Experimental data of six concentric ESPI tests

The data below are from two times three concentric tests, from measurements under multiple load steps as described in section 8.6. The first series of three are from RY bricks with GP mortar joints. The second series of three are from the same Ry bricks but with TL mortar joints.

General purpose mortar joints.

Specimen	1RWDO		2RWDO		3RWDO	
l x t	96*27	step#	97*27	step#	97*27	step#
mm^2	2592		2619		2619	
	kN		kN		kN	
Load 1	5.47	1	4.86	4	5.54	1
Load 2	6.51	3	6.15	6	6.70	3
Load 3	10.85	10	8.59	8	11.76	11
Load 4	12.14	12	9.20	9	13.00	13
Load 5	21.50	20	14.88	20	29.25	39
Load 6	24.00	24	16.13	22	30.50	41
Load 7	40.75	51	28.00	41	35.38	50
Load 8	43.25	55	30.00	44	36.13	52
Load 9	46.38		34.88	52		
Load 10	47.63		36.13	54		
	σ	$\Delta\sigma$	σ	$\Delta\sigma$	σ	$\Delta\sigma$
	N/mm^2	N/mm^2	N/mm^2	N/mm^2	N/mm^2	N/mm^2
Load 1	2.110	0.401		0.493		0.443
Load 2	2.512		2.348		2.558	
Load 3	4.186	0.498		0.233		0.473
Load 4	4.684		3.513		4.964	
Load 5	8.295	0.965		0.477		0.477
Load 6	9.259		6.157		11.646	
Load 7	15.721	0.965		0.764		0.286
Load 8	16.686		11.455		13.793	
Load 9	17.894	0.482		0.477		
Load 10	18.376		13.793			

Thin layer mortar joint specimens

Specimen	1RWTL		2RWTL		3RWTL	
l x t	97*25	step#	97*25	step#	97x24	step#
mm^2	2376.5		2376.5		2366.8	
	kN		kN		kN	
Load 1	10.91	12	3.28	1	3.59	1
Load 2	11.59	14	4.01	3	4.44	3
Load 3	14.63	22	7.93	10	9.39	
Load 4	15.38	24	8.53	11	11.34	
Load 5			12.93	18	15.13	20
Load 6			13.50	19	16.38	22
Load 7			22.25	33	18.88	26
Load 8			22.88	34	20.00	28
Load 9					23.00	35
Load 10					23.75	37
	σ	$\Delta\sigma$	σ	$\Delta\sigma$	σ	$\Delta\sigma$
	N/mm^2	N/mm^2	N/mm^2	N/mm^2	N/mm^2	N/mm^2
Load 1		0.286		0.309		0.359
Load 2	4.877		1.687		1.876	
Load 3		0.316		0.252		0.824
Load 4	6.470		3.587		4.791	
Load 5				0.242		0.528
Load 6			5.681		6.919	
Load 7				0.263		0.475
Load 8			9.625		8.450	
Load 9						0.317
Load 10					10.035	

5.5 List of masonry properties

In the table below some key values for each separate test are given.

First the code of the specimen is presented. This code consists out of a letter identifying the brick type, for convenience also given in column B. Then a number or letter, referring to the mortar used, is presented, followed by a letter for the specimen's size. Finally, the test date is represented.
Brick and mortar compressive strength are given in columns F and G respectively.

A	B	C	D	E	F	G	H	I	J	K	L	M
thickness	100											
		length	height		brick		mortar	B	E_0	$E_{1/3}$	$E_{1/3}$	E_{90}
code				fc,mas	fc,bri	fc,Bo	fc,mor				calc	
		mm	mm	Mpa	MPa	MPa	Mpa		Mpa	Mpa	Mpa	Mpa
B1B22111	JB	420	375	43.04	120	64.8	41.02	1.320	21144	19952	20247	13913
B1B22112	JB	420	375	45.12	120	64.8	41.02	1.187	17589	16089	16203	13396
B1B25111	JB	420	375	51.90	120	64.8	41.02	1.202	16109	15055	15344	12736
B1S21111	JB	420	375	37.57	120	64.8	41.02	1.091	9535	9505	6180	8998
B1S21112	JB	420	375	40.94	120	64.8	41.02	1.044	11633	11385	5796	10478
B1S21113	JB	420	375	40.88	120	64.8	41.02	1.058	10370	10353	6761	10034
B4B15111	JB	420	375	23.44	120	64.8	10.29	1.466	17001	13738	13303	7730
B4B15112	JB	420	375	23.13	120	64.8	10.29	1.472	24277	17137	16731	8191
B4B18111	JB	420	375	24.54	120	64.8	10.29	1.455	14222	12338	12112	6833
B4S13111	JB	210	375	20.49	120	64.8	10.29	1.303	7179	7178	3643	5761
B4S13112	JB	210	375	22.49	120	64.8	10.29	1.325	8346	8281	6823	6409
B4S14111	JB	210	375	19.61	120	64.8	10.29	1.366	7195	7135	5076	5489
B6S29041	JB	210	375	22.83	120	64.8	4.98	1.379	14262	12478	12306	7825
B6S29042	JB	210	375	20.07	120	64.8	4.98	1.425	16259	12189	12067	6909
B6S29043	JB	210	375	18.52	120	64.8	4.98	1.394	13860	9538	9212	5701
BKS27051	JB	210	375	32.70	120	64.8	37.51	1.071	11957	10920	10747	9560
BKS27052	JB	210	375	34.42	120	64.8	37.51	1.248	14892	12134	12069	10198
BKS27053	JB	210	375	19.12	120	64.8	37.51	1.015	15051	13609	13998	12553
E4S01061	ER	210	375	8.68	30	11	10.79	1.268	2862	2436	2424	1787
E4S01062	ER	210	375	8.17	30	11	10.79	1.087	2771	2279	2188	1762
E4S01063	ER	210	375	8.16	30	11	10.79	1.205	2812	2385	2458	-
E6S28042	ER	210	375	7.25	30	11	4.98	1.328	2247	1769	1790	1274
E6S29041	ER	210	375	6.95	30	11	4.98	1.283	2128	1757	1762	1387
E6S29043	ER	210	375	7.91	30	11	4.98	1.341	2492	2291	2305	1660
EKS24051	ER	210	375	10.46	30	11	37.51	1.025	2272	2044	2097	1892
EKS24052	ER	210	375	9.26	30	11	37.51	0.907	2367	1988	2004	1929
EKS24053	ER	210	375	9.28	30	11	37.51	0.869	2710	2188	2189	2098
J1B23102	JO	420	375	38.90	66	35.8	47.89	1.239	36028	22245	23193	15579
J1B23104	JO	420	375	37.96	66	35.8	47.89	1.223	24319	18613	19961	14200
J1B23105	JO	420	375	39.50	66	35.8	47.89	1.219	18649	17279	17072	14412
J1S22101	JO	210	375	32.72	66	35.8	47.89	1.122	12800	12259	8281	11280
J1S23101	JO	210	375	31.38	66	35.8	47.89	1.092	11414	11320	7247	10778
J1S23103	JO	210	375	29.57	66	35.8	47.89	1.007	10446	10505	3747	9718
J2S07101	JO	210	375	13.44	66	35.8	2.27	1.402	10126	7140	6942	3695

A	B	C	D	E	F	G	H	I	J	K	L	M
thickness	100											
		length	height		brick		mortar	B	E_0	$E_{1/3}$	$E_{1/3}$	E_{90}
code				fc,mas	fc,bri	fc,Bo	fc,mor				calc	
		mm	mm	Mpa	MPa	MPa	Mpa		Mpa	Mpa	Mpa	Mpa
J2S07102	JO	210	375	11.66	66	35.8	2.27	1.406	9997	6717	6442	3484
J2S15091	JO	210	375	11.28	66	35.8	3.26	1.353	10154	6867	6926	4211
J2S15092	JO	210	375	13.18	66	35.8	3.26	1.390	11162	8020	7710	3991
J2S17031	JO	210	375	11.42	66	35.8	2.87	1.464	13950	10062	9654	4399
J2S17032	JO	210	375	11.08	66	35.8	2.87	1.421	9678	7626	7410	4306
J2S17033	JO	210	375	12.31	66	35.8	2.87	1.460	14597	11378	10896	5281
J2S19102	JO	210	375	11.69	66	35.8	3.29	1.476	9086	7526	7058	3245
J2S20101	JO	210	375	10.10	66	35.8	3.29	1.502	9171	7561	7041	2904
J2S20102	JO	210	375	10.03	66	35.8	3.29	1.513	7846	5973	3744	2406
J2S24031	JO	210	375	10.33	66	35.8	2.64	1.477	10135	9105	8797	4611
J2S24032	JO	210	375	9.78	66	35.8	2.64	1.487	12246	8615	8606	3487
J2S24033	JO	210	375	10.78	66	35.8	2.64	1.383	12956	9535	9059	5603
J2S26081	JO	210	375	12.47	66	35.8	3.26	1.340	11001	7204	6678	2864
J2S29062	JO	210	375	13.19	66	35.8	2.97	1.385	11354	6880	7439	3285
J2S30061	JO	210	375	13.45	66	35.8	2.97	1.439	10272	6796	6608	3383
J3B05031	JO	420	375	27.43	66	35.8	15.25	1.222	11164	10944	9034	9163
J3B05036	JO	420	375	26.30	66	35.8	15.25	1.274	13618	13245	12498	9999
J3B05037	JO	420	375	26.97	66	35.8	15.25	1.242	10531	10241	9770	8668
J3H03033	JO	105	500	23.62	66	35.8	15.25	1.312	16820	11368	9743	8159
J3H03034	JO	105	500	22.93	66	35.8	15.25	1.368	12831	10963	10928	7952
J3H03035	JO	105	500	23.05	66	35.8	15.25	1.234	10169	9688	10081	8152
J3S03038	JO	210	375	22.81	66	35.8	15.25	1.265	11018	10026	9837	7668
J3S04032	JO	210	375	20.51	66	35.8	15.25	0.767	17504	24421	6946	12875
J3S04039	JO	210	375	21.06	66	35.8	15.25	1.139	8452	8336	8453	7516
J4B04121	JO	420	375	21.13	66	35.8	11.05	1.230	4555	4436	4462	3350
J4B18101	JO	420	375	16.71	66	35.8	9.82	1.505	14728	13351	13356	6673
J4B18102	JO	420	375	17.39	66	35.8	9.82	1.497	14105	12843	11412	6281
J4B21101	JO	420	375	17.42	66	35.8	9.82	1.472	28034	18845	18466	8309
J4S17101	JO	210	375	17.26	66	35.8	9.82	1.408	9567	9242	5663	6484
J4S17102	JO	210	375	16.13	66	35.8	9.82	1.289	8399	8294	2709	7004
J4S17103	JO	210	375	15.55	66	35.8	9.82	1.459	8087	8038	4521	4938
J5S16101	JO	210	375	20.09	66	35.8	26.60	1.423	18159	11645	10998	5367
J5S16102	JO	210	375	18.50	66	35.8	26.60	1.416	26317	11541	9983	4966
J5S17101	JO	210	375	18.81	66	35.8	26.60	1.443	20598	13339	12739	5801
J5S22031	JO	210	375	20.62	66	35.8	6.45	1.418	13300	11983	11793	7750
J5S25031	JO	210	375	20.69	66	35.8	6.45	1.421	13273	11961	11966	7317
J5S27031	JO	210	375	21.00	66	35.8	6.45	1.409	13792	12475	12261	8509
J6S03051	JO	210	375	16.78	66	35.8	4.98	1.248	9429	8076	8320	6329

A	B	C	D	E	F	G	H	I	J	K	L	M
thickness	100											
		length	height		brick		mortar	B	E_0	$E_{1/3}$	$E_{1/3}$	E_{90}
code				fc,mas	fc,bri	fc,Bo	fc,mor				calc	
		mm	mm	Mpa	MPa	MPa	Mpa		Mpa	Mpa	Mpa	Mpa
J6S29041	JO	210	375	17.32	66	35.8	4.98	1.253	7742	7053	6992	5395
J6S29042	JO	210	375	16.41	66	35.8	4.98	1.376	8445	7968	7637	5469
J9B25103	JO	420	375	8.88	66	35.8	2.83	1.526	24917	10956	10021	3401
J9B25104	JO	420	375	9.25	66	35.8	2.83	1.416	7793	4962	4744	2435
J9B28101	JO	420	375	9.02	66	35.8	2.83	1.521	22856	13436	12198	3927
J9S24101	JO	210	375	9.17	66	35.8	2.83	1.306	3800	3708	2000	2677
J9S25101	JO	210	375	8.26	66	35.8	2.83	1.382	3696	3630	2441	2345
J9S25102	JO	210	375	8.99	66	35.8	2.83	1.368	3651	3542	2740	2183
JKS24051	JO	210	375	27.29	66	35.8	37.51	1.213	11331	10614	10807	8685
JKS24053	JO	210	375	28.13	66	35.8	37.51	1.118	10863	9760	9855	8572
JKS25051	JO	210	375	27.02	66	35.8	37.51	1.067	11825	10169	10179	8771
JTB01081	JO	420	375	15.25	66	35.8	6.00	1.478	15459	10938	11027	5180
JTB01082	JO	420	375	15.34	66	35.8	6.00	1.484	12889	12395	11737	5047
JTB01083	JO	420	375	14.56	66	35.8	6.00	1.471	15711	12991	12557	4888
JXB10034	JO	420	375	22.71	66	35.8	17.60	1.170	7702	7656	6939	6958
JXB10035	JO	420	375	25.96	66	35.8	17.60	1.292	10480	10337	9417	8516
JXB10036	JO	420	375	24.14	66	35.8	17.60	1.381	12307	12188	11616	8821
JXH09031	JO	105	500	19.64	66	35.8	17.60	1.336	11580	11236	11416	8463
JXH09032	JO	105	500	22.59	66	35.8	17.60	1.361	12652	11743	11735	8455
JXH09033	JO	105	500	24.87	66	35.8	17.60	1.249	12111	10899	11136	8707
JXS10037	JO	210	375	23.23	66	35.8	17.60	1.203	7328	7246	7048	6312
JXS10038	JO	210	375	21.35	66	35.8	17.60	1.373	12188	10419	10262	7434
JXS10039	JO	210	375	20.93	66	35.8	17.60	1.338	10942	9505	9907	7068
K4B04031	CS	420	375	19.74	35	30	10.42	1.340	11788	9959	9965	7200
K4B05031	CS	420	375	18.79	35	30	10.42	1.277	10155	9741	9850	7430
K4B06031	CS	420	375	19.76	35	30	10.42	1.320	10033	9801	10041	7488
K4H26021	CS	420	375	39.09	35	30	9.82	1.271	12572	12531	8651	11232
K4H27021	CS	420	375	42.67	35	30	9.82	1.322	15102	14794	10403	12712
K4H28021	CS	420	375	35.71	35	30	9.82	1.236	14158	13480	5001	11339
K4S26021	CS	210	375	19.55	35	30	10.42	1.381	9357	9175	9418	7152
K4S27021	CS	210	375	21.33	35	30	10.42	1.336	9673	9154	9290	6854
K4S28021	CS	210	375	17.86	35	30	10.42	1.211	2588	2467	2339	1895
K5S03041	CS	210	375	19.17	35	30	6.45	1.323	6913	5540	5503	3838
K5S26031	CS	210	375	18.27	35	30	6.45	1.283	9426	6860	6456	4715
K5S28031	CS	210	375	16.49	35	30	6.45	1.372	7687	6332	6151	4297
K6B10031	CS	420	375	19.44	35	30	6.26	1.327	10386	8345	8336	5778
K6B11031	CS	420	375	20.72	35	30	6.26	1.322	10659	9848	9948	7214

A	B	C	D	E	F	G	H	I	J	K	L	M
thickness	100											
		length	height		brick		mortar	B	E_0	$E_{1/3}$	$E_{1/3}$	E_{90}
code				fc,mas	fc,bri	fc,Bo	fc,mor				calc	
		mm	mm	Mpa	MPa	MPa	Mpa		Mpa	Mpa	Mpa	Mpa
K6B12031	CS	420	375	19.92	35	30	6.26	1.344	8735	8064	8355	5766
K6S02031	CS	210	375	20.26	35	30	6.26	1.338	9143	7933	8132	5650
K6S03031	CS	210	375	19.03	35	30	6.26	1.227	2376	2316	1589	1795
K6S03032	CS	210	375	19.21	35	30	6.26	1.299	7957	7732	8067	5852
KTB01081	CS	420	375	15.00	35	30	6.00	1.432	9979	7389	7361	4058
KTB01082	CS	420	375	14.81	35	30	6.00	1.425	10128	8166	7062	4017
KTB01083	CS	420	375	14.74	35	30	6.00	1.404	10628	9572	9639	5512
P4B01111	PO	420	375	6.39	10	10	12.54	1.412	4416	4409	3560	3401
P4B01112	PO	420	375	4.30	10	10	12.54	0.703	7269	6304	5804	6453
P4B31104	PO	420	375	5.49	10	10	12.54	1.419	5349	5322	5450	3961
P4S31101	PO	210	375	2.89	10	10	12.54	1.252	1731	1521	1154	1398
P4S31102	PO	210	375	3.37	10	10	12.54	1.292	2344	1963	1769	1647
P4S31103	PO	210	375	3.00	10	10	12.54	1.103	4847	2987	1084	2476
P9B09121	PO	420	375	4.51	10	10	3.33	1.479	9045	7006	7064	2812
P9B09122	PO	420	375	5.05	10	10	3.33	1.466	9512	6138	5773	2724
P9B10121	PO	420	375	5.46	10	10	3.33	1.432	6617	5153	4855	2667
P9S04121	PO	210	375	3.51	10	10	3.33	1.332	2040	1599	1261	1453
P9S04122	PO	210	375	3.80	10	10	3.33	1.196	1439	1328	678	1298
P9S04123	PO	210	375	4.29	10	10	3.33	1.319	1902	1899	1156	1484
V1B21101	VE	420	375	14.13	32	14.2	47.89	1.383	5672	4762	4518	3223
V1B22102	VE	420	375	12.74	32	14.2	47.89	1.339	7535	5888	5818	4125
V1B22105	VE	420	375	12.94	32	14.2	47.89	1.398	7572	5773	5878	3456
V1S22101	VE	210	375	10.34	32	14.2	47.89	1.228	2567	2554	1398	2158
V1S22103	VE	210	375	9.18	32	14.2	47.89	1.296	2205	2203	1790	1759
V1S22104	VE	210	375	12.50	32	14.2	47.89	1.240	3220	3118	1445	2647
V2S07101	VE	210	375	8.78	32	14.2	2.27	1.336	4394	3611	3533	2396
V2S13101	VE	210	375	9.01	32	14.2	3.11	1.396	4534	3632	3568	2253
V2S16101	VE	210	375	8.31	32	14.2	3.11	1.342	7545	4934	4690	2799
V2S19101	VE	210	375	9.01	32	14.2	3.11	1.434	3704	3288	3219	1988
V2S22091	VE	210	375	8.15	32	14.2	2.27	1.379	3798	3189	3164	2066
V2S27101	VE	210	375	9.32	32	14.2	2.39	1.442	3388	3088	3065	1988
V2S28101	VE	210	375	8.69	32	14.2	2.39	1.318	3370	2679	2648	2013
V2S29101	VE	210	375	10.27	32	14.2	2.39	1.378	3976	3294	3239	2281
V4B04121	VE	420	375	11.49	32	14.2	9.82	1.036	5071	5087	4976	4780
V4B17101	VE	420	375	10.90	32	14.2	9.82	1.469	5790	5462	4339	3324
V4B18101	VE	420	375	10.93	32	14.2	9.82	1.447	6956	5177	5173	3043

A	B	C	D	E	F	G	H	I	J	K	L	M
thickness	100											
		length	height		brick		mortar	B	E_0	$E_{1/3}$	$E_{1/3}$	E_{90}
code				fc,mas	fc,bri	fc,Bo	fc,mor				calc	
		mm	mm	Mpa	MPa	MPa	Mpa		Mpa	Mpa	Mpa	Mpa
V4B18102	VE	420	375	11.27	32	14.2	9.82	1.482	4943	4926	4325	3184
V4B30111	VE	420	375	11.49	32	14.2	11.05	1.050	1824	1829	1792	1570
V4S16102	VE	210	375	8.85	32	14.2	9.82	1.387	3176	3144	2607	2372
V4S16103	VE	210	375	9.35	32	14.2	9.82	1.316	3004	2938	1859	2389
V5S05101	VE	210	375	10.43	32	14.2	26.60	1.425	3665	3151	2861	1423
V5S09101	VE	210	375	10.25	32	14.2	26.60	1.425	4044	2992	2667	1244
V5S10101	VE	210	375	9.47	32	14.2	26.60	1.427	3117	2976	2809	1421
V5S14031	VE	210	375	10.10	32	14.2	6.45	1.416	4594	4152	4003	2533
V5S18031	VE	210	375	10.66	32	14.2	6.45	1.448	4291	3924	3711	2385
V5S20031	VE	210	375	11.00	32	14.2	6.45	1.419	6226	5154	4463	3023
V6S03051	VE	210	375	9.44	32	14.2	4.98	1.438	5157	4283	4287	2724
V6S03052	VE	210	375	10.54	32	14.2	4.98	1.441	5251	3950	3860	2488
V6S03053	VE	210	375	10.66	32	14.2	4.98	1.256	4472	4227	4279	3449
V9B25102	VE	420	375	7.00	32	14.2	2.83	1.435	5270	4310	4161	2268
V9B28101	VE	420	375	7.47	32	14.2	2.83	1.468	3601	3317	3252	1848
V9B29101	VE	420	375	8.05	32	14.2	2.83	1.471	5018	4330	3913	2133
V9S24101	VE	210	375	6.25	32	14.2	2.83	1.405	2262	2238	1603	1770
V9S24102	VE	210	375	6.01	32	14.2	2.83	1.271	2657	2627	1661	2132
V9S25101	VE	210	375	7.30	32	14.2	2.83	1.368	2248	2213	1874	1605
VKS28051	VE	210	375	13.48	32	14.2	37.51	1.263	5106	4853	4976	4073
VKS28052	VE	210	375	13.98	32	14.2	37.51	1.233	4877	4639	4758	3711
VKS28053	VE	210	375	12.66	32	14.2	37.51	1.195	4637	4281	4360	3478
VTB03071	VE	420	375	11.90	32	14.2	5.71	1.413	5756	5219	5060	3635
VTB03072	VE	420	375	13.98	32	14.2	5.71	1.442	5794	5584	5574	3763
VTB27061	VE	420	375	11.38	32	14.2	5.71	1.433	6649	5119	4691	3251
VTB27062	VE	420	375	10.59	32	14.2	5.70	1.413	6375	4867	4634	3338
VTB28061	VE	420	375	10.75	32	14.2	5.70	1.414	6160	5873	5524	3996
VTB28062	VE	420	375	10.32	32	14.2	5.70	1.454	6844	5046	4703	2810

A.T. (Ad) Vermeltfoort is in 1952 geboren in Sint-Oedenrode. Na de lagere school ging hij, tegen het advies van de hoofdonderwijzer in, naar de LTS want hij wilde altijd al timmerman worden.
De LTS verliep voorspoedig, hij slaagde met lof, en hij mocht naar de MTS en daarna naar de HTS om bouwkunde te studeren. Direct na de HTS trouwde hij met Margriet Postulart en begon hij aan de studie bouwkunde aan de toenmalige TH nu TU Eindhoven. In de voor toen uitzonderlijk korte tijd van drie jaar en drie maanden studeerde hij af bij Prof. J.W. Kamerling op het ontwerp van een scheepsdieselmotoren fabriek en experimenteel onderzoek naar de rotatiecapaciteit van gewapend betonnen balken.

Daarna begon hij bij bureau Schiebroek Struik waar hij betrokken was bij de bouw van prefab betonnen silo's en het explosiebestendig maken van bedrijfsgebouwen.
In 1982 begon Ad als docent constructieve vakken aan de Pedagogisch Technische Hogeschool Nederland. Daar kwam zijn practische vooropleiding goed van pas bij het opleiden van leraren voor het middelbaar beroepsonderwijs en de nascholing van praktijkleraren van het MTO.
Hij was gedurende vier jaar gedetacheerd bij het Software ontwikkelpunt (SWOP) en vandaaruit o.a. betrokken bij het ontwikkelen van educatieve hulpmiddelen bij het, ook in het HBO en aan de TU/e bekende, programma PC-Frame waarvoor hij tevens een leerboekje schreef. Hij was tevens betrokken bij het LERO project dat diende om de integratie van software voor natuurkunde- en mechanica-onderwijs in het MTO te bevorderen.

In 1990 begon Ad part time (vanaf 1991 full time) als Universitair docent aan de TU/e bij de groep waar hij was afgestudeerd. Naast het verzorgen van onderwijs was hij in de eerste helft van de negentiger jaren rapporteur van CUR commissie B50, o.a. voor op druk belast metselwerk en proeven op op afschuiving belaste muren.
In 1996 was Ad als docent en in 1998 als cursusleider betrokken bij de PAO cursus steenconstructies.
Samen met prof. D.R.W. Martens organiseerde hij de in juli 2004 gehouden 13de Internationale Brick and Block Masonry conference (13th IBMaC).

Naast deze activiteiten was Ad free lance adviseur van een 150 tal woningen en bedrijfsgebouwen. Het grootste project was een showroom met magazijn en kantoor voor een automobielbedrijf, het mooiste een clubgebouw voor een tennisvereniging.
Ad is bijna 30 jaar getrouwd, heeft drie volwassen dochters, interesse in Heemkunde en hij fietst vaak naar zijn werk.